QUANTITATIVE DAMAGE ASSESSMENT OF CONCRETE STRUCTURES USING ACOUSTIC EMISSION

PhD Thesis

Paul Beck (BSc)

Cardiff School of Engineering
University of Wales, Cardiff
UK
2004

Prifysgol Cymru **SUMMARY OF THESIS** **University of Wales**

Candidate's Surname: Beck

Candidate's Forenames: Paul

Candidate for the Degree of: PhD

Institution at which study pursued:

University of Wales Cardiff

Full title of Thesis: Quantitative Damage Assessment of Concrete Structures using Acoustic Emission

Summary:

This thesis examines the role of Acoustic Emission (AE) as a non-destructive testing technique for concrete structures. The work focuses on the development of experimental techniques and data analysis methods for the detection, location and assessment of AE from the failure of plain and reinforced concrete specimens. Four key topics are investigated:

1. The identification of the optimum AE set-up for concrete monitoring.

Experimental results from a series of laboratory-based studies on concrete specimens are presented. The work considers the most suitable sensor and method of attachment for optimum sensitivity in the monitoring of concrete structures.

2. Methods of analysis for laboratory-based concrete specimens

Experimental results from a series of laboratory studies are presented. The work investigates methods of analysis including the parameter-based approach and a waveform-based analysis known as Moment Tensor Analysis.

3. Source location trials of AE from fatigue cracks

The applicability of AE techniques to monitor the integrity of the steel reinforcement encased in concrete is evaluated. The work considers the ability of AE sensors mounted to both the reinforcement and the concrete to detect fatigue produced by different loading methods. The ability to locate steel fatigue on sensors attached to both the steel reinforcement and the concrete is also explored.

4. **The detection of damage within an in-service concrete hinge joint**

Experimental results from an in-situ monitoring study of a concrete hinge joint are presented. The work considers the ability of AE methods to monitor concrete hinge joints (most significantly the condition of the reinforcement within the structure) via the study of AE source characteristics and the capabilities of source location.

Key Words: *Acoustic Emission, Plain Concrete and Reinforced Concrete, Moment Tensor Analysis, Reinforcement Fatigue, damage detection.*

ACKNOWLEDGEMENTS

I take this opportunity to express my great debt of gratitude to Dr. Karen Holford, Dr. Bob Lark and Mr Phil Cole for their excellent guidance, support and invaluable patience throughout this work. I thank Dr Rhys Pullin who for three years provided great friendship, moral support and technical assistance.

My thanks also to the staff of the Cardiff University Mechanical and Structural Engineering Divisions, particularly Dr. Aled Davies, Dr Sam Evans, Allan Coughlin, Alan Rowlands, Brian Hooper, Des Sanford, Len Czekaj, Carl Wadsworth, Andrew Sweeney, Harry Lane, Paul Leach, Mal Lyllal, Lisa James, Chris Lee and Bethan James.

I am also grateful to Timothy Bradshaw and Jon Watson of Physical Acoustics Ltd for their technical feedback and advice.

Finally I would like thank my family, especially my wife Helen for her financial and emotional support without whom I would have surely crumbled and folded before finishing this thesis.

GLOSSARY OF TERMS FOR AE TESTING

Absolute Energy: This is the true energy measure of an AE hit whose units are measured in attoJoules. Absolute energy is derived from the integral of the squared voltage signal divided by the reference resistance over the duration of the AE waveform packet.

AE Count: The number of times the signal amplitude exceeds the pre-set reference threshold.

AE Rate: The number of times the amplitude has exceeded the threshold in a specific unit of time.

AE Signal: The electrical signal obtained through the detection of AE.

Array: A group of sensors used for source location.

Attenuation: The reduction in AE signal amplitude as a wave propagates through a medium

Auto-Sensor-Test (AST): AST is a method of applying an artificial source to the structure by pulsing the PZT within the sensor. This method is generally used to distinguish the degradation of the contact between the sensor and the surface over a period of time.

Broad Band Sensors: High sensitivity over a wide frequency range.

Burst Emission: A qualitative term applied to AE when bursts are observed.

Continuous Emission: A qualitative term applied to AE when bursts or pulses are not discernible.

Couplant: A substance providing an acoustic link between the propagation medium and the sensor.

Duration: The interval between the first and last time the threshold has been exceeded by the signal.

Energy (MARSE): MARSE (**M**easured **A**rea under the **R**ectified **S**ignal **E**nvelope) energy is a relative value proportional to the true energy of the source event.

Event: A single AE source produces a transient mechanical wave that propagates in all directions in a medium. The AE wave is detected in the form of hits on one or more channels. An event therefore, is the group of AE hits that was received from a single source.

Event Rate: The number of events detected in a specified unit of time.

Felicity Ratio: The measurement of the felicity effect. Defined as the ratio between the applied load at which the AE reappears during the next application of loading and the previous maximum applied load.

Global Monitoring: Large scale monitoring of a structure where no specific flaws are known.

Hit: A hit is the term used to indicate that a given AE channel has detected and processed an AE transient.

Kaiser Effect: The absence of detectable AE until the previous maximum applied stress level has been exceeded.

Lamb Wave: In a medium bounded by two surfaces, i.e. a plate, at distances greater than a few centimetres from an AE source surface waves can couple to produce Lamb waves.

Location Group: An array of AE sensors (based on known placement between one another) for the purpose of determining the general or exact location of an event occurring near or within its detection area.

Local Monitoring: A source location examination of a known flaw.

Location Plot: Representation of sources of AE computed using an array of sensors.

Lockout Time: The minimum time following the detection of an event before the analysis software resumes event processing within a location group. This is typically set to the period of time taken for an AE signal to propagate from one sensor in a group to the most distant sensor in the given group. Use of a lockout time is intended to prevent reflections from a single source event being incorrectly identified as new events by the source location algorithm.

Noise: The signal obtained in the absence of any AE, the signal has electrical and mechanical backgrounds.

Parametric Inputs: Environmental variables (e.g. load, pressure, temperature) that can be measured and stored as part of the AE signal description

Peak Amplitude: Maximum signal amplitude within the duration of the signal.

Pencil Source: An artificial source using the fracture of a brittle graphite lead in a suitable fitting to simulate an AE event (also known as an Hsu-Nielson source).

Rayleigh Wave: Rayleigh waves are longitudinal and transverse waves which propagate in the bulk of the material combine in the region close to the surface.

Reference Threshold: A pre-set voltage level that has to be exceeded before an AE signal is detected and processed.

Resonant Sensor: A sensor that uses the mechanical amplification due to a resonant frequency to give high sensitivity in a narrow band.

Rise-time: The interval between the first threshold crossing and the maximum amplitude of the signal.

Sensor: A device that converts the physical parameters of a wave into an electrical signal.

Shear Crack: A crack is said to be a shear crack or have a shear dislocation motion when the displacement discontinuity is perpendicular to the normal.

Source: The place where an event takes place.

Source Location: The computed origin of AE signal.

Tensile Crack: A crack is said to be a tensile crack or have a tensile dislocation motion when the displacement discontinuity is parallel to the normal.

Velocity: The speed at which an AE wave propagates from one sensor to another. In some applications it is sufficient to use a velocity provided from a velocity chart for the material being tested. However, the effects of different wave propagation modes and structural geometry make it desirable to measure propagation velocity in a given source location application empirically, this is discussed further in section 3.3.4.

Wrap: In many source location cases the geometry of the structure is such that the sensors can be considered “wrapped”. A simple example is the case where one dimensional source location is performed around the circumference of a cylindrical specimen. In this case source location is also performed between the first and last sensor in the location group, i.e. in addition to the first and second sensor, the second and third, etc. In this way, source location around the entire circumference of a specimen can be achieved.

NOMECLATURE

$\boldsymbol{A}$	*Peak amplitude of arrival #1 signal*	*(V)*
$\boldsymbol{b}$	*Crack magnitude*	
$\boldsymbol{D}$	*Sensor spacing*	*(m)*
$G_{ip,\, q}$	*Spatial derivative of Greens function*	
l_k	*Vector which describes the crack motion*	
M_{pq}	*Moment tensor matrix, which is a 3x3 symmetrical matrix*	
n_k	*Normal vector to the crack surface*	
$\boldsymbol{R}$	*Distance from an AE source y to the sensor point x*	*(m)*
V_p	*Velocity of the P-wave*	*(m/s)*
Vref	*Reference Voltage*	*(V)*
Δt	*AE Signal arrival delay*	*(s)*
λ, μ	*Lame's constants*	
ν	Poisson's Ratio	
γ_l	*Direction Cosine*	
ρ	*Density of material*	*(kg/m^3)*

INDEX OF CONTENTS

CHAPTER 1. STRUCTURAL INTEGRITY ASSESSMENT OF CONCRETE STRUCTURES

1.1. INTRODUCTION

Due to the increasing age of concrete structures such as bridges and dams, there is a need for a practical non-destructive evaluation technique that can provide information about their structural integrity. Concrete bridges represent approximately 57% of the UK Bridge stock (Colombo *et. al.* 2001). The average age of these is of the order of 25-35 years and many are starting to show signs of deterioration. Because of this situation, the investigation of these bridges is a matter of topical concern. Similarly, in the USA, 29% of bridges are ranked structurally deficient and between 2001 and 2007 1.3 trillion dollars will be needed to rectify the problems (Frangopol *et. al.* 2001).

There are many reasons for deterioration in the UK concrete bridge stock. These include chloride contamination, sulphate and other environmental attacks, thermal effects, insufficient reinforcement, lack of protection against rain water, floods and fatigue which is caused by heavy vehicle loading. Many of these mechanisms have been studied using different types of non-destructive methods and much of the work on structural integrity has been undertaken in Japan where there is a particular need for monitoring due to the added problem of earthquakes.

This thesis examines the role of the Acoustic Emission (AE) technique for the monitoring of plain and reinforced concrete specimens and structures. The work focuses on the development of expertise, techniques and data for the detection, location and assessment of AE from crack sources. The aim of this research is to develop AE techniques for use in global and local structural monitoring of concrete damage, in order to provide a commercial tool for the non-destructive evaluation of concrete structures. This thesis comprises four primary themes:

- The identification of the optimum AE set-up for concrete monitoring.
- Methods of analysis for laboratory-based concrete specimens.
- The detection of steel rebar fatigue in laboratory-based reinforced concrete specimens.
- The detection of damage within an in-service concrete hinge joint.

The content of this thesis is made up over a total of nine chapters. Chapters 1 and 2 present background research and reference work. Chapter 3 details instrumentation and experimental techniques common to all the experimental work conducted. Chapters 4, 5, 6 and 7 describe all the experimental and analytical work undertaken. Each chapter is arranged such that the experimental procedure of each test set-up is described, followed by a discussion of the test results and the conclusions from each of the tests. Chapter 8 concludes the thesis drawing together all of the work described earlier, highlighting the most important and significant results. This chapter includes recommendations for further work. A glossary of all terms used throughout this work can be found at the start of the thesis. Chapter 9 provides a list of published material referenced throughout this thesis.

1.2. PROPERTIES OF CONCRETE

Concrete is an anistropic composite material composed of a coarse granular material (the aggregate) embedded in a hard matrix of cement paste (the binder), usually Portland cement and water. The historical development of Portland cement can be found in Neville (1999). The general composition of concrete includes 7-15% Portland cement, 14-21% water, 0.2-8% air, 24-30% fine aggregate and 31-51% coarse aggregate.

Concrete is often used as a structural material given its many advantages. These advantages include its ability to be cast, ability to be cast on site, durability, fire resistance and economy. However, it does have a few disadvantages. From an engineering viewpoint, it has low tensile strength, low ductility and suffers from some shrinkage over time. The low tensile strength of concrete can be related to the number of voids within the concrete specimen. Strictly speaking, the volume of all voids in concrete, capillary pores, entrapped air, gel pores and entrained air influence the strength of concrete. These will be discussed in the next section.

1.3. INTERNAL STRUCTURE AND STRAIN LOCALISATION OF CONCRETE

As already mentioned, concrete is a composite material containing cement, fine and coarse aggregate and water. The cement hydrates with the water to produce a cement paste; aggregate is dispersed in the paste to form the monolith known as concrete. At a mezo-level, concrete can be classified as a two-phase material, the cement paste and the aggregate, however the internal voids (with sizes ranging up to a couple of millimetres) may be included as another major component of the material. These voids include pores in the cement paste, cracks at the matrix-aggregate interface, shrinkage and thermal cracking (Shah and Ouyang 1994). These voids play an important role in the mechanical behaviour of concrete.

The interface between the aggregate and the cement paste is known as the interfacial transition zone (Shah and Ouyang 1994). Usually bleeding and segregation occurs in fresh concrete, thus some cracks form at the interface when the concrete is hardened. On the other hand, since the aggregate and matrix have different in modulus of elasticity, in their thermal expansion coefficient and response in change of moisture content, the transition zone is weaker than the bulk cement matrix (Neville 1999, Mehta and Monteiro 1993).

Hardening of fresh concrete is accompanied by the loss of moisture in the cement paste, causing shrinkage. Shrinkage is not usually uniform in cement paste because the loss of moisture is different for the interior part and surface area of the concrete. Shrinkage is usually restrained by the aggregate and the boundary conditions of the structure whilst casting. Both the non-uniformity of the shrinkage, the restraining power of the aggregate and boundary conditions create tensile stresses in some parts of the concrete, which may cause shrinkage cracks before loading. Similarly, an exothermic reaction is created during hardening and due to the non-uniform temperature distributions; thermal cracks may result (Shah and Ouyang 1994).

A range of non-destructive testing techniques have been used to study the strain localisation and internal structure of concrete. Shah and Choi (1999) used AE, digital speckle pattern interferometry and x-ray microtomography to study the behaviour of concrete in tension and compression. Maji and Shah (1988) used AE techniques to investigate the cracking and fracture mechanics of concrete and mortar beams.

1.4. FATIGUE

Fatigue is precisely defined by the American Society of Testing and Materials (ASTM, 1996) as "The process of progressive localised permanent structural change occurring in a material subject to conditions that produce fluctuating stresses and strains at some point or points and that may culminate in cracks or complete fracture after a sufficient number of fluctuations". Fatigue is an insidious form of mechanical fracture, although strictly speaking it is a cumulative damage phenomenon; deterioration may begin after only a few stress cycles, yet the visible signs of crack propagation leading to fracture may not appear until just before failure. The fatigue behaviour of structural components under dynamic loads is highly sensitive to a variety of parameters, including material properties, microstructure, component geometry, surface finish, loading history and environmental conditions, rendering a quantitative analysis of fatigue behaviour extremely difficult. Fatigue crack growth variation is exponential; therefore the rate of crack growth increases as the crack gets longer. This emphasises the importance of detecting cracks at the early stages of their development and growth.

1.5. FRACTURE MECHANICS OF CONCRETE

Crack propagation in concrete is difficult and complicated to follow due to the different mechanisms involved in the failure process. In recent years, a reasonable consensus has emerged among researchers and practitioners alike that the introduction of fracture mechanics concepts into the design of plain and reinforced concrete structures can improve structural reliability. The usual method is to use Linear Elastic Fracture Mechanics (LEFM), the mainstay of which is the stress intensity factor (K).

1.5.1. Linear Elastic Fracture Mechanics (LEFM)

When considering LEFM, it is important to distinguish the type of loading used. Loading is categorised into three types, as shown in Fig. 1.1: Mode 1 which is an opening mode (Tension), Mode 2 which is a shear mode and Mode 3 which is a tearing mode (Broek 1988, Karihaloo 1995).

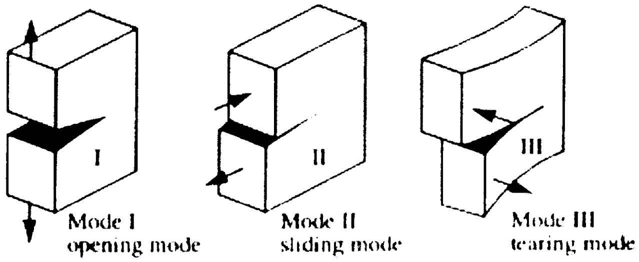

Figure 1.1. Classification of cracks in concrete specimens (Broek 1988)

When a concrete specimen is loaded in mode 1 a crack will propagate through the material. It is assumed that a crack with initial length a_0 will critically propagate through the material once the stress intensity factor at the tip of the crack reaches the critical value K_{ic} (Jenq and Shah 1988). This value is known as the fracture toughness of the material (Karihaloo 1995).

Many tests on concrete specimens have been performed to find the stress intensity factor or the energy release rate, which is related to the stress intensity factor. Munwam and Ohtsu (1999) studied stress intensity factors in concrete by using the AE technique, moment tensor analysis. Shah and Ouyang (1994) recommended using three-point loading on a beam notched at the centre and controlled by the amount of crack mouth opening, to determine the critical stress intensity factor.

1.5.2. Fracture Process Zone and Toughening Mechanisms

Since an inelastic region must exist at the crack tip of all real materials, stresses do not become singular. This region is often referred to as the fracture process zone, and since it is the one reason why LEFM is invalid, the topic is one of the most controversial in fracture mechanics.

If the fracture process zone (FPZ) is small compared with the specimen size then LEFM is still valid but since it has been found that the FPZ in concrete is not small then LEFM cannot be used. The presence of a large FPZ may be due to the heterogeneity of concrete. Many mechanisms that dissipate energy from the crack have been found responsible for the size of the FPZ. These include microcracking zones at the tip of the crack, bridging between two aggregate particles, deflection and arrest as a macrocrack reaches an aggregate particle and the friction caused as the crack surfaces move together. A full description of these mechanisms and how each effect concrete failure is given in Shah and Ouyang (1994), Francois (1984), Jenq and Shah (1988) and Shah and Ouyang (1993).

Many researchers have investigated the shape and size of the FPZ. A question which is frequently asked is whether the FPZ is located in front of the crack tip or behind it. Shah and Choi (1999) stated that the FPZ is active near the macrocrack tip. Based on the work of Castro-Montero *et. al.* (1990) using holographic interferometry it was found that the FPZ can be split into a wake zone located behind the crack tip and a smaller zone located at the front of the crack. The wake zone was found to increase with the size of the crack as a load is applied, but the front zone stayed primarily the same. Thus it was assumed that most of the toughening occurs behind the tip.

Other researchers who have used non-destructive methods to study the FPZ include; Zhang and Wu (1999) who compared AE data with load deflection data on beams undergoing three-point loading to study the FPZ, Shah and Choi (1999) who used a combination AE, and digital speckle pattern interferometry and x-ray microtomography to study the FPZ. Shah and Ouyang (1993) used laser holographic interferometry, image analysis and AE techniques to understand the toughening mechanisms found in quasi-brittle materials such as concrete.

1.6. PROPERTIES OF STEEL REINFORCED CONCRETE

The use of reinforced concrete as a structural material is derived from the combination of concrete that is strong and relatively durable in compression, with reinforcement that is strong and ductile in tension. Types of reinforcement include steel wire ropes or tendons, which have been used in grouted and un-grouted post-tensioned concrete bridges (Holford 1987, Cullington *et. al.* 2001) steel rebar, which has been used in a variety of different structures including concrete hinge joints (Lark and Mawson 2003, Pullin *et. al.* 2003) and composite materials such as fibre-reinforced plastics which have been used in the repair of damaged structures (Mouring *et. al.* 2001).

Much deterioration of structural concrete can be attributed to damage of the reinforcement. A range of diagnostic NDTs, such as impact-echo, ground penetrating radar and acoustic emission, have been used to monitor the integrity of reinforced concrete (RC). RC structures are susceptible to deterioration caused when aggressive agents permeate the surface layer of concrete and react with the steel reinforcement, resulting in corrosion. As the reinforcement corrodes, it expands and cracks the remaining cover of the concrete, accelerating the rate of corrosion. The deterioration process continues until the concrete covering the reinforcement spalls off leaving the reinforcement completely exposed to the environment (Yoon *et. al.* 1999). Another danger for the safety of a structure is pitting corrosion, which rapidly reduces the cross section of the reinforced bars at specific locations and creates areas of strain concentrations. This could lead to fatigue cracks propagating through the reinforcement.

When damage such as fatigue and corrosion occur, there is a need to monitor the integrity of the reinforcement within a structure as well as the cover concrete. The following section describes NDT techniques and their ability to detect steel and concrete damage.

1.7. NON-DESTRUCTIVE METHODS AND THEIR APPLICATION TO CONCRETE STRUCTURES

Material properties govern structural design. In the case of concrete structures, compressive strength is the one of the more important properties. The quality of a concrete structure depends on good construction practice especially during mixing, pouring, vibrating and curing. Inspections of concrete structures are needed periodically to maintain standards during construction. Non-destructive testing (NDT) has been widely used in the inspection of the condition of metallic structures but for concrete such techniques are less well developed, amongst which are radiographic, ultrasonic, magnetic, electrical, AE and thermography methods (Halmshaw 1991).. When deciding on which NDT technique to use there are many factors that need to be considered (McCann and Forde 2001) including:

(a) The required depth of penetration into the structure;
(b) The vertical and lateral resolution required for the anticipated structure;
(c) The contrast in physical properties between the structure and its surroundings;
(d) Signal to noise ratio for the physical property measured at the structure under investigation;
(e) Historical information concerning the methods used in the construction of the structure.

After considering these five factors an NDT technique or a combination of NDT techniques can be chosen.

1.7.1. Visual Inspection and Penetrant Methods

Visual methods with or without optical aids, tend to be neglected as a non-destructive testing technique but are, nevertheless, important. Using aids such as a pen-torch and magnifiers, cracks on the surface of the material can be found. Generally, though, this method is limited since defects can only be found on the surface of the material. To locate smaller defects, expensive magnifiers have to be used. In a large structure, this technique is time consuming and the use of visual methods can only take place in good light, which might not be suitable for all parts of a structure. Lark and Mawson (2003) conducted the visual inspection of the reinforcement of an exposed hinge joint. No damage was found which correlated with the results predicted by an x-ray inspection of the same joint.

Penetrant flaw detection methods are used for detecting surface defects such as cracks, laps and folds and can only be used on materials that have non-absorbent surfaces. Many cracks in engineering materials can be deep in spite of having a very small crack width on the surface. These cracks can be difficult to detect visually, so penetrant flaw detection is used as an extension of the method of visual inspection. Penetrants are coloured solutions or fluorescent dyes in oil based liquids. The basic principle is that a liquid, which wets the surface, migrates into the crack. Excess liquid on the surface is removed, and then a developer draws out the dye. This can allow cracks to become more visible. Since concrete is an absorbent material penetrant methods are not suitable.

1.7.2. Ultrasonic Testing (UT) Methods

Ultrasonic waves are mechanical vibrations, with a frequency above the human audible limit. The typical range of these vibrations for metals is between 500kHz and 10MHz (McCann and Forde 2001) but for concrete, is much lower. In fact, frequencies as low as 1kHz-20kHz have been used in concrete (Ohtsu and Sakata 1992) due to the high attenuation of high frequency waves in concrete.

In ultrasonic testing elastic waves are driven into the specimen and received by an output sensor. Since cracks and other deformities diffract elastic waves, the received waves can contain information on the geometry of cracks and defects.

Ultrasonic waves are generated and detected by piezo-electric (PZT) materials, which transform electrical energy into mechanical energy and mechanical energy into electrical energy. In ultrasonic testing, ultrasonic energy is generated in the form of pulse. These pulses travel through the specimen with some spreading and attenuation and will be reflected or scattered at any surface or discontinuity, such as a crack, within the specimen. This reflected or scattered energy can be detected by a second suitably placed piezo-electric sensor, which will convert the mechanical energy into electrical energy. The input transducer is known as the transmitter and the output transducer is known as the receiver. On some occasions it is necessary for the transmitter to be a receiver as well, these are known as transceivers (Halmshaw 1991).

Ultrasonic flaw detection has been used both in the laboratory and on real structures. Ohtsu and Sakata (1992) used ultrasonic testing to determine the crack depth of notched beams made out of plain concrete, steel-fibre reinforced concrete and reinforced concrete. Martin *et. al.* (2001) used ultrasonic testing on grouted duct post-tensioned reinforced concrete bridge beams to detect flaws and maintain the integrity of the structure.

As with all NDT techniques, ultrasonic testing has its advantages and disadvantages. Its advantages are that it can detect many defect types including voids, delaminations, impact damage, broken fibres, cracks, and inclusions. The technique is also very sensitive and can accurately measure crack depths of up to +/- 0.1mm. Its disadvantages include the time taken to perform the technique, the need for sensors to be attached to the specimen, the transmitters need for an electrical supply, which could be difficult when testing in remote places, and the fact that, due to attenuation, ultrasonic testing can only examine a small area at a time.

1.7.3. Impact-Echo

The impact-echo technique is based on the use of transient stress waves for non-destructive testing. The technique is very similar ultrasonic testing, except that the stress waves are generated by the mechanical impact of a small hammer. These pulses travel through the specimen with some attenuation and will be reflected or scattered at any surface or discontinuity such as a crack within the specimen. The receiver is placed adjacent to the impact to record reflected waves (Sansalone 1997).

Impact-echo was developed for use as a non-destructive testing technique for concrete in the 1980s', and can be used to detect the following (Sansalone 1997);

1. Structural Geometry; plates, circles, squares or rectangular bars and hollow cylinders such as pipes.
2. Flaws; cracks, voids, delaminations, honeycombing, surface-opening cracks.
3. The acoustic behaviour of interfaces between materials, as found in layered structures, repaired structures and in reinforced and pre-stressed structures.

Impact-echo was used in the diagnoses and repair of stone masonry structures (Sadri 2001) and the assessment of bridge decks (Scott *et. al.* 2003). The advantages of impact-echo are similar to the advantages of ultrasonic testing except that the time taken to produce the stress wave is quicker since the hammer is not attached to the surface. This can be a disadvantage since a strike by a hammer cannot be performed in all instances especially in compact locations and may not be repeatable.

1.7.4. Radiological Methods

Ever since X-rays were discovered in 1895, it has been acknowledged that they could be used as a non-destructive testing method. Records of industrial radiographs have been dated as early as 1896. X-rays are a form of electromagnetic radiation, of the same physical nature as visible waves, ultra-violet waves, radio waves etc. They have a wavelength range of 10nm to 10^{-4}nm, which allows them to penetrate materials with partial absorption during transmission. “Hard” high strength X-rays will penetrate up to 500mm of steel (Halmshaw 1991). Radioactive isotopes emit gamma rays, and like X-rays, they are used widely in industrial radiology. Gamma rays have similar properties to X-rays since they can penetrate many materials and are partially absorbed during transmission.

The amount of absorption will depend upon the thickness and the density of the specimen. Radiation will pass through the body and be can be detected and recorded on film, sensitive paper, fluorescence screens, Geiger Muller tubes and scintillation counters. Lead plates are placed behind this apparatus to absorb any remaining radiation that has passed through both the sample and recording apparatus.

Radiology is capable of detecting any fracture in a component or structure provided there are sufficient differences in thickness or density to that of the test piece (McCann and Forde 2001). Radiology has been mainly used in checking welds and in many cases; radiology is specified for the inspection of components. Very little radiology has been used in concrete structures, since its high density absorbs X-rays and gamma rays. An X-ray study was conducted on the River Usk Crossing, South Wales, to monitor the integrity of a concrete hinge joint. Results were very inconclusive although they did correlate with the findings of the intrusive study of the reinforcement (Lark and Mawson 2003). The advantages of radiology is that, due to its ability to penetrate, it can detect voids, internal cracks, variations in density and composition of concrete. The disadvantages of radiology are that for successful testing two sides of the structure are needed.

1.7.5. Infrared Thermography

Infrared thermography is a well-established tool for non-destructive testing. It is a process in which heat at any temperature can be converted into a thermal image using specialised thermal cameras. The range of applications for infrared thermography is varied; military applications, industrial applications, civil applications and medical applications (Titman 2001). It can be used to investigate a wide range of situations where fluctuations in the surface temperatures indicate defects or inclusions below the surface.

There are three types of conditions where thermography can be useful (Titman 2001).

a) If an object or defect in the structure has a different temperature, whether hotter or colder, to its surroundings a variation in the surface temperature will occur above the object. This variation may be an indication of the location of an object or defect, depending on the difference in temperature compared to the structure and the depth of the object or defect.
b) If the temperature difference between two surfaces (thermal gradient) is stable, and there is no significant variation in the thermal conductivity of the materials in the specimen then the surface temperatures over the warm and cool faces will be constant. If there is any object or defect present then there will be fluctuations in the surface temperature.
c) If the two previous conditions do not apply then the structure can be heated at one surface so that a stable thermal gradient is achieved. The heat applied depends on the thermal resistance of the materials and the initial temperatures of the two surfaces.

Since infrared thermography is temperature dependent, there are some situations where it is not applicable. Wind and rain both affect the surface temperature of the surface of the structure so a constant temperature gradient cannot be reached. During summer months, the initial temperature of the surfaces will mean that to create a stable thermal gradient the induced heat on the structure maybe so high that the structure is damaged. Infrared thermography is thus very sensitive to the environment and climate near the structure. Infra-red thermography has been used to monitor delaminations within a concrete viaduct (Clark *et. al.* 2001)

The advantages of infrared thermography are that due to the development of sophisticated portable thermal imaging cameras the procedure can be completed rapidly and with minimal access requirements. Thermography, unlike many NDT techniques does not require the shut down of structures to perform the testing. In fact, in many cases it is necessary in order to produce optimum conditions for the technique.

1.7.6. Fibre-Optic Sensors

Over the last few decades, electrical transducers and gauges have been the technology of choice for non-destructive measurements. Recently, fibre-optic methods have been developed and employed in many fields such as astrophysics, military, aeronautics, manufacturing and the power industry but very little work has been carried out with fibre-optics a concrete structures.

A fibre-optic is a glass fibre with a cylindrical core surrounded by a concentric cladding (Leung 2001), where the refractive index of the cladding is higher than that of the core. When light is sent through the core at low angles, total internal reflection takes place such that the light signal will be transmitted along the fibre with very small loss allowing a signal to travel great distances. The fibre is protected from scratches and environmental attack by a coating normally made of a polymer but in some cases can be aluminium or gold. The fibre may be attached to the material coupling with an adhesive or they may be set in the material during casting.

When an optical fibre is deformed, the signal is affected. For example, if the optical fibre is stretched then the light will travel a further distance from one end to another and there will be a change in phase of the optical signal. Similarly, if the optical fibre is flexed then some of the light will be refracted from the core into the cladding and will be dissipated into the material. As a result, the intensity of the light will decrease. These changes in property form the basis of fibre optic sensing (Huston *et. al.* 1992).

One major advantage of optical fibre sensors is that there is no electric current passing through the sensor, so optical sensors are not affected by electromagnetic interference. In addition, since glass fibres are not conductors, lightning will not damage the sensor or its instrumentation. Since light can travel great distance in optical fibres, they can be used to cover large distances. This is again suitable for monitoring bridges and dams. A significant disadvantage of using optical fibres for flaw detection is the cost of the method. Due to the novelty of the technique, the cost of the equipment and instrumentation is extremely high.

1.7.7. Ground Penetrating/Impulse Radar

Ground penetrating radar and impulse radar are two similar non-destructive testing techniques used for flaw detection in materials. The typical frequency range for ground penetrating radar is between 500MHz to 1 GHz but higher frequencies are used for impulse radar (McCann and Forde 2001).

In ground penetrating and impulse radar, electromagnetic waves are driven into a specimen by an antenna. Changes in the dielectric properties of the material caused by flaws, voids and inclusions results in the reflection of the electromagnetic waves. A suitably placed receiving antenna can detect these pulses. Given the velocity of the impulse radar wave through the different materials and the time interval between the transmission and received radar pulse, the distance from the surface and the reflecting object can be found. The velocity of the radar wave through the different materials can be found in many ways, Gordon *et. al.* (2001) describes these.

The applications of radar techniques for non-destructive testing are varied. The technique can locate voids, embedded reinforcement, delaminations, flaws and utilities embedded in the ground. Maierhofer and Leipold 2001 used radar investigations on masonry structures to detect air voids. Similarly a radar survey was undertaken on the historic masonry Bell tower at Cremona, Italy to detect air voids between leaves (McCann and Forde 2001).

The advantages in using radar techniques are that the method is quick, portable and accurate and the material is not damaged during testing. The disadvantages are that the technique is climate sensitive and only flaws near the apparatus are detected.

1.7.8. Summary

NDT methods have been described for the assessment of concrete structures. Application of the majority of these methods is still under research, but all of them have the potential for application to the reinforced concrete structures. Other NDT testing methods not discussed in this thesis include electrical methods such as the resistivity measurements and half-cell potential measurements and electromagnetic methods. Electrical methods use the resistance and potential difference measurements of a structure to determine the moisture content and rate of corrosion of the structure. These methods are quick and inexpensive and provide information about the integrity of the reinforcement within a structure. Electromagnetic methods are used to determine the depth and location of the reinforcement within a structure. Similar to electrical methods, electromagnetic methods are quick and inexpensive but are limited since they are affected by temperature and are only suitable for local monitoring.

Choice of the most appropriate procedure is usually based on a combination of factors as a cost, speed, reliability, and accuracy of the given method. Each of the methods has certain advantages and disadvantages. Adopting several testing methods and combining the results obtained usually acquires the best results.

CHAPTER 2. PRINCIPLES OF ACOUSTIC EMISSION (AE) AND ITS APPLICATION IN CONCRETE ENGINEERING

2.1. INTRODUCTION

Acoustic Emission (AE) is the term used to describe the spontaneous release of transient elastic waves resulting from local internal micro-displacements in a material. When a material experiences some form of structural alteration, transient elastic waves are generated. This phenomenon may be a result of an internally or externally applied mechanical stress that gives rise to changes in the material at atomic level. The result is a rapid release of strain energy and hence the generation of elastic waves (Spanner 1974). As these waves travel through the material, they become distorted. The modified signal, which arrives at the surface, is known as AE. The term AE also describes the technical discipline and measurement technique relating to this phenomenon.

From the definitions of AE, any damage process in a material that causes sudden localised changes in stress will result in the generation of transient elastic waves. In metals, these include plastic deformation by the slip mechanism, which involves the movement of dislocations and twinning, grain boundary sliding, fatigue and phase transformation. The definitions and details of these processes can be found in Smith (1996). AE sources in fibre composites include matrix crazing, fibre debonding and pullout, fibre-bundle failure, delamination and bond-line failures (Hanstead, 1998). In concrete or cement-based material, AE result primarily from micro cracking and other fracture processes (Shah and Choi, 1999).

The technology of AE traditionally had its beginning in the 1950s with the work of Joseph Kaiser. During the late 1950s and 1960s, researchers delved into the fundamentals of AE, developed instrumentation specifically for AE, and characterised the AE behaviour of many materials. In the 1970s, research activity became more co-ordinated towards NDT. Since the 1970s, AE has been used in many industries including nuclear, chemical and petroleum, aerospace, welding inspection and civil engineering. In these industries, the phenomenon of AE has been used for material characterisation, flaw detection and the integrity monitoring for structures (Beattie 1983). Drouillard (1996) has written a brief history of AE, its applications and its pioneers.

2.2. CHARACTERISTICS OF AE

AE sources are internal to the sample or material to be tested, originating from defects. The AE technique is a dynamic, "real-time" technique detected only if the stress field changes. This is in contrast to the static measurement made by conventional non-destructive tests such as ultrasonic testing methods and radiography. AE is irreversible since defect growth is irreversible. AE signals are transient and random in time.

2.2.1. Wave Propagation

The propagation of AE in a solid material is extremely complex. In an infinite medium waves propagate as bulk waves in two basic modes; as longitudinal waves (P-waves) and transverse waves (S-waves), each with a characteristic velocity that can be calculated from the density and elastic constants of the solid. If a surface boundary is introduced, both of these waves combine in the region close to the surface, so that the overall particle motion is neither purely longitudinal nor transverse. This type of surface wave is called a Rayleigh wave. The characteristic velocity of a Rayleigh wave can also be calculated and is generally slower than the bulk wave velocities. Another type of surface wave is called a Lamb wave, which is formed in a medium bounded by two surfaces. Lamb waves or plate waves are not generally found in concrete specimens or structures. The type of wave produced will affect the ability of AE techniques to monitor and locate AE from damage within a structure. A full description of each of these wave types can be seen in Pollock (1986) and Rindorf (1981).

2.2.2. Kaiser Effect

An important characteristic of AE is the Kaiser effect, which is named in honour of the researcher who first reported it. In practice it is often found that once a given load has been applied and the AE from that stress has ceased, additional AE will not occur until the stress level is exceeded, even if the load is completely removed and reapplied. This property has been found true in many materials but is not exhibited in others such as fibre-reinforced plastics.

Many researchers have suggested the appropriateness of the Kaiser effect for assessing the deterioration of concrete structures. Researchers discovered that the break down in the Kaiser effect correlated with the deterioration of the concrete specimen (Yuyama *et. al.* 1999a). Shiotani *et. al.* (1999) applied the principle of the

Kaiser effect to monitor the amount of damage within prestressed high-strength concrete piles. Yuyama *et. al.* (1995a) described a damage evaluation method for concrete structures based on the Kaiser effect, comparing the Load ratio (load at the onset of AE activity under the repeated loading / previous load) with the Calm ratio (the cumulative AE activity during unloading / total AE activity at the previous maximum loading cycle) to assess the amount of damage within the structure. Fig. 2.1 displays the relationship between the two ratios and the amount of damage. Similarly Yuyama *et. al.* (1999a) used the break down of the Kaiser effect to evaluate the integrity of an aging reinforced concrete dock that underwent three different loads. Yuyama and Ohtsu (2000) and Yuyama *et. al.* (1999b) describe a series of tests that were used to investigate the applicability of the Kaiser effect to monitor the integrity of RC structures.

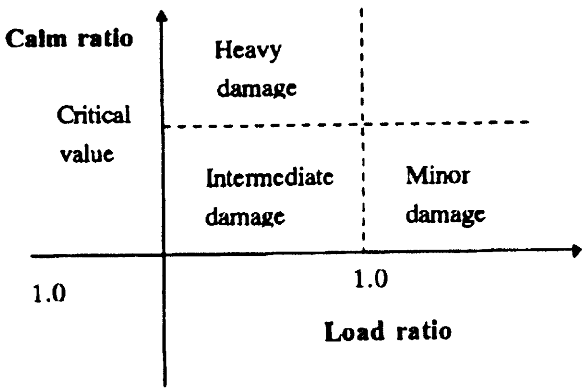

Figure 2.1. A damage evaluation method based on the Kaiser effect (Yuyama *et. al.* 1999a).

2.2.3. Attenuation

Another important characteristic of AE is the amount of attenuation of a signal as it travels through the material. As a stress wave propagates through a material from source to surface, the amplitude will remain constant in the absence of any dissipative mechanisms. In practice, there are always such mechanisms, and these cause the amplitude of the wave to decrease with distance. This is known as attenuation and is an important factor since the amplitude governs the detectability of the wave. The four causes of attenuation are:

1. Geometric spreading
2. Internal friction
3. Dissipation of the wave into adjacent media
4. Dispersion of signal components

In the region close to the source (the near field), the dominant attenuation mechanism is geometric spreading. In plates, where wave propagation can be considered two-dimensional, the signal amplitude decreases inversely as the square root of the propagation distance; this can give rise to relatively high attenuation levels over the first few centimetres of propagation. Further away from the source (the far field) where the majority of structural AE monitoring measurements are made, attenuation becomes dominated by absorption or conversion of sound energy into heat. Absorption usually has an exponential relationship with distance and a far-field attenuation co-efficient can be calculated, with units of dB per unit distance.

Dissipation attenuation can be caused by inhomogeneities in the propagation medium, which scatter the sound wave in the same material, for example grain structure in metals. However, it is most prevalent in specimens in contact with an adjacent liquid, for example a pipe or pressure vessel where energy can propagate readily into the surrounding media.

Attenuation due to velocity dispersion is caused because the different frequency components of a broadband Lamb wave travel at different velocities and the resulting spreading in time causes a loss in amplitude. The magnitude of amplitude loss depends on the slope of the dispersion curves and bandwidth of the signal.

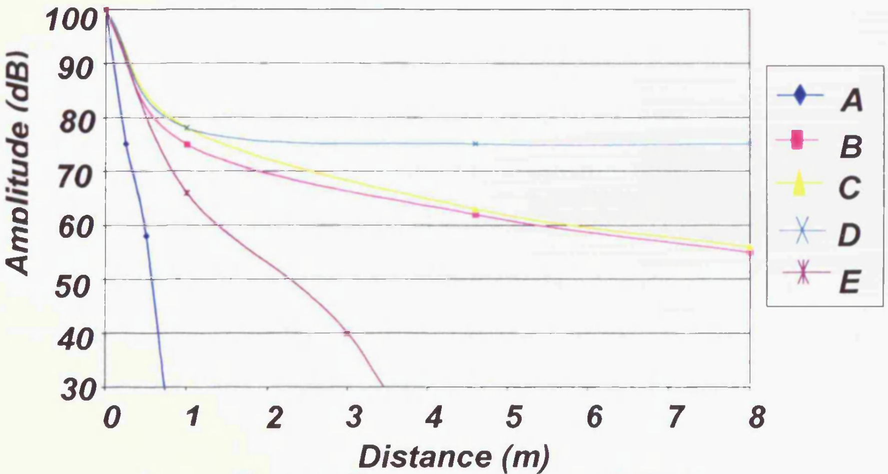

A= Carbon fibre composite - 150kHz

B= Inch thick steel pressure vessel – 150kHz

C= Steel pipeline – 60 kHz

D= Steel pipeline – 30 kHz

E= GRP composite – 60 kHz

Figure 2.2. Attenuation of transient signals for different structures and frequencies (Cole 1988)

Fig. 2.2 shows attenuation curves (signal amplitude versus distance) for a number of test objects, at different detection frequencies. It can be seen that at lower detection frequencies the signal will travel further. Ohtsu (1987) found that high frequency components in the MHz range are attenuated strongly due to the frequency dependence of attenuation and were impractical to detect in concrete.

2.3. BURST AND CONTINUOUS EMISSION

Traditionally AE has been classified into two different types, burst emission and continuous emission. Both of these are qualitative descriptions of the type of emission. Burst emission results in discrete signals, which are related to individual emission event(s) occurring within the material. The signal amplitude of a burst emission is much higher than that of continuous emission and the duration is much shorter. The main difference between burst emission and continuous emission is in the average event rate. Above certain values of average event rate, the length of the burst exceeds the time interval between them, leading to the inability of the instrumentation to resolve two successive burst emissions. The resulting superposition of the two bursts creates what is known as a continuous emission (Scruby 1985a). Burst emission appearing as discrete signals tends to offer more parameters for analysis. AE events in concrete are of the burst type (Ohtsu, 1987).

2.4. SIGNAL PARAMETERS OF AE

The objective of an AE test is to detect the presence of emission sources and to supply as much information as possible about the source. The technology for detecting and locating sources is well established and AE can provide large amounts of information about the source and the material under scrutiny.

Discrete or burst emission can be described by relatively simple parameters. Although emissions are rarely simple waveforms, they usually rise rapidly to a maximum amplitude and then decay exponentially to the level of background noise. Thus, they can be represented by a dampened sinusoidal wave.

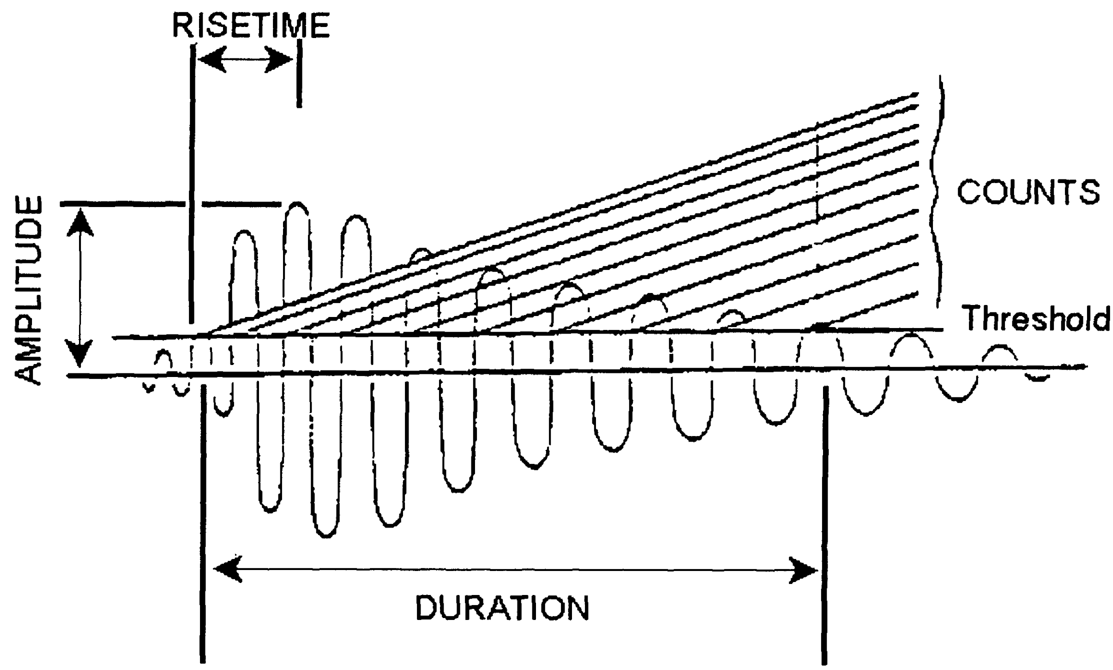

Figure 2.3. Waveform parameters (Miller and McIntire, 1987)

The threshold is the prime variable that controls the channel sensitivity, it also serves as a reference for the measurement of some waveform features used to characterise the hit. Parameters such as amplitude and duration, which can be used to detect the presence of damage, are displayed in Fig. 2.3.

One of the easiest methods of analysing AE is by the measurement of the AE count, also known as ring down counting (RDC). The principle of RDC is to count the number of times a threshold voltage is crossed by the waveform produced by the AE (Brindley *et. al.* 1973, Raj and Jha 1994). Count rate is the rate at which emission counts occur. The alternative to the ring-down counts is to count a whole burst of oscillations as one event. The disadvantages of using RDC are that it is geometry dependent, dependent on the transducer type and its coupling, it depends upon the precise detection threshold of the system (Raj and Jha 1994) and it fails to distinguish between a few large events compared with many small events (Dukes and Culpan 1984).

Other more important parameters of AE include the peak amplitude of the waveform, the amount of energy produced by the waveform, the duration of a waveform and the rise time of a waveform. The amplitude of an AE signal is the value of the highest peak attained by the waveform. Amplitude can be related to the intensity of an AE source and directly determines its detectability. To cope with the wide range of signal amplitudes that are produced, most modern AE systems measure the amplitude on a logarithmic scale in decibels (dB). The MISTRAS system measures the signal amplitude relative to a one μV signal at the transducer, the amplitude in dB is then given according to equation 2.1.

$$A = 20\log_{10}\left(\frac{V_s}{V_{ref}}\right) \tag{2.1}$$

Where: A = signal amplitude in dB
V_s = signal amplitude in μV
V_{ref} = reference voltage (1μV)

AE energy is the total elastic energy released by the material undergoing local changes. Therefore, the energy content of the AE signal can be related to this energy release. AE energy can be calculated using two different methods; the MARSE technique and the absolute energy technique. MARSE - the **M**easured **A**rea under the **R**ectified **S**ignal **E**nvelope- energy is not a true measure of the total energy of a source event, but a relative value proportional to the true energy of the source event. Absolute Energy is the true energy measure of an AE hit whose units are measured in attoJoules. Absolute energy is derived from the integral of the squared voltage signal divided by the reference resistance over the duration of the AE waveform packet. This method of calculating the energy of an AE hit is used throughout this thesis. Energy measurement has several advantages over count information because is it influenced not only by amplitude, but also by signal duration and is less dependent on the threshold setting.

Signal duration is the elapsed time (measured in microseconds) between the first threshold crossing to the last as shown in Fig. 2.3. Signal rise-time is the elapsed time from the first threshold crossing to the signal peak. The duration and rise-time of an AE signal is strongly governed by wave propagation processes and may be employed as a crude measure of signal dispersion. In some cases, rise time and duration can be useful in source discrimination, however, source characteristics and wave propagation effects in the test specimen must be well understood. Yoon et. al. (1999) showed that AE signals in reinforced concrete specimens could be separated into distinct bands by sorting on the basis of the duration and amplitude of the AE signals, which corresponds to microcracking within the concrete and bond loss between the reinforcement and the concrete.

Parameter analysis can also calculate the frequency of a hit using a number of different methods. The names given to each of these different frequencies are the average frequency, the reverberation frequency and the initiation frequency. The average frequency, reported in kHz, determines an average frequency over the entire AE hit. It is derived from other collected AE features, namely, AE counts and duration. The following real time calculation is performed to determine the average frequency.

Average frequency = AE Counts / Duration **(2.2)**

Reverberation frequency can be thought of as the "ring down" frequency since this is the average frequency determined after the peak of the AE waveform. Reverberation frequency is derived from AE features such as AE counts, counts to peak, duration and risetime. The following real time calculation is performed to determine the reverberation frequency.

Reverberation frequency = (AE Counts – Counts to Peak) / (Duration – Risetime) **(2.3)**

The initiation frequency can be thought of as the "Rise Time" frequency. This feature calculates the average frequency during the portion of the waveform from the initial threshold crossing to the peak of the AE waveform. This parameter has been used through this study since it best represents the frequency of the source. The following real time calculation is performed to determine the initiation frequency.

Initiation Frequency = AE Counts to Peak / Risetime **(2.4)**

Measurements of events, counts and energy generally provide an indication of source intensity or severity. Therefore, signal characterisation can be useful in providing an indication of the amount of damage that is accumulating within the test material. Modern techniques of processing and analysis, such as transient data capture, expert systems, computing neural networks, Fast Fourier Transforms (FFT), pattern recognition and adaptive learning networks, enable more detailed characterisation to be conducted.

2.5. LOCATION OF A SOURCE

One of the most useful aspects of AE monitoring, as a NDT method, is its source location capability. Several transducers are used over a large area of a structure to locate defects. Limited access to a structure is sufficient and the method is not affected by surface flaws or by defect size. The following methods are used to detect sources of AE in one dimension, two dimensions and three dimensions.

The zone location method is used to give an approximate location of a defect within a material. Given an array of sensors located on the surface of the structure, the sensor that records the higher amplitudes will be closer to the source. This occurs because the signal detected at the closest sensor has less attenuation than the others do. From this method, an approximate location can be estimated (Raj and Jha 1994, Carter 2000).

There are many ways of deducing the location of acoustic activity from the electrical output of AE sensors. Source location techniques may be classified by the type of AE source mechanism (continuous or discrete) and include amplitude measurement techniques, such as the zone and attenuation measurement methods and timing techniques, such as the cross-correlation, coherence and time of arrival (TOA) approaches. Some techniques are common to both categories, however, only the pertinent TOA methods for discrete source location are considered here.

Many source location applications are concerned with one dimensional source location. The method used to locate emissions in one dimension is known as linear location. If a source is known to be somewhere along a straight line between a pair of transducers a difference in the measured arrival times at the two transducers uniquely determines the source location. Pullin (2001) describes a method to determine the location of an event in one dimension between two sensors where the velocity of the source and the time of arrival on the sensors is known.

The method of locating a source of AE in two dimensions is known as triangulation. To be able to use triangulation, the velocity of the wave must be calculated and a minimum of three sensors must be attached to the structure. From the travel times and speeds of the waves arriving at each sensor, it is possible to calculate the distance between the source and each sensor. Knowing the distance, circles can be drawn centred at the sensors. The intersection of the three circles drawn from the three sensors should be the focus of the source (Pao 1978). The precision of source location is dependent on wave velocity calculation, time difference measurements and the accuracy of sensor positions. However, if the source cannot generate waves of sufficient strength for detection by the required number of sensors, then it will not be possible to calculate the location of the source. In many applications, when the area of interest lies beneath the surface, locating a source in three dimensions becomes important. This method is very similar to the one dimension and two-dimension location (Scruby *et. al.* 1986).

Source locations are valid over the entire area of the surface on which the sensors are mounted. There are practical limitations, but often the area of interest may represent a small area relative to the whole surface such as a joint or a weld. Secondary emissions produced outside the area of significance need to be rejected since they could limit the computer processing time available for data from the particular zone of interest. Guard sensors placed outside the zone of interest are used to limit the operational zone. If AE is detected so that the first sensor to be hit is a guard, then that signal is rejected and not processed. Only AE that first hits an active sensor is processed, limiting the monitored area. A diagram of this arrangement can be seen in Fig. 2.4.

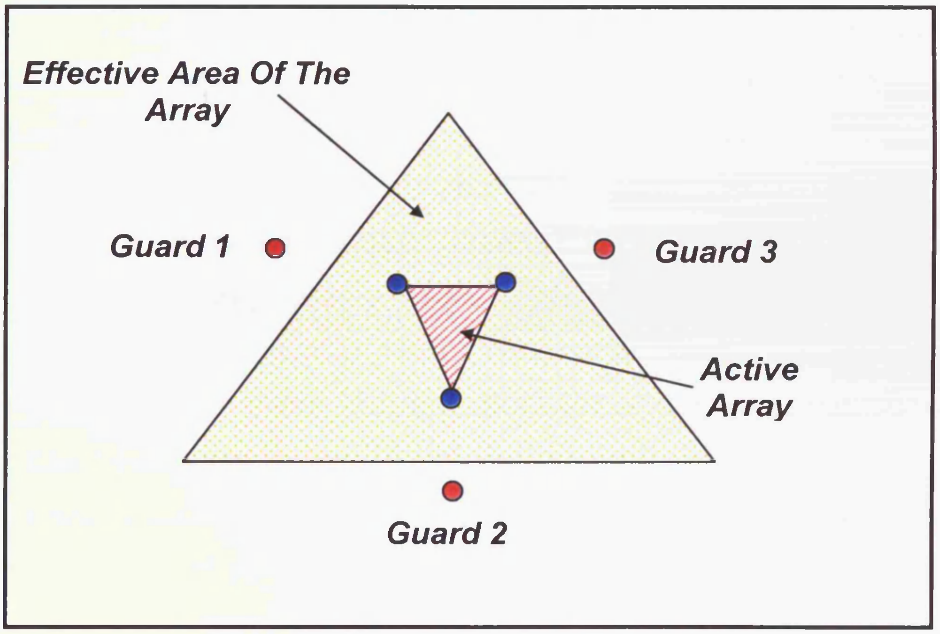

Figure 2.4. Restricting the active source location region using guard sensors (Carter, 2000)

Even though the accuracy of source location is affected by ambiguous solutions, weak acoustic sources, wave velocity calculations and time difference measurement calculations, source location is a helpful and necessary tool for NDT.

2.6. THE APPLICATION OF AE IN CONCRETE MONITORING

A variety of inspection methods have been studied to provide an early detection and warning for defects. As well as structural integrity, there is a need for an inspection method that can provide useful information about concrete, such as the development of cementitious materials and the study of fracture mechanics of concrete. A technique, which has been used to provide information on these topics, is AE.

Drouillard (1986) listed 76 papers referencing work performed on concrete with AE. Although not completely exhaustive, the list gives a useful compilation of the literature published on this subject from 1959 to the date of the article. Since 1986 many more papers have been published on AE and concrete. Much of this research has been conducted in Japan.

AE techniques have been applied to a variety of different applications in the field of concrete engineering. AE has been used to develop cement-based materials including high alumina cement and asbestos cement (Ohtsu 1996). An application to the concrete hardening process has also been reported in the development of autoclaved aerated concrete (Ohtsu 1989a).

Another application of AE in concrete engineering is to detect deterioration of concrete due to harsh environmental conditions such as freezing and thawing. Since concrete contains moisture, freezing results in micro cracking around water voids due to their increase in volume (Ohtsu 1996). There is another volumetric change after thawing. This results in micro cracking throughout the concrete specimen. AE monitoring has been used to investigate the damage caused by the freezing and thawing process in concrete. Ohtsu and Watanabe (2001) studied the effect of freezing and thawing of cylindrical concrete specimens over 300 cycles using AE methods.

The importance of fracture mechanics to determine the integrity of a concrete specimen or structure has been identified previously. AE measurements have been used to study micro and macro crack propagation in concrete. Based on the time differences between detection of the event at different sensors, crack sources can be located. From this it is possible to study the fracture mechanics of a propagating crack, such as the fracture parameters and the fracture process zone.

The fracture process zone (FPZ) is a much researched area because of its importance in the fracture of materials where linear elastic fracture mechanics does not apply, such as concrete. Frequently asked questions about the FPZ include: "Is the size of the FPZ a material parameter?" and "Does it depend on the shape and size of the specimen?" Zhang and Wu (1999) studied the FPZ by monitoring a notched concrete beam loaded under three-point bending using AE methods. It was found that the length of the FPZ was not a material parameter.

2.7. MONITORING OF CONCRETE STRUCTURES

AE is a NDT technique, which has been used to monitor many types of concrete structure including bridges, dams, tunnels, slopes and embankments (Ohtsu 1989a). In these structures, detailed observation is needed for the prediction of their service life. AE is a useful technique for the monitoring of structures since it is a dynamic inspection method that provides information on the growth of a discontinuity or defect and it can detect and evaluate emissions generated throughout an entire structure in a single test. In addition, AE methods will not interfere with the users of the structure, such as traffic and pedestrians.

The majority of in-service concrete structures in the field are reinforced with steel. The durability of concrete structures has become a matter of concern, primarily because of the corrosion of steel reinforcement. Research has been conducted to detect the initiation of corrosion. Li *et. al.* (1998b) applied AE techniques to detect steel rebar corrosion. By attaching an AE sensor to a length of steel rebar partially submerged in an HCl solution, the relationship between AE rate and rebar corrosion rate was studied. It was found that AE methods detected the onset of rebar corrosion earlier than other methods such as galvanic current and half-cell potential measurements. Idrissi and Limam (2003) performed similar tests using AE methods and found a perfect correlation between the evolution of the acoustic activity and the corrosion density current.

As well as monitoring the integrity of the reinforcement within a concrete structure, there has been a large amount of research into the use of AE techniques for monitoring laboratory-based specimens and in-service structures. Idrissi and Limam (2003) studied AE parameters such as duration and risetime to characterise

AE from concrete deterioration caused by steel reinforcement corrosion. Suaris and Van Mier (1995) characterised AE detected in concrete under biaxial loading. The source location from time of arrival methods was found to be in good agreement with the crack trajectories. As well as the parameter based approach and source location techniques, Moment Tensor Analysis has been used to provide information about concrete failure for laboratory and in-field specimens.

2.8. MOMENT TENSOR ANALYSIS

2.8.1. Introduction

For the monitoring of concrete structures it is commonly considered that there are two methods to analyse data acquired by conventional AE instrumentation. The first one, which has been more frequently employed, is the parameter-based approach. This method analyses AE based on the measurement of AE features such as amplitude, energy, duration, counts etc as described in section 2.4. The second method of analysis, which will be described in this section is a quantitative waveform analysis known as moment tensor analysis (MTA).

MTA is an AE post-test analysis technique used to identify the crack kinematics (crack type and crack orientation) from the recorded AE waveforms. The procedure developed for MTA was discovered by Ohtsu (1991) and is called *SiGMA* (*Si*mplified *G*reens function for *M*oment tensor *A*nalysis). This procedure determines the initial P-wave arrival time and amplitude of a recorded event from which a 3*3 symmetrical matrix can be calculated. After determining the eigenvalues of the moment tensor matrix, each eigenvalue can be separated into three individual components: the shear component, the CLVD component (compensated linear vector dipole) and the hydrostatic / mean component. By considering the ratios of these components, the AE sources can be classified as either tensile, mixed-mode or shear cracks. Secondly, the eigenvectors of the moment tensor will allow the orientation of the crack and the direction of the normal of the crack to be discovered. A full description of the theory behind MTA can be found below.

2.8.2 Theory of MTA

The displacement U_i (x, t) at a location x, at time t, due to a crack displacement b_K(y,t) is given by the integral (Ohtsu and Ono 1984)

$$U_i(x,t) = \int G_{ip,q}(x,y,t) M_{pq} s(t) ds \,. \qquad \textbf{(2.5)}$$

Where:

$G_{ip,q}$ = Spatial derivative of Greens function

s (t) = Source kinematics

M_{pq} is the moment tensor, which is a 3x3 symmetrical matrix as shown below.

$$M_{pq} = b\begin{bmatrix} \lambda l_k n_k + 2\mu l_1 n_1 & \mu(l_1 n_2 + l_2 n_1) & \mu(l_1 n_3 + l_3 n_1) \\ Symm & \lambda l_k n_k + 2\mu l_2 n_2 & \mu(l_2 n_3 + l_3 n_2) \\ Symm & Symm & \lambda l_k n_k + 2\mu l_3 n_3 \end{bmatrix}. \quad \textbf{(2.6)}$$

Where:

l_k = (l_1,l_2,l_3) = Displacement vector of the crack

n_k = (n_1,n_2,n_3) =Normal vector to the crack surface

λ,μ = Lame's constants

b = Magnitude of crack

Comparing simulated waveforms in a half space with detected waveforms, it is realised that the first portions of detected waveforms are in reasonable agreement with theoretical waveforms (Ohtsu and Ono 1988). The latter portions do not agree with the theoretical waveform due to the superposition of S-waves, reflected waves and surface waves. This suggests that only the first motions of the P-wave are discriminative in practical AE.

To solve equation 2.5, the original integral must be simplified so that only the initial motion of the P–wave is considered. The simplified integral can be represented as (Ohtsu 1991):

$$U(x,t) = \frac{\gamma_i \gamma_p \gamma_q M_{pq}}{4\pi\rho R(V_p)^3} \quad \textbf{(2.7)}$$

Where:

R = Distance from an AE source y to the sensor point x.

γ = Direction cosine

V_p = Velocity of the P-wave

ρ = Density of material

So, when an AE waveform due to a crack formation is recorded at the sensor, the amplitude of the wave's first motion is represented by the above formula. This means that when the AE waveforms are detected at six or more sensors, the AE source location procedure will attain information on the distance R, its direction cosine

$\gamma=(\gamma_1,\gamma_p,\gamma_q)$, and the amplitude of the initial P-wave. To summarise, from the AE source location and the material being used, the velocity of the P-wave, the density of the material, the distance from source to sensor, its direction cosine and the amplitude of the P-wave are known. Consequently, each component of the moment tensor M_{pq} can be calculated.

The kinematics of a crack is closely related to the principal components of the moment tensor. Since the moment tensor, represented by the matrix in Eq. 2.6, is a second rank tensor, determination of the principal components is readily performed by an eigenvalue analysis. For an isotropic material, the three eigenvalues are obtained from Eq. 2.6 as follows:

Maximum eigenvalue;

$$\omega = \mu b\left(\frac{l_k n_k}{1-2v}+1\right). \tag{2.8}$$

Intermediate eigenvalue:

$$\omega = \frac{2\mu b l_k n_k}{1-2v}. \tag{2.9}$$

Minimum eigenvalue;

$$\omega = \mu b\left(\frac{l_k n_k}{1-2v}-1\right). \tag{2.10}$$

Where v is Poisson's ratio.

Three eigenvectors corresponding to these eigenvalues are also determined.

$$\text{Maximum Eigenvector } = l_k + n_k. \tag{2.11}$$

$$\text{Intermediate Eigenvector } = l_k n_k. \tag{2.12}$$

$$\text{Minimum Eigenvector } = l_k - n_k. \tag{2.13}$$

The eigenvectors and eigenvalues determined from the moment tensor can be used to determine the orientation and the crack type of the source. The definition of a tensile and shear crack with respect to moment tensor is based on the dislocation motion or the displacement discontinuity of the crack surface. In the case that the displacement discontinuity is perpendicular to the normal, the crack is classified as a shear crack or has a shear dislocation motion. Conversely, for a tensile crack, the displacement discontinuity is parallel to the normal.

Considering this definition, for a pure **shear crack**, the angle between l and n is ninety degrees. Mathematically this means the dot product of l and n is zero, substituting this into the eigenvalues gives:

Maximum eigenvalue; $\omega = \mu b$. **(2.14)**

Intermediate eigenvalue; $\omega = 0$. **(2.15)**

Minimum eigenvalue; $\omega = -\mu b$. **(2.16)**

The eigenvalues can be represented by the vector *(X, 0, -X)*.

Similarly, for a **tensile crack,** the directions of l and n are parallel. Mathematically this means that the dot product of l and n is equal to one. This can be substituted into the eigenvalues in a similar method to the above to give:

Maximum eigenvalue $\omega = \dfrac{2\mu b(1-v)}{1-2v}$. **(2.17)**

Intermediate eigenvalue = minimum eigenvalue $\omega = \dfrac{2\mu bv}{1-2v}$. **(2.18)**

Two components, the deviatoric component and the Mean/Hydrostatic component represent a tensile crack. In seismology, the deviatoric components are known as the compensated linear vector dipole (**CLVD**) (Ohtsu 1989b, Knopoff and Randall 1970). The mean component can be calculated by adding the three eigenvalues and then dividing by three. The CLVD component is calculated by adding equations 2.17 and 2.18 and subtracting the mean component. The mean/hydrostatic component for all the eigenvalues is equal to:

$$\omega = \frac{2\mu b(1+v)}{3(1-2v)}. \quad \textbf{(2.19)}$$

The eigenvalues for the CLVD component are:

Maximum eigenvalue; $\omega = \dfrac{4}{3}\mu b$. **(2.20)**

Intermediate/Minimum eigenvalue; $\omega = \dfrac{-2}{3}\mu b$. **(2.21)**

From these values, the vector *(Y, -0.5Y, -0.5Y)* represents the eigenvalues for the CLVD component and the vector *(Z, Z, Z)* represents the eigenvalues for the mean component. This is shown diagrammatically in Fig. 2.5.

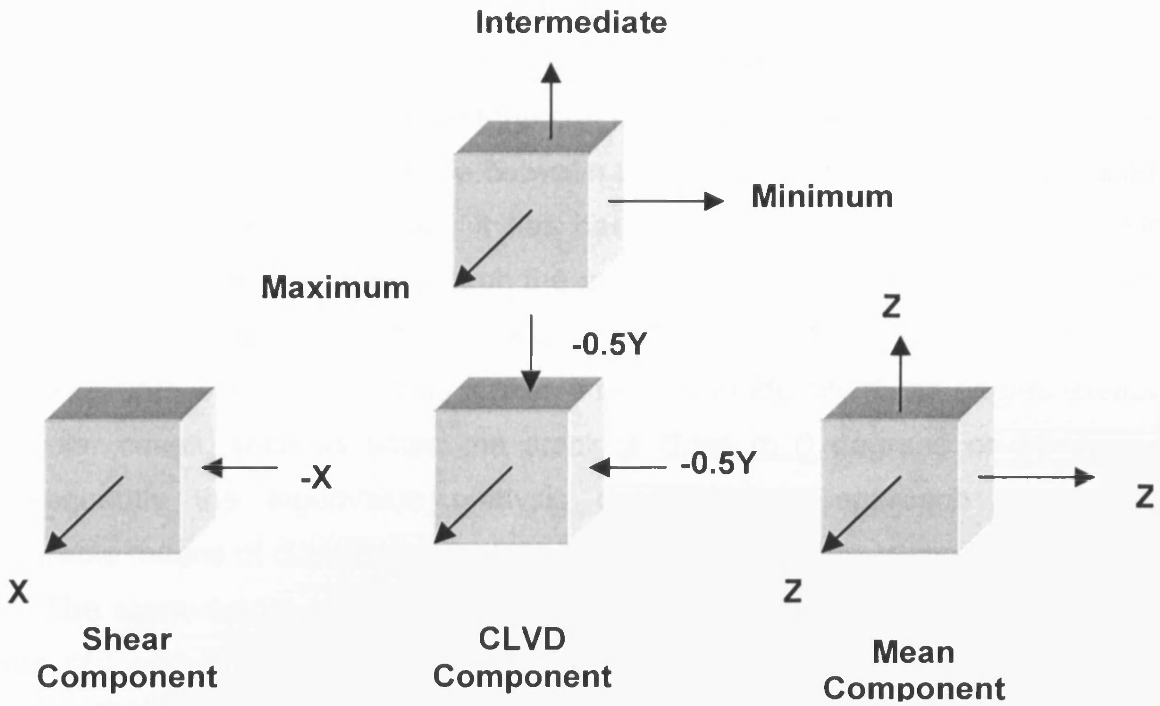

Figure 2.5. Illustration of eigenvalues for the three crack components (Shigeishi and Ohtsu 1999)

By comparing each side of the cubes and normalising by the maximum eigenvalue, equations 2.22, 2.23 and 2.24 can be derived.

$$\frac{MaxEigenvalue}{MaxEigenvalue} = X + Y + Z = 1 . \tag{2.22}$$

$$\frac{IntermediateEigenvalue}{MaxEigenvalue} = -0.5Y + Z . \tag{2.23}$$

$$\frac{MinEigenvalue}{MaxEigenvalue} = -X - 0.5Y + Z . \tag{2.24}$$

Since the eigenvalues are known, these equations can be solved simultaneously so that the values for X, Y and Z can be calculated. Since X is defined as the shear component, for a pure shear crack X = 100%. Similarly if X = 0%, then there is no shear component and the crack can be classified as a pure tensile crack. If the X component is less than 40% then the crack is tensile. If the X component is between 40% and 60% the crack is a mixed-mode crack. For X values greater than 60% the crack can be classified as a shear crack. These values, which are used to categorise events into shear, tensile or mixed-mode are the commonly used values and were suggested by Ohtsu (1991).

It has been previously stated that for a shear crack the angle between the direction of motion and the crack normal are perpendicular whereas the angle between the direction of motion and the crack normal are parallel for tensile cracks. It has been suggested that the angle between the motion and normal could be used to classify the crack type. However it has been demonstrated (Ohtsu *et. al.* 1998a, Ohtsu *et. al.* 1998b) that even though the angle between the two directions could be over 50 degrees, the dislocation between the two crack faces could still be mainly tensile (events with X < 40). This makes it difficult to identify these angles except in particular cases, such as when the crack is close to 0 degrees or 90 degrees. Consequently the eigenvalue analysis decomposition approach is the most favourable means of classifying cracks as shear, tensile or mixed-mode.

The eigenvectors of the moment tensor matrix in Eq. 2.6 can be represented in terms of I and n (the orientation and the normal of the crack). From eigenvalue, analysis the eigenvectors can be calculated, as given in equations 2.11, 2.12 and 2.13. Using these equations, the direction of motion and the normal of a crack can be calculated. Throughout this thesis, the SiGMA procedure has been performed using software known as MT-TRA, supplied by PAC (Physical Acoustics Corporation).

2.8.3. P-wave Determination and Error Estimation

To perform moment tensor analysis on recorded waveforms the initial amplitude and time of the P-wave have to be determined. An example of P-wave selection can be seen in Fig. 2.6. To be able to locate in three-dimensions and determine the components of the moment tensor matrix an array of six sensors is needed, thus for one event the initial P-wave amplitude and time must be selected for six waveforms. Li *et. al.* (2000) and Landis *et. al.* (1991) discussed P-wave arrival determination for concrete specimens. These papers review techniques used previously for P-wave selection including a procedure for the automated determination of P-wave a rrival time for AE source location using an adaptive moving average filter for removing random noise and Laplacian filters to enhance the amplitudes of the first motion. In this study visual inspecting methods similar to those used by Li and Shah (1994) are used to determine the initial P-wave arrival times and amplitude.

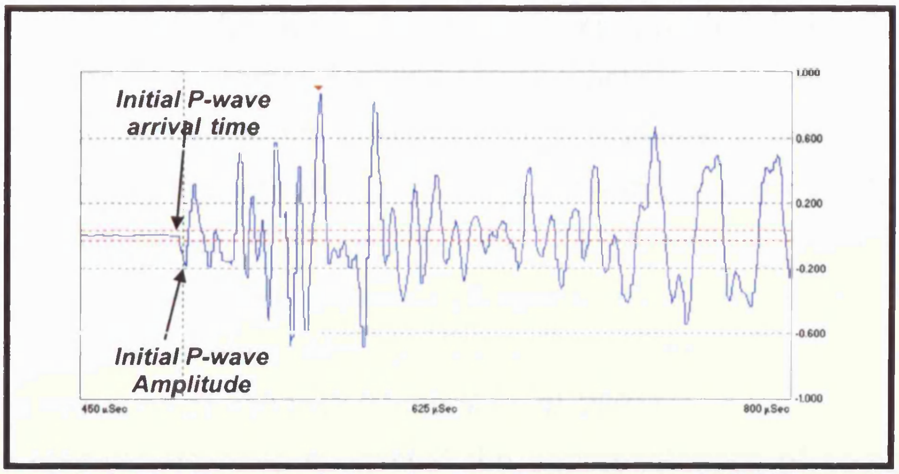

Figure 2.6. Initial P-wave determination from a recorded AE waveform.

Because cracks are produced from inside the material and the location accuracy of the AE events is limited, the verification of SiGMA solutions cannot be performed visually. To estimate the errors in SiGMA solutions and screen out solutions, a post-test procedure has been developed by Ohtsu *et. al.* (1994). Synthesized AE waveforms are first computed using equation 2.5 from the crack kinematics determined from the SiGMA solutions obtained from experiments. Then, the SiGMA procedure is applied to the synthesized waveforms. If the moment tensor analysis of the synthesized event produces a reasonable agreement to the original moment tensor analysis (a difference of less than 5mm for source location and a difference of less than 5% of the shear ratio) then the event can be selected as a reliable solution. The researchers claim that this method allows screening out of the poor solutions and verification of the solutions determined from the experiments.

2.8.4. Applications of MTA

The moment tensor representation has been used mainly to model the mechanisms of earthquakes. The mechanisms of earthquakes and of AE sources are in principal the same, in spite of the fact that the strengths and frequencies differ by orders of magnitude. Therefore, similar modelling can be used for AE sources. MTA has been used successfully on concrete in many applications. An early use of MTA was reported by Ohtsu (1989) who performed a pullout test on an anchor plate embedded into a concrete specimen. AE was collected using six AE sensors and was analysed using MTA software. The results showed both shear and tensile cracks situated around the pullout area.

Li *et. al.* (1998) performed MTA on waveforms recorded during the loading of concrete specimens with carbon-fibre reinforced plastics and glass-fibre reinforced plastics externally bonded to the bottom of the specimens. It was shown that AE techniques detected crack initiation, source location and could classify crack type and orientation effectively. Other applications of MTA include: the study of plain concrete and other cementious materials (Shigeishi and Ohtsu 2001), the study of fracture mechanic parameters (Munwam and Ohtsu 1999), and the study of other rock like materials such as salt rock (Manthei *et. al.* 2001).

Many researchers have suggested the appropriateness of comparing MTA results with the breakdown of the Kaiser effect to assess the deterioration of concrete structures. Yuyama *et. al.* (1995a) compared MTA results from events recorded during the failure of a reinforced concrete beam, loaded and unloaded with increasing loads in flexure with the breakdown of the Kaiser effect and showed that during the deterioration of the Kaiser effect the contribution of shear cracks increased with the progress of the fracture.

Yuyama and Ohtsu (2000) and Yuyama *et. al.* (1999b) review the results of laboratory-based tests and field applications. These articles cited research described above and discuss results from other articles such as: MTA of RC beams deteriorated due to corrosion of the reinforcement (Murakami *et. al.* 1993), MTA of an arch dam during construction cooling and grouting (Minemura *et. al.* 1998) and MTA of a grout injection process of a dam (Ueda *et. al.* 1991)

CHAPTER 3. EXPERIMENTAL EQUIPMENT, PROCEDURES AND ANALYTICAL TECHNIQUES

In this chapter, specific aspects of AE equipment are considered and some important terminology, conventions, procedures, analytical techniques and data used throughout this thesis are described.

3.1. INSTRUMENTATION

Equipment for processing AE signals is available in a variety of forms ranging from small portable instruments used for routine field tests to large multi-channel systems. Common components to all systems are sensors (often termed as "transducers"), preamplifiers, filters, amplifiers, microcomputers and analysis software. Methods used for measurement, display and storage vary widely accordingly to the application and its demands. The following sections introduce the key aspects of AE instrumentation with specific references to the hardware used throughout this study, the MISTRAS 2001 system (PAC 1995) and the DISP system (PAC 2001), manufactured by Physical Acoustics Corporation (PAC).

3.1.1. Data Acquisition

(a) MISTRAS

The MISTRAS system (**M**assively **I**nstrumented **S**ensor **T**echnology for **R**eceived **A**coustic **S**ignals) is a fully digital, multi-channel computerised system that performs AE signal waveform acquisition and feature extraction and stores, displays and analyses the resulting data in real time.

The AE signals from the loaded structure are converted into electrical signals by the sensors, amplified to usable voltage levels by pre-amplifiers and measured in the AEDSP (**A**coustic **E**mission **D**igital **S**ignal **P**rocessor) cards. A simplified block diagram of an AEDSP board is shown in Fig. 3.1. Each board provides two AE channels and is plugged in to the ISA (**I**ndustry **S**tandard **A**rchitecture) slot of a Personal Computer (PC). Multiple boards can be configured to provide the desired number of channels. A simplified block diagram of the entire AE system is shown in Fig. 3.2.

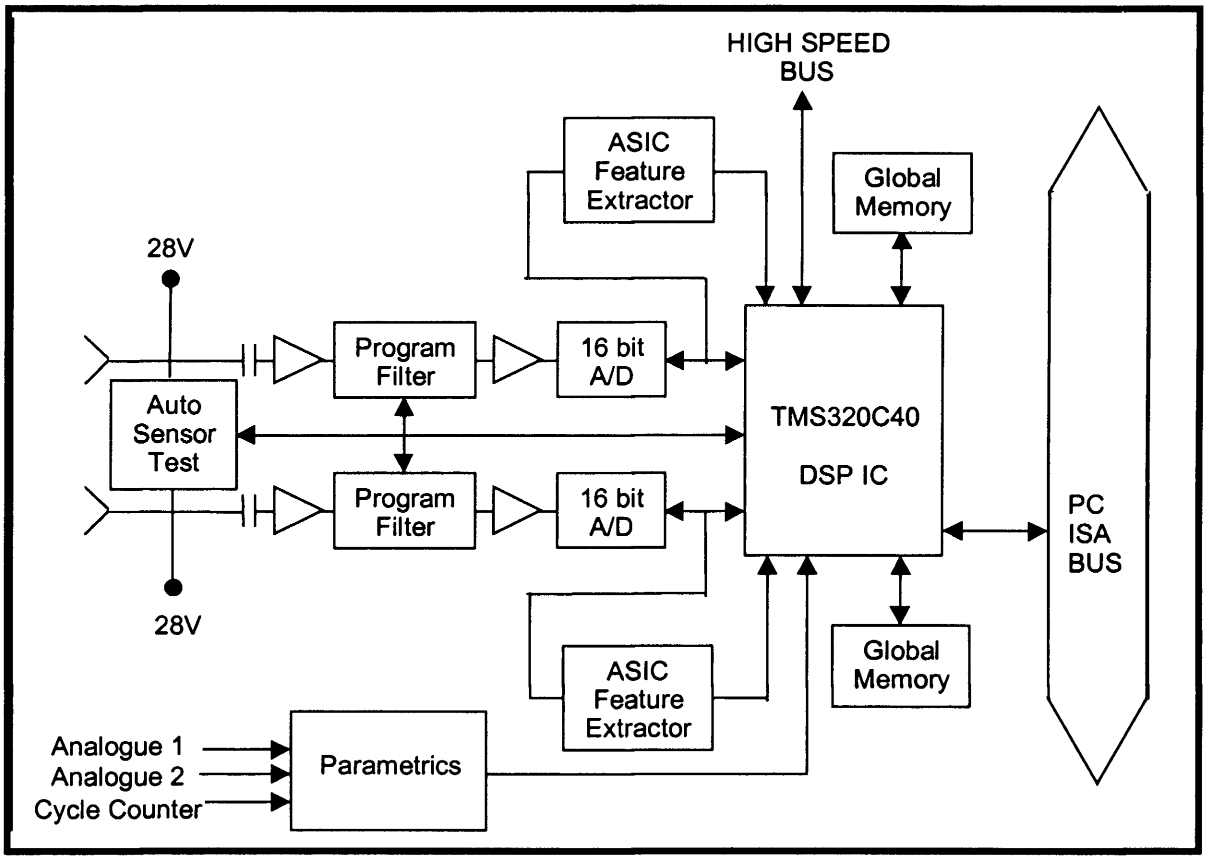

Figure 3.1. AEDSP block diagram (PAC, 1995)

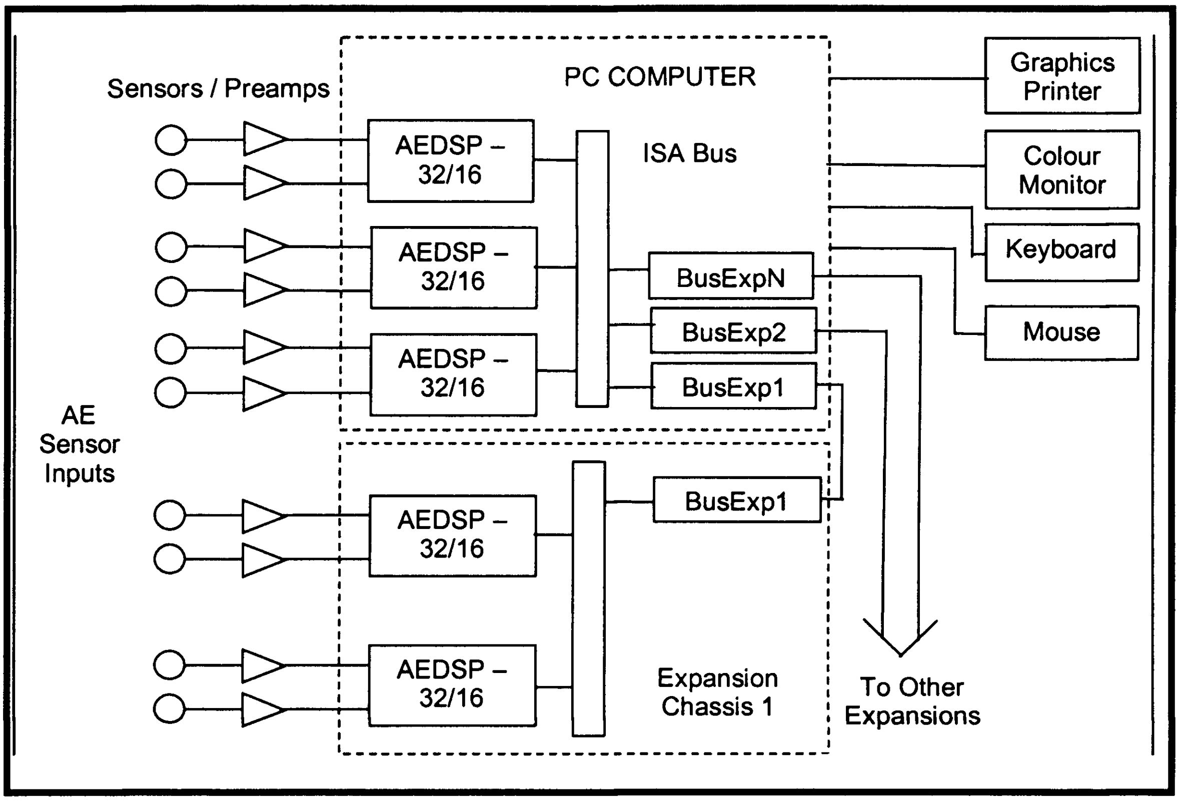

Figure 3.2. MISTRAS system block diagrams (PAC, 1995)

The AEDSP boards can operate in two modes, depending on the type of data required. The software known as MI-LOC (**MI**STRAS **LOC**ATION) is primarily used for source location and to provide AE feature data for a statistical analysis of the detected AE signals. AE signal features are measured via a hardware-based feature extraction process at a rate in excess of 20000 hits per second. The AEDSP boards can also perform time-based feature extraction at programmable intervals from 1msec to 60 seconds. The time-based information can include parametric data from two channels. A parametric input is an external voltage proportional to some test parameter such as load, strain or deflection, which can aid in the analysis of AE data. Since AE monitoring is carried out in the presence of background noise, there is a need for a detection level set somewhat above the background level. This level, known as the threshold level, is a pre-set voltage level that has to be exceeded before an AE signal is detected and processed. The threshold is fixed at a certain value prior to monitoring.

The second mode of operation is the "MI-TRA" (MISTRAS TRANSIENT RECORD ANALYSIS) software. This is used to measure and store full AE signal waveforms (transient signals), providing a complete record of individual source events. In this mode a detailed analysis of both time and frequency domain characteristics can be performed. Parametric data associated with each signal can also be recorded. Using this software, AE signal waveforms can be recorded both independently on all channels or synchronised. In synchronised mode, the first hit channel triggers all other synchronised channels. Therefore the hit time arrival between different channels can be seen. This is useful for certain post-test analysis techniques especially moment tensor analysis as described in section 2.8.

(b) DISP

DiSP (**Di**gital **SP**artan) is the name for the PAC AE product based on integrating one or more PCI-DSP cards into a computer or a multi channel chassis. Similar to the MISTRAS, the DiSP is a fully digital, multi-channel computerised system that performs AE signal waveform acquisition and feature extraction and stores, displays and analyses the resulting data in real time.

The terminology DSP describes the Digital Signal Processor that resides on the PCI-DSP card. A DSP is a special purpose microprocessor that is specifically made for high speed processing, data manipulation and mathematics relating to the processing of digital signals. The PCI or Peripheral Component Interconnect is a high speed PC computer bus available in most of today's PC computers. It offers 32 bit wide data paths and up to 132Mbytes/second data transfer speeds. A simplified block diagram of a PCI-DSP board is shown in Fig. 3.3. Each board provides four AE channels.

An advantage of the DiSP is that it can record up to 8 parametrics with update rates up to 10,000 readings per second. The DiSP software (DiSP-LOC and DiSP-TRA) is similar to the MISTRAS system, providing information such as source location, feature extraction, and time-domain transients including the ability to compute the Fast-Fourier Transform of the transient. Both of these multiple processing systems will be used throughout this study.

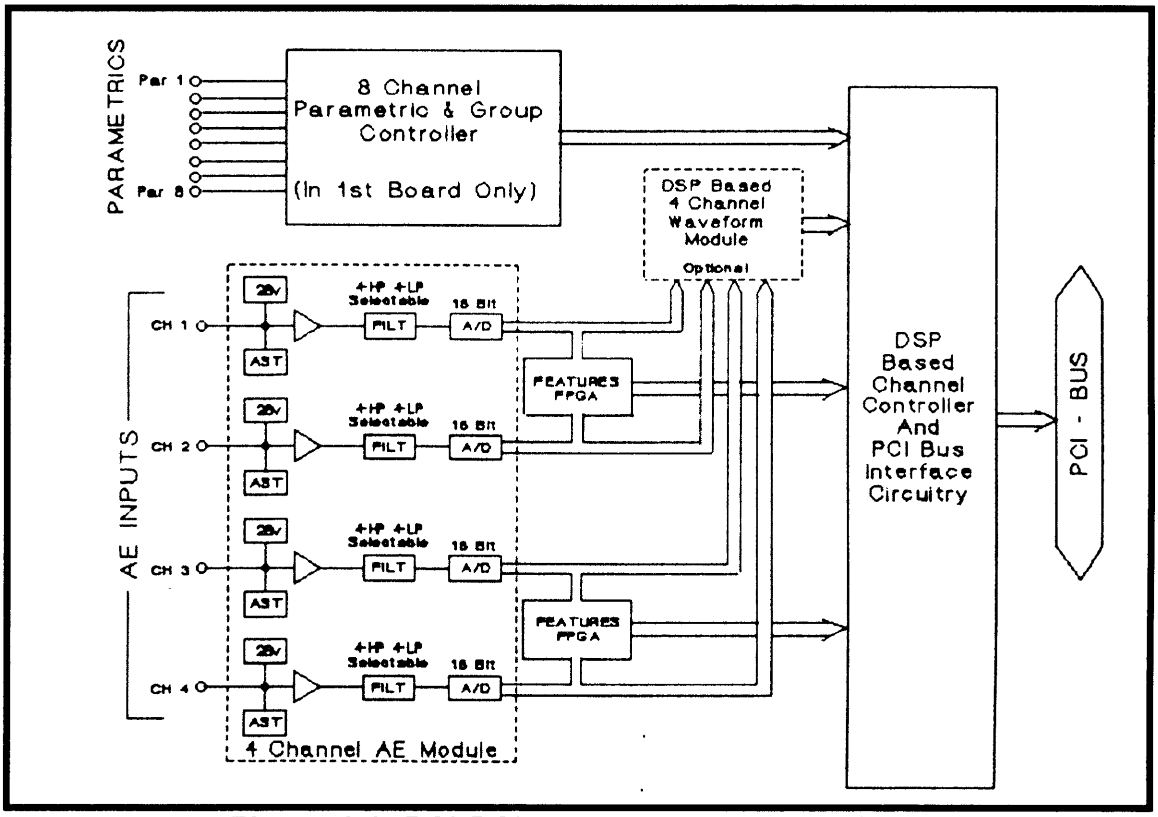

Figure 3.3. PCI-DSP board block diagram (PAC 2001)

Another software package used throughout this study is known as NOESIS. This package enables analysis of data recorded on both the MISTRAS and the DiSP systems. NOESIS is a sophisticated pattern analysis and recognition software for the use of both AE features and waveform data. This software includes statistical and neural network based analysis and classification, data clustering and data visualization in two and three dimensions. NOESIS also allows for advanced post-test manipulation, filtering and data visualization compatibilities. NOESIS does not allow the analysis of data with respect to location.

3.1.2. AE Sensors

AE sensors fall into two general categories, (a) resonant, which use transduction devices known as piezoelectric (PZT) crystals and, (b) non-resonant, such as electromagnetic, strain, capacitance and laser interferometry (Swindlehurst 1973, Scruby 1985b). Non-resonant sensors can be used to detect emissions of frequencies up to 20MHz. PZT resonant sensors have a frequency range from 10kHz-1MHz. PZT sensors are mainly used due to their higher sensitivity, robustness, and ease of application and availability of a wide range of response characteristics at relatively low costs. In this section only PZT transducers will be discussed. A transducer converts mechanical movement into an electric signal.

A PZT element contains a crystalline structure such as quartz. In more sensitive sensors, ferroelectric materials, such as Lead Zirconate Titanate, are used (Beattie 1983, Wadley et al. 1980). When the crystal lattice is deformed, relative displacement of the positive and negative charge generates a voltage between opposite faces of the crystal. This voltage is directly proportional to the degree of distortion. Microscopic deformations at the surface of the specimen produce a voltage signal, which can be amplified and analysed. Fig 3.4 is a schematic diagram of a typical AE sensor mounted on a test object. The active element is a piezoelectric ceramic with electrodes on each face. One electrode is connected to electrical ground and the other is connected to signal lead. A wear plate protects the active element. Surrounding the active element is a damping material that is designed so that acoustic waves can easily propagate into it with little reflection back to the active element. The sensor casing provides a shield to minimise electromagnetic interference.

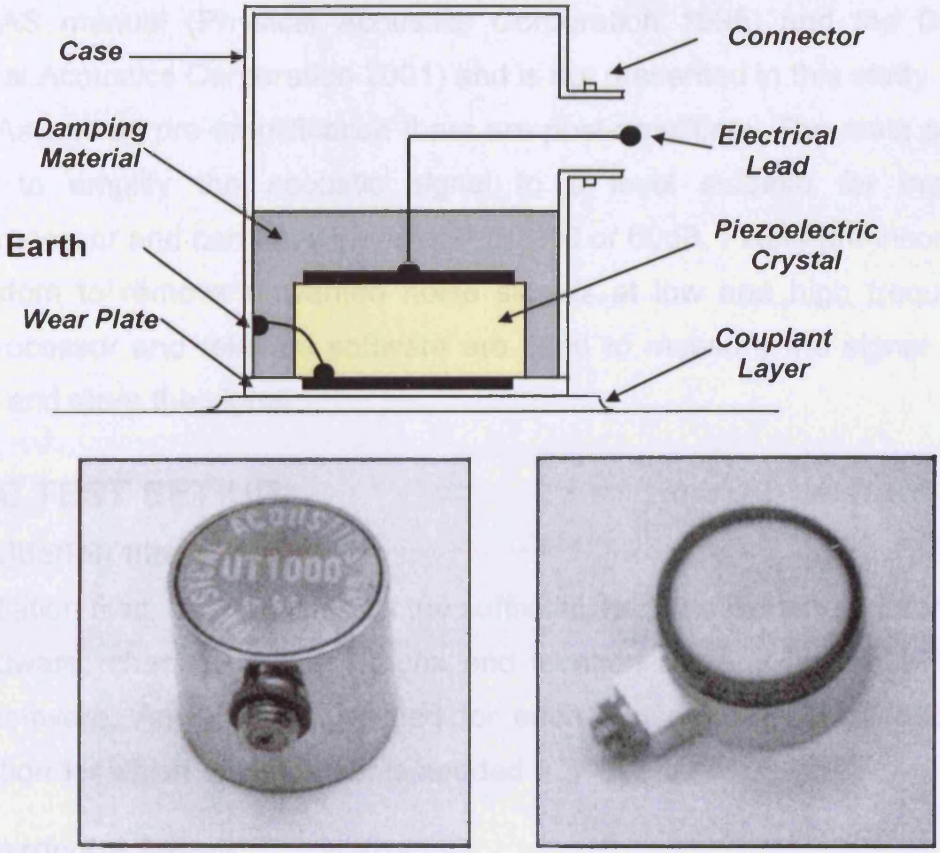

Figure 3.4. AE sensor construction and two typical sensors (Miller & McIntire 1987)

3.1.3. The Preamplifier, Main Amplifier and Microcomputer

Amplification is necessary to magnify the small signals collected into data that can be analysed and to eliminate environmental disturbances (Lenain 1981). When a sensor is connected to an amplifier through a long coaxial cable, there will be a loss of sensor sensitivity (Beattie 1983). The common solution to the problem is to separate the amplifier into a fixed gain preamplifier situated near to the sensor (often it is actually incorporated into the sensor) and a variable gain amplifier set in the main instrumentation. The preamplifier provides the necessary filtering; gain (which is usually 40dB) and cable drive capability. During this study both sensors with both integrated pre-amplifiers and sensors with external preamplifiers were used. The sensors R1.5I, R3I, R15I and WDI (all supplied by PAC) are sensors with integrated pre-amplifiers and sensors R0.45 and R6D (supplied by PAC) are sensors that need external pre-amplifiers. A full description of the external pre-amplifiers used in this thesis (including the specifications of each pre-amplifier) is documented in the

MISTRAS manual (Physical Acoustics Corporation 1995) and the DiSP manual (Physical Acoustics Corporation 2001) and is not presented in this study.

As well as pre-amplification there are post-amplifiers. The main post-amplifier serves to amplify the acoustic signal to a level suitable for input into the microprocessor and can have gains of 0, 20, 40 or 60dB. Filters are incorporated into the system to remove unwanted noise signals at low and high frequencies. The microprocessor and relevant software are used to measure the signal in real time, display and store the signal.

3.2. AE TEST SET-UP

3.2.1 Initiation files

The initiation files, distinguished by the suffix .ini, hold the AE set-up information such as hardware, channels used, graphs and location settings for the MISTRAS and DiSP software. An ini file is needed for each sensor and will be depend on the application for which each sensor is needed.

3.2.2 Hardware Set-up

Hardware settings include the variables threshold, gain, sample rate, pre-trigger, hit length, peak definition time (PDT), hit definition time (HDT) and hit lock-out time (HLT). These variables can be set individually for each channel. The hardware setting also includes the headings: hit data set, parametrics and cycle counter. Both the MISTRAS manual (Physical Acoustics Corporation 1995) and the DiSP manual (Physical Acoustics Corporation 2001) describe the definition of each of the titles in the hardware set-up and recommend suitable values for general purpose testing. These values will depend on the objectives of the test including the test set-up and are at the discretion of the user.

The hit data set allows selection of the measured parameters to be included in the description of each AE hit. In the current research, time, amplitude, absolute energy, counts, rise-time, duration, initiation frequency, two parametrics (load and deflection) and waveforms enabled have been used when collecting data.

The parametric set-up allows scaling of the voltage measured at the parametric input such that the system displays the corresponding load or deflection values. The parametric scaling process used by the MISTRAS and DiSP software involves multiplying the measured voltage by a multiplier and then adding an offset. These values are placed into the hardware set-up.

3.2.3 Source Location Modes and Set-up

A single AE source produces a transient mechanical wave that propagates through the material in all directions. The AE wave can be detected in the form of hits on one or more channels. A group of hits that is received from a single signal source phenomenon is an event.

An array of sensors may be used to locate an AE event based on their positions and the wave velocity of the source. The theory of source location has been reported by Pao (1978). The MISTRAS software provides eight different source locations modes. These are zonal, linear, four planar modes (rectangular, triangular, dual triangular and F-placement) and two special I modes (arbitrary and linear x-y). In this study only two modes will be used, linear and arbitrary. These modes represent the events in both one dimension and two dimensions. Linear location is useful for monitoring beams pipes or along a weld line and can be "wrapped" to monitor a ring or circle. The arbitrary location method is better for monitoring complex structures, as there is no restriction in sensor placement.

3.2.4 Graphical Data Displays

In this study three different software packages, NOESIS, MI-LOC, and DISP-LOC were used to produce a variety of graphical displays. NOESIS in particular is used for post-test analysis. The user is not limited to the graphical display observed during the test as the display can be redisplayed, changed and verified during the post-test analysis. In the next section a brief description of the different types of display are discussed.

1. **Historical plot**

Historical plots illustrate the change in AE parameter with respect to time. Fig. 3.5 and Fig. 3.6 represent historical plots of absolute energy versus time in cumulative and rate form respectively. They illustrate the change in an AE parameter with time and provide an indication of source activity level throughout a test. Fig. 3.5 and Fig. 3.6 represent the same data. The data displayed in this section is produced during the experimental work of this thesis and is discussed in later chapters.

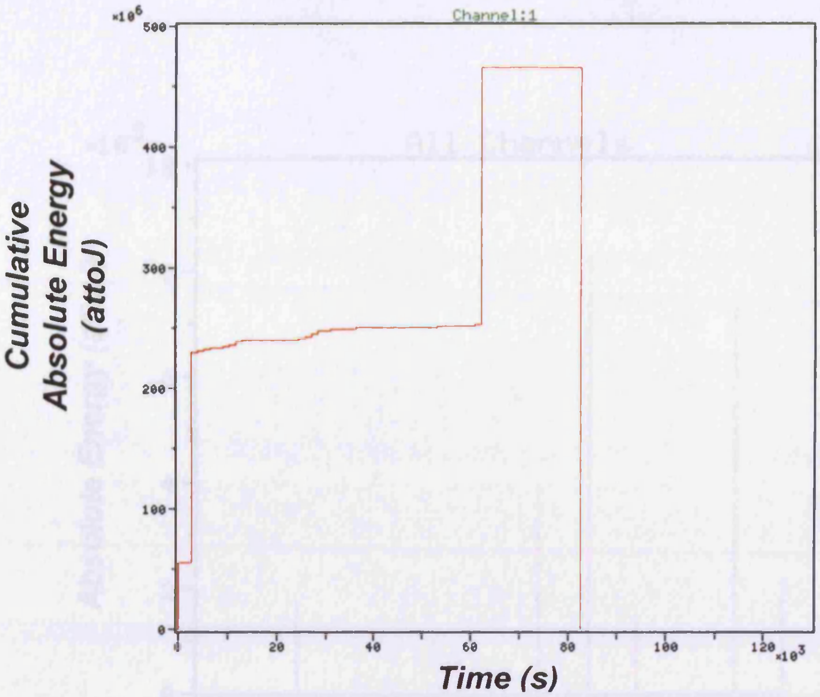

Figure 3.5. Cumulative absolute energy recorded with respect to time

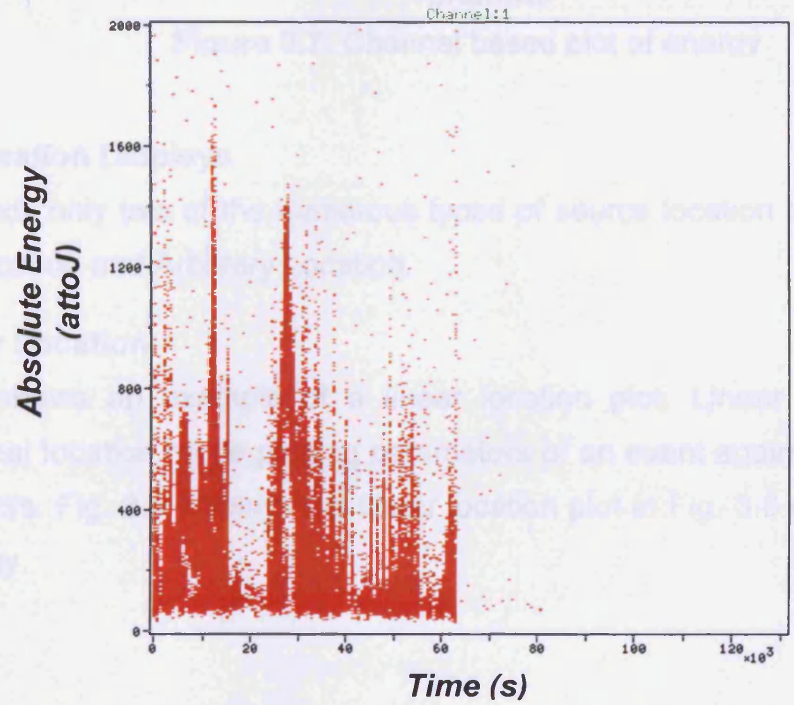

Figure 3.6. Absolute energy recorded with respect to time

2. Channel plots

Channel plots provide information on the distribution of emissions over a range of channels. Channel plots maybe used for highlighting active regions and can be used as a crude method of location. An example of a channel-based plot is shown in Fig.3.7.

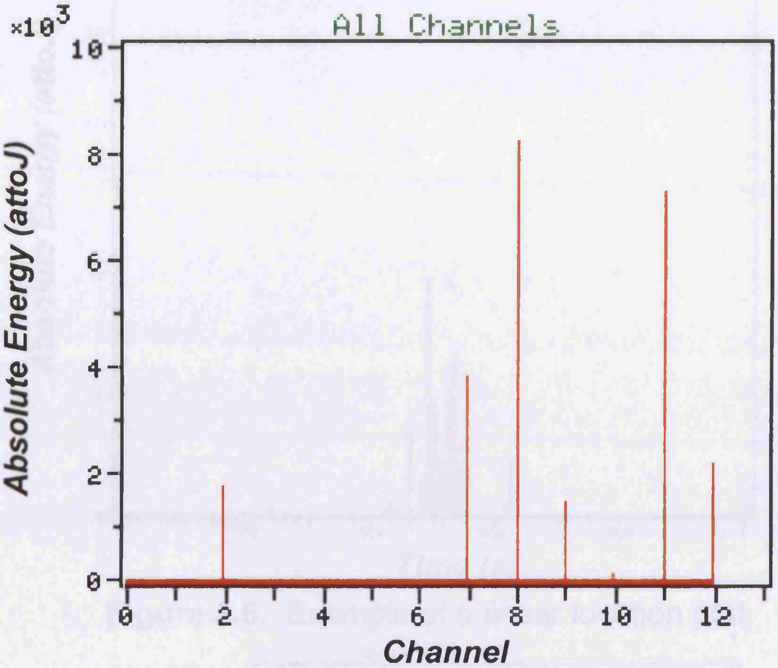

Figure 3.7. Channel based plot of energy

3. Location Displays

In this study only two of the numerous types of source location algorithms are used Linear Location and Arbitrary Location.

a) Linear Location

Fig. 3.8 shows an example of a linear location plot. Linear location is a one-dimensional location mode plotting parameters of an event against position between sensor pairs. Fig. 3.9 displays the linear location plot in Fig. 3.8 with respect to time and energy.

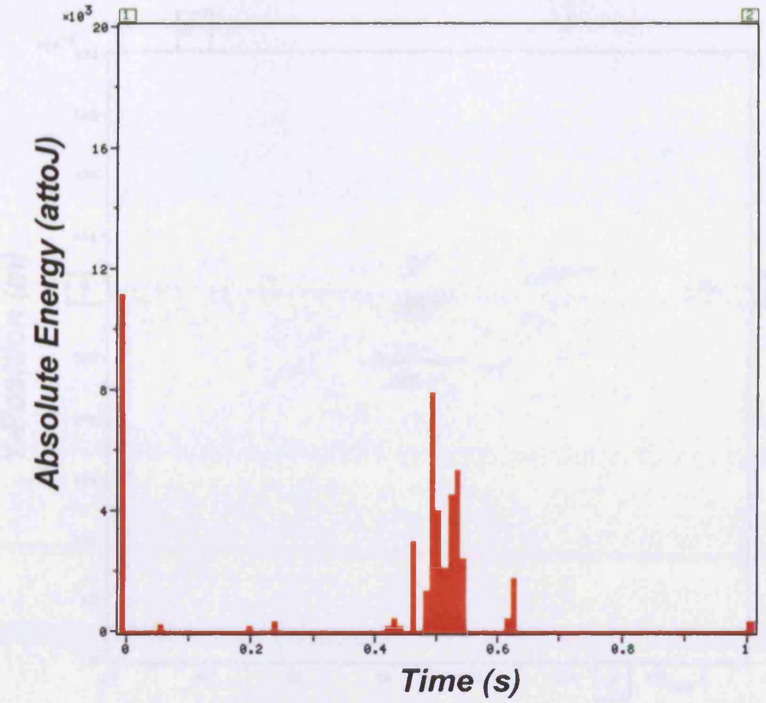

Figure 3.8. Example of a linear location plot

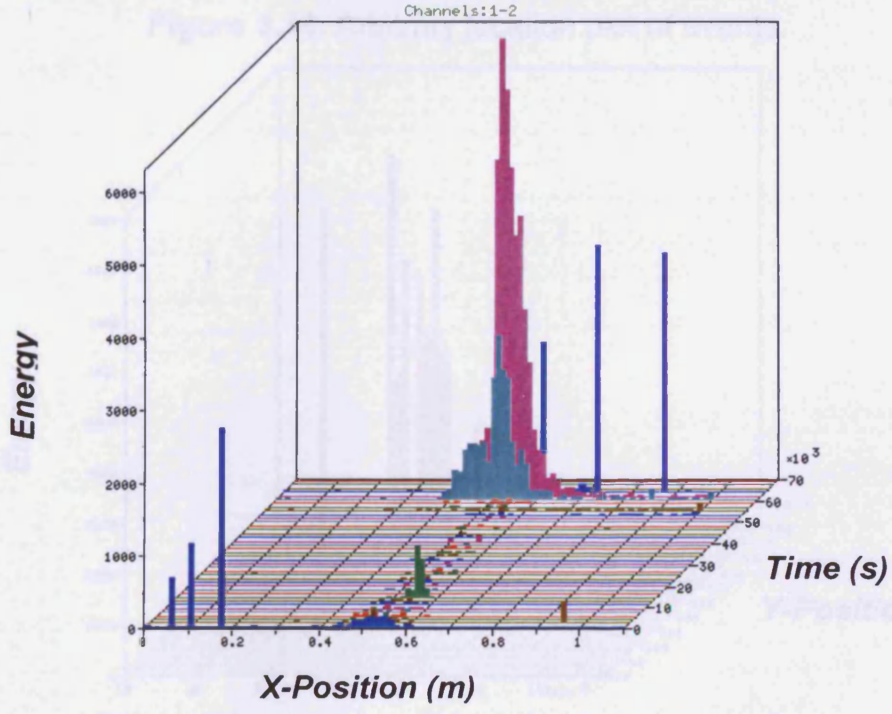

Figure 3.9. Linear location plot with respect to time.

b) Arbitrary Location

An example of an arbitrary location plot is shown in Fig. 3.10. Arbitrary location is a two-dimensional location mode obtained by plotting an event against its "x" and "y" position in a defined group of sensors. Fig. 3.11 displays the same data in a three-dimensional plot showing the relations of energy of events with the position.

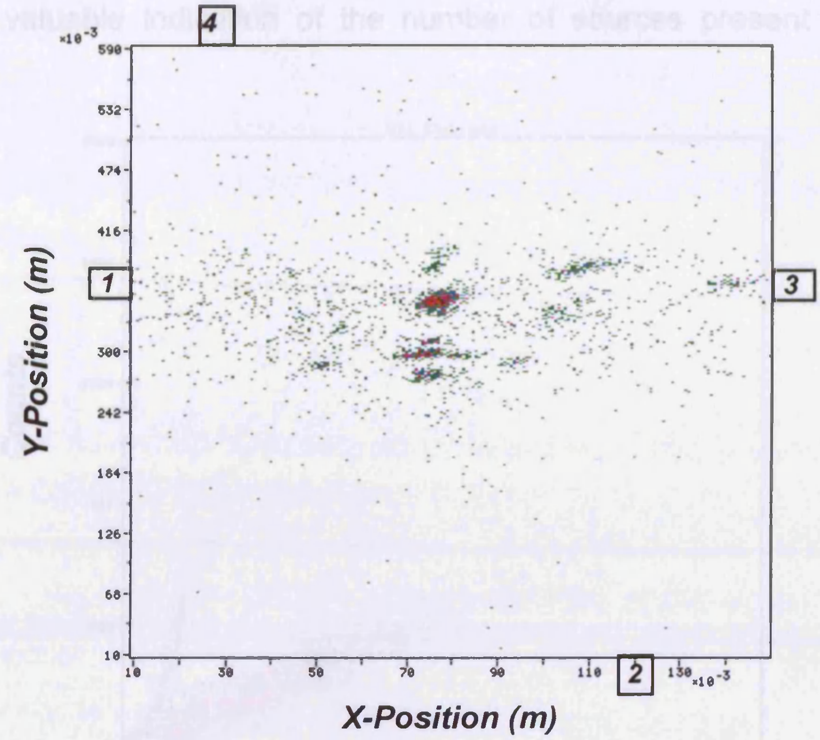

Figure 3.10. Arbitrary location plot of events.

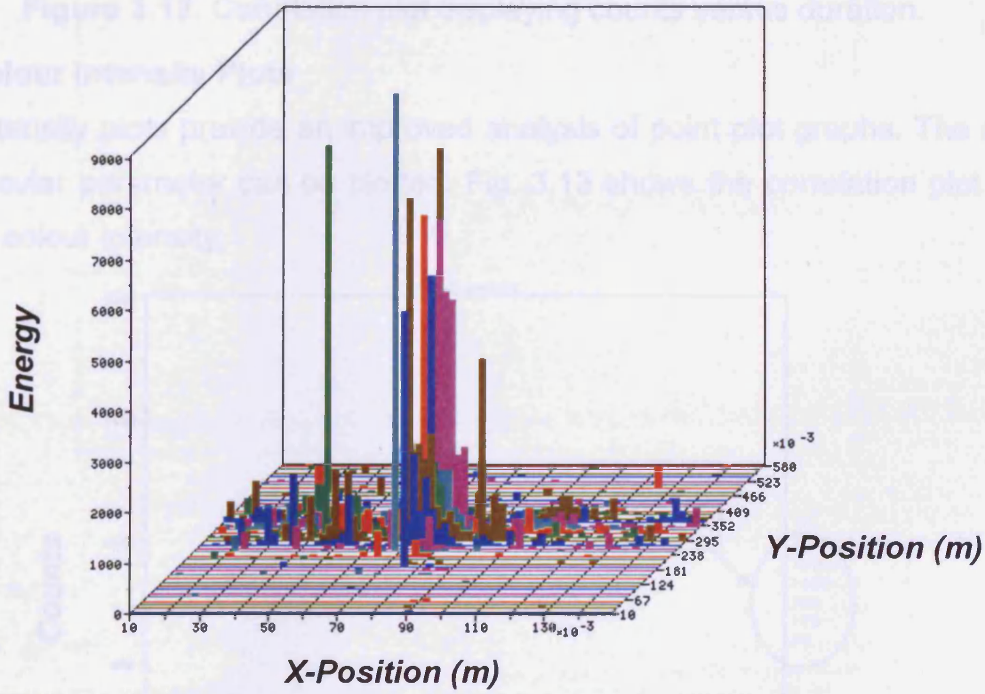

Figure 3.11. Arbitrary location plot with respect to energy.

4. **Correlation Plots**

Correlation plots are point plots that show the relationship between two AE parameters. Certain plots, for example counts versus duration as shown in Fig. 3.12, provide a valuable indication of the number of sources present and the type of source.

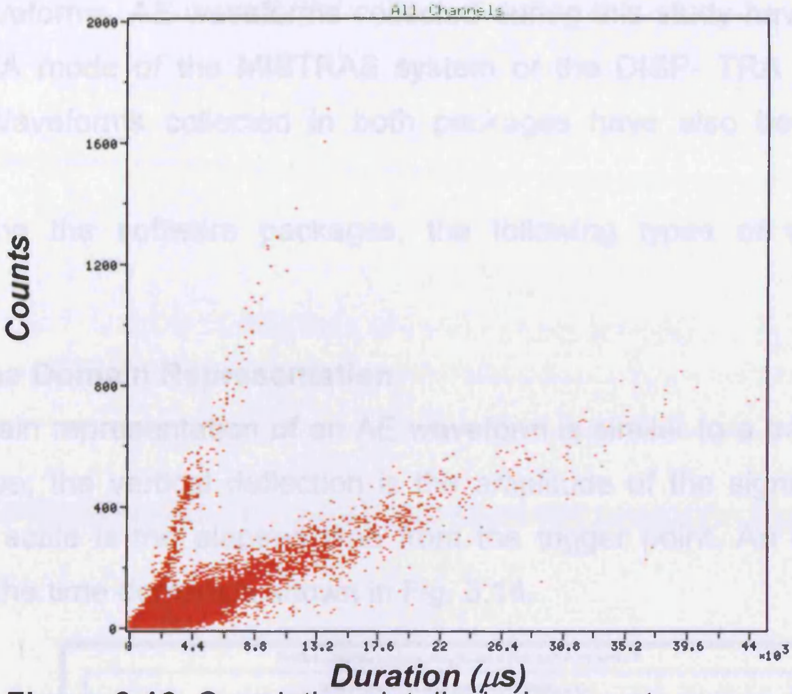

Figure 3.12. Correlation plot displaying counts versus duration.

5. **Colour Intensity Plots**

Colour intensity plots provide an improved analysis of point plot graphs. The density of a particular parameter can be plotted. Fig. 3.13 shows the correlation plot in Fig. 3.12 with colour intensity.

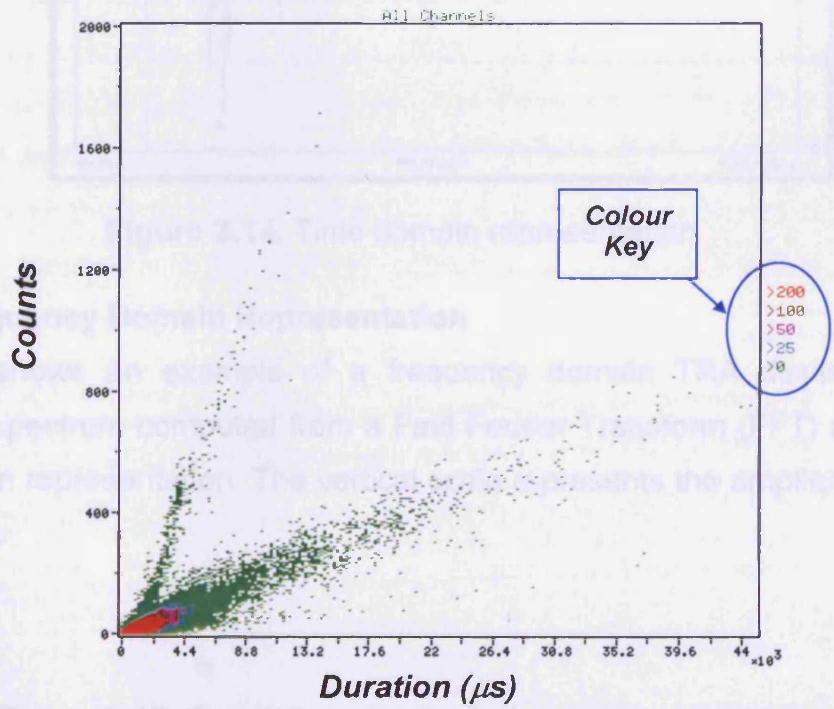

Figure 3.13. Correlation plot displaying counts versus duration.

3.2.5 Transient Records

Another important tool of AE analysis is the analysis of transient records also known as AE waveforms. AE waveforms collected during this study have been acquired in the MI-TRA mode of the MISTRAS system or the DISP- TRA mode of the DISP system. Waveforms collected in both packages have also been analysed using NOESIS.

Using the software packages, the following types of waveforms can be produced.

I. Time Domain Representation

Time domain representation of an AE waveform is similar to a trace captured on an oscilloscope; the vertical deflection is the amplitude of the signal in volts, and the horizontal scale is the elapsed time from the trigger point. An example of a TRA display in the time domain is shown in Fig. 3.14.

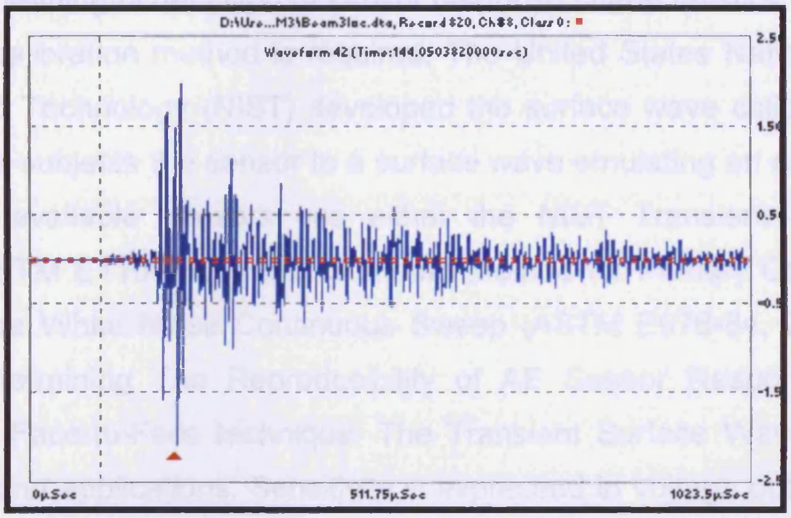

Figure 3.14. Time domain representation

II. Frequency Domain Representation

Fig. 3.15 shows an example of a frequency domain TRA display. This is the frequency spectrum computed from a Fast Fourier Transform (FFT) algorithm of the time domain representation. The vertical scale represents the amplitude in dB at that frequency.

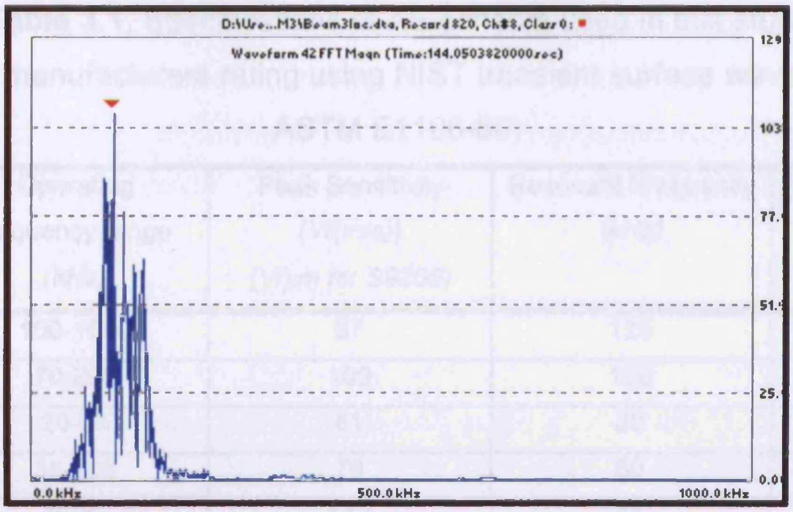

Figure 3.15. Frequency domain Transient

3.3. EXPERIMENTAL PROCEDURES

3.3.1. Sensor Calibration

To provide a meaningful definition of sensor response characteristics, an appropriate standardised calibration method is required. The United States National Institute of Standards and Technology (NIST) developed the surface wave calibration method. This procedure subjects the sensor to a surface wave emulating an actual AE event. Commercially available sensors use either the NIST Transient Surface Wave Calibration (ASTM E1106-86, 1992, Standard Method for Primary Calibration of AE Sensors) or the White Noise Continuous Sweep (ASTM E976-84, 2001, Standard Guide for Determining The Reproducibility of AE Sensor Response), otherwise known as the Face-to-Face technique. The Transient Surface Wave Technique is ideal for AE burst applications. Sensitivity is expressed in voltage output per vertical velocity versus frequency. The Face-to-Face technique is based on voltage output per unit of pressure input and is recommended for continuous AE monitoring applications.

Six types of AE sensor were used in this study, their response characteristics, rated by the manufacturer in accordance with calibration to ASTM E1106, are tabulated in table 3.1.

Table 3.1. Specifications of AE sensors used in this study
(According to manufacturers rating using NIST transient surface wave calibration to ASTM E1106-86)

PAC Sensor Type	Operating frequency range *(kHz)*	Peak Sensitivity *(V/(m/s))* (*V/μm for S9208*)	Resonant Frequency *(kHz)*	Preamplifier Gain *(dB)*
WDI	100-1000	87	125	*40*
R15I	70-200	109	150	*40*
R3I	20-55	81	30	*40*
R6d	35-100	78	60	--
R1.5I	6-25	142	15	*40*
R0.45	6-90	87	7	--

3.3.2 Hsu-Nielsen source

In practice, the sensor type and the material monitored influence the frequency spectrum of an AE source. Other factors that have an effect on the signal include the geometry of the specimen, the acoustic properties and the quality of the surface. Therefore there is a need for an artificial source to be used in-situ to ensure both that results are comparable between tests and to verify that the system is responding in a satisfactory way. Many methods of calibration have been studied, including impact by a dry jet of helium (Hsu and Breckenridge 1981) ball bearing drops and spark impulses (Raj and Jha 1994). Piezoelectric transducers similar to those used in ultrasonic testing (Scruby 1985b, Raj and Jha 1994) have been used for calibration. However the practicality of these methods for assessing mounted sensitivity was deemed unsuitable for this study. The most popular method of mounted sensor verification is the Hsu-Nielsen (H-N) source known as the Pencil Lead Fracture test (PLF). This method has been adopted as an ASTM standard.

Hsu and Breckenridge (1981) exploited the remarkably repeatable fracture energy of continuous pencil lead. Using a clutch action holder and a constant length of lead he demonstrated a cheap and reliable standard source could be produced. Nielsen (1980) carried out an extensive test programme and developed a small guide attachment to the pencil holder, allowing testers to produce about 80% of breakage's within a small energy band.

The pencil is a commercial 0.5mm; type 2H lead with a 4mm fixed guide tube on which a smaller guide ring is mounted as shown in Fig. 3.16. The pencil is placed on to the surface of the specimen at an angle of thirty degrees, with a lead of length 3mm. By means of the plastic guide, it is possible to reproduce a similar emission time after time.

The recommended application procedure is as follows:

- The lead feed button on the pencil is pressed repeatedly until the lead protrudes.
- The end of the lead is levelled with the end of the guide tube by pressing the tip of the pencil perpendicularly towards an even surface while the feed button is pressed down.
- The button is pressed six times causing the lead to protrude 3mm.
- The pencil is guided obliquely towards the structure until the guide ring rests on the specimen.

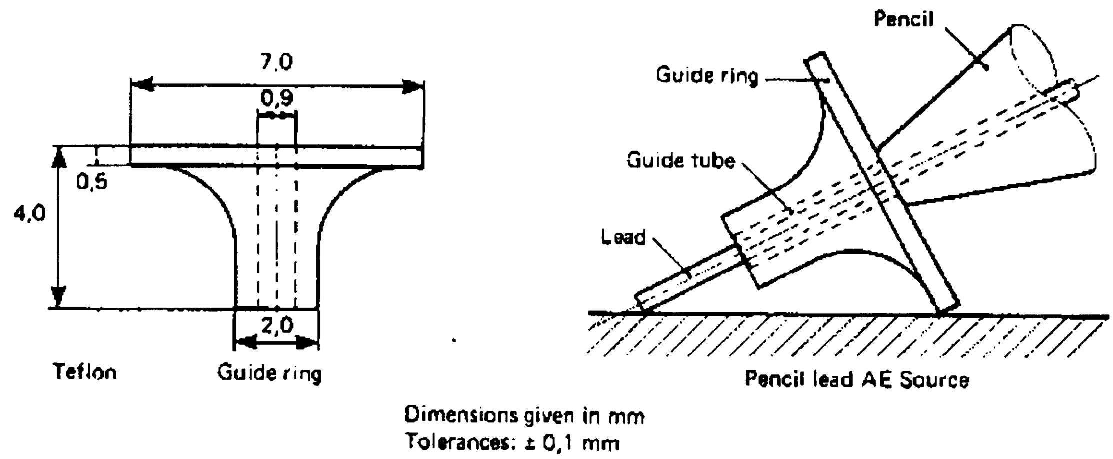

Figure 3.16. The H-N source method and guide ring (Rindorf, 1981)

- The pencil is pivoted about the point of contact towards a steeper position thus causing the lead to break.

3.3.3. Sensor Mounting

During an AE test, it is important that the sensor is attached to the specimen correctly. A technique known as coupling ensures transmission of AE from the material to the sensor by the means of a suitable medium. This medium, known as a couplant, can be categorised into two groups: fluid couplants and solid couplants. Fluid coupling is achieved using water, silicone grease or any fluid that allows the motion of the wave to pass through with no attenuation. Solid coupling is achieved by using glue or cement, similarly allowing waves to pass free of attenuation. Using an adhesive to attach sensors to the material can result in damage to the sensor when removed, so generally fluid couplants are used (Dukes and Culpan 1984). The couplant must be applied to the sensor consistently so that the whole face of the sensor is covered uniformly.

It is very important when mounting a sensor that 1) the couplant is suitable for the application, 2) a necessary mechanical pressure is being applied and 3) the surface condition of the material is in good condition (Higo and Inaba 1991). Since the majority of testing is conducted outdoors, it is necessary that the couplant does not degrade with the weather or temperature. Thus the choice of couplant is important.

To keep a constant pressure so that the sensors do not slip, magnets can be used on some metallic structures. On non-metallic structures, such as concrete, an adhesive can be used to attach the sensors to the material or steel plates can be attached to the structure so that the magnets can be used. The mounting of sensors to the test structure is a very important part of any investigation. Poor mounting can result in severely reduced sensitivity and the loss of important AE data for the location and monitoring of cracks.

After mounting, the sensitivity of the sensor is verified using an H-N source as described. A pencil lead fracture is recorded adjacent to the sensor. A sensor that is well mounted should record a signal between 97-100dB. If a sensor response is below 97dB the sensor is remounted and the connection is checked again. If the response is still low, the cable is checked by performing a pencil lead fracture on the face of the. If the signal response is again low the cable is removed and replaced, if failure of calibration continues the sensor should be removed, reported as damaged and replaced. In this study steel clamps and tape were used to hold the sensors onto the surface of the test specimens.

3.3.4. Measurement of AE Signal Velocity

Throughout this work, reference is made to the measurement of AE signal velocity. For the purposes of this study, "measured velocity" describes the speed at which an AE signal is observed to travel between two fixed points on a propagation medium. The measured velocity of a signal from a given source is strongly dependent on the individual test configuration, especially the sensor spacing, which defines the propagation distance over which the signal velocity is measured.

Figure 3.17 is an example of two AE signal waveforms produced from a H-N source. The upper figure shows the signal measured adjacent to the source, the lower figure shows the signal measured 2m from the source. The signals were recorded synchronously using a pre-trigger, (recording was triggered on both sensors simultaneously by the first threshold crossing).

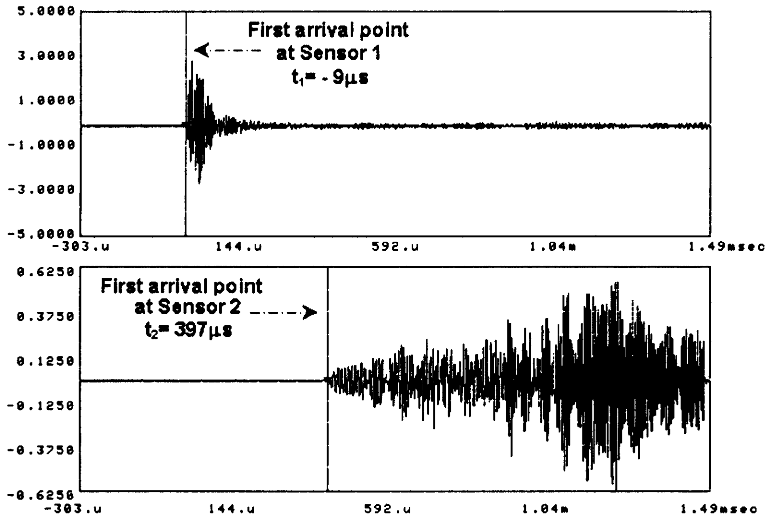

Figure 3.17. Measuring AE signal velocity (Carter 2000)

The arrival times (t_1 & t_2) of the initial component of the signal at each sensor are –9μs and 397μs, respectively. Since the measured propagation velocity (C_{AE}) of the signal can be determined from Equation 3.2, the velocity of the signal in Fig. 3.17 can be determined as 4926m/s.

$$C_{AE} = \frac{D}{t_2 - t_1} \qquad \textbf{(3.2)}$$

where D= 2m.

Once the velocity of a signal is determined, the time of arrival location algorithm described by Pao (1978) can be used to calculate locations of AE events.

CHAPTER 4. OPTIMUM SELECTION OF AE SENSOR AND ATTACHMENT METHOD FOR CONCRETE MONITORING

4.1. INTRODUCTION

The single and most important factor in AE testing is the correct selection of AE sensor. When selecting a sensor, it is essential to contemplate the following (Beattie 1983, Cole 1988 and Miller and McIntire 1987):

- The frequency range needed.
- The sensitivity of the sensor.
- Environmental characteristics (Temperature, water proofing).
- Physical characteristics (Size, shape and mass of the sensor).

For AE measurement in concrete, the frequency dependence of attenuation is the critical factor in determining the frequency range of a system. Ohtsu (1987) found that high frequency components in the MHz range are attenuated strongly due to the frequency dependence of attenuation, the same author later used a range of 10kHz - 300kHz for the detection of AE in concrete (Ohtsu 1996). Similarly Yuyama et al. (1999) discussed the ability of AE techniques to evaluate the structural integrity of a reinforced aging dock. Both 150kHz resonant frequency sensors and 60kHz resonant frequency sensors were attached to record AE from structural damage. It was found that only data collected by the 60kHz resonant frequency sensors could be analysed since there were no significant AE signals detected by the 150kHz resonant frequency sensors. The same authors suggested that 60kHz resonant frequency sensors are suitable for monitoring AE over large areas whereas 150kHz resonant frequency sensors were only suitable over small areas. Likewise 30kHz resonant frequency sensors were used by Shigeishi et al. (2001) to monitor the structural integrity of masonry and RC bridges. Pullin et al. (2003) used broadband and 150kHz resonant frequency sensors to globally monitor steel box girders, for the Saltings Viaduct, Neath, South Wales. A series of tests are needed to discover the ideal sensor for concrete monitoring.

Once the optimum sensor for the application is chosen correct attachment ensures high sensitivity. It is very important that the chosen couplant is suitable for the application with a necessary mechanical pressure being applied. The surface condition of the material must also be in good condition. Poor mounting can result in severely reduced sensitivity and the loss of important AE data. Generally sensors are protected from conditions such as rain and wind using a covering but sensitivity can be lost depending on the condition of the couplant or the sensor attachment method. Since much testing is conducted outdoors, it is necessary that the couplant does not degrade with the weather or temperature. Choices of material that allow waves to pass free of attenuation include silicon grease, silicon sealant, water, petroleum jelly and glue. For in-service structures, AST (Auto Sensor Test) functions have been used to assess the connectivity of an array of sensors over a period of time from a remote position.

A series of laboratory tests were performed using a range of AE sensors, couplants and attachment methods to produce the ideal set-up for concrete monitoring. It was observed that low frequency resonant sensors were suited to detecting AE in concrete since high frequencies attenuated quickly. Steel clamps and silicon bathroom sealant provided the optimum attachment method for AE sensors on concrete specimens since there was little decrease in sensitivity over a period of time.

4.2. AIMS AND OBJECTIVES

This chapter assesses the optimum selection of AE sensor and attachment method for concrete monitoring. There were two aims of this research. Firstly, to determine the frequency range of AE from concrete failure so that a suitable sensor could be applied to detect these emissions and secondly, to determine the most suitable method of attachment which would allow optimum sensitivity over a period of time.

The experimental objectives were to:

- Attach a broad range of sensors using the same attachment method to detect AE during concrete failure.
- Attach sensors to a concrete surface using a variety of different couplants.

4.3. SENSOR SELECTION

4.3.1. Experimental Procedure

Centre notched concrete beams were failed in four-point bending. The mix proportions of the concrete beams were 1:1.8:2.8:0.5 by mass of cement (Portland cement), fine aggregate, coarse aggregate and water. The concrete specimens were 100mm wide, 150mm deep and 1000mm long and after 28 days had a compressive strength of 40MPa. Six specimens were loaded at a constant deflection rate using an Avery-Denison actuator. With such loading, cracks were encouraged to grow within a determined crack area in an upward direction. The configuration of the specimens and sensor locations are shown in Fig. 4.1.

The twelve-channel "PAC MISTRAS" system was used to record AE for the test. During each of these tests, six different sensors were used; five of these sensors were resonant sensors and one a broadband sensor. The resonant frequency sensors included a 7kHz sensor, a 15kHz sensor, a 30kHz sensor, a 60kHz sensor and a 150kHz sensor. These sensors were attached to channels 1,2,3,4, and 5 respectively. The broadband sensor was attached to channel 6. The sensor attached to channel 1 had a resonant frequency of 7kHz but could record over a wide range, meaning a broad frequency range was covered. The calibration certificates of each of these sensor types can be seen in Appendix A. The AE set-up used for each channel is presented in table B.1 in Appendix B.

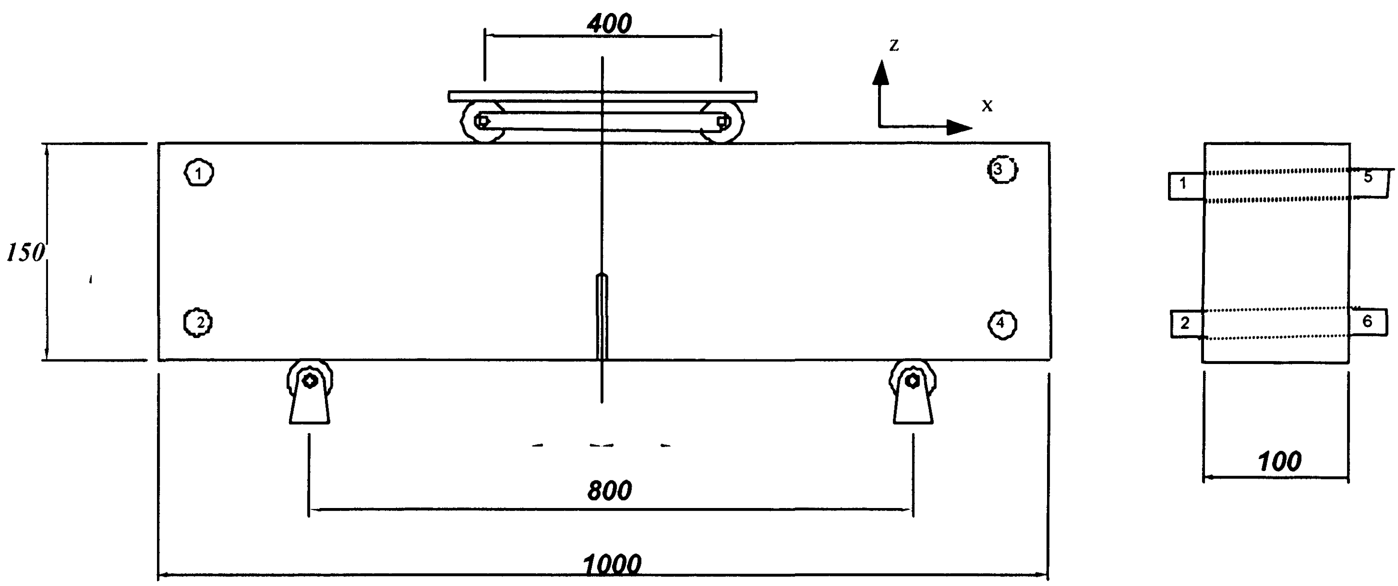

Figure 4.1. Illustrations of four-point bend test with AE sensor locations

4.3.2. Results and Discussion

The following plots display the amplitude and absolute energy of emissions recorded on each of the sensors during the loading of the first specimen. Similar plots for subsequent tests are not presented. The peak amplitude and absolute energies recorded on each channel for specimen 1 can be seen in tables 4.1 and 4.2.

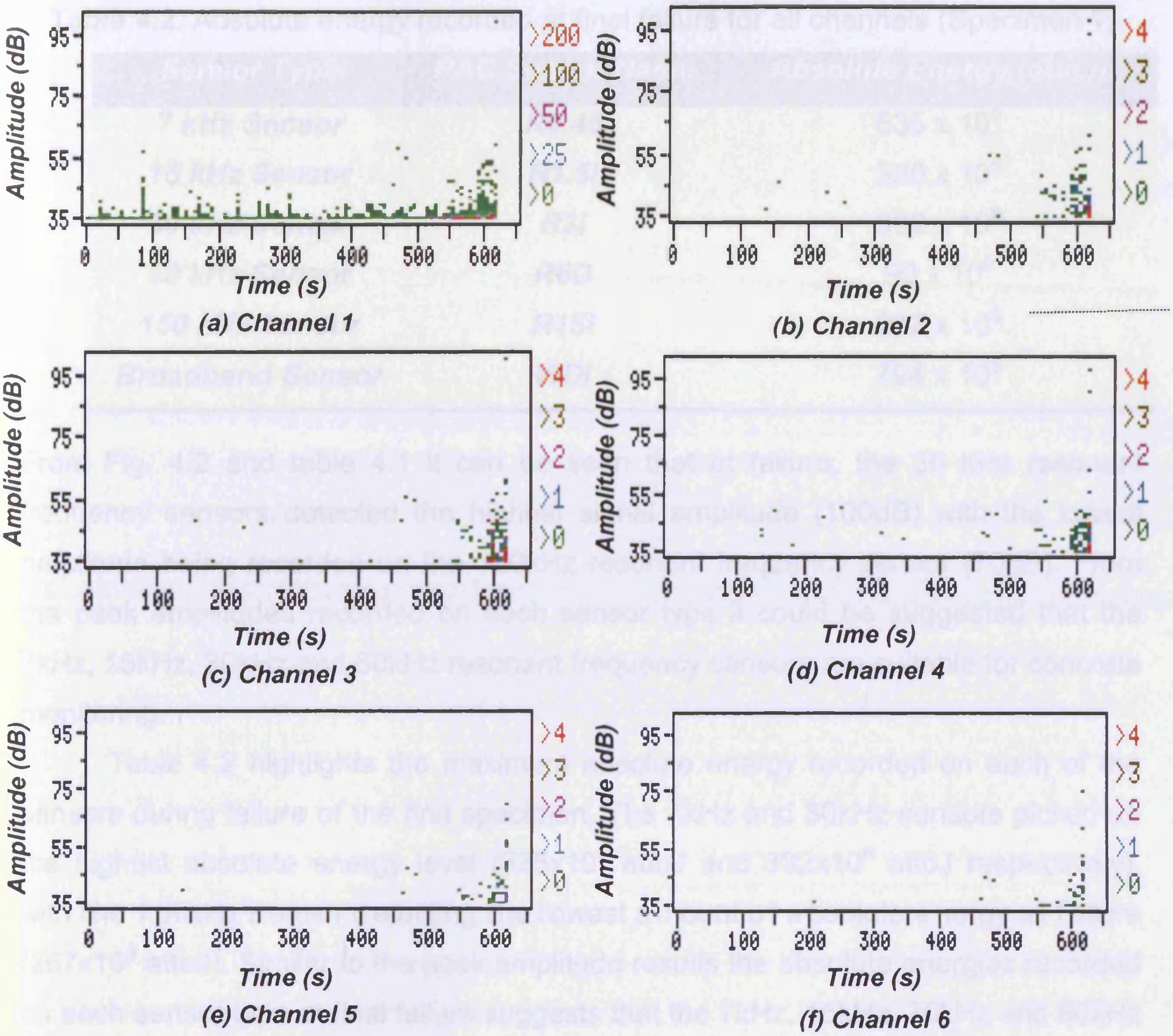

Figure 4.2. Variation of Amplitude with Time for all channels (Specimen 1)

Table 4.1. Peak amplitude recorded at final failure on all channels for specimen 1

Sensor Type	PAC Sensor Name	Amplitude (dB)
7 kHz Sensor	***R0.45***	99
15 kHz Sensor	***R1.5I***	98
30 kHz Sensor	***R3I***	100
60 kHz Sensor	***R6D***	98
150 kHz Sensor	***R15I***	70
Broadband Sensor	***WDI***	76

Table 4.2. Absolute energy recorded at final failure for all channels (Specimen 1)

Sensor Type	PAC Sensor Name	Absolute Energy (attoJ)
7 kHz Sensor	*R0.45*	535×10^6
15 kHz Sensor	*R1.5I*	330×10^6
30 kHz Sensor	*R3I*	332×10^6
60 kHz Sensor	*R6D*	90×10^6
150 kHz Sensor	*R15I*	267×10^3
Broadband Sensor	*WDI*	794×10^3

From Fig. 4.2 and table 4.1 it can be seen that at failure, the 30 kHz resonant frequency sensors detected the highest signal amplitude (100dB) with the lowest amplitude being recorded on the 150kHz resonant frequency sensor (70dB). From the peak amplitudes recorded on each sensor type it could be suggested that the 7kHz, 15kHz, 30kHz and 60kHz resonant frequency sensors are suitable for concrete monitoring.

Table 4.2 highlights the maximum absolute energy recorded on each of the sensors during failure of the first specimen. The 7kHz and 30kHz sensors picked up the highest absolute energy level (535×10^6 attoJ and 332×10^6 attoJ respectively), with the 150kHz sensor detecting the lowest amount of absolute energy at failure (267×10^3 attoJ). Similar to the peak amplitude results the absolute energies recorded on each sensor type at final failure suggests that the 7kHz, 15kHz, 30kHz and 60kHz resonant frequency sensors are suitable for concrete monitoring.

Fig. 4.4 represents the maximum amplitude recorded on each channel for all of the tests. This plot will show the consistency of each sensor type for all tests.

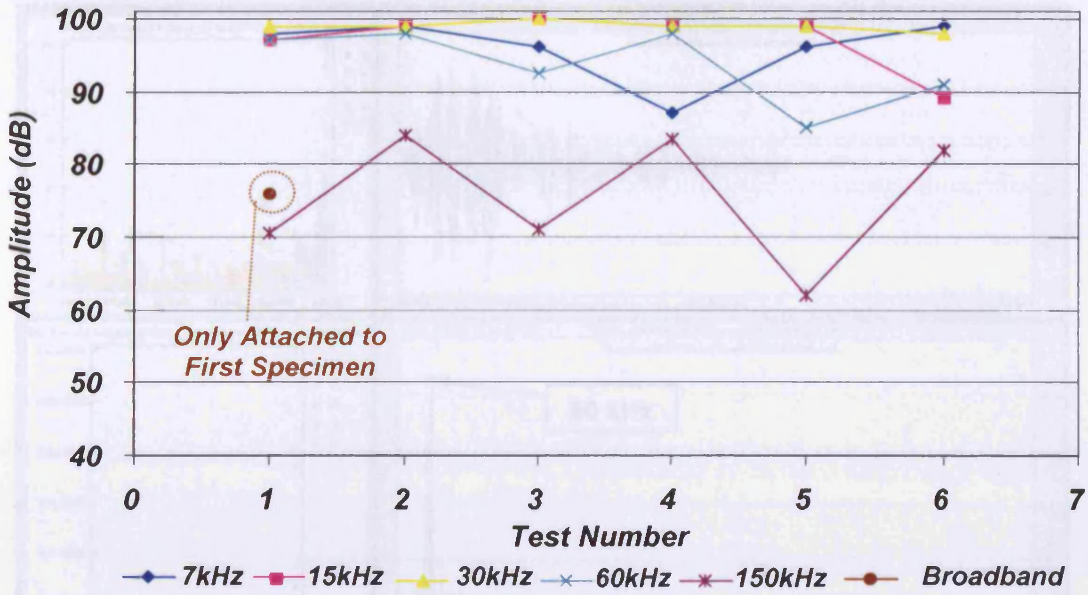

Figure 4.4. The amplitude produced on each sensor at final failure for all specimens

Examination of this plot suggests that the sensors with resonant frequencies 7kHz, 15kHz, 30kHz and 60kHz recorded high amplitudes for each of the specimens. The maximum amplitudes produced on the 150kHz sensor at failure for all specimens are considerably lower than the latter. This reiterates the previous results suggesting that for concrete monitoring low frequency sensors are more appropriate due to the attenuation of higher frequencies.

The FFT (Fast-Fourier Transform) of a waveform can produce the frequency content of an emission. Figs. 4.5, 4.6 and 4.7 show both the time domain display and the frequency domain display produced by the FFT of the time domain display, of an emission recorded on the broadband sensor (channel 6), the 7kHz resonant frequency sensor (channel 1) and the 30kHz resonant frequency sensor (channel 3), respectively for the specimen failed first.

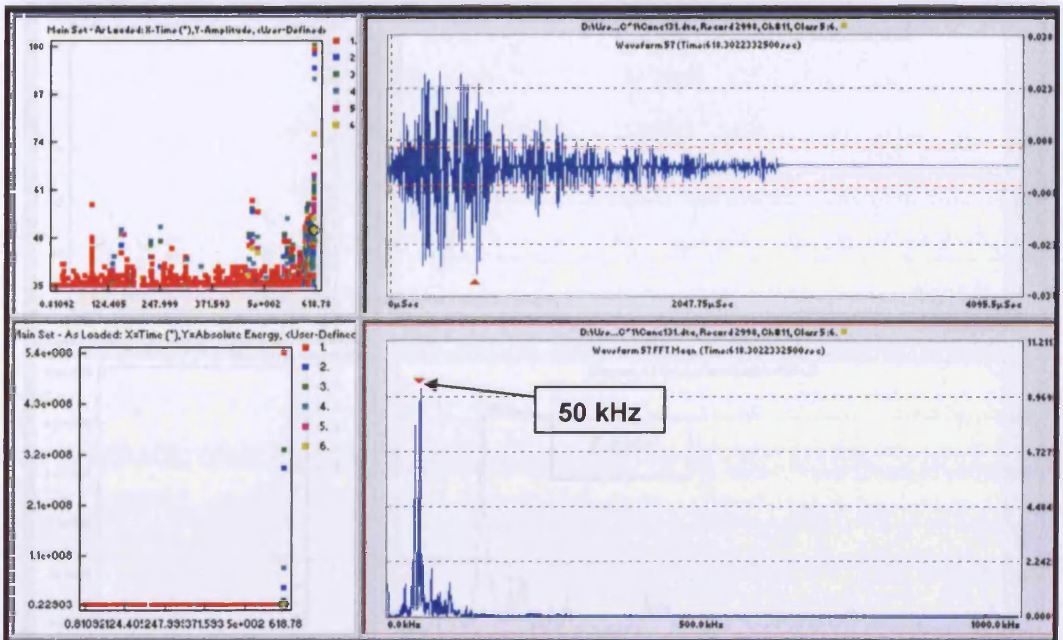

Risetime	Counts to Peak	Counts	Energy	Duration	Amplitude	Threshold	Absolute Ener
554	26	56	15	1711	50	35	1200.22
776	3	4	2	912	38	35	44.1089
1	1	1	0	35	36	35	4.63452

Figure 4.5. Time domain display and frequency domain display of a waveform recorded during failure on the broadband sensor (Specimen 6)

The frequency content of an emission recorded during failure on the broadband sensor is displayed in Fig. 4.5 and shows a frequency range between 0kHz and 250kHz. In particular, there are large peaks at 50kHz. This suggests that even though frequencies up-to 250kHz travel through concrete, the majority of the waveform frequency content is low. The frequency content of an emission recorded on the 7kHz resonant frequency sensors and the 30kHz resonant frequency sensors can be seen in Figs. 4.6 and 4.7.

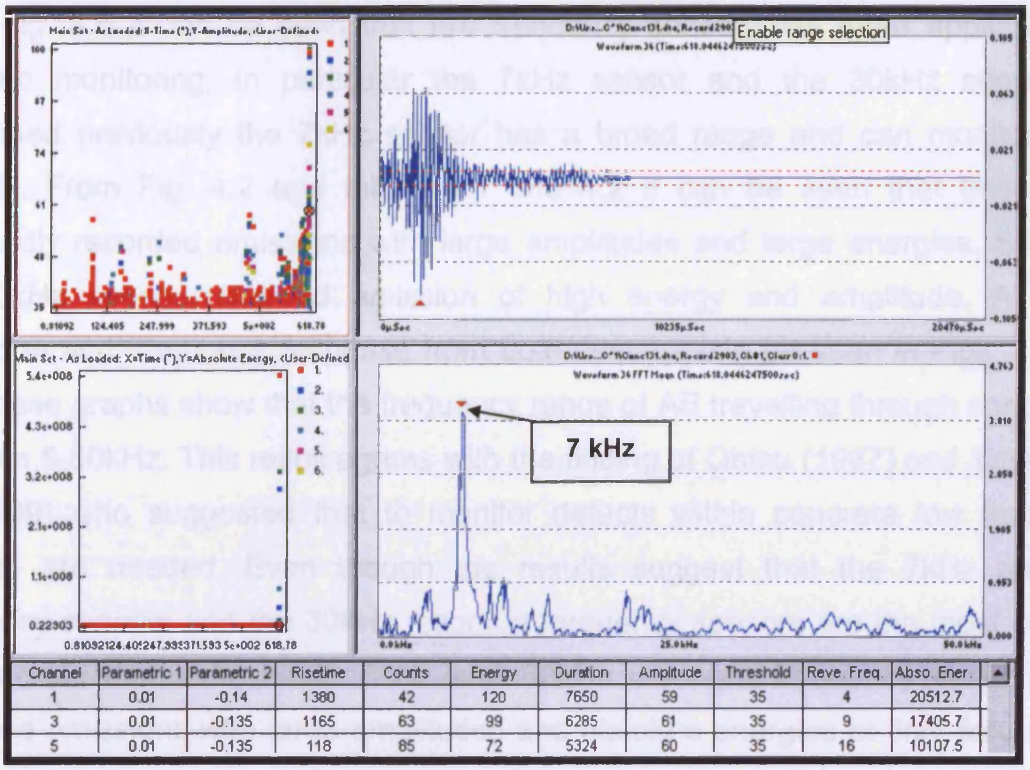

Figure 4.6. Time domain display and frequency domain display of a waveform recorded during failure on channel 1

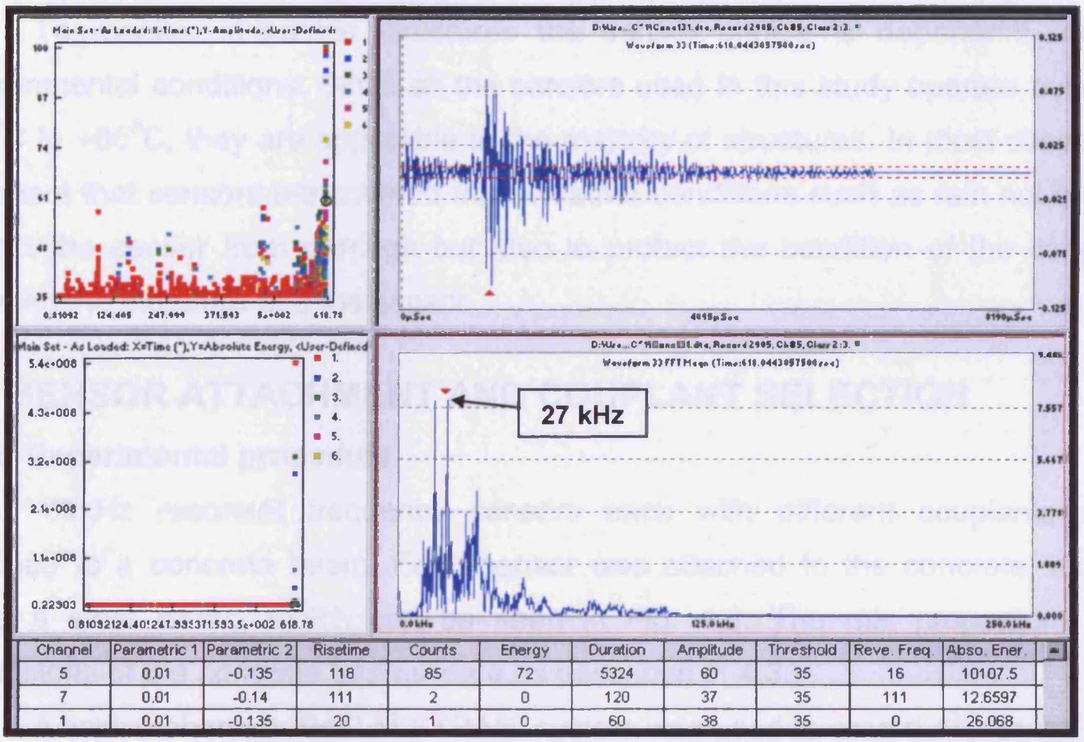

Figure 4.7. Time domain display and frequency domain display of a waveform recorded during failure on channel 3

From Fig. 4.5 it can be seen that low frequency sensors are more applicable for concrete monitoring, in particular the 7kHz sensor and the 30kHz sensor. As mentioned previously the 7kHz sensor has a broad range and can monitor up-to 100kHz. From Fig. 4.2 and tables 4.1 and 4.2 it can be seen that this sensor repeatedly recorded emissions with large amplitudes and large energies. Similarly, the 30kHz sensor recorded emission of high energy and amplitude. A typical waveform and frequency response from both sensors can be seen in Figs. 4.6 and 4.7. These graphs show that the frequency range of AE travelling through concrete is between 5-50kHz. This result agrees with the finding of Ohtsu (1987) and Yuyama et al. (1999) who suggested that to monitor defects within concrete low frequency sensors are needed. Even though the results suggest that the 7kHz resonant frequency sensors and the 30kHz resonant frequency sensors are the most suitable for concrete monitoring, the 15kHz and 60kHz resonant frequency sensors also recorded emissions with large amplitudes and absolute energies at final failure. The advantages of using the 60kHz resonant frequency sensor in particular is that it will not be as susceptible to background noise as the other sensors due to the higher operating frequency.

To monitor in-service structures the sensor choice is dependant on the environmental conditions. Since all the sensors used in this study operate between -45^0C to $+85^0$C, they are applicable to the majority of structures. In most cases it is important that sensors are covered from weather conditions such as rain not only to protect the sensor from damage but also to protect the condition of the couplant between the structure and the sensor.

4.4. SENSOR ATTACHMENT AND COUPLANT SELECTION

4.4.1. Experimental procedure

Three 60kHz resonant frequency sensors each with different couplants were attached to a concrete beam. Each sensor was attached to the concrete surface using a steel clamp, which can be seen in Fig. 4.8. The mix proportions and dimensions of the concrete beams were as described in 4.3.

A twelve-channel "PAC MISTRAS" system was used to record AE for the test. The sensors were attached using three different types of couplant, silicon grease, silicon bathroom sealant and petroleum jelly (Vaseline). A PLF test was repeatedly performed adjacent to each sensor over a period of 38 days. The amplitude of each

PLF was recorded and the loss of signal over time was studied. The set-up used for each sensor is described in table B.3 in Appendix B.

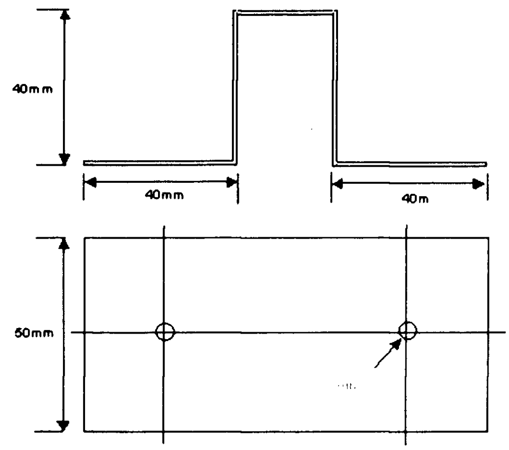

Figure 4.8. Dimensions of steel clamp used to hold the sensors onto the concrete specimen

4.4.2. Results and Discussion

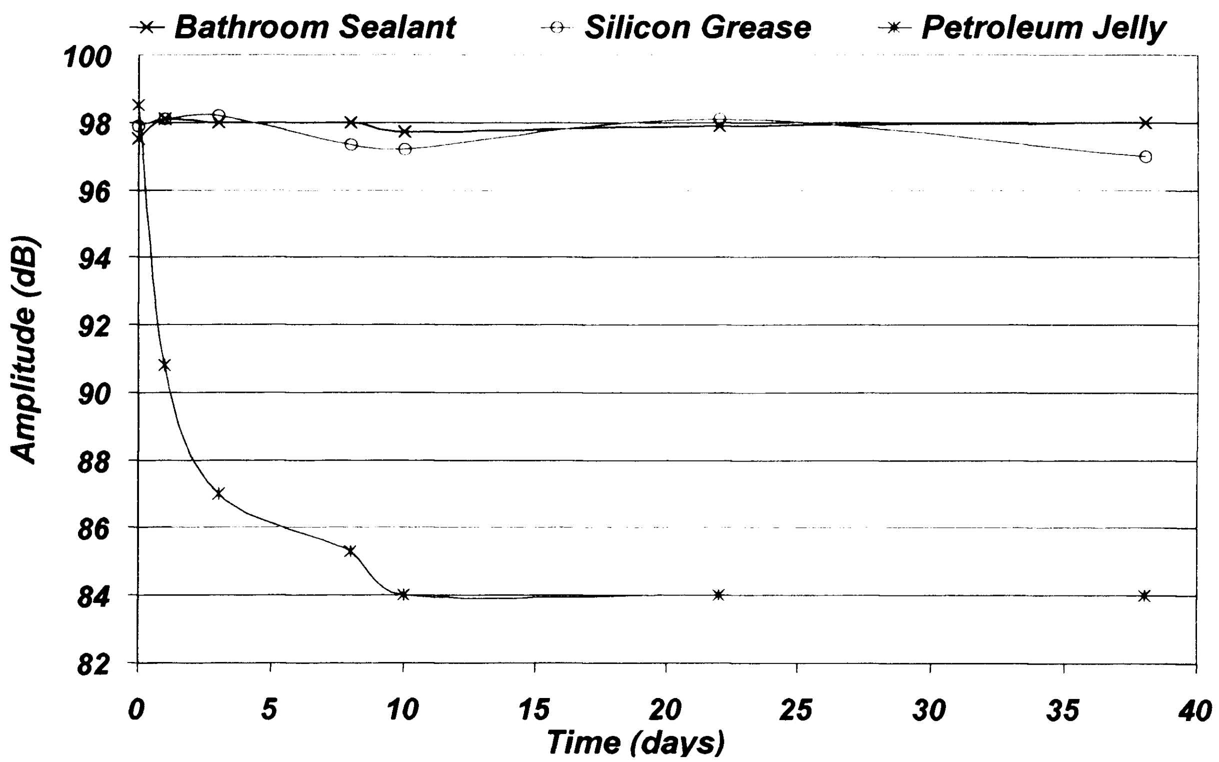

Figure 4.9. Amplitude recorded on all channels with respect to time

Fig. 4.9 shows how the amplitude varies with time for sensors attached to the concrete specimen using the same clamping method but different couplants. The red line in Fig. 4.9 shows that there is a large change in amplitude with respect to time for the sensor coupled to the surface of the concrete beam with petroleum jelly. In fact, over a period of 38 days, there was a loss of 24dB. Since amplitude in dB is given by equation 2.1, this corresponds to a voltage reduction of 94% loss. This suggests that there was some degradation between the specimen and the couplant. In fact, after removal of the sensor it could be seen that some of the couplant had soaked into the specimen and therefore it was concluded that petroleum jelly was not suitable as a couplant for concrete monitoring.

Over a period of 28 days, there was a small loss of amplitude on the sensor coupled to the specimen by silicon grease. In fact, there was only a loss of 2dB over this time. It is suggested that to ensure a good connection between the sensor and surface of the material that a PLF test produces a signal of amplitude between 97-100dB (Rindorf 1981, Pullin 2001). Since the signal produced by the PLF is still above 97dB the connection between the sensor and concrete specimen is good. This may not be the case over a longer period. Once again after removal of the sensor, it could be seen that some of the couplant had soaked into the specimen.

Similarly, there was only a small loss of amplitude on the sensor coupled to the surface of the specimen by silicon bathroom sealant. It was expected that this medium would permit large amplitudes to pass through whilst it was in a liquid state but would lose sensitivity as it cured. This was not the case, as large amplitudes were recorded over the 38-day period without any loss of signal. Not only did this material have no loss in sensitivity, it also provided some adhesive properties. Another advantageous property of this material is that it will not degrade or wash away in rain or other adverse weather conditions.

Various methods have been used to clamp sensors onto concrete specimens. One method is to attach steel plates to the material so that spring loaded magnets can be used to hold the sensor in place. Insulation tape has been used to attach sensors but this method is only suitable on laboratory specimens of certain geometry. Initially insulation tape provides the correct amount of pressure to the sensor but over longer periods of time, this may not be the case since the tape may loose its adhesive quality. In this experiment steel clamps were used to attach the sensor on to the concrete surface. These clamps (due to their size) can only be used for certain geometries but since they keep a constant pressure on the sensor, they are the preferred method for concrete monitoring. Alternatively, an epoxy resin or other semi-permanent bond may be used as both an attachment and couplant, however, extreme care must be taken to avoid damaging the sensors when they are removed from the structure.

4.5. CONCLUSIONS

Concrete specimens were failed in four-point bending with the aim of discovering the optimum sensor to use in concrete monitoring. By comparing sensors of different resonant frequency, it was found that high frequencies attenuated quickly in concrete. This result was also shown by the FFT of a waveform produced during failure on a broadband sensor. In fact, the typical frequency range of an emission in concrete was found to be between 5-55kHz.

Even though the results suggested that the 7kHz resonant frequency sensors and the 30kHz resonant frequency sensors were the most suitable for concrete monitoring, the 15kHz and 60kHz resonant frequency sensors also recorded emissions with large amplitudes and absolute energies at final failure. The advantages of using the 60kHz resonant frequency sensor in particular is that it will not be as susceptible to background noise as the other sensors due to the operating frequency.

Sensors were attached to a concrete beam with the aim of discovering the best couplant to monitor AE in both laboratory and field based specimens. Over 38 days, both silicon bathroom sealant and silicon grease proved to be adequate couplant for laboratory test pieces. Petroleum jelly on the other hand was not suitable because there was some degradation between the specimen and the sensor. For longer periods of time, silicon bathroom sealant may prove to be the better material because it did not soak into the concrete specimen. This experiment needs to be repeated over a greater period of time. Silicon bathroom sealant also provided some adhesive qualities that could be advantageous.

CHAPTER 5. AE TECHNIQUES FOR THE MONITORING OF LABORATORY- BASED PLAIN CONCRETE SPECIMENS

5.1. INTRODUCTION

As previously stated it is generally considered that there are two main approaches to the analysis of data acquired by AE instrumentation – the parameter analysis technique and the quantitative or signal-based technique. The parameter-based approach evaluates relative AE activities based on the measurement of parameters such as hit, amplitude, energy, etc. This method of analysis has been shown to be sensitive to the initiation and the growth of cracks within materials and structures. Quantitative signal-based techniques include moment tensor analysis (MTA). Both of these methods will be discussed in this chapter and their ability to monitor laboratory-based plain concrete specimens will be considered.

Although AE techniques have been extensively studied in concrete and have been applied to monitor in-service concrete structures, there has been very little research to study the relationship between AE parameters, such as energy and physical properties such as crack area and crack depth. Landis and Baillon (2002) tried to relate AE energy to fracture energy by monitoring mortar and concrete specimens loaded in flexure. It was found that mortar samples produced similar amounts of fracture energy and cumulative AE energy during each test. The concrete specimens did not produce regular results. The authors believed that this result was due to the inaccurate fracture energy calculation. Additional research to test this hypothesis is needed.

The quantitative waveform analysis known, as MTA, is an AE post-test analysis technique used to identify crack kinematics (crack type and crack orientation) from the recorded AE waveforms. This procedure determines the crack kinematics by investigating the eigenvalue analysis of a moment tensor. The theory of MTA has been discussed in chapter 2 and will be applied to a series of tests in this chapter.

5.2. AIMS AND OBJECTIVES

This chapter details experiments using both the parameter-based approach to analysis and MTA. The aim of the experiments using parameter analysis was to attempt to relate AE energy to physical crack parameters. The aim of the experiments using MTA was to provide an understanding of the effectiveness of MTA in predicting failure mechanisms.

For the experiment involving the study of AE energy and fracture dimensions, the experimental objectives were to:

- Fail specimens with different crack areas, crack depths and crack widths monitoring each failure using AE techniques.

For the experiments involving the study of moment tensor analysis, the experimental objectives were to:

- Produce events with clear and defined initial P-waves (on at least six sensors) such that the SiGMA procedure can be successfully executed.
- To calculate the crack type and orientation of each event from the eigenvalue analysis of each moment tensor matrix and to relate them to the failure mechanism expected during loading.

5.3. A STUDY OF THE RELATIONSHIP BETWEEN CONCRETE CRACK PARAMETERS AND ACOUSTIC EMISSION ENERGY

To discover if a relationship between AE energy and crack area exists, mortar specimens grouted into a concrete beam were failed by a 1kg mass. This work is described in a paper (Beck *et. al.* 2003a), which is presented in Appendix D. Initial investigations using the procedure suggested that AE energy may be dependent not only on crack area but also on crack depth. No relationship between AE energy and crack area or crack depth was found. Since this was a preliminary study, more investigations are required to discover if AE energy is related to the physical properties of a crack.

5.4. MTA OF AE PRODUCED BY A PIEZOELECTRIC DEVICE ENCASED IN CONCRETE

5.4.1. Experimental Procedure

The SiGMA procedure was applied to AE waveforms recorded during the pulsing of a PZT embedded within a mortar cube and AE sensors attached to the surface. The mortar cube has dimensions 150mm*150mm*150mm and the mix proportions of the cement, fine aggregate and water were 1:1.8:0.5 by mass respectively. Before casting, the PZT was held at the centre of the mould using wires attached to the edge of the PZT disc. The characteristics of the PZT disc are given in table 5.1. The resonant frequency of the disc is much lower than concrete failure but was the highest frequency disc available. The disc was pulsed using a TGP11010MHz pulse generator (Thurlby-Thander Instruments). The pulse generated was a square wave with a period of 10μs, a pulse width of 50μs and a voltage of 20V.

Six 60kHz resonant frequency sensors were attached to the concrete specimen to detect the AE waveforms created by the pulsed PZT. AE waveforms detected at the sensors were recorded by a digital memory, which converted analogue records into digital records at a sampling rate of 1MHz. The AE set-up used for each channel is given in table B.4 in Appendix B. The number of AE events recorded was 20, all of which all were selected for the SiGMA analysis. The P-wave velocity in concrete was calculated to be approximately 4000m/s. Fig. 5.1 shows the positioning of the sensors on the cube. Table 5.2 shows the sensor location in terms of its co-ordinates.

Table 5.1. The characteristics of the piezoelectric device embedded within the mortar cube.

Characteristics	35mm Piezoelectric Device
Resonant Frequency	2.8kHz ±0.5kHz
Impedance at resonance	450Ω
Capacitance	20nF±30%
Max. input voltage	30v p-p
Operating temperature	-20°C+70°C

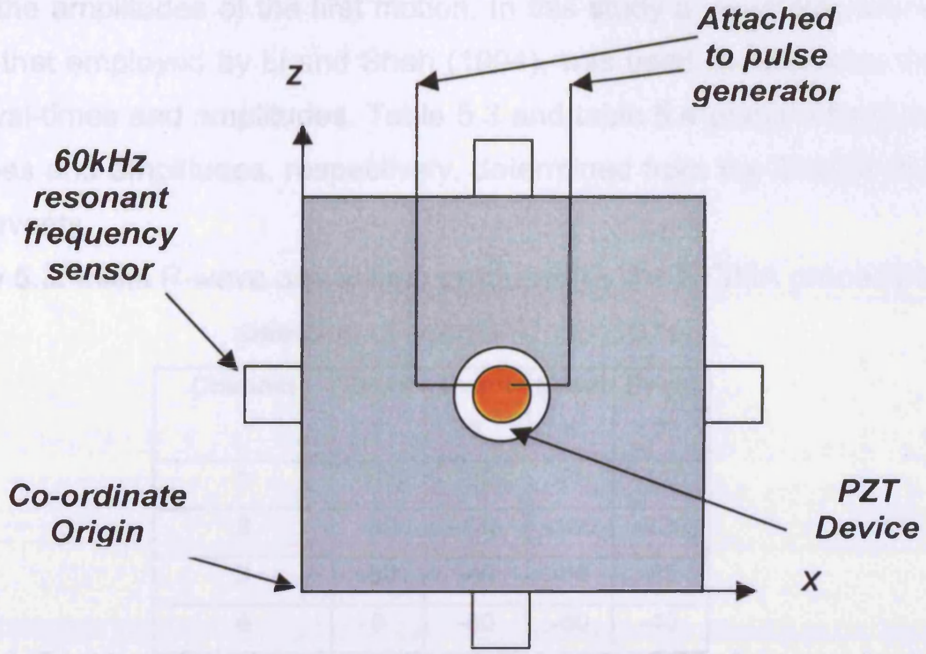

Figure 5.1. Position of each sensor with relation to the PZT. A sensor is also placed on the front and the back at the centre of the cube.

Table 5.2. Co-ordinate position of the sensors attached to the mortar cube

Channel	X position (m)	Y position (m)	Z position (m)
1	0.075	0.000	0.075
2	0.150	0.075	0.100
3	0.075	0.150	0.075
4	0.000	0.075	0.100
5	0.075	0.120	0.150
6	0.075	0.030	0.000

5.4.2. Results and Discussion

By embedding a PZT device within a concrete cube to represent an artificial source, it was anticipated that repeatable emissions with clear and distinct initial P-waves would be detected on each sensor making it possible to perform MTA with a defined region of events with similar crack kinematics. If the artificial source produced a repeatable emission then it was expected that the initial P-wave arrival-times and amplitudes should be similar. Li et al. (2000) and Landis et al. (1991) discussed P-wave arrival determination for concrete specimens. These papers reviewed the techniques used previously for P-wave selection including a procedure for the automated determination of P-wave arrival time for AE source location using an adaptive moving average filter for removing random noise and Laplacian filters to enhance the amplitudes of the first motion. In this study a visual inspection method, similar to that employed by Li and Shah (1994), was used to determine the initial P-wave arrival-times and amplitudes. Table 5.3 and table 5.4 present the initial P-wave arrival times and amplitudes, respectively, determined from the SiGMA procedure of selected events.

Table 5.3. Initial P-wave arrival time produced by the SiGMA procedure for a selection of events (Units=10^{-6}s)

Channel	Event 1	Event 3	Event 4	Event 7
1	-100	-80	-80	-120
2	-60	-120	-160	-220
3	-80	-40	-60	-80
4	0	-60	-60	-40
5	-60	-40	-60	-80
6	40	0	20	0

Table 5.4. Initial P-wave amplitude, produced by the SiGMA procedure, for a selection of events (Units=V)

Channel	Event 1	Event 3	Event 4	Event 7
1	-1.54	-1.48	-1.39	-1.66
2	1.33	1.31	1.20	1.32
3	-2.90	-2.87	-2.80	-2.86
4	1.67	1.67	1.36	1.65
5	0.51	0.54	0.57	0.68
6	0.25	0.21	0.23	0.24

From tables 5.3 and 5.4 it can be seen that for each channel the initial P-wave arrival-times and amplitudes are very similar for each separate pulse. Some variation was expected for the initial arrival-times since the PZT device had a diameter of 35mm. These small variations suggest that each event was in close proximity to the rest of the events with similar crack kinematics. Table 5.5 displays the locations; the shear percentage and the orientation of the motion and the normal of each analysed event. This table is represented graphically in Fig. 5.2 where each located event is classified as either tensile, mixed-mode or shear. The arrows represent the direction of the motion of each event in the x-z plane.

Table 5.5. The location, the shear percentage, the orientation of the motion and the normal of all events processed by the SiGMA procedure.

EVENT NUMBER	LOCATION			SHEAR %	MOTION			NORMAL		
	X (mm)	Y (mm)	Z (mm)		X	Y	Z	X	Y	Z
1	**85**	**58**	**100**	**58**	-0.722	0.656	0.220	-0.525	-0.251	0.814
2	**120**	**55**	**126**	**85**	-0.428	0.834	0.349	-0.678	-0.45	0.589
3	**93**	**65**	**94**	**32**	-0.01	-0.51	0.855	-0.879	-0.24	0.412
4	**102**	**68**	**101**	**20**	0.625	0.595	-0.505	-0.133	0.775	-0.617
5	**120**	**53**	**112**	**76**	-0.541	0.744	0.392	-0.58	-0.51	0.637
6	**113**	**52**	**123**	**71**	-0.481	0.798	0.362	-0.682	-0.4	0.614
7	**115**	**64**	**103**	**32**	-0.326	0.909	-0.261	0.545	0.633	-0.550
8	**109**	**72**	**105**	**25**	0.694	0.543	0.473	-0.146	0.76	-0.633
9	**109**	**59**	**96**	**25**	-0.303	0.861	-0.410	0.508	0.642	-0.574
10	**116**	**75**	**107**	**23**	0.126	-0.72	0.686	-0.687	-0.52	0.506
11	**120**	**52**	**125**	**70**	-0.476	0.787	0.392	-0.666	-0.41	0.629
12	**96**	**64**	**102**	**51**	-0.323	0.932	-0.163	0.641	0.485	-0.594
13	**100**	**63**	**100**	**37**	-0.271	0.888	-0.377	0.655	0.548	-0.520
14	**96**	**93**	**84**	**57**	0.46	-0.79	0.399	-0.423	-0.13	0.897
15	**96**	**66**	**101**	**36**	0.768	0.497	-0.405	-0.162	0.773	-0.613
16	**85**	**76**	**90**	**85**	-0.397	-0.53	0.747	-0.811	0.569	0.136
17	**103**	**68**	**102**	**30**	0.148	-0.76	0.683	-0.733	-0.5	0.459
18	**109**	**60**	**126**	**90**	-0.308	0.912	0.184	0.727	0.429	-0.537
19	**116**	**76**	**104**	**18**	0.667	0.466	-0.586	-0.026	0.656	-0.754

A small variation in location can be seen in Fig. 5.2 where there is a range of approximately 35mm-40mm in both the x direction and the z direction suggesting that moment tensor analysis is precise. The location and crack kinematics of events in the x-y plane are not displayed in this study but show a comparable range of depth in the y direction. From Fig. 5.2, it can be seen that even though there is a cluster of events the location of the events identified by the MTA is not at the centre as expected, therefore indicating a lack of accuracy.

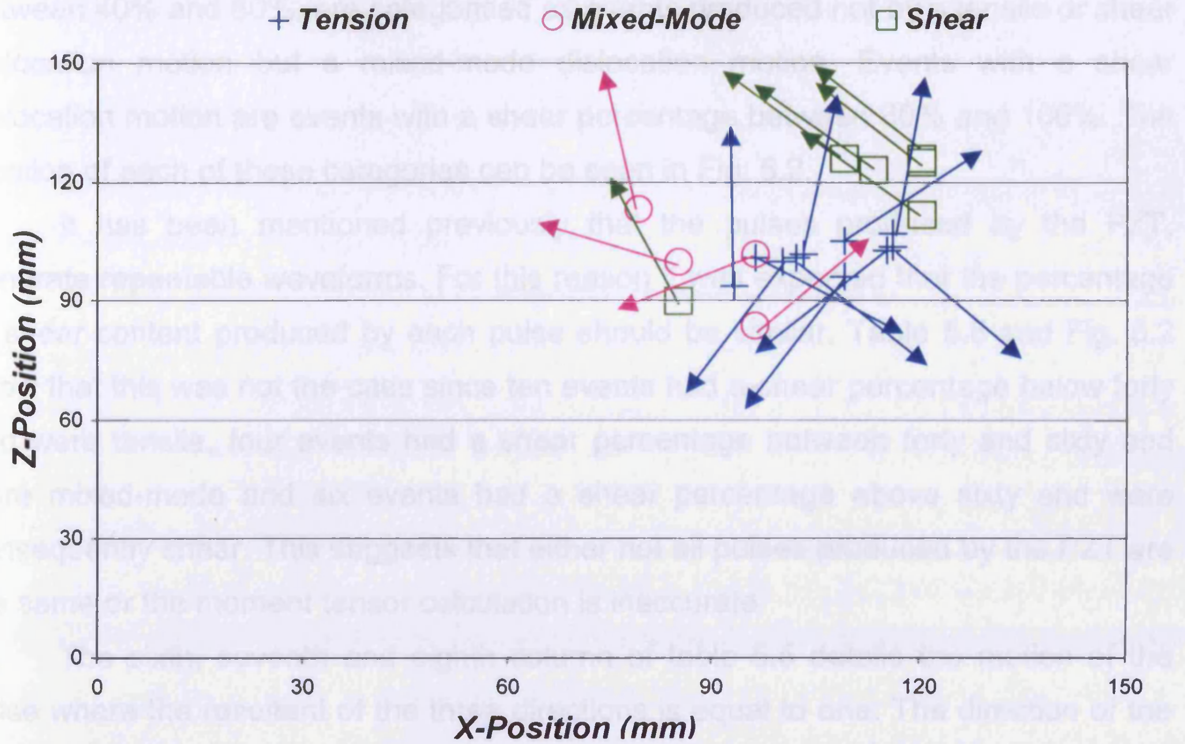

Figure 5.2. The location, crack type and orientation of motion in the x-z plane produced by the MTA.

The inaccurate location could be due to an incorrect determination of the P-wave velocity. The "measured velocity" describes the speed at which an AE signal is observed to travel between two fixed points in a propagation medium. To calculate the velocity of an emission, the time difference of an emission produced by an artificial source between two sensors separated at a known distance is recorded. This technique is described in chapter 3. This method determines the velocity of a wave from the first threshold crossing. Since the initial P-wave is produced prior to the first threshold crossing, the wave velocity determined may be incorrect. This would produce an inaccurate location.

Another reason for this failure to locate at the centre could be due to the wires attached to the PZT to help support the device during casting. When the PZT is pulsed with a known current, the two disks of the device open producing a signal. This signal then travels through the medium eventually reaching the sensors on the surface. Since the wires were attached to the PZT, some of the signal travels along the wires. This could affect the P-wave and the location of each event.

The fifth column of table 5.5 represents the shear percentage of each event. Events with a shear percentage of forty percent or below are categorised as events produced by a tensile displacement discontinuity. Events with a shear percentage between 40% and 60%, are categorised as events produced not by a tensile or shear dislocation motion but a mixed-mode dislocation motion. Events with a shear dislocation motion are events with a shear percentage between 60% and 100%. The location of each of these categories can be seen in Fig. 5.2.

It has been mentioned previously that the pulses produced by the PZT, generate repeatable waveforms. For this reason it was expected that the percentage of shear content produced by each pulse should be similar. Table 5.5 and Fig. 5.2 show that this was not the case since ten events had a shear percentage below forty and were tensile, four events had a shear percentage between forty and sixty and were mixed-mode and six events had a shear percentage above sixty and were consequently shear. This suggests that either not all pulses produced by the PZT are the same or the moment tensor calculation is inaccurate.

The sixth, seventh and eighth column of table 5.5 details the motion of the pulse where the resultant of the three directions is equal to one. The direction of the motion in the x-z plane is predicted in Fig. 5.2 and is represented by the direction of the arrow. From table 5.5 and Fig 5.2 it can be seen that the direction of the arrows are not the same for each event. Considering that the P-wave values are similar for each event but the crack kinematics vary, it is likely that any inaccuracy in determining the P-wave arrival times and amplitudes of the waveforms of an event will greatly effect the crack kinematics and location.

It was expected that by using a PZT device as an artificial source, repeatable waveforms with clear and defined P-waves would be recorded. Since the nature of the pulse of the PZT device is unknown it has not been possible to validate the crack kinematics of each pulse. In fact, it has been found that even though the waveforms produced are very similar, different types of emissions were detected. To further investigate the use of MTA as a post-test analysis technique, the method was therefore now applied to actual concrete failure to avoid the added complications such as the supporting frame for the PZT.

5.5. MTA OF AE IN CONCRETE SPECIMENS FAILED STATICALLY IN FLEXURE

5.5.1. Experimental Procedure

The SiGMA procedure was employed to AE waveforms recorded during the failure of a notched concrete beam loaded statically in four-point bending. This work is described in a paper (Beck et. al. 2003b), which is presented in Appendix C. Initial investigation suggested that tensile cracks were produced ahead of the notch tip, propagating in an upward direction. Results discovered in a further investigation are discussed in this section.

5.5.2. Results and Discussion

By failing a notched concrete specimen in flexure, it was hoped that waveforms with a clear and definitive initial P-wave could be detected on each sensor. From 65-recorded events it was possible to analyse only 15 events using the SiGMA procedure. The number of events to which the analysis was applicable was limited because many events did not have six clear P-wave portions due to excessive attenuation. To calculate the six moment tensor components the initial P-wave arrival-time and amplitude is needed on a minimum of six sensors. Due to a lack of processed events, it is difficult to correlate the locations produced with the actual motion of the crack.

Fig. 5.3 displays a typical event where the initial P-wave arrival-time and amplitude can be chosen on each of the channels. Table 5.6 displays the locations; the shear percentage and the orientation of the motion and the normal of each of the analysed events. This table is presented graphically in Figs. 5.4 and 5.5 where the location of each event, the crack type and the orientation of each event in the x-z and x-y planes respectively, are displayed with respect to the co-ordinate origin.

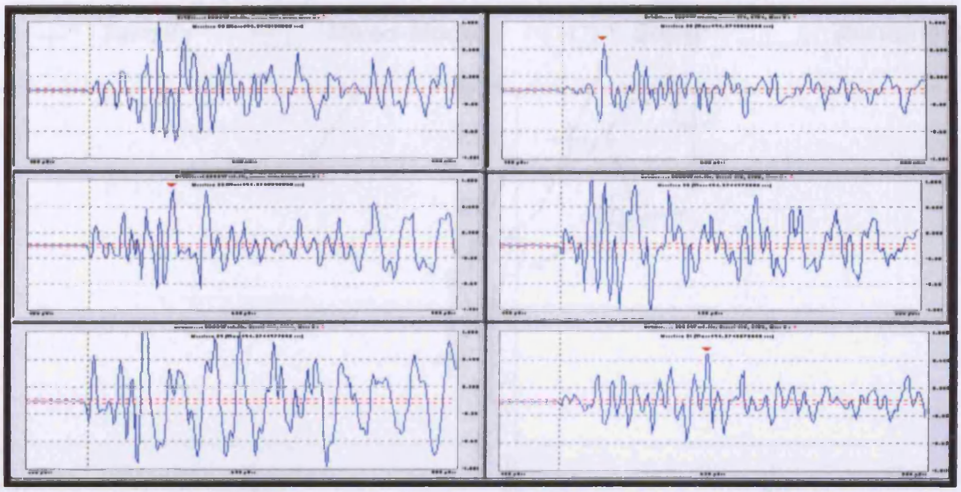

Figure 5.3. AE waveforms of an event recorded on all channels during failure of the first concrete specimen.

Table 5.6. The location, the shear percentage, the orientation of the motion and the normal of all events processed by the SiGMA procedure.

EVENT N°	LOCATION X (mm)	LOCATION Y (mm)	LOCATION Z (mm)	SHEAR %	MOTION X	MOTION Y	MOTION Z	NORMAL X	NORMAL Y	NORMAL Z	ANGLE IN X-Z PLANE	ANGLE IN X-Y PLANE
2	9	137	-16	50	0.677	0.077	-0.732	-0.425	-0.101	-0.899	313	6
4	-5	96	16	25	-0.022	-0.478	0.878	0.630	0.168	0.758	91	267
12	10	121	77	10	0.405	-0.019	0.914	0.788	-0.340	0.513	66	357
17	-12	108	22	13	-0.072	-0.109	0.991	0.548	-0.054	0.835	94	237
21	-13	111	21	8	0.061	-0.224	0.973	0.504	-0.120	0.856	86	285
22	34	110	85	60	0.036	0.422	0.906	-0.746	0.665	-0.037	268	85
33	-40	3	72	22	0.461	0.541	0.703	0.959	-0.056	0.279	57	50
52	16	43	56	24	0.989	-0.06	0.132	0.693	0.626	-0.358	8	357
54	-4	42	33	26	0.178	0.177	0.968	0.678	-0.499	0.540	80	45
56	-9	86	47	25	0.342	-0.159	0.926	0.674	0.561	0.481	70	335
57	-1	55	-20	84	0.032	-0.535	0.844	0.445	0.714	0.541	88	273
58	17	13	55	90	-0.798	-0.466	-0.383	0.394	0.193	-0.899	206	390
59	-5	64	7	55	-0.366	-0.574	0.733	-0.798	-0.548	-0.250	117	238
60	22	16	59	96	-0.312	-0.363	0.878	0.879	0.242	0.411	110	229
62	-6	5	24	24	-0.194	-0.157	0.968	0.640	0.048	0.767	101	219

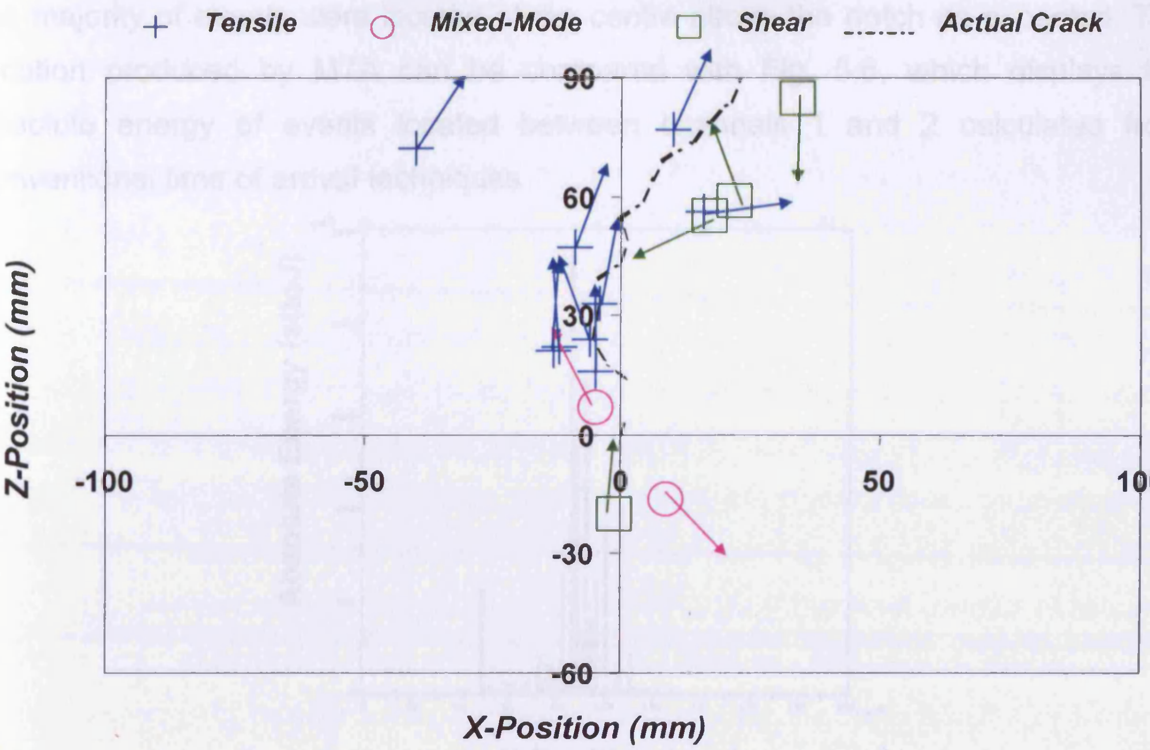

Figure 5.4. Location of AE sources and their crack kinematics produced by moment tensor analysis in the x-z plane.

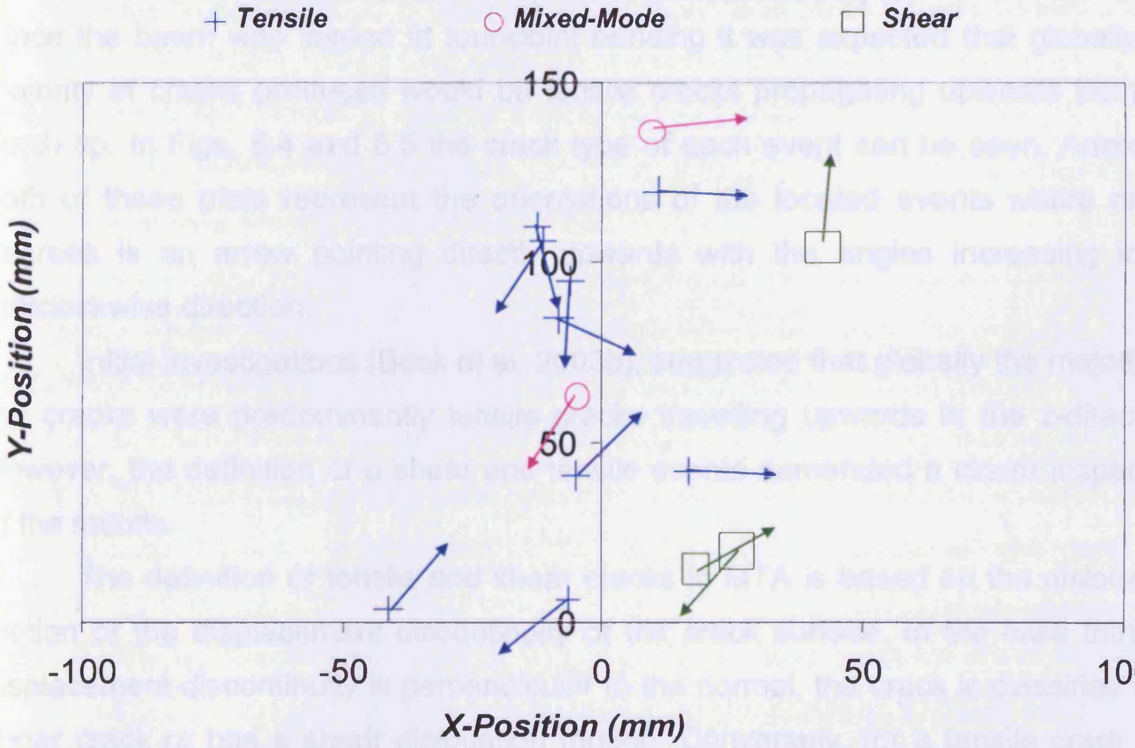

Figure 5.5. Location of AE sources and their crack kinematics produced by moment tensor analysis in the x-y plane.

All the located AE events are classified as either tensile, shear or mixed-mode cracks. The location of the events produced by the moment tensor analysis show that the majority of events were located at the centre above the notch as expected. The location produced by MTA can be compared with Fig. 5.6, which displays the absolute energy of events located between channels 1 and 2 calculated from conventional time of arrival techniques

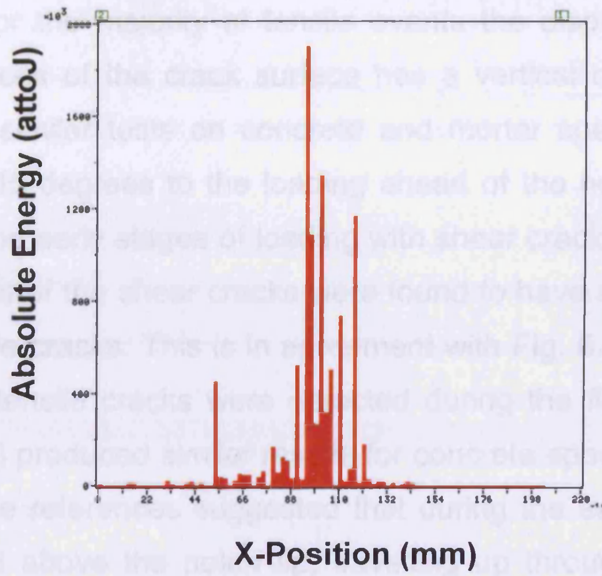

Figure 5.6. Absolute energy located between channels 1 and 2 using conventional time of arrival location techniques

Since the beam was loaded in four-point bending it was expected that globally the majority of cracks produced would be tensile cracks propagating upwards from the notch tip. In Figs. 5.4 and 5.5 the crack type of each event can be seen. Arrows in both of these plots represent the orientations of the located events where ninety degrees is an arrow pointing directly upwards with the angles increasing in an anticlockwise direction.

Initial investigations (Beck et al. 2003b), suggested that globally the majority of the cracks were predominantly tensile cracks travelling upwards in the z-direction. However, the definition of a shear and tensile events demanded a closer inspection of the results.

The definition of tensile and shear cracks in MTA is based on the dislocation motion or the displacement discontinuity of the crack surface. In the case that the displacement discontinuity is perpendicular to the normal, the crack is classified as a shear crack or has a shear dislocation motion. Conversely, for a tensile crack, the displacement discontinuity is parallel to the normal. Since the material is non-homogeneous, local stress patterns are particularly complex resulting in intricate crack mechanisms that do not readily lend themselves to being classified as pure tensile or shear mechanisms. As a result, even though macroscopically the crack propagates in the tensile mode, microscopically shear and mixed-mode cracks may exist.

By comparing the definition of a tensile crack with the orientations in Fig. 5.4 it can be seen that for the majority of tensile events the displacement discontinuity between the two faces of the crack surface has a vertical direction. Ohtsu et. al. (1998a) performed similar tests on concrete and mortar specimens where tensile cracks were found 45 degrees to the loading ahead of the notch tip. These cracks were found during the early stages of loading with shear cracks recorded at the later stages. The locations of the shear cracks were found to have a wider range than the location of the tensile cracks. This is in agreement with Fig. 5.4 and table 5.6 where four of the six non-tensile cracks were detected during the final stages of loading. Ohtsu et. al. (1998a) produced similar results for concrete specimens loaded in four-point bending. These references suggested that during the early stages of loading, events were located above the notch tip, travelling up through the specimen with increasing damage.

Considering table 5.6 it can be seen that there is no sequence of events with respect to the z-axis. Since the majority of events are tensile cracks with vertical displacement discontinuities and no sequence with respect to the z-axis it could be suggested that microcracking occurs randomly throughout the loading even though the high stresses are expected at the notch.

Even though concrete consists of cement paste and aggregate, internal voids (with sizes ranging up to a couple of millimetres) can exist within the material. These voids include pores in the cement paste, cracks at the matrix-aggregate interface, shrinkage and thermal cracking (Shah and Ouyang 1994) and can play an important role in the mechanical behaviour of concrete. Due to the high stress intensity at the notch during loading, it is expected that cracks occur ahead of the notch tip Considering that concrete initially contains voids and from the results displayed in Fig. 5.4, it is suggested that during loading microcracks in the form of tensile cracks occur parallel to the load with the macrocrack propagating up through each of the initial microcracks.

Since only a small number of events were appropriate for the SiGMA procedure it is difficult to correlate the locations and crack kinematics with the actual motion of the crack. Due to background noise from the test set-up, an initial threshold of 65dB was set to trigger the recording of the sensors. This threshold allowed 65 events to be recorded where only 17 were suitable for the SiGMA procedure. It is possible that the threshold did not allow the recording of emissions from all modes of failure. Similarly due to the nature of the signals from different failure mechanisms within the specimen not all failure types may produce six clear and defined initial P-waves. This suggests moment tensor analysis may not distinguish the location and crack kinematics for all failure mechanisms for all test set-ups.

5.6. MTA OF AE PRODUCED DURING THE PUSHOUT OF STEEL REINFORCEMENT BAR ENCASED IN CONCRETE

5.6.1. Experimental Procedure

The SiGMA procedure was applied to AE waveforms recorded on sensors attached to a concrete surface, during the loading of a length of steel rebar encased within a concrete specimen. The specimen was of dimensions 800mm long by 500mm square, with the 32mm deformed steel rebar centred within it and protruding from the concrete by approximately 42mm. The concrete block was further reinforced by a cage to control surface cracking. The configuration of the specimen is given in Fig. 5.7. Sensors (channels 5 and 6) were also attached to the back of the specimen as were channels 1 and 2.

A load was applied to the specimen via a steel plate, which was placed on the protruding steel reinforcement. An Avery 1000kN test machine was used in compression mode. Fig. 5.8 shows a photograph of the specimen and the loading arrangement. The load history for the specimen can be seen in Fig. 5.9.

Six 30kHz resonant frequency sensors with an amplification of 40dB were attached to the concrete specimen to detect AE waveforms during failure. 60kHz sensors were also attached to the specimen to provide location of damage using conventional methods. Tables B.5 and B.6 in Appendix B display the set-up used for each channel for both sensor types. The P-wave velocity in concrete was calculated as approximately 4100m/s.

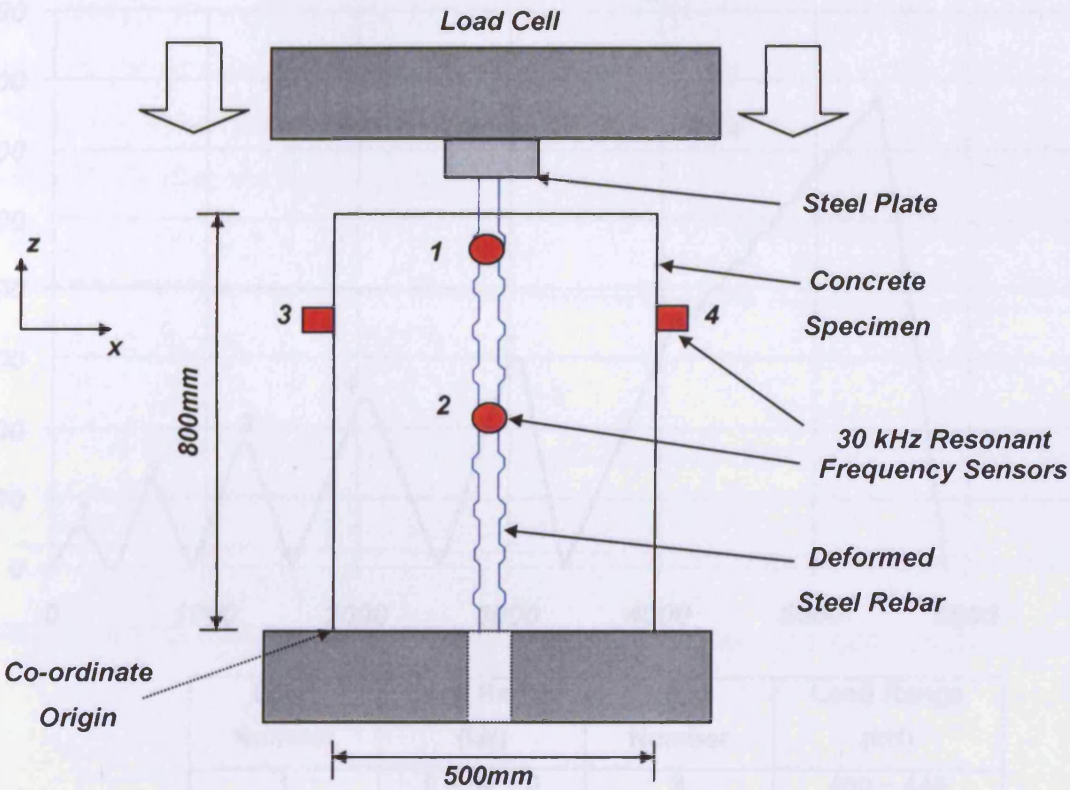

Figure 5.7. Loading method and sensor location.

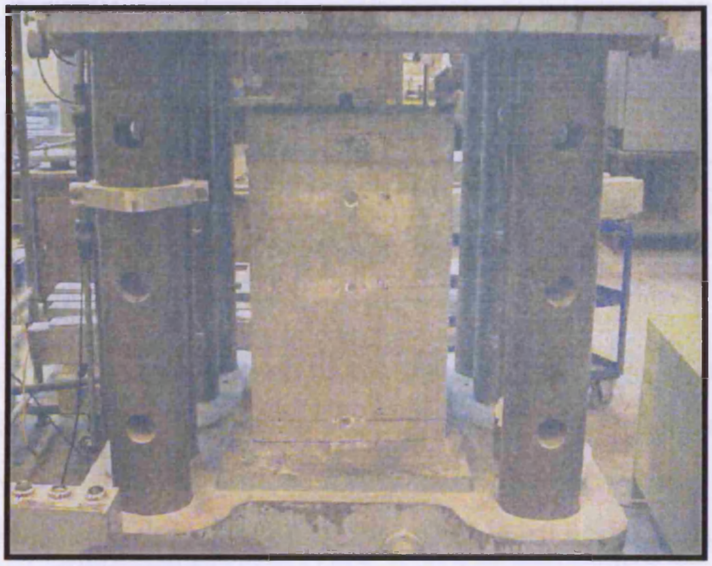

Figure 5.8. Photograph of concrete specimen in the test machine .

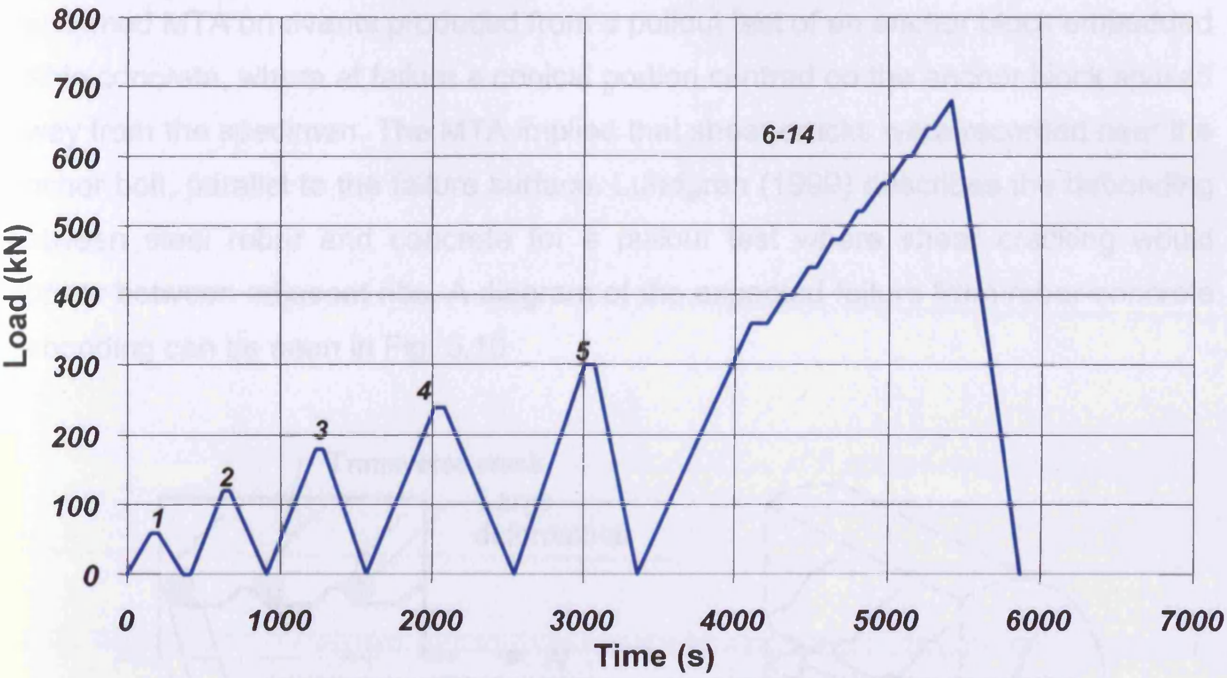

Load Number	Load Range (kN)	Load Number	Load Range (kN)
1	0 – 60 – 0	8	400 – 440
2	0 – 120 – 0	9	440 – 480
3	0 – 180 – 0	10	480 – 520
4	0 – 240 – 0	11	520 – 560
5	0 – 300 – 0	12	560 – 600
6	0 – 360	13	600 – 640
7	360 – 400	14	640 – 680

Figure 5.9. Load history of the complete test

5.6.2. Results and Discussion

Due to the length of the rebar encased within the concrete specimen, it was predicted that the outer section of the rebar not encased in concrete would yield in compression before the rebar and concrete debonded completely. The specimen was therefore loaded until deformation of the outer steel could be seen. Even though the specimen did not completely fail, 131 events were recorded, with clear and well-defined initial P-waves.

During loading of the rebar, if stresses in the concrete specimen became large enough it was expected that transverse microcracks would originate at the tips of the ribs. These cracks are due to the local pressure in front of the ribs, which gives rise to stresses at the tips of the ribs (Lundgren and Gylltoft 1999). Ohtsu (1989b) performed MTA on events produced from a pullout test of an anchor block embedded within concrete, where at failure a conical portion centred on the anchor block spalled away from the specimen. The MTA implied that shear cracks were recorded near the anchor bolt, parallel to the failure surface. Lundgren (1999) describes the debonding between steel rebar and concrete for a pullout test where shear cracking would appear between adjacent ribs. A diagram of the expected failure from rebar-concrete debonding can be seen in Fig. 5.10

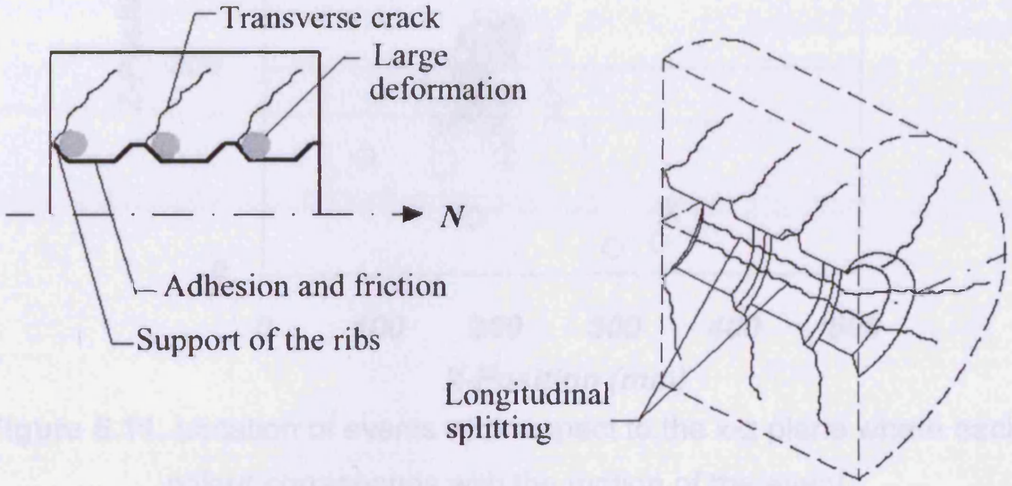

Figure 5.10. Expected failures between steel rebar and concrete for a pullout test (Lundgren 1999)

The locations, the shear percentage and the orientation of the motion and the normal of each of the analysed events are tabulated in table C.1 in Appendix C. This table is graphically represented in Figs. 5.11, 5.12 and 5.13 where the location of each event in the x-z plane, x-y plane and y-z plane respectively is displayed. Each event has been arranged with respect to the motion of the event

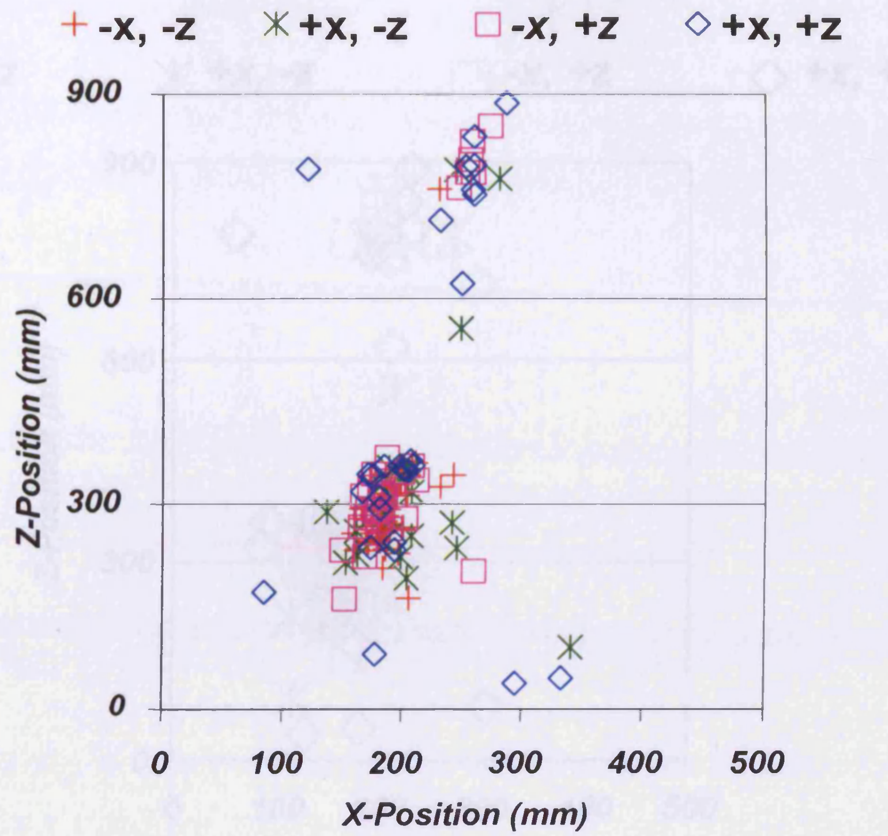

Figure 5.11. Location of events with respect to the x-z plane where each colour corresponds with the motion of the event

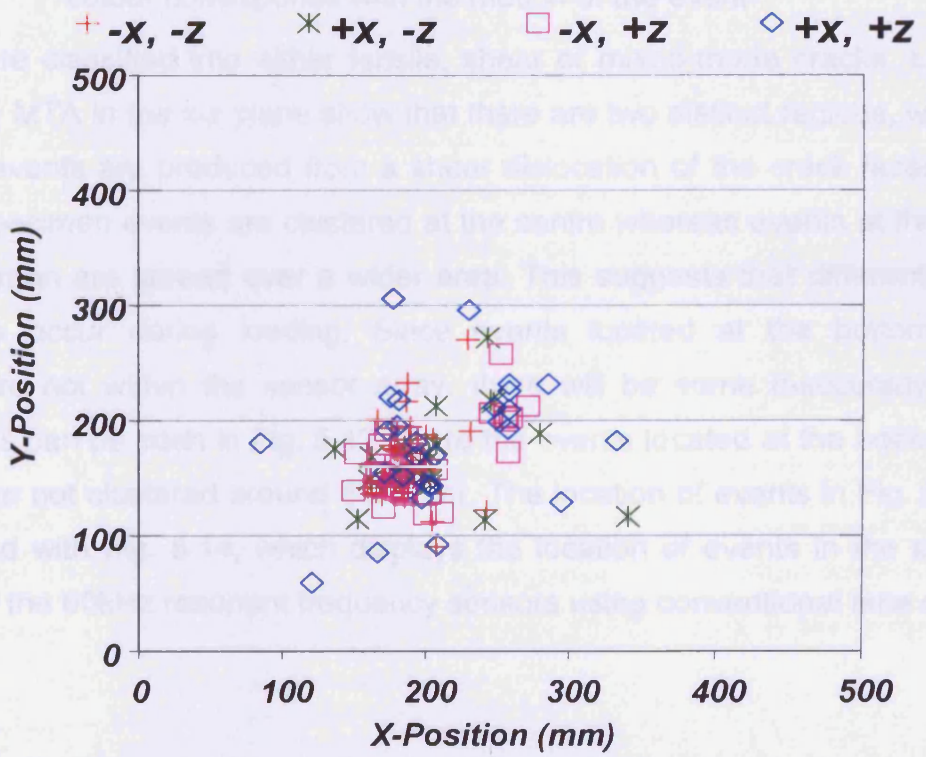

Figure 5.12. Location of events with respect to the x-y plane where each colour corresponds with the motion of the event

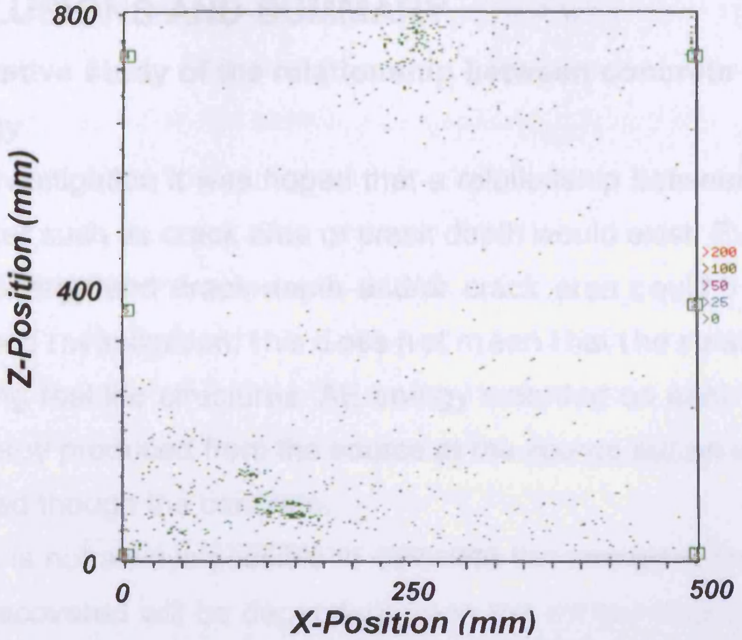

Figure 5.14. Location of event s recorded upon the 60kHz resonant frequency sensors

Examination of Fig. 5.11 shows that events with a negative z motion are located mainly at the base of the specimen where events with a positive z motion are located in both regions. Prior to loading it was hoped that even though the specimen would not fail, some debonding between the rebar and concrete would occur. Since the specimen is loaded through the bar and supported at the base it is possible that some concrete failure may occur as a result of the compression stresses in the support area. Given the loading arrangement, both failure modes would produce events with a shear dislocation motion between the crack faces.

Events located at the top of the specimen are more likely to have been produced by debonding of the concrete and the rebar. At the base of the specimen, failure mechanisms such as concrete failure are intricate and complex, which could produce events of varied crack type and orientation. This can be seen in Figs. 5.11, 5.12 and 5.13 where events have variable orientation and have a wider scatter whereas events located at the top of the specimen are clustered around the concrete-steel interface. Because of this it is suggested that in future when using this test arrangement the steel rebar is debonded from the concrete at the bottom of the specimen to minimise this concrete failure.

5.7. CONCLUSIONS AND SUMMARY

5.7.1. Quantitative study of the relationship between concrete crack parameters and AE energy

Prior to any investigation it was hoped that a relationship between AE energy and a crack parameter such as crack area or crack depth would exist. Even if a relationship between AE energy and crack depth and/or crack area could be discovered by a laboratory-based investigation, this does not mean that the relationship is suitable when assessing real life structures. AE energy recorded on each sensor type would not be the energy produced from the source at the source but an energy that would a have attenuated though the concrete.

Since it is not always possible to calculate the energy at the source itself, any relationship discovered will be dependant upon the sensor-source distance. Another factor, which will affect the applicability of a relationship discovered within the laboratory, is the actual material. In laboratory-based specimens, the mix proportions and curing conditions are known and can be controlled.

Considering the sensor-source distance and the difference in material properties, it could be suggested that any laboratory-based relationship would only be appropriate for the testing of structures of a similar size and detail. This makes it difficult to discover a relationship between AE energy and crack dimensions such as depth and area for in-service structures. For this reason, the study between AE energy and crack depth or crack area was not investigated any further.

5.7.2. MTA of AE in concrete specimens

Laboratory-based tests were conducted to determine the applicability of the method to provide qualitative information concerning the condition of real-life concrete structures. The following section discusses the conclusions of each test with a final summary about the limitations and advantages of the technique.

MTA of AE produced by a piezoelectric device encased in concrete

The location of the events, calculated from the initial P-wave arrival-time on all sensors, indicated that the majority of events were located within close proximity of a single source even though events were not clustered at the centre of the concrete cube where the PZT was held. It was found that the MTA produced a mixture of shear, tensile and mixed-mode displacement discontinuities even though the PZT device produced very similar waveforms for each event. This suggests each pulse does not produce the same crack kinematics and that either not all pulses produced by the PZT are the same or the moment tensor calculation is inaccurate.

Examination of the motion of each event shows that the direction of each event is not the same even though the P-wave arrival times and amplitude are similar for each event. Given that the P-wave values are similar for each event but the crack kinematics vary, it is likely that any inaccuracy in determining the P-wave arrival times and amplitudes of the waveforms of an event will greatly effect the crack kinematics and location.

To be able to use MTA as a quantifiable post-test analysis technique, the method needs to be performed on actual concrete failure where there are no complexities such as supporting the PZT and a constant method of opening is produced.

MTA of AE in concrete specimens failed statically in flexure

From 65-recorded events it was possible to analyse only 17 using the SiGMA procedure. Due to the lack of processed events, it is difficult to correlate the locations and crack kinematics of sources from MTA calculations with the actual motion of the crack.

Since the beam was loaded in four-point bending it was expected globally that the majority of cracks produced would be tensile cracks propagating upwards from the notch tip. The location of the events produced by MTA show that the majority of events are located at the centre above the notch as expected. The location produced by MTA was validated by conventional time of arrival location techniques where large absolute energies were located at the centre.

By considering the definition of a shear and tensile crack and the direction of motion of the analysed events it can be seen that for the majority of tensile events the displacement discontinuity between the two faces of the crack surface have a vertical direction. There was also no sequence to the events with respect to the z-axis. From the results it can be suggested that micro-cracking occurs randomly throughout the loading even though the high stresses are expected to be at the notch. As a result it would appear that a macrocrack propagates through each of the initial microcracks at final failure.

MTA of AE produced during the push-out of a steel reinforcement bar encased in concrete

Location of each event calculated from the MTA show that there are two distinct regions. As expected the majority of events were determined to have a shear dislocation motion between the crack faces. At the top of the specimen events are clustered at the centre whereas events at the bottom of the specimen have a wider range. This suggests that two different fracture mechanisms occur during loading. The locations of the events determined by MTA are similar to the location identified by conventional time of arrival methods.

At the base of the specimen, local stress patterns were particularly complex resulting in intricate crack mechanisms that do not readily lend themselves to being classified as pure tensile or shear mechanisms. As a result, it is not unreasonable that locally tensile, shear and mixed-mode cracks may be generated, propagating in a variety of directions.

Since concrete failure would occur at the base of the specimen it is likely that events located at the top of the specimen are produced from debonding of the concrete and the rebar. This can be seen from the results of the MTA where events have variable orientation and have a wider scatter at the base of the specimen. To reduce the effect of concrete failure so that only debonding between the steel rebar and concrete exists it has been suggested that the concrete and steel at the bottom of the specimen is debonded prior to loading.

Applicability of MTA for the monitoring of in-field structures

Determining the initial arrival-times and amplitudes of an event can be a long and tedious task. Since the P-wave amplitude and arrival time of each channel is needed to complete the analysis any error in determining the correct P-wave components can lead to inaccuracies in location and the crack kinematics. Determining the initial P-waves of an event for moment tensor analysis by visual methods can be highly subjective, as well as time consuming. Since the only method of determining the P-wave arrival-times and amplitudes is by visual methods, MTA is not suitable for large amounts of data.

The majority of research conducted using MTA has been performed on laboratory-based specimens where the loading conditions and the specimen size can be controlled. For optimum results, an array of six sensors situated on at least two different faces in the region where damage is expected is preferred. For the series of tests described in this chapter the specimens dimensions and the position of each sensor was chosen to provide the best possible results. For the cases where MTA was performed on emissions recorded from a pulsed PZT and on emissions produced during the loading of a concrete beam in four-point bending, the technique did not produce results that could be validated from each test set-up.

From the series of tests discussed in this chapter, it is recommended that even though in theory MTA is a relevant post-test technique, it is only suitable for monitoring in-service structures when used in tandem with conventional parameter-based monitoring. From the specimen failed in four-point bending it was shown that not all failure mechanisms produce clear and defined initial P-waves. This limits the applicability of the technique for in-service monitoring because not all failure mechanisms are identified.

CHAPTER 6. THE DETECTION OF STEEL FATIGUE DAMAGE IN LABORATORY SPECIMENS USING AE TECHNIQUES

6.1. INTRODUCTION

The deterioration of reinforced concrete structures is of major concern. Much of the damage that occurs is a consequence of reinforcement (steel-rebar) corrosion and the consequent potential for the propagation of fatigue cracks. Therefore, the early detection of corrosion and of fatigue cracks using non-destructive techniques is important not only from an academic point of view but also in practical applications for assessing the maintenance and repair of structures.

AE techniques have been applied to both laboratory and in-service structures with steel reinforcement. Yuyama *et. al.* (2001) showed that AE can be used to study and compare the fatigue damage of in-service and laboratory tested reinforced concrete (RC) slabs. Henkel and Wood (1991) monitored concrete reinforced with bonded surface plates using AE methods. Similar research has been carried out on reinforced concrete beams and cylinders including: Yuyama *et. al.* (1999b), Yuyama *et. al.* (1995a) and Shiotani *et. al.* (1999).

When monitoring the reinforcement of a concrete structure for fatigue cracks, it is not always possible to gain access to the steel without removing the concrete, and then only small areas are accessible. Thus it would be ideal to be able to monitor the integrity of the reinforcement through the concrete itself.

6.2. AIMS AND OBJECTIVES

This chapter assesses the ability of AE to detect, locate and monitor steel rebar fatigue. AE techniques are used to monitor the fatigue of deformed steel rebar and deformed steel rebar encased in concrete. Both types of specimen were fatigued in flexure and in tension. The aim of this research was to monitor fatigue cracks produced in flexure and in tension using both steel mounted sensors and sensors mounted on the concrete. From this study it is hoped that similar techniques can be used to monitor the behaviour of in-service reinforced concrete structures.

The experimental objectives were to:

- Attach sensors to the steel rebar both with and without concrete, via machined flats or waveguides, to monitor and locate emissions during fatigue.
- Eliminate any spurious signals that would impede the detection and location of emissions produced during the propagation of fatigue cracks.
- Collect a database of signals from the plain rebar tests so that any located sources during similar tests with concrete encasing the rebar can be validated.
- Attach sensors to the concrete encasement (for sections 6.5 and 6.6), to detect and locate steel fatigue.
- Compare AE data recorded on the concrete sensors during propagation of the fatigue crack with the data recorded upon the steel sensors.
- Study the effects the concrete encasing has on AE signals arising from steel fatigue cracks.
- Gain an understanding of steel fatigue and the use of AE techniques to monitor and locate fatigue damage in reinforcing bar such that similar methods can be used to monitor the reinforcement of in-service structures.

6.3. DEFORMED REBAR LOADED DYNAMICALLY IN FLEXURE

6.3.1. Experimental Procedure

Steel fatigue in flexure was generated in a 1m length of 32mm diameter deformed steel rebar using a dynamic four-point loading arrangement. A notch was placed on the underside at the centre of the bar to initiate a crack. A DARTEC actuator (static range 0-550kN / dynamic range 0-500kN) was used. The load was applied at a frequency of 1Hz. Deflection control was used to maintain the load range adopted.

Four AE sensors of 150kHz resonant frequency were attached to the steel rebar via machined flats to detect and record AE produced during loading. AE waveforms detected at the sensors were recorded at a sampling rate of 1MHz. The frequency detection range was 10 - 200 kHz. The AE set-up used for each channel can be seen in table B.7 in Appendix B. Fig. 6.1 shows a schematic diagram of the load arrangement and the position of the sensors attached to the rebar. Fig. 6.2

shows the steel rebar under cyclic loading with the sensors attached to the flats via a silicon sealant couplant using insulation tape.

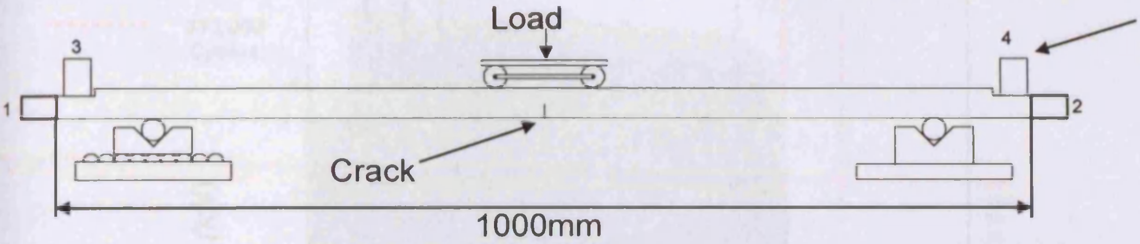

Figure 6.1. Sensor and specimen set-up for steel rebar dynamically failed in flexure.

Figure 6.2. Photograph of the loading arrangement and the sensor positioning.

6.3.2. Results and Discussion

Since the loading of the bar was restrained in deflection control, any drop in the load sequence suggests that some damage had occurred in the bar. Fig. 6.3 shows the load sequence for the 300,000 cycles of the test. Since there is a large amount of data, a number of acquisition files were used to monitor the fatigue test. Fig. 6.3 displays the loading of the bar with respect to time for the complete test (each file has been linked).

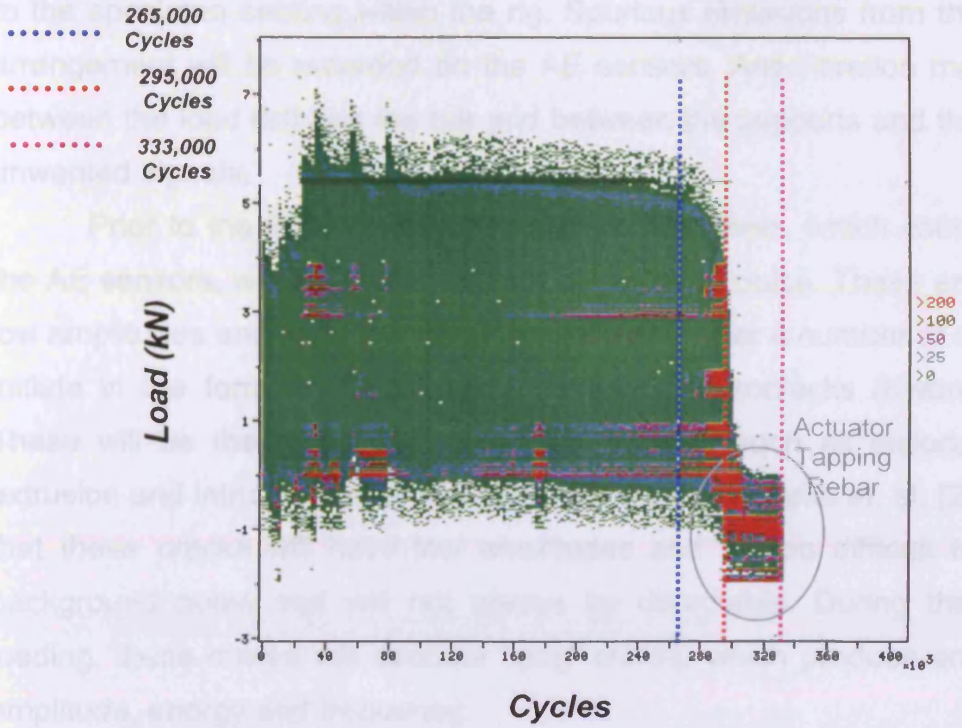

Figure 6.3. Complete load history during dynamic loading of steel rebar

After 333,000 cycles the specimen had failed and the bar was experiencing a small amount of load from the actuator (tapping). From Fig. 6.3 it can be seen that for the majority of the test, the specimen was loaded between 0.5-5kN. As already stated any drop in the load sequence suggests that some damage has occurred in the bar. The first change in load occurs after 265,000 cycles. The grey circle in Fig 6.3 indicates the region where tapping occurred and can be ignored in the analysis of the results.

AE is often classified into two categories, *primary* and *secondary*. The term "primary" is used to describe emission from sources internal to a material and is commonly associated with the micro-structural mechanisms that accompany fatigue crack development. The term "noise" is often used to describe the presence of secondary AE that impedes detection or isolation of primary sources. Carter (2000) defines noise as any emission of no interest or relevance to the study. The difficulty of using AE to locate and detect damage events from a source within a body, is in interpreting and categorising the large quantity of data and in rejecting the spurious information. Of fundamental importance to the advancement of the current state of AE technology is the isolation and identification of the signal from a fatigue crack.

Throughout the loading of the steel rebar, secondary AE can be expected and must be eliminated. During the early stages of loading secondary AE is expected due to the specimen settling within the rig. Spurious emissions from the rig and loading arrangement will be recorded on the AE sensors. Anti-vibration matting was placed between the load cell and the bar and between the supports and the rebar to reduce unwanted signals.

Prior to the initiation of fatigue, the only signals, which could be detected on the AE sensors, will be produced from background noise. These emissions will have low amplitudes and have low frequency content. After a number of cycles, fatigue will initiate in the form of short fatigue cracks or microcracks (Kwon and Lee 2000). These will be the result of microscopic features such as dislocations, slip band, extrusion and intrusion, grain boundary and so on. Yuyama et. al. (2000) have shown that these cracks will have low amplitudes and will be difficult to identify due to background noise and will not always be detectable. During the later stages of loading, these cracks will become "long" cracks, which produce emissions of larger amplitude, energy and frequency.

During the dynamic loading of the rebar, emissions are expected from background noise, fatigue cracks and tearing cracks. Prior to the initiation of damage within the specimen the only signals that could be detected on the AE sensors, will be produced from background noise. Once fatigue has begun, short cracks will propagate through the specimen until large cracks form. Fatigue will continue through the specimen until the stress becomes too large for the remaining section. At this stage the two pieces of the specimen will tear at the notch. From this assumption it could be suggested that any change in AE parameters such as amplitude and energy could be used to determine the approximate time that each of these failure mechanisms occur.

Fig 6.4 shows the amplitude of the signals recorded on all the sensors for the whole of the test.

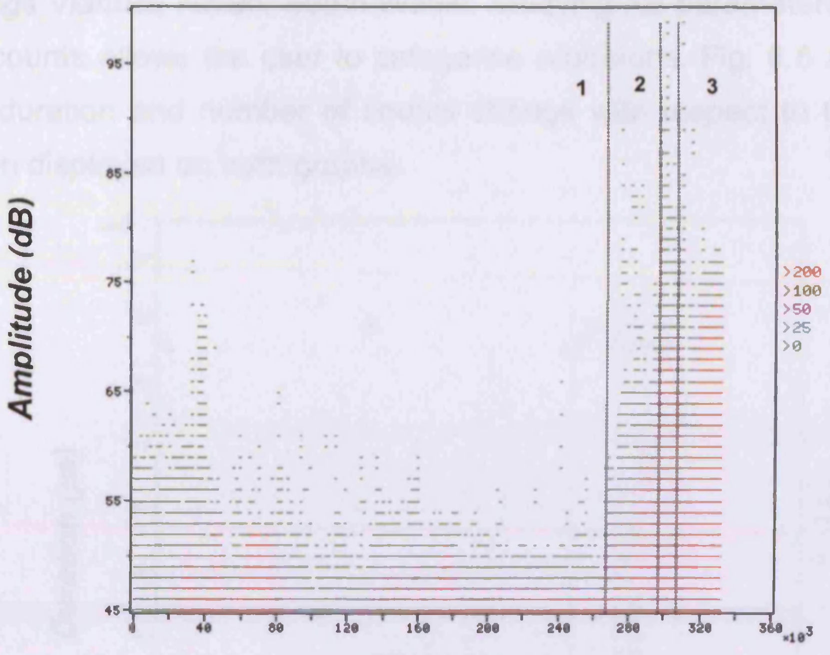

Figure 6.4. Amplitude produced on all sensors with respect to time.

Even though Fig. 6.4 displays the results recorded on all the sensors, similar results were seen on each of the sensors. Examination of Fig. 6.4 shows there is a significant increase in amplitudes after 265,000 cycles (displayed by the first dashed line 1 in Fig. 6.4). At 295,000 cycles (the second dashed line 2 in Fig. 6.4) there is a greater increase in the amplitudes of the emissions. Between 295,000 cycles and 304,000 cycles (the third dashed line 3) there is little change in amplitude. After 304,000 cycles there is a decrease in amplitudes. Assuming that the initial increase in amplitude is associated with fatigue it could be suggested that fatigue occurs from 265,000 cycles until 295,000 cycles and between 295,000 cycles until 304,000 cycles, emissions are generated from the tearing of the rebar. After 304,000 cycles, spurious emissions are recorded from signals produced by the tapping of the actuator. This result is in agreement with the load history of the specimen where an initial drop in load occurs at 295,000 cycles leading to a complete removal of load after 304,000 cycles.

To aid distinguishing primary signals from secondary signals, the duration and the number of counts of each emission can be studied. Pullin (2001) correlated AE counts with amplitude to detect fatigue cracks within steel box sections tested in the laboratory and Carter (2000) correlated counts with amplitude with the aim of detecting and locating fatigue cracks from signals emitted during the monitoring of the Saltings Viaduct, Neath, South Wales. Studying AE parameters such as duration and AE counts allows the user to categorise emissions. Fig. 6.5 and Fig. 6.6 show how the duration and number of counts change with respect to time. Four regions have been displayed on both graphs.

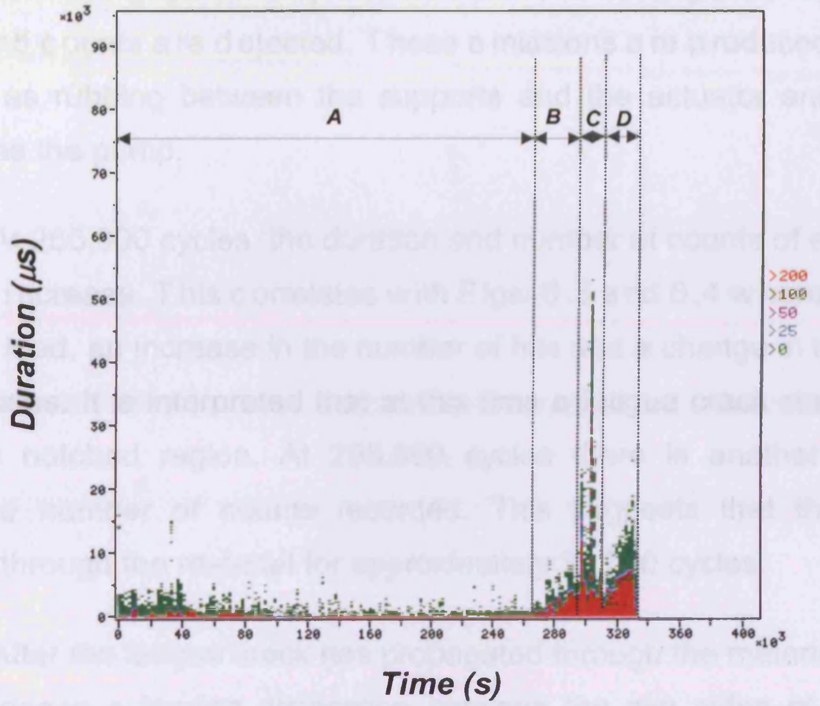

Figure 6.5. Duration of recorded hits detected on all sensors with respect to time.

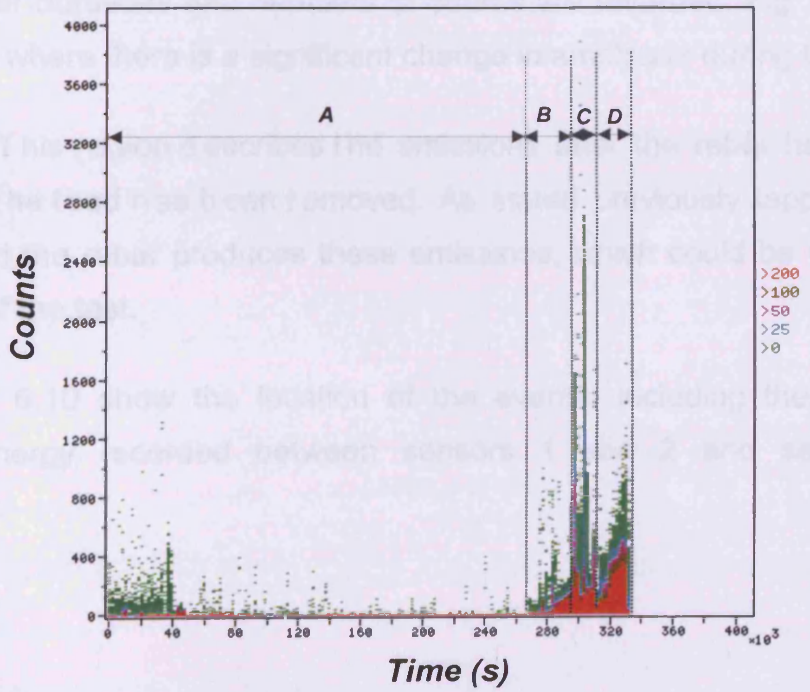

Figure 6.6. Number of counts recorded on all sensors with respect to time.

These regions are defined as follows.

Region A: This region displays the data recorded prior to failure. Early stages show larger durations and counts. This could be due to the specimen settling into the rig and noise from the grips as they bed in. After this initial period signals with small durations and counts are detected. These emissions are produced by mechanical noise such as rubbing between the supports and the actuator and other actuator noise such as the pump.

Region B: At 265,000 cycles, the duration and number of counts of each detected hit significantly increase. This correlates with Figs. 6.3 and 6.4 where there is also a decrease in load, an increase in the number of hits and a change in the magnitude of their amplitudes. It is interpreted that at this time a fatigue crack starts to propagate through the notched region. At 295,000 cycles there is another change in the duration and number of counts recorded. This suggests that the fatigue crack propagated through the material for approximately 30,000 cycles.

Region C: After the fatigue crack has propagated through the material, the specimen would experience a tearing dislocation between the two sides of the notch. It is believed that this is recorded between 295,000 cycles and 304,000 cycles. In this period, larger durations and numbers of counts are recorded. Fig. 6.4 supports this observation where there is a significant change in amplitude during this period.

Region D: This region describes the emissions after the rebar has failed and the majority of the load has been removed. As stated previously tapping between the actuator and the rebar produces these emissions, which could be visually observed at the end of the test.

Figs. 6.7 – 6.10 show the location of the events, including their amplitude and absolute energy recorded between sensors 1 and 2 and sensors 3 and 4 respectively.

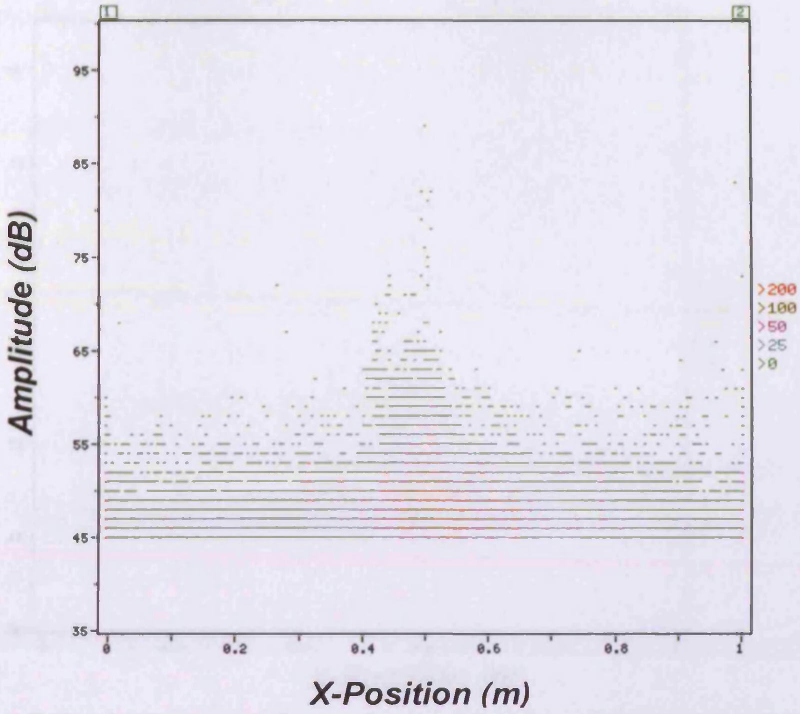

Figure 6.7. Amplitude of events produced by fatigue between sensors 1 and 2.

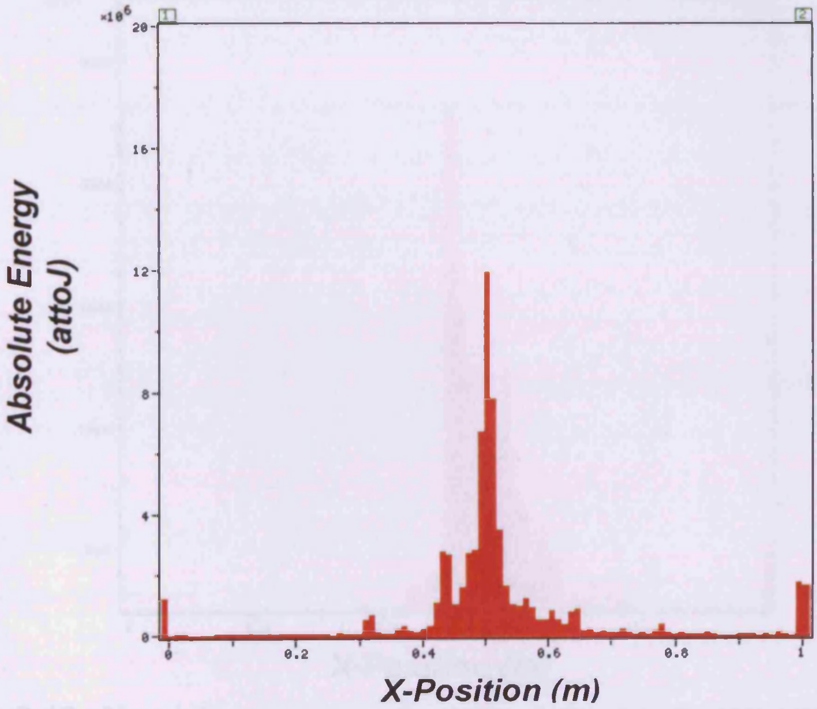

Figure 6.8. Absolute energy of events produced by fatigue between sensors 1 and 2.

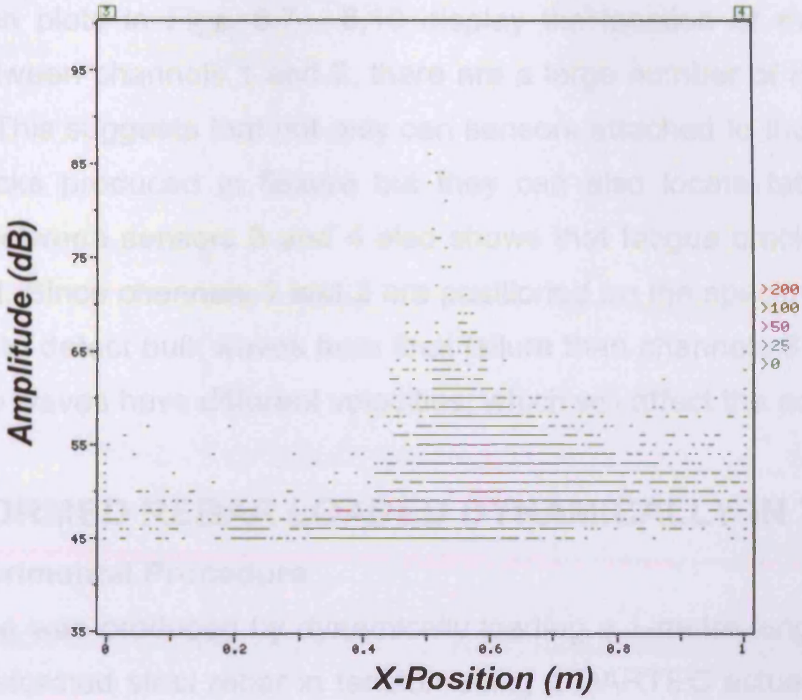

Figure 6.9. Amplitude of events produced by fatigue between sensors 3 and 4.

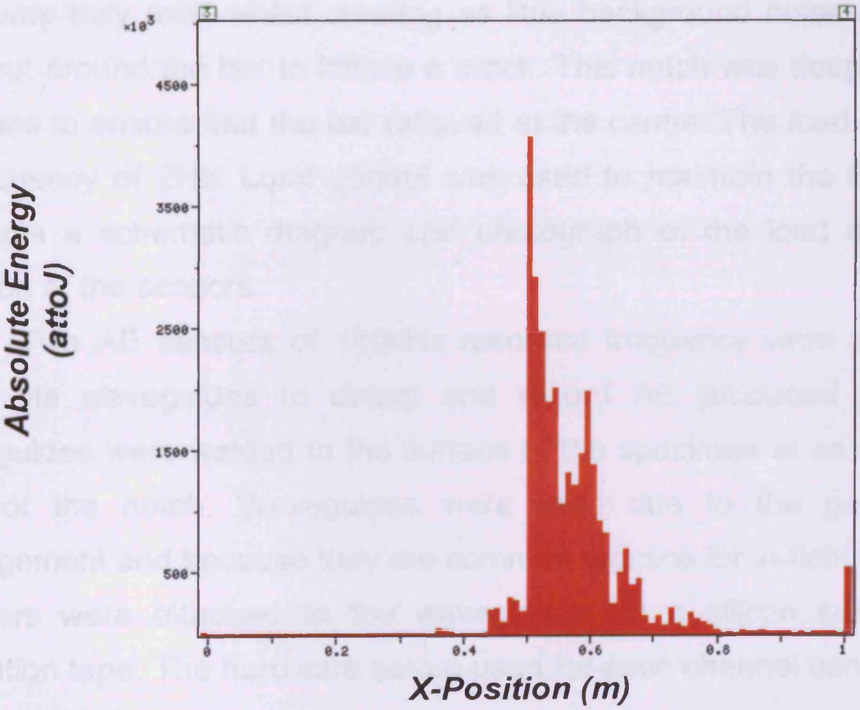

Figure 6.10. Absolute energy produced by fatigue between sensors 3 and 4.

The location plots in Figs. 6.7 - 6.10 display the location of events produced by fatigue. Between channels 1 and 2, there are a large number of hits at the centre of the beam. This suggests that not only can sensors attached to the steel rebar detect fatigue cracks produced in flexure but they can also locate fatigue. The location produced between sensors 3 and 4 also shows that fatigue cracks can be detected and located. Since channels 1 and 2 are positioned on the specimens' ends they are more likely to detect bulk waves from final failure than channels 3 and 4. Bulk waves and surface waves have different velocities, which will affect the accuracy of location.

6.4. DEFORMED REBAR LOADED DYNAMICALLY IN TENSION

6.4.1. Experimental Procedure

Steel fatigue was produced by dynamically loading a 1-metre length of 24-millimetre diameter deformed steel rebar in tension using a DARTEC actuator (static range 0-550kN / dynamic range 0-500kN). The rebar was threaded at both ends to enable the bar to be connected to the actuator and the base in such a way as to ensure that the load was truly axial whilst creating as little background noise as possible. A notch was cut around the bar to initiate a crack. This notch was deeper than the threaded sections to ensure that the bar fatigued at the centre. The load range was applied at a frequency of 2Hz. Load control was used to maintain the load range. Fig. 6.11 presents a schematic diagram and photograph of the load arrangement and the position of the sensors.

Two AE sensors of 150kHz resonant frequency were attached to the steel rebar via waveguides to detect and record AE produced during loading. The waveguides were welded to the surface of the specimen at an equal distance either side of the notch. Waveguides were used due to the geometry and loading arrangement and because they are common practice for in-field structural monitoring. Sensors were attached to the waveguides via a silicon sealant couplant using insulation tape. The hardware set-up used for each channel can be seen in table B.8 in Appendix B.

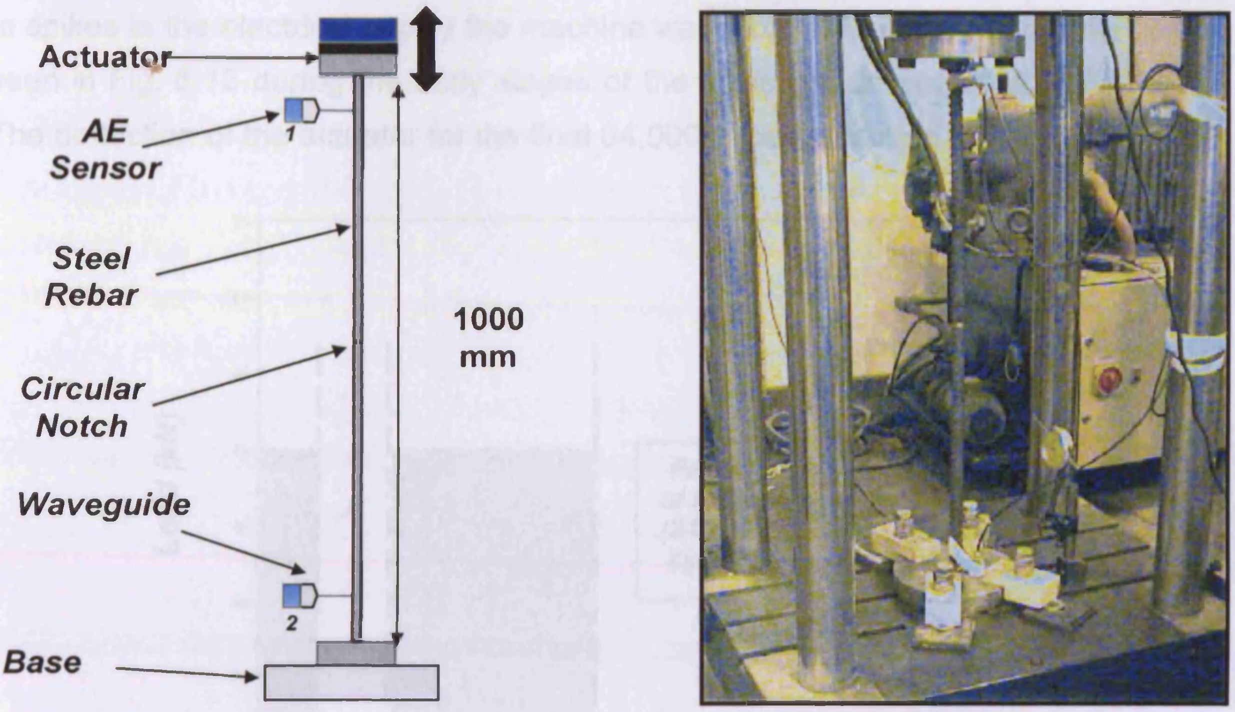

Figure 6.11. Sensor and specimen set-up for steel rebar dynamically failed in tension.

6.4.2. Results and Discussion

During failure, two different types of emission were expected, emission from fatigue and tearing. Fig. 6.12 is a photograph of the notched region after failure, which shows the original notch, the fatigue region and the tearing region.

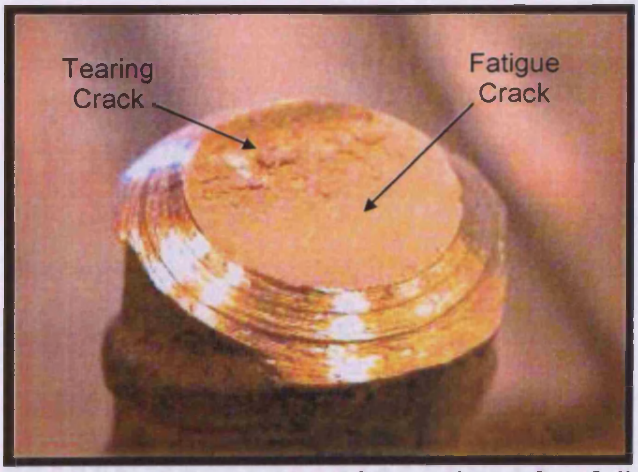

Figure 6.12. Photograph of the centre of the rebar after failure of specimen

Fig. 6.13 shows the load history of the complete test. Since there was a large amount of data, a number of acquisition files were used to store the data as in the flexure test. Since load control was used (lower and upper limits were set to 4 and 40kN respectively), a trip was set so that if the deflection of the actuator was greater than 46mm then the DARTEC testing machine would switch off, removing any load. Due to spikes in the electrical supply the machine was tripped during loading. This can be seen in Fig. 6.13 during the early stages of the investigation (region **A** in Fig. 6.13). The deflection of the actuator for the final 64,000 cycles is plotted in Fig. 6.14

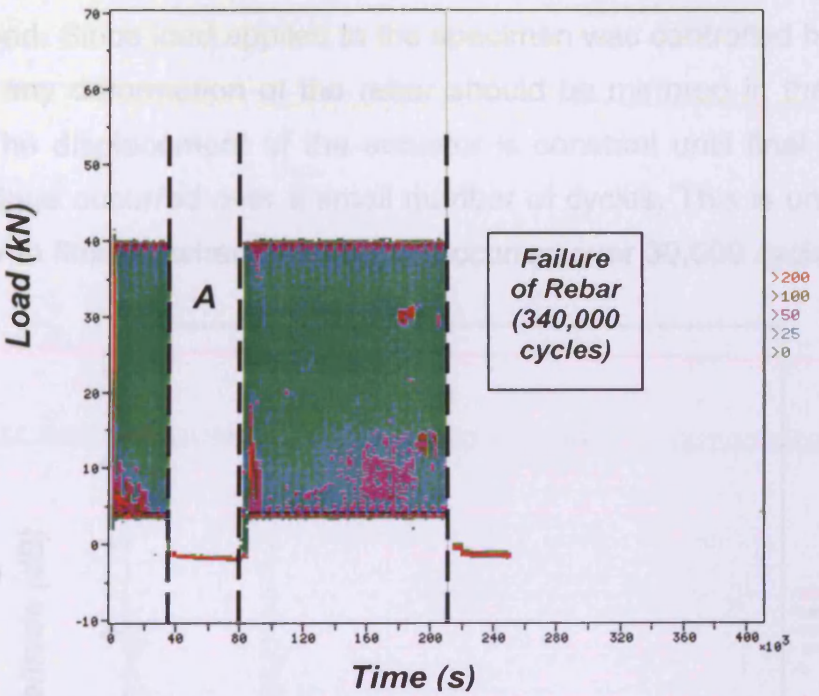

Figure 6.13. Complete load history during dynamic loading of steel rebar

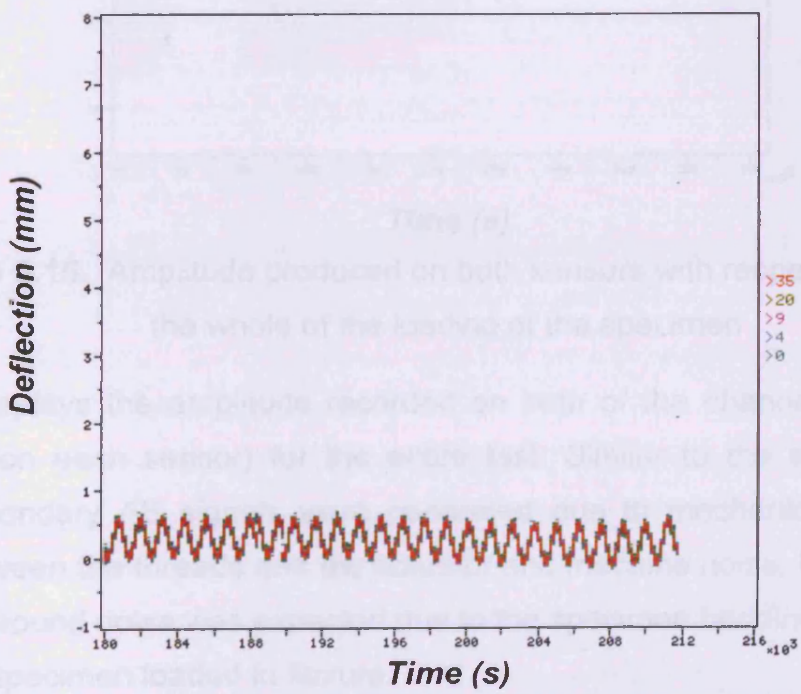

Figure 6.14. Deflection of actuator with respect to time during dynamic loading of the steel rebar (276,000 cycles – 340,000 cycles)

At a frequency of 2Hz, the specimen failed after approximately 340,000 cycles (region A is not included in the total number of cycles). After 340,000 cycles the specimen failed and the load dropped as displayed in Fig. 6.13. Fig. 6.14 shows the magnitude of the displacement of the actuator between 276,000 cycles and 340,000 cycles of load. Since load applied to the specimen was controlled by upper and lower load limits any deformation of the rebar should be mirrored in the deflection of the actuator. The displacement of the actuator is constant until final failure suggesting that the fatigue occurred over a small number of cycles. This is unlike the behaviour of the rebar in flexure, where the fatigue occurred over 30,000 cycles.

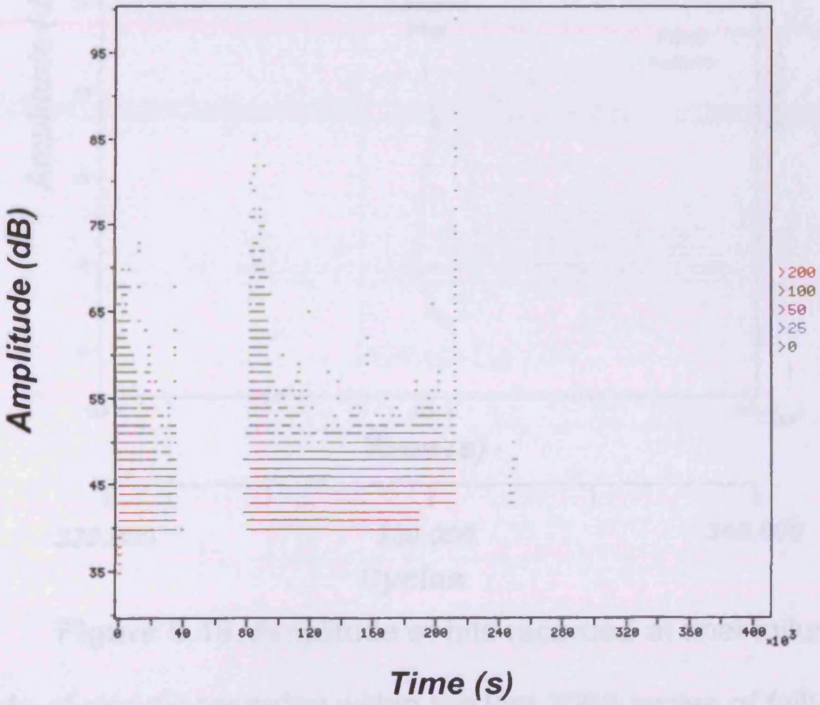

Figure 6.15. Amplitude produced on both sensors with respect to time for the whole of the loading of the specimen

Fig. 6.15 displays the amplitude recorded on both of the channels (similar results were seen on each sensor) for the entire test. Similar to the specimen failed in flexure, secondary AE signals were generated due to mechanical noise such as rubbing between the threads and the actuator and machine noise. In the early stages some background noise was expected due to the specimen bedding down into the rig as with the specimen loaded in flexure.

From Fig. 6.15 it can be seen that no significant change in amplitude occurred until final failure, which is consistent with Fig. 6.12 and Fig 6.13, which suggest that the fatigue crack propagated quickly at the end. Looking closely at the region just before final failure there is a small but significant change in the AE signals detected. This can be seen in Fig. 6.16.

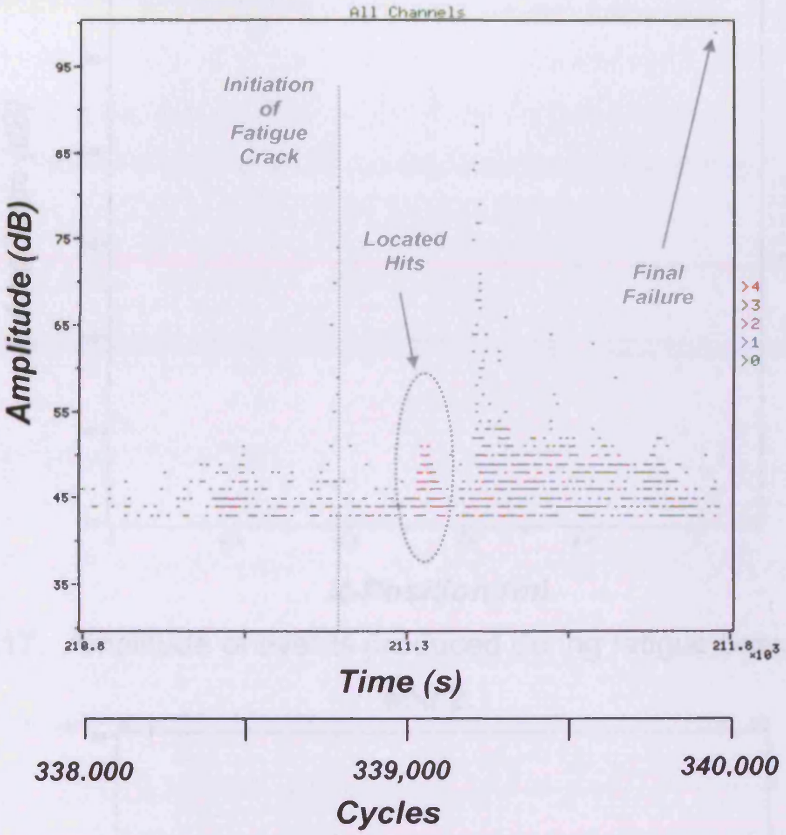

Figure 6.16. Amplitude of hits recorded at final failure

The amplitude of signals recorded within the last 2000 cycles of failure is displayed in Fig. 6.16. Since it is known that the period of failure for the specimen is very small it is difficult to distinguish the emissions recorded during fatigue and tearing. For a hit to be located, the signal has to be detected on both of the channels. A small number of events were located during the complete test and these are identified in the region circled in Fig. 6.16. It is believed that these events are produced by fatigue cracks since they are located at the centre of the specimen. This can be seen in Figs. 6.17 and 6.18. It is also believed that the initial increase in amplitude, as displayed in Fig. 6.16, represents the start of a fatigue crack. These hits are not located since they are not recorded on both channels. Final failure between the two sides of the notch can be seen in the 100dB reading recorded on both sensors.

Figs. 6.17 and 6.18 show the location of the events identified above together with the magnitude of their amplitude and the absolute energy recorded between sensors 1 and 2.

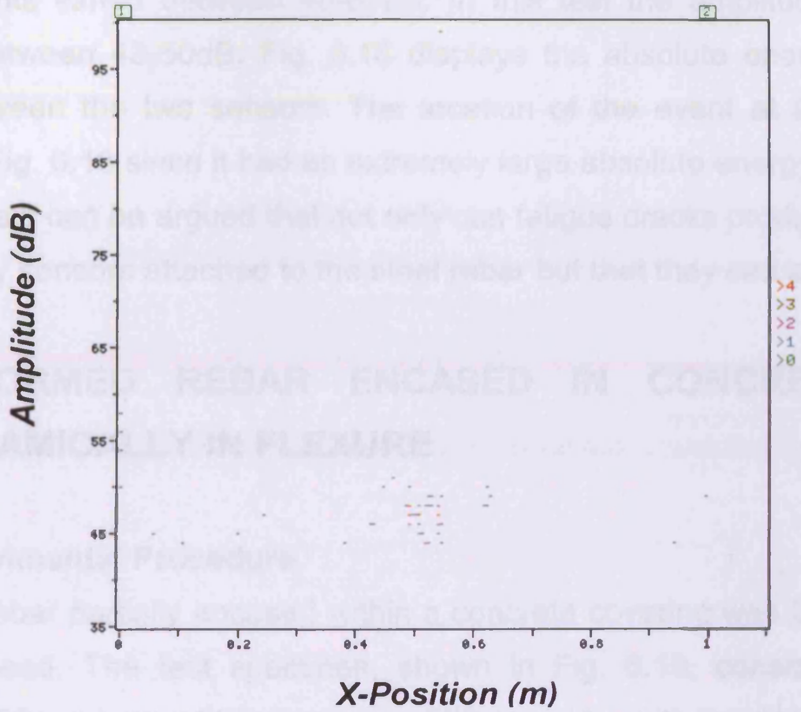

Figure 6.17. Amplitude of events produced during fatigue between sensors 1 and 2.

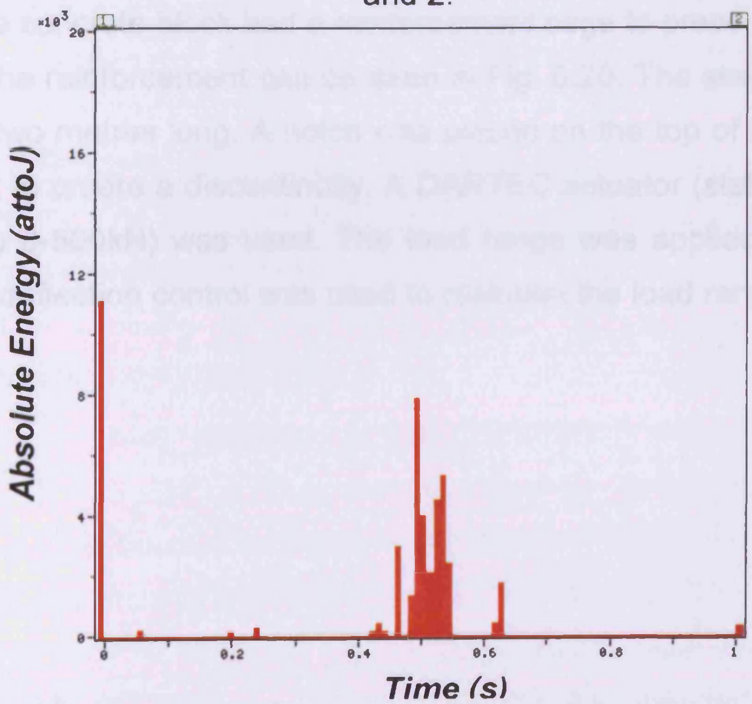

Figure 6.18. Absolute energy of events produced during fatigue between sensors 1 and 2.

These locations are generated by emissions produced within the circled region, and are therefore believed to be signals from a fatigue crack. The majority of these hits are at the centre of the beam as expected. For the flexural tests, the amplitude of the located events varied between 40-87dB. In this test the amplitude of the located events is between 43-50dB. Fig. 6.18 displays the absolute energy of the events located between the two sensors. The location of the event at final failure is not included in Fig. 6.18 since it had an extremely large absolute energy. From these two location plots it can be argued that not only can fatigue cracks produced in tension be monitored by sensors attached to the steel rebar but that they can also be located.

6.5. DEFORMED REBAR ENCASED IN CONCRETE LOADED DYNAMICALLY IN FLEXURE

6.5.1. Experimental Procedure

Plain steel rebar partially encased within a concrete covering was failed in flexure by a dynamic load. The test specimen, shown in Fig. 6.19, consists of a concrete specimen, 850mm long x 500mm deep x 500mm wide, with the deformed steel rebar cast through the centre of it and protruding 200mm and 950mm from the block at either end. The concrete block had a reinforcement cage to prevent surface cracking. A diagram of the reinforcement can be seen in Fig. 6.20. The steel rebar was 32mm diameter and two metres long. A notch was placed on the top of the bar outside the concrete block to create a discontinuity. A DARTEC actuator (static range 0-550kN / dynamic range 0-500kN) was used. The load range was applied at a frequency of 0.25Hz where deflection control was used to maintain the load range adopted.

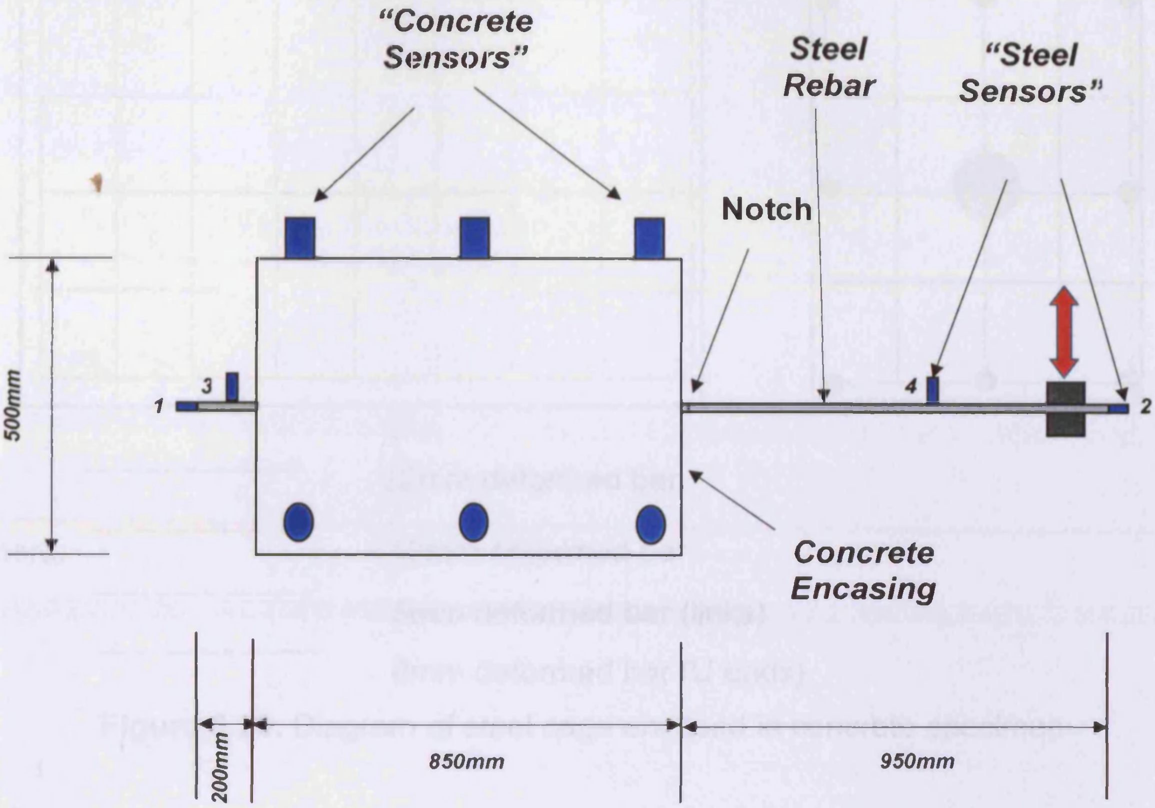

Figure 6.19. Sensor and specimen set-up for steel rebar encased in concrete dynamically failed in flexure

Four AE sensors of 150kHz resonant frequency were attached to the steel rebar via machined flats to detect and record the AE produced during loading. Twelve sensors were attached to the concrete block using clamps as described in chapter 4, five of a 30kHz resonant frequency, six of a 60kHz resonant frequency and one of 7kHz resonant frequency. The hardware set-up of each sensor can be seen in table B.9 in appendix B. The calibration certificates of each of these sensor types can be seen in Appendix A. The concrete sensors were coupled to the specimen using silicon sealant and attached using steel clamps. Fig. 6.21 shows the position of each sensor attached to the concrete covering. The actual loading arrangement and sensor positioning on the specimen can be seen in Fig. 6.22. Between the notch and the concrete block a steel block was placed to act as a pivot and reduce any background noise caused by crushing at the interface between the concrete and the steel rebar. To reduce the amount of spurious signals recorded on each sensor; anti-vibration matting was placed between the load cell and the bar and between the concrete block and the floor.

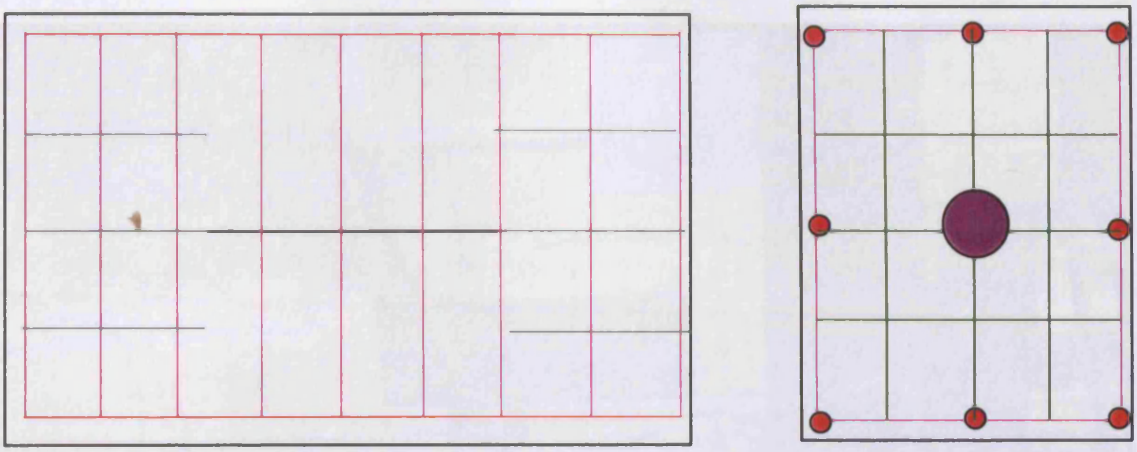

Where:

32mm deformed bar

12mm deformed bar

8mm deformed bar (links)

8mm deformed bar (U ends)

Figure 6.20. Diagram of steel cage encased in concrete specimen

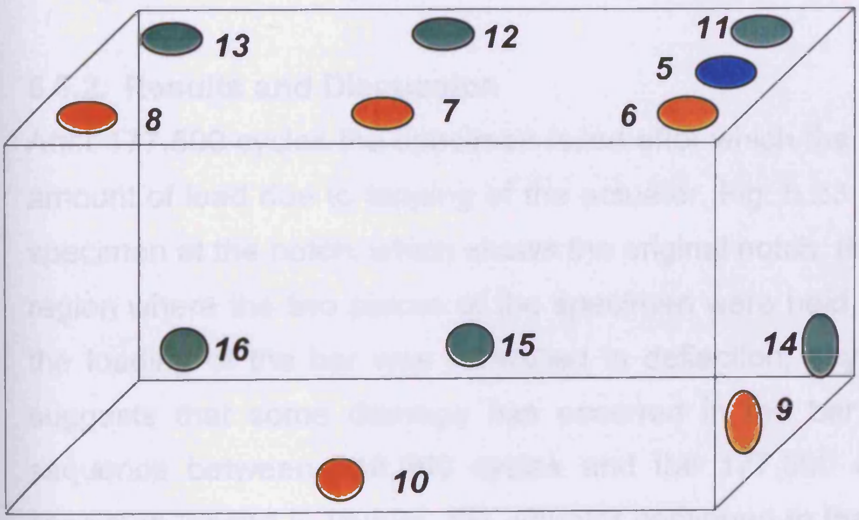

Channel	Sensor Type
5	7kHz
6-10	30kHz
11-16	60kHz

Figure 6.21. Positioning of sensors attached to the concrete specimen

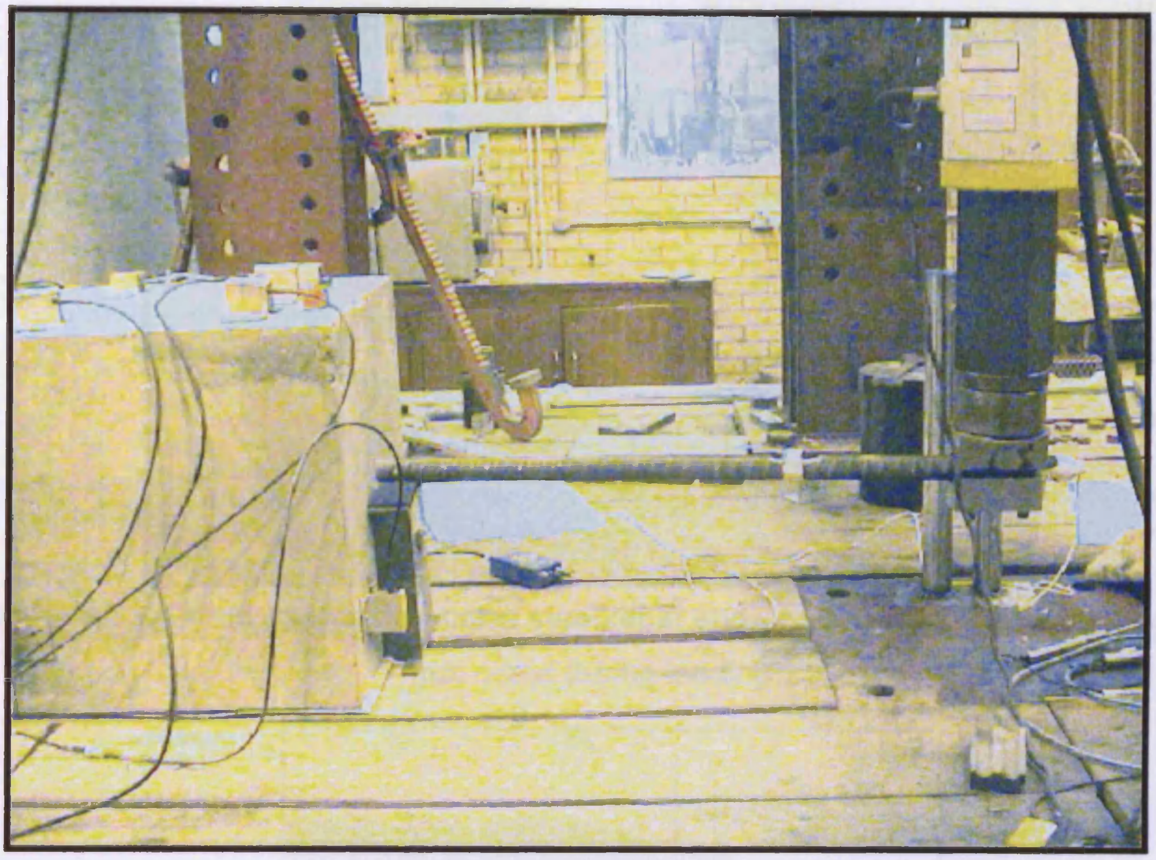

Figure 6.22. Photograph of the loading arrangement and the sensor positioning

6.5.2. Results and Discussion

After 177,500 cycles the specimen failed after which the bar experienced just a small amount of load due to tapping of the actuator. Fig. 6.23 is a photograph of the failed specimen at the notch, which shows the original notch, the fatigue region and the thin region where the two pieces of the specimen were held together after failure. Since the loading of the bar was controlled in deflection, any drop in the load sequence suggests that some damage has occurred in the bar. Fig. 6.24 shows the load sequence between 118,500 cycles and the 177,500 cycles. Similar to the plain specimen loaded in flexure, the actuator continued to load the specimen after failure (tapping). This region can be seen in Fig. 6.24. Due to software problems the whole test could not be merged and only the last 59,000 cycles of the test are displayed.

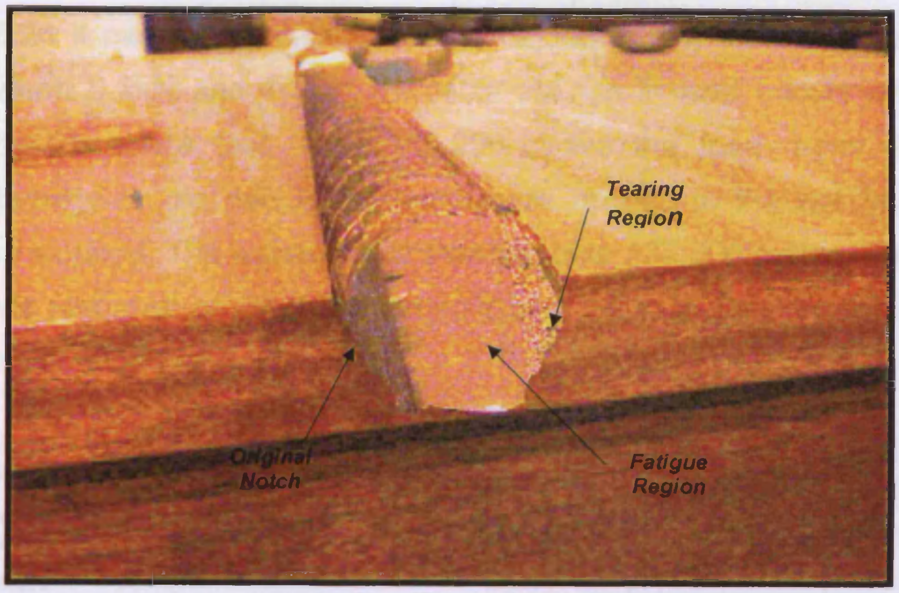

Figure 6.23. Photograph of the failed steel rebar showing the different failure modes that occur during loading

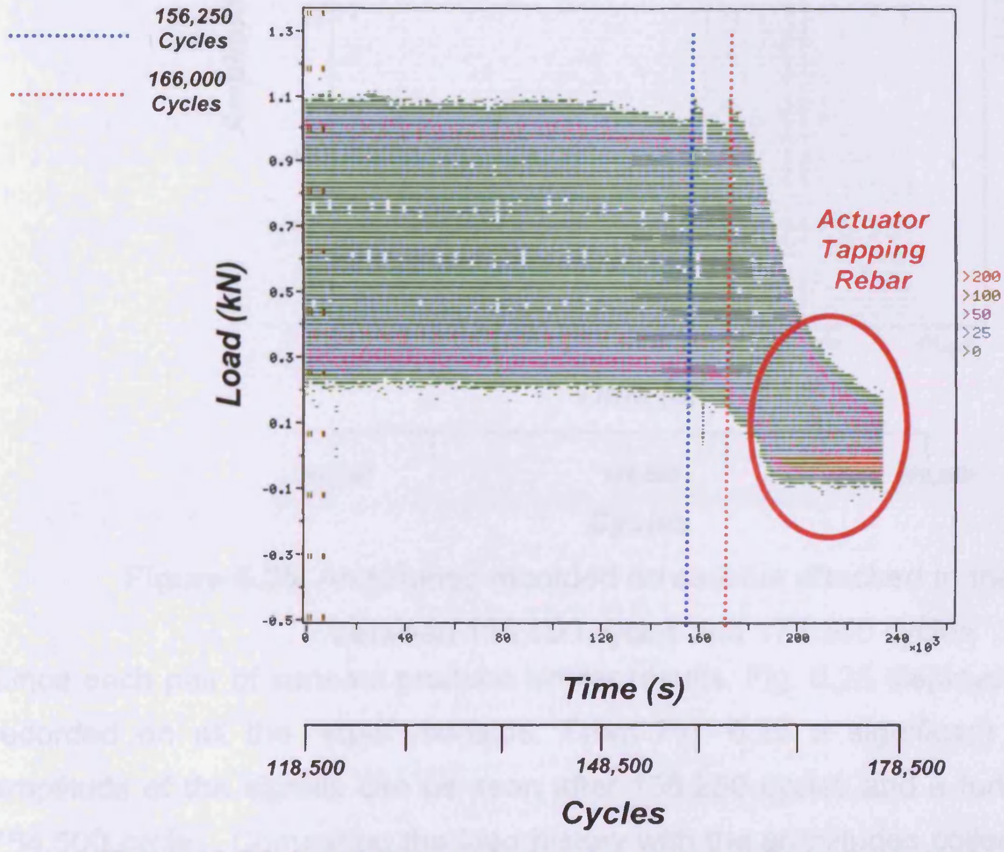

Figure 6.24. Load history during dynamic loading of steel rebar between 118,500 cycles and the 177,500 cycles

From Fig. 6.24 it can be seen that for the majority of the test, the specimen was loaded between 0.2kN and 1.1kN. An initial change in load occurs after 156,250 cycles of the complete test. After 166,000 cycles the load drops considerably indicating damage to the bar. A small load was applied to the specimen until the actuator was stopped. The actuator was stopped after 177,500 cycles. The amplitude of the signals recorded on the steel sensors between 118,500 cycles and 177,500 cycles can be seen in Fig. 6.25.

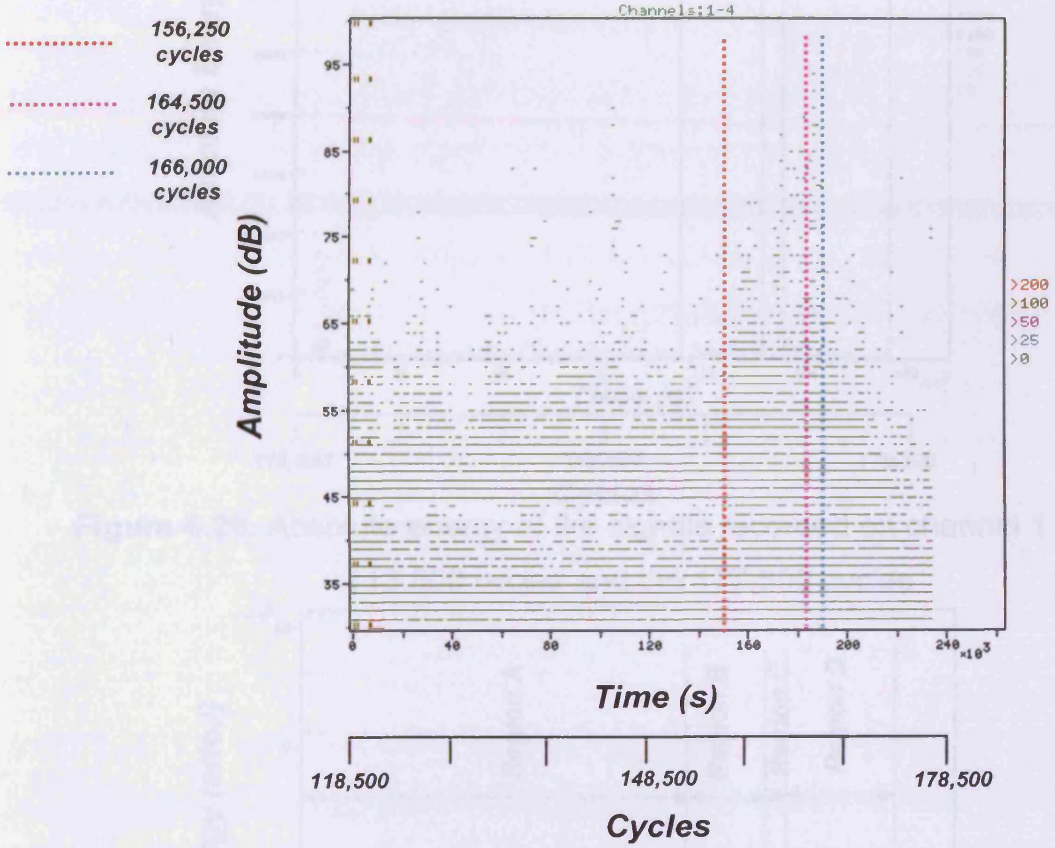

Figure 6.25. Amplitudes recorded on sensors attached to the steel rebar between 118,500 cycles and 177,500 cycles

Since each pair of sensors produce similar results, Fig. 6.25 displays the amplitudes recorded on all the "steel" sensors. From Fig. 6.25 a significant change in the amplitude of the signals can be seen after 156,250 cycles and a further increase at 164,500 cycles. Comparing the load history with the amplitudes collected throughout the test suggests that deformation of the bar begins at 156,250 cycles since the load decreases and the amplitude increases. The rebar continues to fail until 166,000 cycles where the load drops to zero. To distinguish the fatigue crack from the tearing crack in this region, a further examination of the signals is needed.

Figs. 6.26 and 6.27 display the absolute energy of emissions recorded after 118,500 cycles of the test on channels 1 and 2 respectively. Four separate regions are displayed.

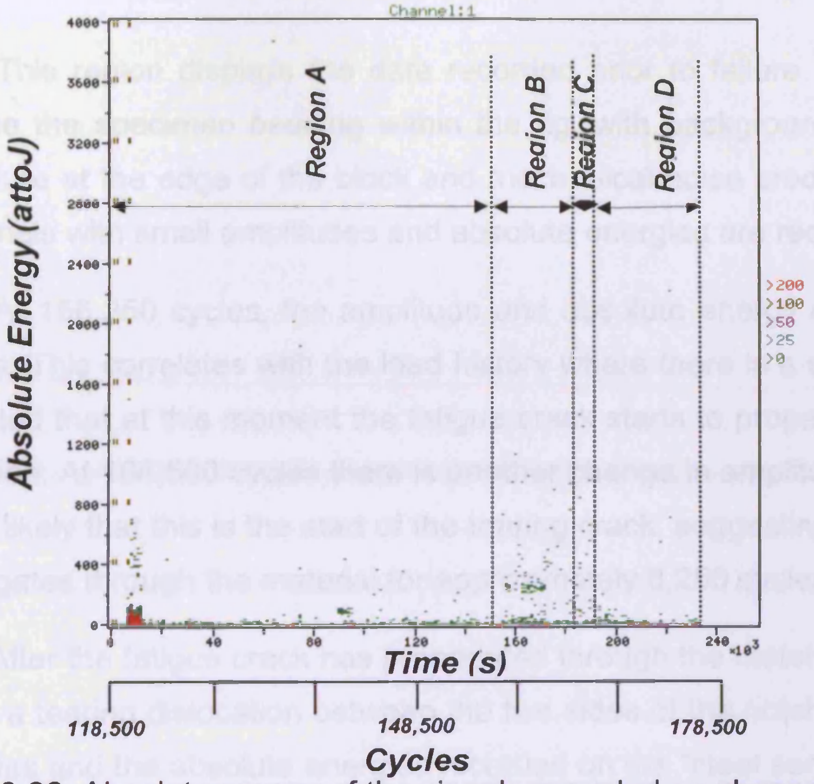

Figure 6.26. Absolute energy of the signals recorded on channel 1 between 118,500 cycles and the 177,500 cycles

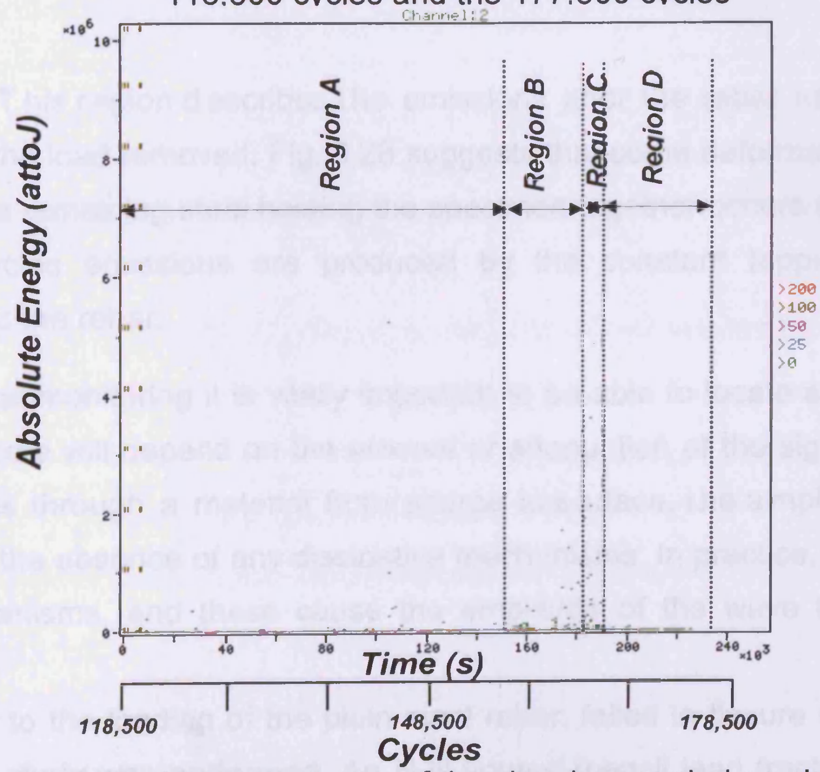

Figure 6.27. Absolute energy of the signals recorded on channel 2 between 118,500 cycles and the 177,500 cycles

Assuming that initially emissions are expected from background noise, then from fatigue cracks and finally from tearing cracks, the regions have been defined as follows.

Region A: This region displays the data recorded prior to failure. Early emissions could be due the specimen bedding within the rig, with background noise such as concrete failure at the edge of the block and mechanical noise produced throughout the test. Signals with small amplitudes and absolute energies are recorded.

Region B: At 156,250 cycles, the amplitude and absolute energy of each detected hit increases. This correlates with the load history where there is a decrease in load. It is interpreted that at this moment the fatigue crack starts to propagate through the notched region. At 164,500 cycles there is another change in amplitude and absolute energy. It is likely that this is the start of the tearing crack, suggesting that the fatigue crack propagates through the material for approximately 8,250 cycles.

Region C: After the fatigue crack has propagated through the material, it is expected that there is a tearing dislocation between the two sides of the notch. Examination of the amplitudes and the absolute energies recorded on the "steel sensors" suggests it is likely that the tearing dislocation occurs between the 164,500 cycles and 165,000 cycles.

Region D: This region describes the emissions after the rebar has failed and the majority of the load removed. Fig. 6.28 suggests that some deformation such as final failure of the remaining steel holding the specimen together occurs after failure. After 165,000 cycles emissions are produced by the constant tapping between the actuator and the rebar.

For structural monitoring it is vitally important to be able to locate such defects. The ability to locate will depend on the amount of attenuation of the signals. As a stress wave travels through a material from source to surface, the amplitude will remain constant in the absence of any dissipative mechanisms. In practice, there are always such mechanisms, and these cause the amplitude of the wave to decrease with distance.

Prior to the loading of the plain steel rebar, failed in flexure (section 6.3.), an attenuation study was performed. An H-N source (pencil lead fracture) was applied on the rebar at specific locations to see how an artificial source travelled through the beam. It was found that an H-N source at the notched region resulted in amplitudes of 95dB being recorded on all sensors and thus a loss of 10dB/metre across the specimen assuming that the H-N source would be detected as 100dB at the notch. Performing the H-N source at the notch for this investigation resulted in a significant loss of amplitude across the concrete section. Table 6.1 displays the amplitudes recorded on the "steel" sensors for this specimen. It is assumed that at the notch the amplitude of the H-N source would be detected as 100dB. From this study it can be seen that from the notch to channel 2 there is a 7dB loss which is consistent with the previous study but there is a loss of 40dB from the notch to channel 1 i.e. 40dB per metre (for near field attenuation). Similarly it must also be mentioned that high frequencies will attenuate more than low frequencies. This suggests that any signal produced during fatigue will heavily attenuate through the concrete block.

Due to the test set-up the lowest threshold possible on the steel sensors was 32 dB. Since the concrete block may attenuate signals by 40dB, any signals produced at the notch will need initial amplitude greater than 72dB-assuming signals produced by damage will attenuate in the same way as an H-N source. Thus not all signals from the fatigue crack will be located. If the lowest possible threshold (subject to background noises) is large then it may not always be possible to detect defects within a structure.

Table 6.1. Amplitudes recorded on steel sensors from a pencil lead fracture at the notch

Channel	First Fracture (dB)	Second Fracture (dB)	Third Fracture (dB)	Average Amplitude (dB)
1	55	54	54	54.6
2	93	92	92	92.6
3	53	50	51	51.3
4	94	91	95	93.3

To monitor the integrity of the reinforcement of a concrete structure it is vital that any defects can be located on both "steel" and "concrete" mounted sensors. The ability of AE methods to locate a source will heavily depend on the amount of attenuation that occurs within the material and the lowest possible threshold. If attenuation is high then sensors spacing will need to be reduced. The following location plots show the position of events between sensors 1 and 2 and between sensors 3 and 4 during the fatigue test.

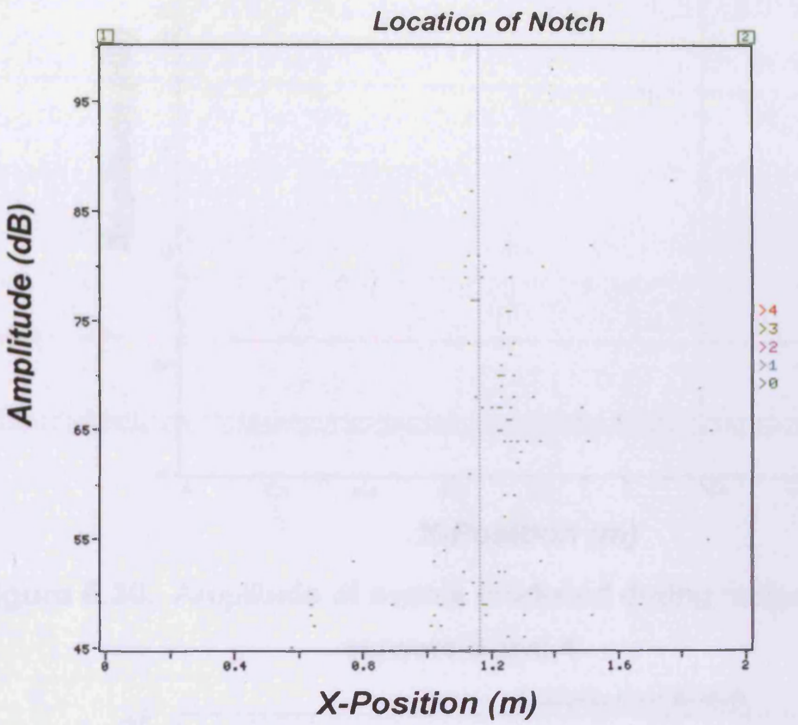

Figure 6.28. Amplitude of events located during the test between sensors 1 and 2.

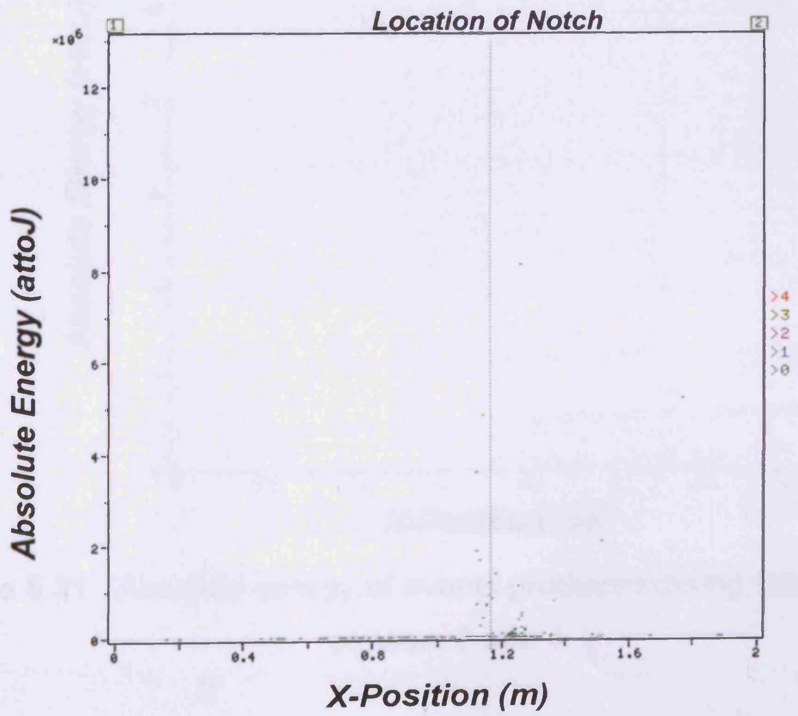

Figure 6.29. Absolute energy of events located during the test between sensors 1 and 2.

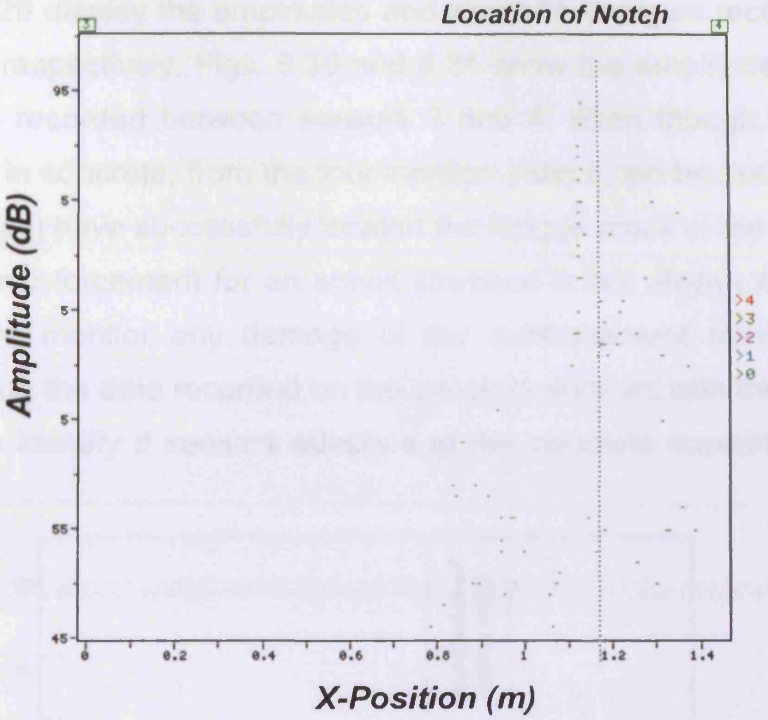

Figure 6.30. Amplitude of events produced during fatigue between sensors 3 and 4.

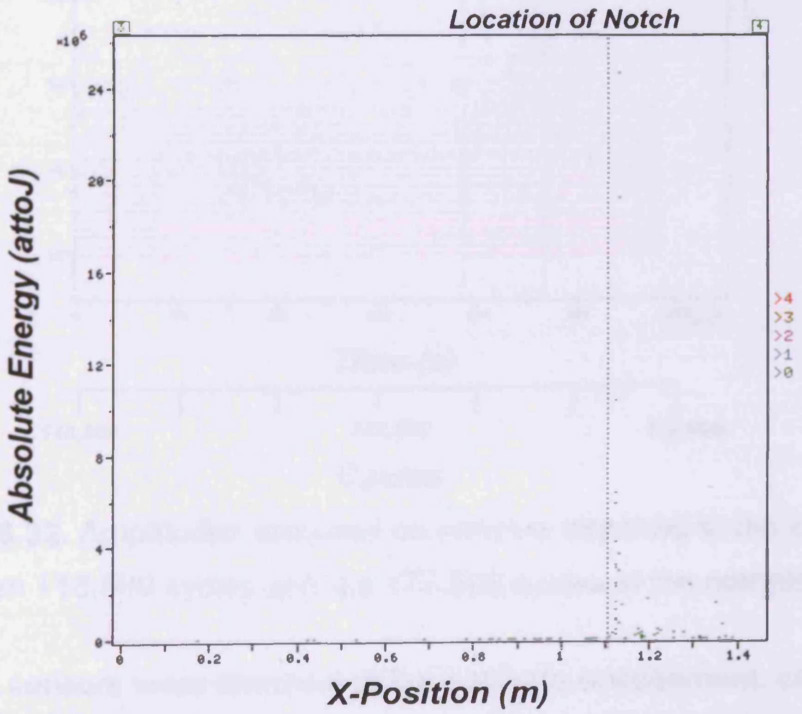

Figure 6.31. Absolute energy of events produced during fatigue between sensors 3 and 4.

Figs. 6.28 and 6.29 display the amplitudes and absolute energies recorded between sensors 1 and 2 respectively. Figs. 6.30 and 6.31 show the amplitude and absolute energy of events recorded between sensors 3 and 4. Even though the rebar was partially encased in concrete, from the four location plots it can be seen that sensors attached to the steel have successfully located the fatigue crack at the notch.

Since the reinforcement for an actual structure is not always accessible, it is also necessary to monitor any damage of the reinforcement from the concrete surface. Correlating the data recorded on the concrete sensors with the steel sensors it is of interest to identify if sensors attached to the concrete covering could detect steel fatigue.

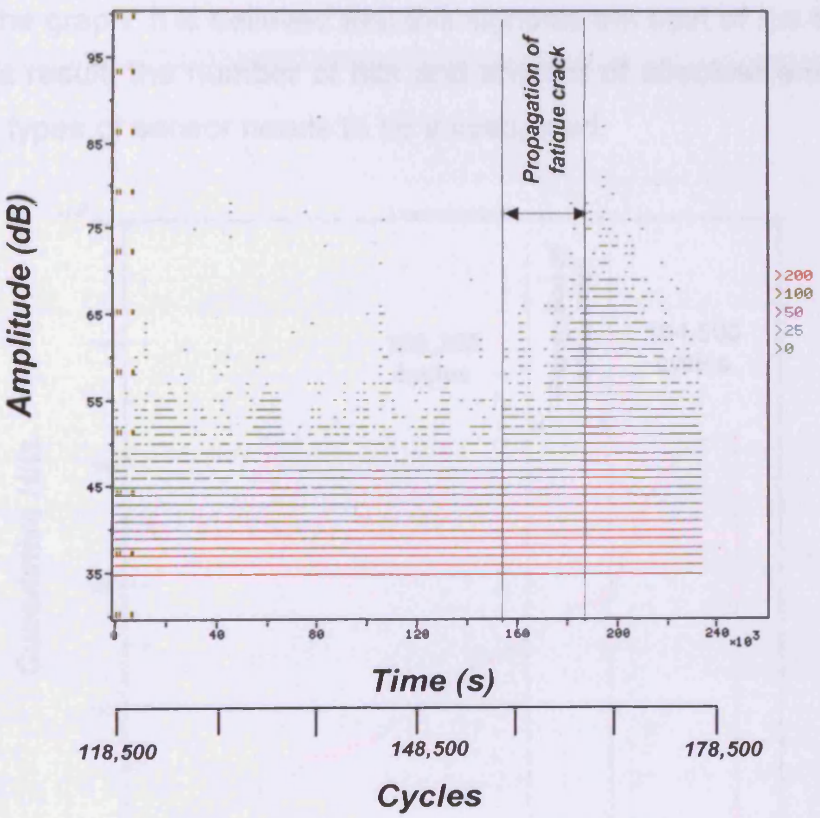

Figure 6.32. Amplitudes recorded on sensors attached to the concrete between 118,500 cycles and the 177,500 cycles of the complete test

A variety of AE sensors were attached to the concrete encasement, covering a broad frequency range during fatigue of the steel rebar. Fig. 6.32 displays the amplitudes recorded on all the "concrete" sensors between 118,500 cycles and 177,500 cycles of the test, where the region between the dashed lines represents the duration of steel fatigue.

Prior to fatigue, secondary emissions (noise) were recorded on each of the concrete sensors. These emissions could be due to background noise and failure of the concrete due to the displacement of the rebar. If the “concrete” sensors can monitor damage occurring within the steel rebar, a change in the magnitude of AE parameters such as amplitude is expected since fatigue will produce different emissions to that of the secondary signals. At 156,250 cycles there is an increase in the amplitude of the recorded AE. It is believed that this increase in amplitude represents the initiation of the fatigue crack. At 164,500 cycles there is another dramatic change in amplitude. Not only is there a significant change to the magnitude of the signals but also there is an increase in the number of hits shown by the colour intensity of the graph. It is believed that this signifies the start of the tearing crack. To establish this result, the number of hits and amount of absolute energy recorded on the different types of sensor needs to be investigated.

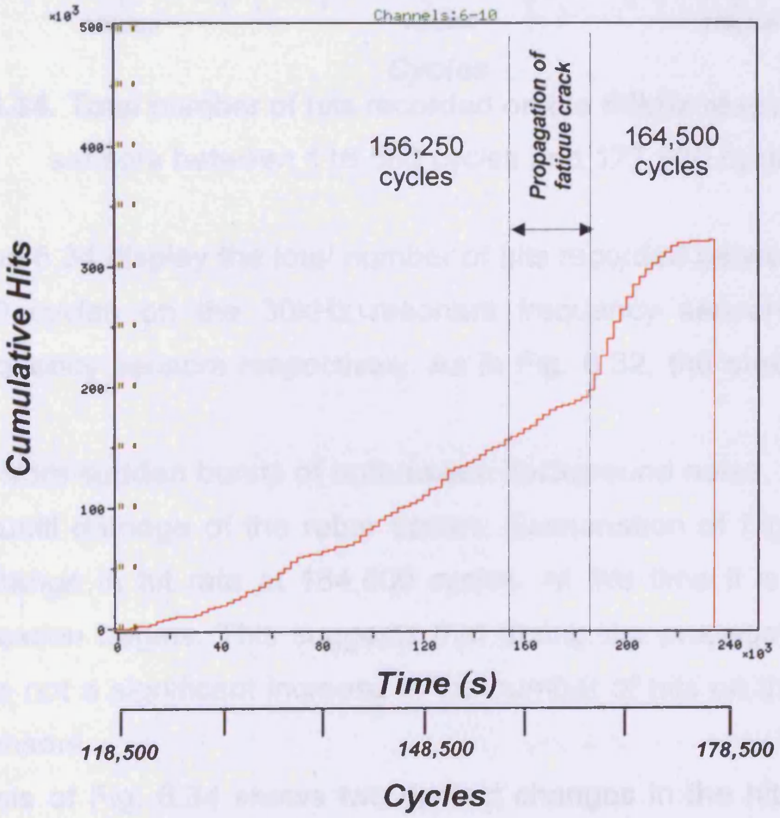

Figure 6.33. Total number of hits recorded on the 30kHz resonant frequency sensors between 118,500 cycles and 177,500 cycles

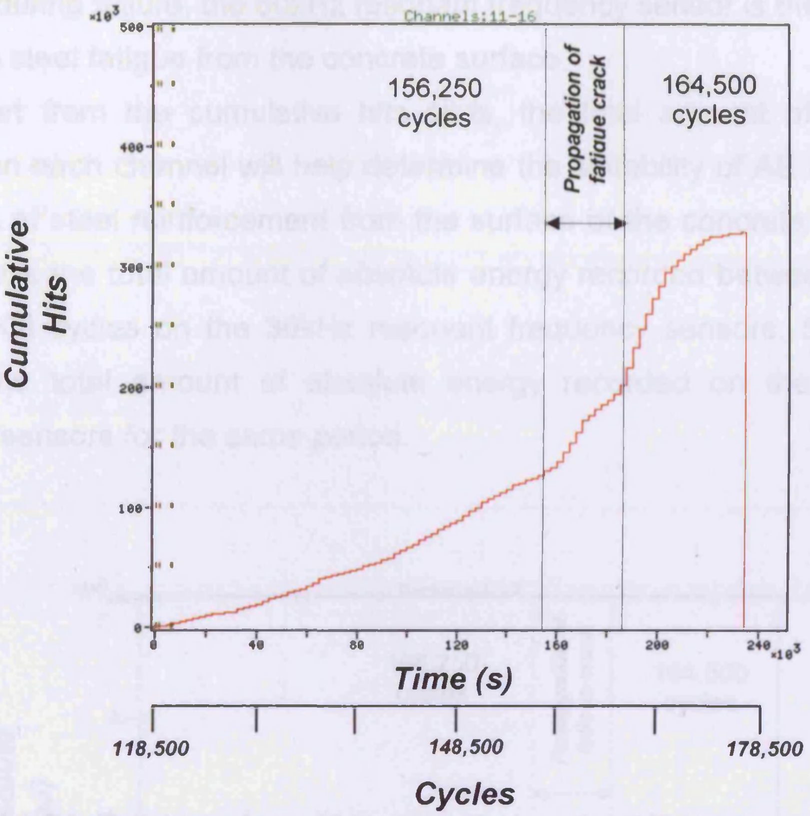

Figure 6.34. Total number of hits recorded on the 60kHz resonant frequency sensors between 118,500 cycles and 177,500 cycles

Figs. 6.33 and 6.34 display the total number of hits recorded between 118,500 cycles and 177,500 cycles on the 30kHz resonant frequency sensors and the 60kHz resonant frequency sensors respectively. As in Fig. 6.32, the steel fatigue region is displayed.

Apart from sudden bursts of unforeseen background noise, a constant hit rate is expected until damage of the rebar occurs. Examination of Fig. 6.33 shows that there is a change in hit rate at 164,500 cycles. At this time it is believed that the tearing dislocation begins. This suggests that during the propagation of the fatigue crack there is not a significant increase in the number of hits on the 30kHz resonant frequency sensors.

Analysis of Fig. 6.34 shows two distinct changes in the hit rate between the 118,500 cycles and 177,500 cycles. The first increase occurs at 156,250 cycles, which corresponds with the start of the fatigue crack. After 164,500 cycles, there is a greater increase in the hit rate. The latter is consistent with the beginning of the tearing crack. This suggests that even though both types of sensor detected AE produced during failure, the 60kHz resonant frequency sensor is the most suitable for monitoring steel fatigue from the concrete surface.

Apart from the cumulative hits plots, the total amount of absolute energy detected on each channel will help determine the suitability of AE techniques for the monitoring of steel reinforcement from the surface of the concrete encasement. Fig. 6.38 displays the total amount of absolute energy recorded between 118,500 cycles and 177,500 cycles on the 30kHz resonant frequency sensors. Similarly Fig. 6.35 displays the total amount of absolute energy recorded on the 60kHz resonant frequency sensors for the same period.

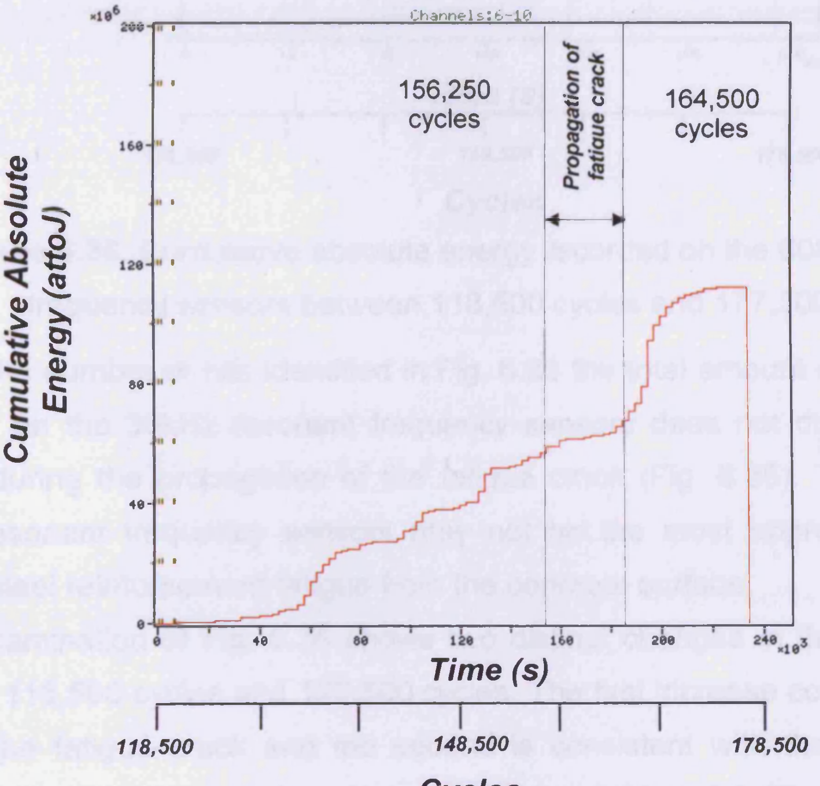

Figure 6.35. Cumulative absolute energy recorded on the 30kHz resonant frequency sensors between 118,500 cycles and 177,500 cycles

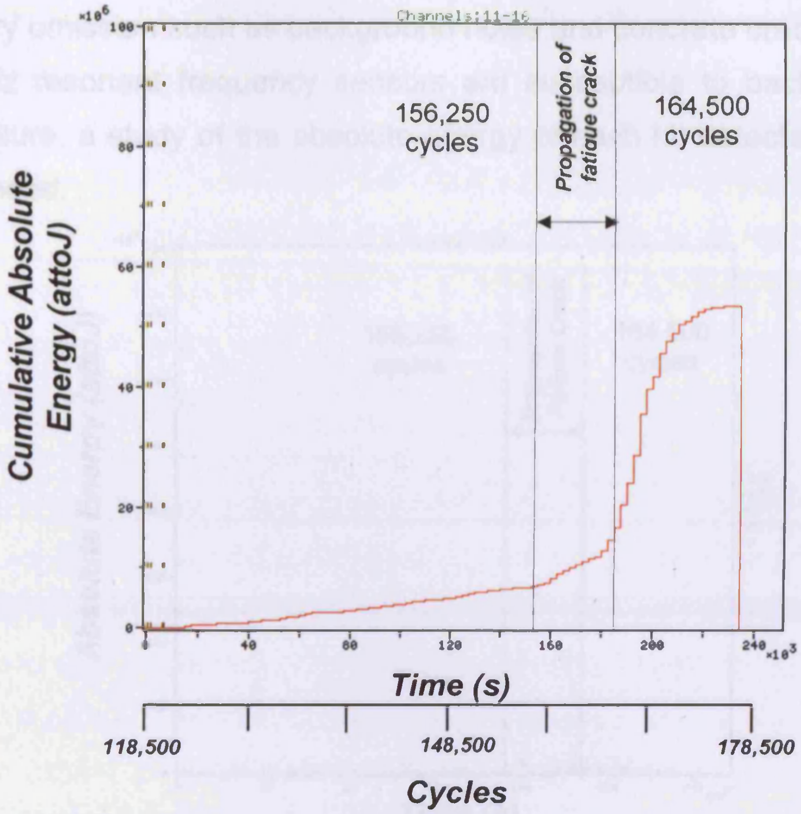

Figure 6.36. Cumulative absolute energy recorded on the 60kHz resonant frequency sensors between 118,500 cycles and 177,500 cycles

As with the number of hits identified in Fig. 6.33 the total amount of absolute energy recorded on the 30kHz resonant frequency sensors does not display a significant change during the propagation of the fatigue crack (Fig. 6.35). This suggests that 30kHz resonant frequency sensors may not be the most appropriate sensors to monitor steel reinforcement fatigue from the concrete surface.

Examination of Fig. 6.36 shows two distinct changes in the absolute energy between 118,500 cycles and 177,500 cycles. The first increase corresponds with the start of the fatigue crack and the second is consistent with the beginning of the tearing crack. The observations agree with Figs. 6.33 and 6.34 where even though both types of sensor detected emissions during failure, the 60kHz resonant frequency sensor was identified as the most suitable for monitoring steel fatigue from the concrete surface.

The gradient of the slope prior and during fatigue for both the number of hits and the absolute energy plots is affected by the amount of background noise that each sensor detects. Since there is no increase in slope for the 30kHz resonant frequency sensors during fatigue it is believed that these sensors may be susceptible to secondary emission such as background noise and concrete cracking. To discover if the 30kHz resonant frequency sensors are susceptible to background noise or concrete failure, a study of the absolute energy of each hit detected on both sensor types is needed.

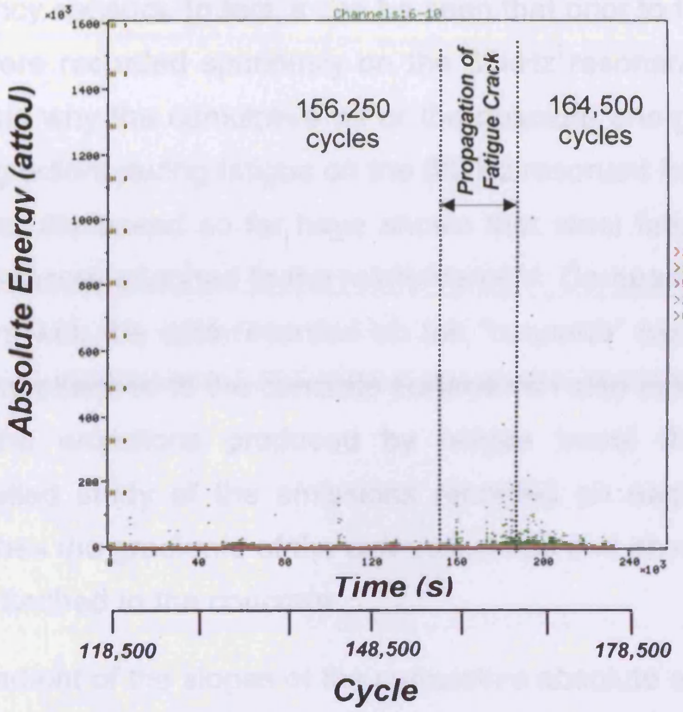

Figure 6.37. Absolute energy recorded on 30kHz resonant frequency sensors between 118,500 cycles and 177,500 cycles

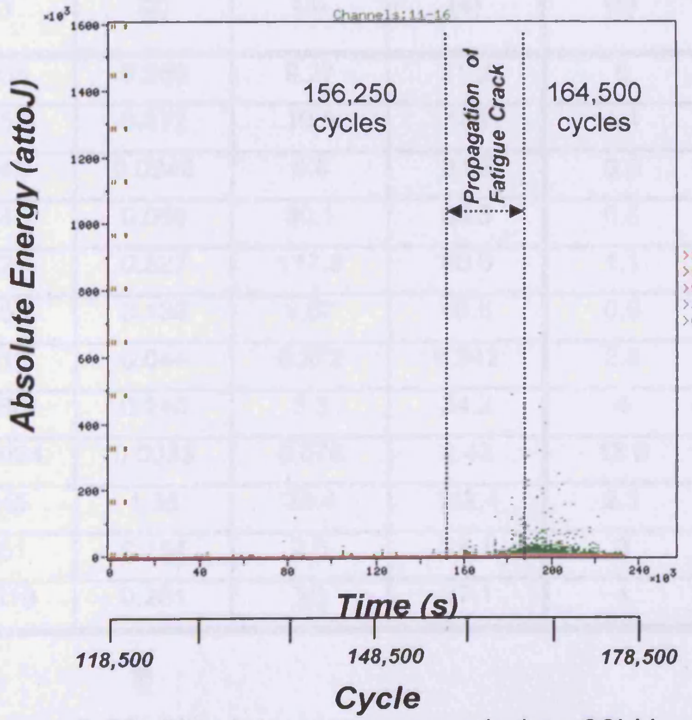

Figure 6.38. Absolute energy recorded on 60kHz resonant frequency sensors between 118,500 cycles and the 177,500 cycles

Fig. 6.37 and Fig. 6.38 display the absolute energy of emissions recorded between 118,500 cycles and 177,500 cycles on the 30kHz resonant frequency sensors and 60kHz resonant frequency sensors, respectively. The two plots differ prior to fatigue where there are fewer emissions with smaller absolute energies on the 60kHz resonant frequency sensors. In fact, it can be seen that prior to fatigue large absolute energy peaks were recorded spuriously on the 30kHz resonant frequency sensors. This could explain why the cumulative hit or the absolute energy plots did not show any increase in gradient during fatigue on the 30kHz resonant frequency sensors.

The results discussed so far have shown that steel fatigue can be detected and located by sensors attached to the reinforcement. Comparing the data recorded on these sensors with the data recorded on the "concrete" sensors it is possible to show that sensors attached to the concrete surface can also monitor steel fatigue. To discover how the emissions produced by fatigue travel through the concrete covering, a detailed study of the emissions recorded on each sensor is needed. Table 6.3 describes the gradients of the cumulative hits and absolute energy plots for all the sensors attached to the concrete.

Table 6.3. Gradient of the slopes of the cumulative absolute energy and hit plots showing the difference before and during fatigue on the concrete sensors

Channel	(1)	(2)	(3)	(4)	(5)	(6)	(7)
5	0.065	0.388	9.27	21.2	6	2.3	**0.4**
6	0.259	0.372	10.9	103	1.4	9.5	**6.8**
7	0.045	0.0248	8.6	9.09	0.5	1.1	**2.2**
8	0.145	0.069	80.1	66.6	0.5	0.8	**1.6**
9	0.420	0.527	117.8	60.6	1.1	0.5	**0.5**
10	0.155	0.139	9.07	63.6	0.9	7	**7.9**
11	0.016	0.044	0.372	6.842	2.8	18.4	**6.5**
12	0.060	0.240	3.3	24.2	4	7.3	**1.8**
13	0.00024	0.0033	0.076	1.43	13.8	18.8	**1.4**
14	0.645	1.35	36.4	142.4	2.1	4	**2**
15	0.051	0.154	2.5	27.1	3	11	**3.7**
16	0.0619	0.261	20	27.1	4	13.6	**3.4**

Where:

(1) = Gradient of the cumulative hit plot for emissions recorded prior to the propagation of the fatigue crack (hits/second)

(2) = Gradient of the cumulative hit plot for emissions recorded during the propagation of the fatigue crack (hits/second).

(3) = Gradient of the cumulative absolute energy plot for emissions recorded prior to the propagation of the fatigue crack (atto Joules/second).

(4) = Gradient of the cumulative absolute energy plot for emissions recorded during the propagation of the fatigue crack (atto Joules /second).

(5) = Ratio of the gradients described in (1) and (2)

(6) = Ratio of the gradients described in (3) and (4)

(7) = Absolute energy per hit for emissions recorded during the propagation of the fatigue crack = Ratio of gradients described in (5) and (6)

From the analysis of Figs. 6.33, and 6.35 no significant change in gradient for the cumulative hits and absolute energy plots occurs during the fatigue crack propagation. It has been suggested that this result is due to unwanted background noise. Looking at column "(7)" in table 6.3 it can be seen that for the 30kHz resonant frequency sensors all channels except channel 9 have an increase in the amount of energy for each hit during the fatigue region.

Channel 9 is the sensor placed below the notch and will predominantly record emissions produced by crushing of the concrete at the concrete edge. Table 6.3 shows that even though there is the same rate of hits before and during fatigue, each hit detected during fatigue has half the absolute energy of the hits prior to fatigue. This suggests that concrete failure (crushing) caused by the motion of the rebar diminishes during the propagation of the fatigue crack and that the crushing at the rebar-concrete block edge produces the unwanted signals that mask the gradients of the plots in Figs. 6.33 and 6.34.

As already stated, the rest of the 30kHz resonant frequency sensors have an increase in the amount of energy for each hit during the fatigue region. It can be seen from channels 6, 7 and 8 that the absolute energy per hit increases by 6.8, 2.2 and 1.6 times the absolute energy recorded prior to failure, respectively. From the position of each sensor (see Fig. 6.21) it can be seen that the absolute energy per hit decreases across the concrete. This suggests that even though the change in absolute energy per hit decreases across the concrete encasement the fatigue crack was detected on all of the 30kHz resonant frequency sensors.

For the 60kHz resonant frequency sensors there is an increase in the number of hits per second and in the energy per hit during the fatigue region. Similar to the 30kHz resonant frequency sensors there is a decrease in absolute energy across sensors 11-13 which are situated on top of the specimen (Fig. 6.21) suggesting that the signal attenuates through the specimen.

Channels 10, 15 and 16 represent the channels situated on the side of the specimen. Comparing the change in absolute energy per hit during the fatigue region on channels 15 and 16, it can be seen that there is little loss in the change in absolute energy per hit. This suggests that the detection of the signal produced by the fatigue crack not only depend upon the distance between the source and sensor but also on the orientation of the sensor. An additional study of the effects the sensor orientation has on the detection of steel fatigue is needed.

6.6. DEFORMED REBAR ENCASED IN CONCRETE LOADED DYNAMICALLY IN TENSION

6.6.1. Experimental Procedure

Deformed steel rebar partially encased within a concrete covering was fatigued in tension using a dynamic load. The test specimen, shown in Fig. 6.39, consists of a concrete specimen 600mm long x 150mm deep x 150mm wide, with the deformed steel rebar cast through the centre of it, extending beyond the concrete mass. The concrete encasement is reinforced with a steel cage similar to that in the specimen used in section 6.5.

The rebar used for this study had the same dimensions as the plain rebar failed in tension (section 6.4) and was loaded in the same way. A notch was cut around the bar to initiate a crack. This notch was deeper than the threaded sections to ensure that the bar failed at the centre. Acoustic insulation was placed at the supports with the aim of dampening unwanted background noise such as that produced by rubbing, friction and mechanical sources. The load range (10kN-70kN) was applied at a frequency of 2Hz. Load control was used to maintain the load range by the AE system with deflection and load monitored by the AE system. A DARTEC actuator (static range 0-550kN / dynamic range 0-500kN) was used to apply the load to the specimen. Fig. 6.39 represents a schematic diagram of the load arrangement and the position of the sensors attached to the rebar and concrete. Fig. 6.40 is a photograph taken of the specimen prior to failure.

Two AE 150kHz resonant frequency sensors were attached to the steel rebar via waveguides to detect and record AE produced during loading. The AE set-up used for each channel can be seen in table B.10 in appendix B. Four 30kHz resonant frequency sensors were attached to the concrete block with the aim of monitoring the fatigue crack in the rebar. The concrete sensors were coupled to the specimen using silicon sealant and attached to the specimen using steel clamps. Prior to loading the wave-guide connection was checked using a HN source and similar emissions were recorded.

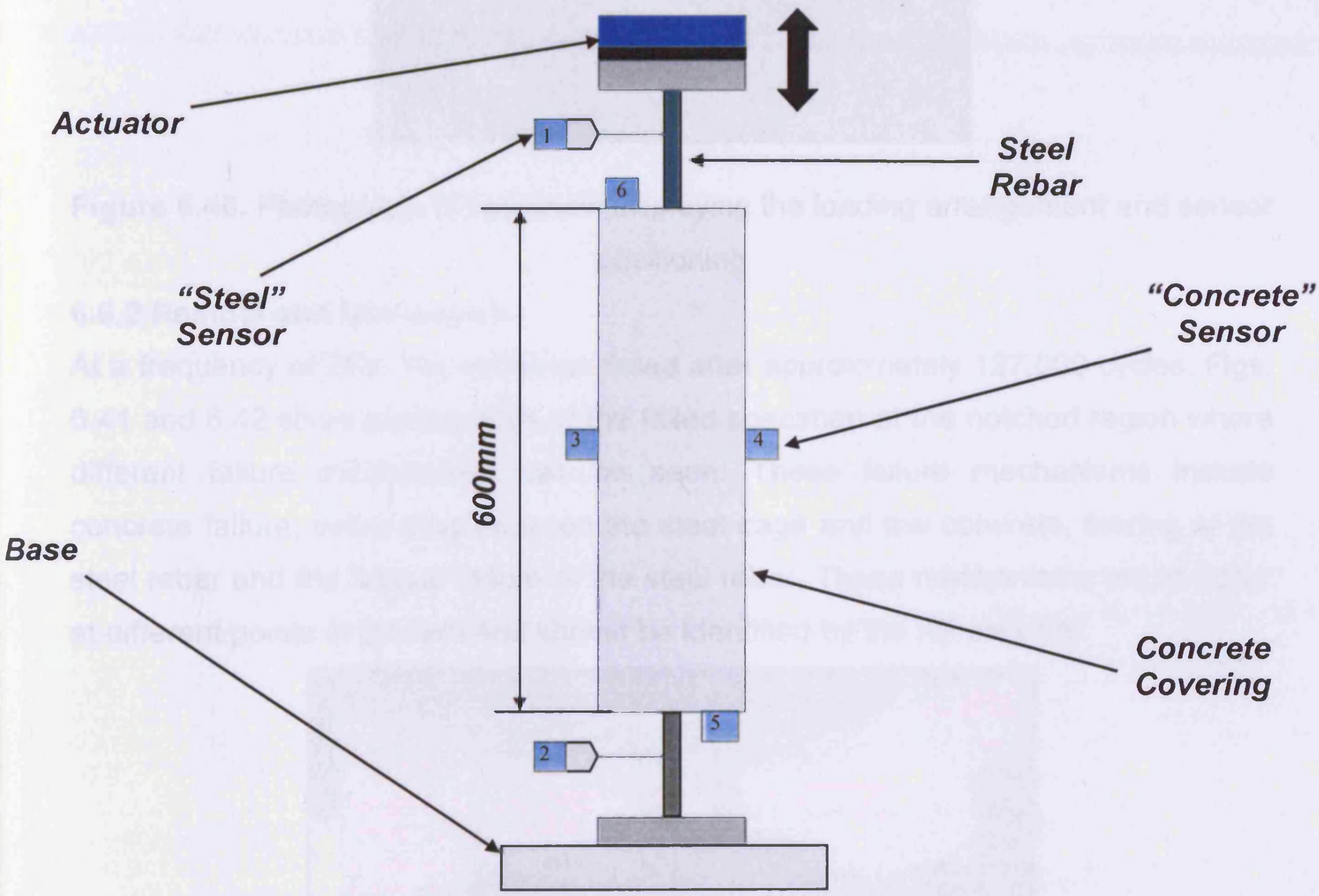

Figure 6.39. Sensor and specimen set-up for steel rebar encased in concrete failed dynamically in tension

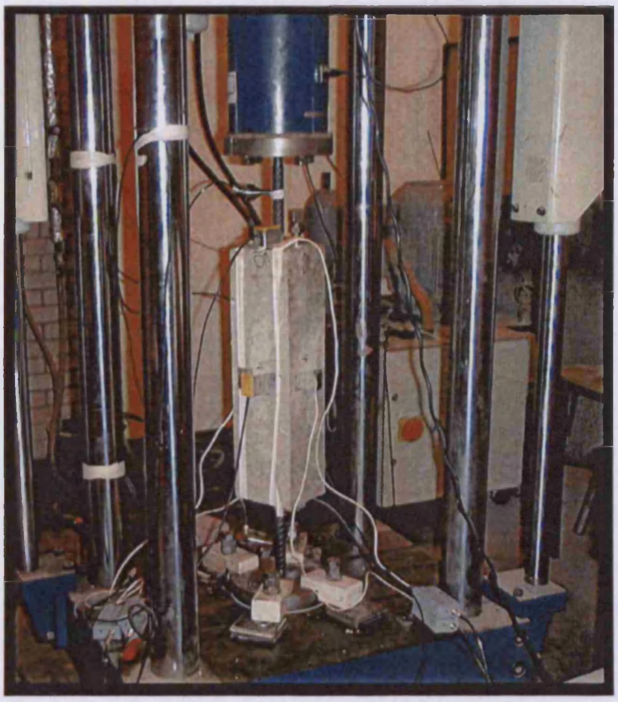

Figure 6.40. Photograph of specimen displaying the loading arrangement and sensor positioning

6.6.2 Results and Discussion

At a frequency of 2Hz, the specimen failed after approximately 127,000 cycles. Figs. 6.41 and 6.42 show photographs of the failed specimen at the notched region where different failure mechanisms can be seen. These failure mechanisms include concrete failure, debonding between the steel cage and the concrete, tearing of the steel rebar and the fatigue failure of the steel rebar. These mechanisms would occur at different points in the test and should be identified by the AE sensors.

Figure 6.41. Photograph of the centre of the specimen after failure

Figure 6.42. Photograph of the centre of the specimen after failure displaying the steel rebar

Fig. 6.43 displays the load history of the rebar for the complete test. Fig. 6.44 displays the deflection of the actuator for the last 16,600 cycles (between 110,000 cycles-126, 000 cycles). As the load applied to the specimen was controlled by upper and lower limits any deformation of the rebar will change the amount of deflection of the actuator. It can be seen that there is a distinct change in the deflection range at approximately 125,000 cycles. It is suggested that at this time the propagation of the fatigue crack has finished and the steel rebar experiences a tearing dislocation at the notch. This suggests that the tearing dislocation occurs over 2000 cycles.

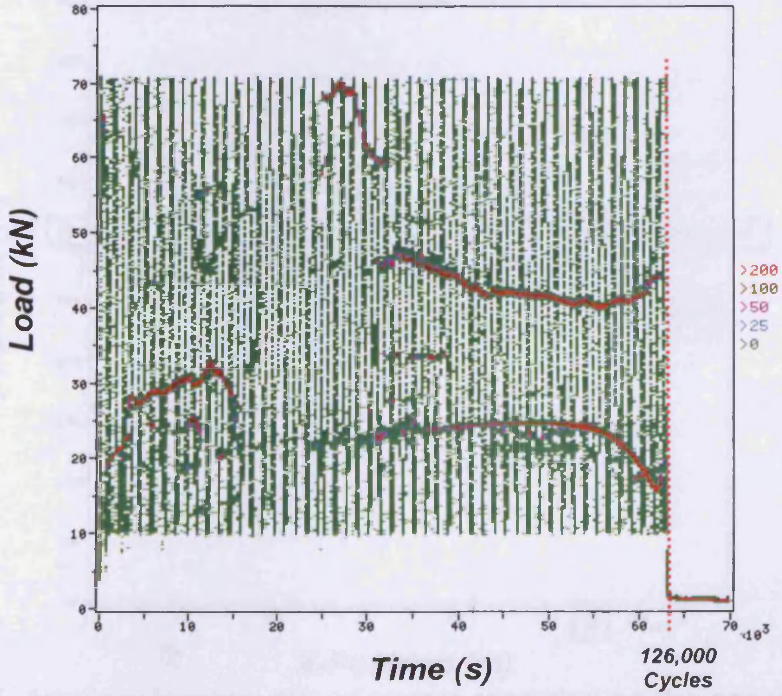

Figure 6.43. Load history during the dynamic loading of the steel rebar partially encased in concrete

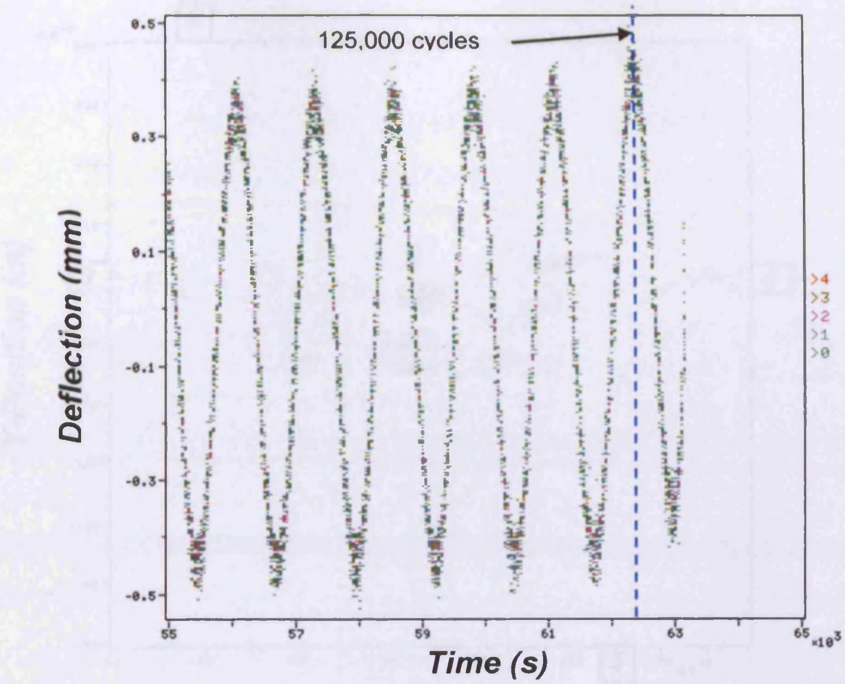

Figure 6.44. Deflection of actuator with respect to time during the dynamic loading of the steel rebar

The event and energy located on the "concrete" sensors during the test is displayed in the following figures.

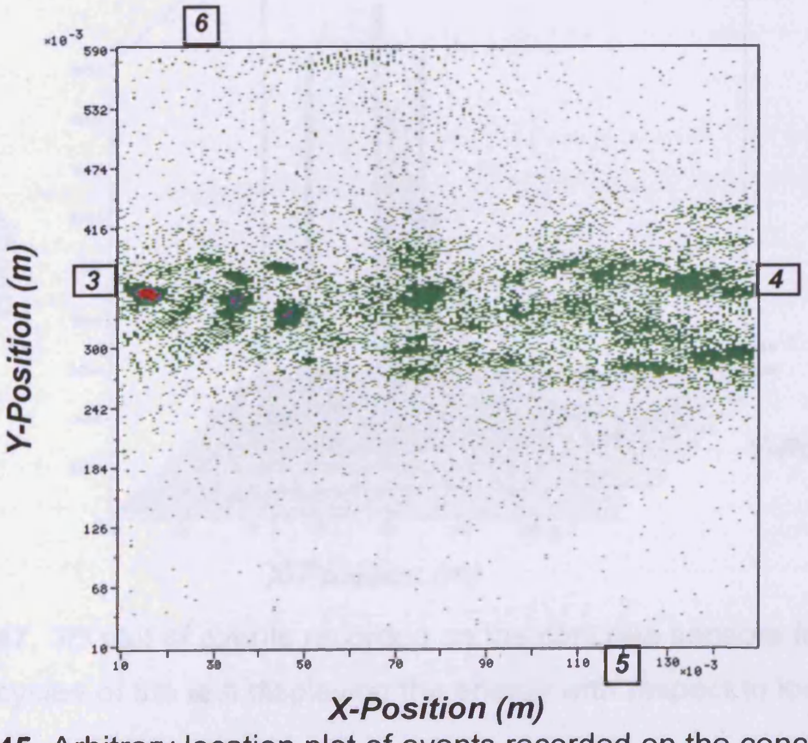

Figure 6.45. Arbitrary location plot of events recorded on the concrete sensors for the whole of the test.

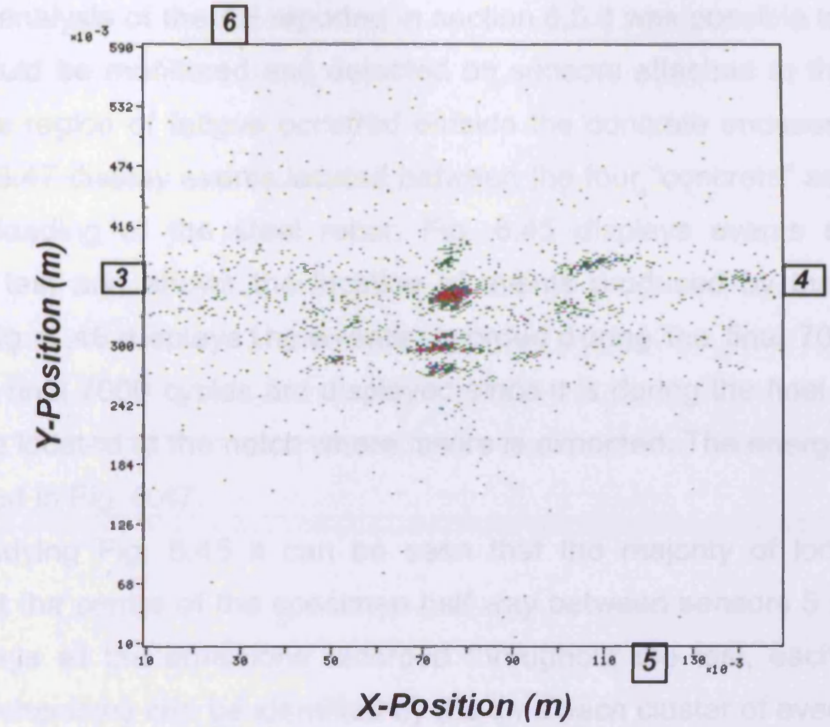

Figure 6.46. Arbitrary location plot of events recorded on the concrete sensors for the final 7000 cycles of the test.

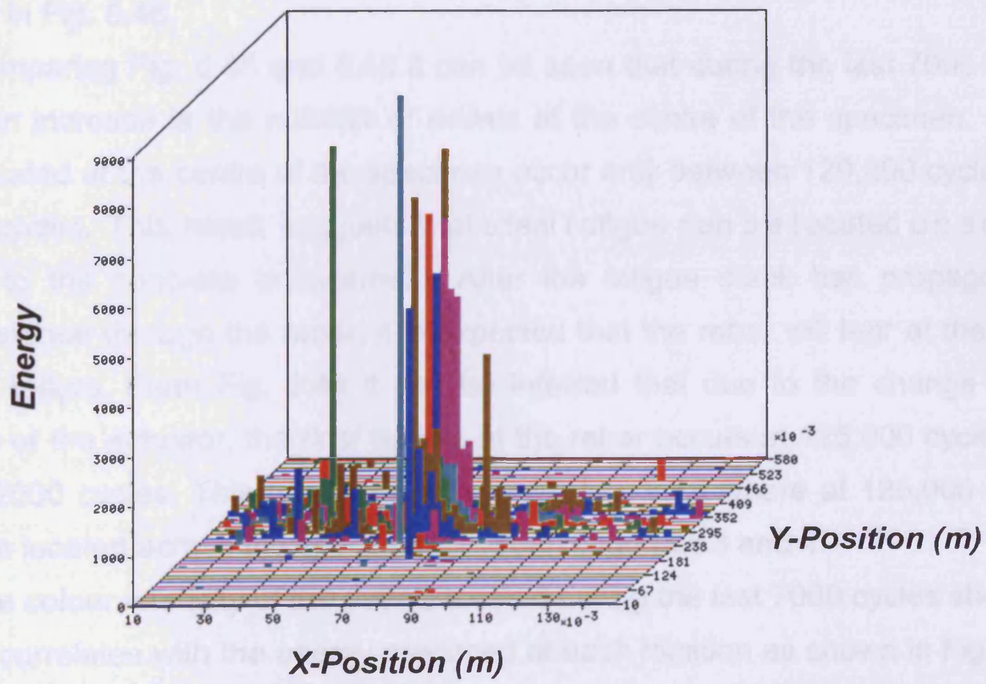

Figure 6.47. 3D plot of events recorded on the concrete sensors for the final 7000 cycles of the test displaying the energy with respect to location.

From the analysis of the AE reported in section 6.5 it was possible to show that steel fatigue could be monitored and detected on sensors attached to the concrete even though the region of fatigue occurred outside the concrete encasement. Figs. 6.45, 6.46 and 6.47 display events located between the four "concrete" sensors during the dynamic loading of the steel rebar. Fig. 6.45 displays events recorded for the complete test and shows the location of events produced by the different failure modes. Fig. 6.46 displays the events recorded during the final 7000 cycles of the test. The final 7000 cycles are displayed since it is during the final 7000 cycles that events are located at the notch where failure is expected. The energy of these events is displayed in Fig. 6.47.

Studying Fig. 6.45 it can be seen that the majority of located events are situated at the centre of the specimen half way between sensors 5 and 6. Since this plot displays all the emissions recorded throughout the test, each of the different failure mechanisms can be identified by the time each cluster of events is located. An analysis of events located in the later region of the test should show if sensors attached to the concrete could locate steel fatigue. The location of these events are displayed in Fig. 6.46.

Comparing Fig. 6.45 and 6.46 it can be seen that during the last 7000 cycles there is an increase in the number of events at the centre of the specimen. In fact events located at the centre of the specimen occur only between 120,200 cycles and 125,000 cycles. This result suggests that steel fatigue can be located on sensors attached to the concrete encasement. After the fatigue crack has propagated a certain distance through the rebar, it is expected that the rebar will tear at the notch until final failure. From Fig. 6.44 it can be inferred that due to the change in the deflection of the actuator, the final tearing of the rebar occurs at 125,000 cycles and lasts for 2000 cycles. This result correlates with Fig. 6.45 where at 125,000 cycles events are located across the specimen between channels 3 and 4.

The colour intensity of the events located during the last 7000 cycles shown in Fig. 6.46 correlates with the energy produced at each location as shown in Fig. 6.47. It can be seen that the majority of the energy recorded between 120,200 cycles and 125,000 cycles is at the centre. After 125,000 cycles, events were located between channels 3 and 4 sporadically. Comparing the arbitrary location plots of the concrete sensors with the deflection of the actuator with respect to time suggests that at 120,200 cycles into the test fatigue crack propagation occurs in the rebar for approximately 4800 cycles. At 125,000 cycles the steel rebar fails by the tearing dislocation of the notched steel rebar until final failure occurs at 127,000 cycles. Both types of failure of the steel rebar can be seen in Fig. 6.42.

Previous sections have shown that steel fatigue can be monitored by AE sensors attached to the rebar itself via machined flats or waveguides welded to the actual rebar. To prove that steel fatigue can be monitored at the surface of the concrete encasement it is important that the location of events by sensors attached to the steel rebar correlate with those located by the “concrete” sensors.

Fig. 6.48 and Fig. 6.49 display the amplitude and the initiation frequency of events recorded between channels 1 and 2, respectively.

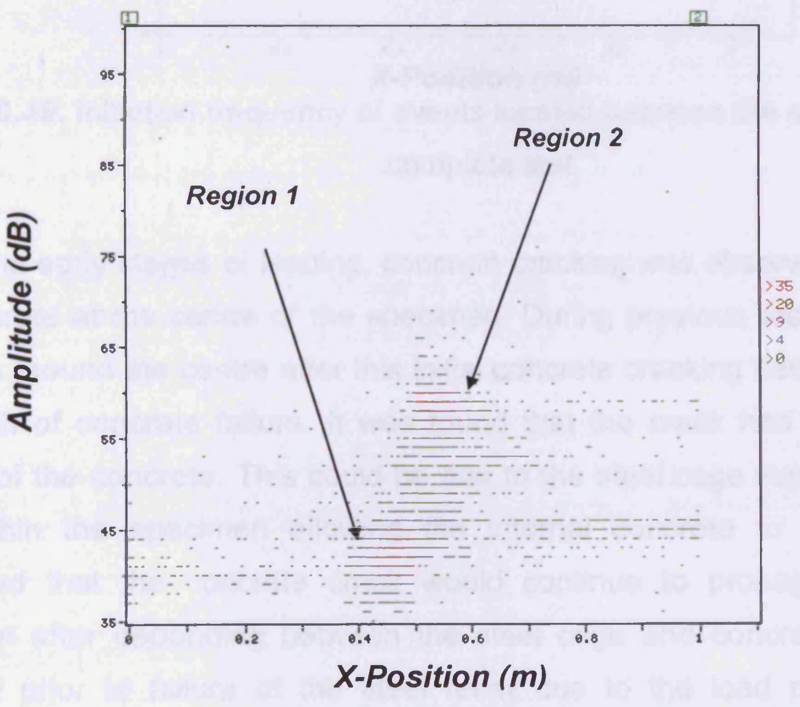

Figure 6.48. Amplitude of events located between the steel sensors for the complete test.

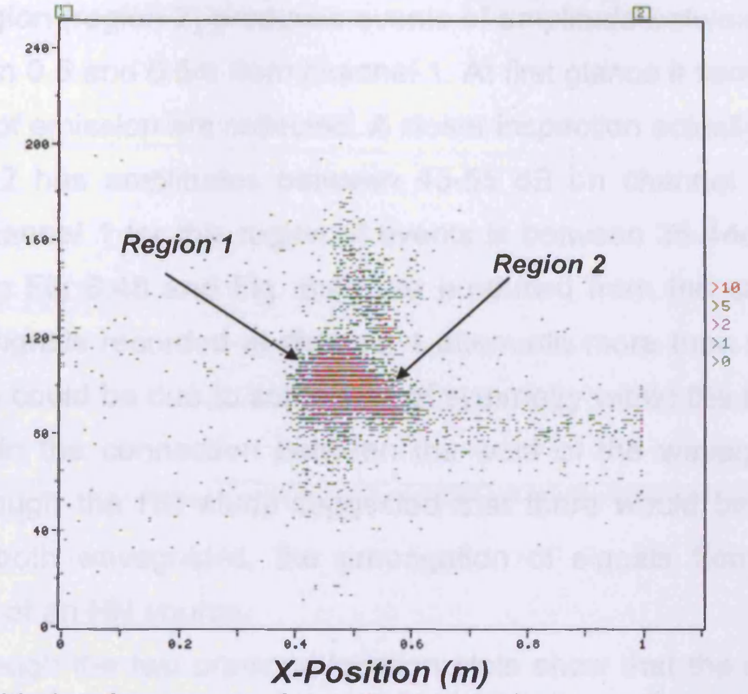

Figure 6.49. Initiation frequency of events located between the steel sensors for the complete test.

During the early stages of loading, concrete cracking was observed on the surface of the concrete at the centre of the specimen. During previous tests the concrete was cut open around the centre after this initial concrete cracking had occurred to inspect the depth of concrete failure. It was found that the crack had only opened at the surface of the concrete. This could be due to the steel cage supporting some of the load within the specimen allowing the internal concrete to remain intact. It is suggested that the concrete crack would continue to propagate throughout the specimen after debonding between the steel cage and concrete. This must have occurred prior to failure of the steel rebar due to the load range used. In fact, locations of events on the steel sensors show different types of emission were recorded at different times.

The location plots in Fig. 6.48 and 6.49 are linear location plots where the location of each event is calculated using conventional time of arrival techniques as described in chapter 2. The sensor at which the located source is detected first determines the displayed parameters such as amplitude and initiation frequency of the located event. In Fig. 6.51 it can be seen that between 0.4 and 0.6 metres from channel 1 there are two distinct regions. The first region (region 1) has events of amplitudes between 36-44dB and is located between 0.4 and 0.5m from channel 1.

The second region (region 2) produces events of amplitude between 45-55dB and is located between 0.5 and 0.6m from channel 1. At first glance it seems as though two different types of emission are collected. A closer inspection actually shows that even though region 2 has amplitudes between 45-55 dB on channel 2 the amplitudes recorded on channel 1 for this region of events is between 36-44dB. Thus region 1 and region 2 in Fig 6.48 and Fig. 6.49 are produced from the same source. This suggests that signals recorded at channel 1 attenuate more than those recorded at channel 2. This could be due to some lack of symmetry within the specimen such as the difference in the connection between the weld of the waveguide on both the channels. Although the HN study suggested that there would be a similar loss in signal across both waveguides, the propagation of signals from fatigue may be different to that of an HN source.

Even though the two previous location plots show that the majority of events are located at the centre of the specimen, to distinguish the period of time the steel rebar fatigue it is important to study each event with respect to time. Fig. 6.50 displays the cumulative energy of events recorded between the two steel sensors where the depth of the plot represents the time of the located event.

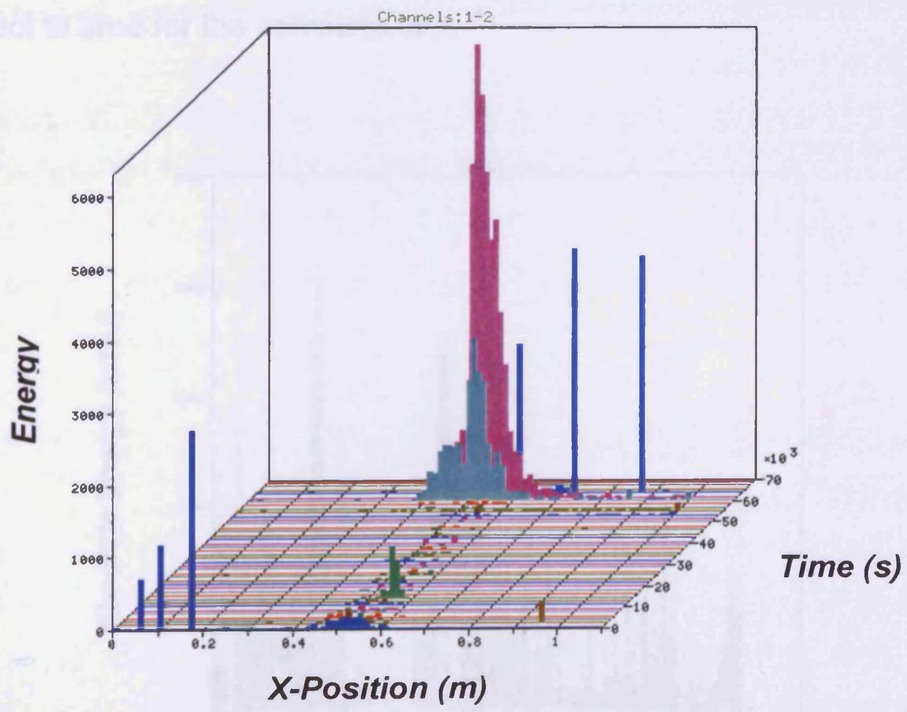

Figure 6.50. Amplitude of events located between the steel sensors with respect to time.

Studying Figs. 6.48 and 6.49 it can be seen that the majority of events located between the two sensors are situated at the centre of the steel rebar which corresponds to the location of the notch. In the early stages of loading these located events could be due to concrete cracking of the specimen at the surface. The concrete failure would continue throughout the test producing emissions at the centre of the specimen. Similarly rubbing and friction caused by the concrete failure would produce events. From Fig. 6.50 an increase in the energy recorded at each position can be seen to occur at the end of the test. In fact this increase in energy occurs at approximately 120,000 cycles. This correlates with the location plots from the concrete sensors where there is an increase in the number of events and energy at a comparable time. Comparing the arrival times of events located on the steel sensors and on the concrete sensors suggests that steel fatigue can be detected and located on sensors attached to both the steel rebar and the concrete encasement.

Even though the location plots have shown that fatigue signals were located after 120,000 cycles it is possible that steel fatigue may have actually occurred prior to this. A closer analysis of emissions recorded on each sensor is needed. Figs. 6.51 and 6.52 display the absolute energy recorded on channels 1 and 2, respectively, with respect to time for the complete test.

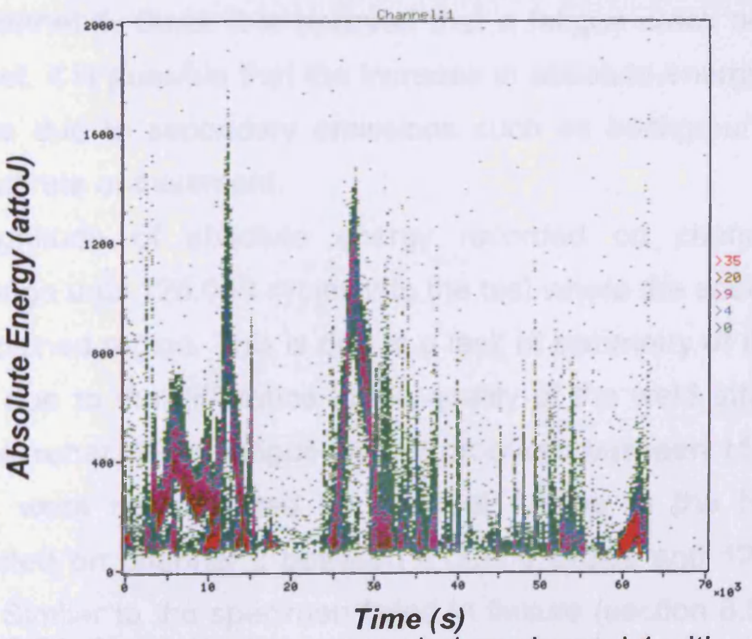

Figure 6.51. Absolute energy recorded on channel 1 with respect to time for the complete test

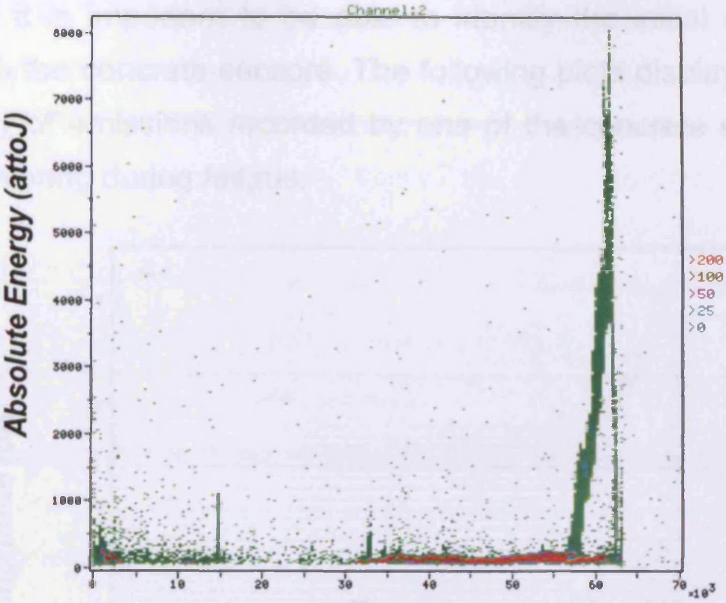

Figure 6.52. Absolute energy recorded on channel 2 with respect to time for the complete test

Any change in an AE parameter such as absolute energy can be used to detect damage within the specimen. Examination of Fig. 6.51 and Fig. 6.52 show that there is a significant change in absolute energy on channel 2 after 113,800 cycles. This change in energy is not apparent on channel 1, although where there is a change in the number of emissions as shown by the colour intensity at 120,000 cycles. At approximately 50,000 cycles into the test there is a large increase in absolute energy recorded on channel 1. Since it is believed that a fatigue crack occurs at the later stages of the test, it is possible that the increase in absolute energy on channel 1 at 50,000 cycles is due to secondary emissions such as background noise and the failure of the concrete encasement.

The magnitude of absolute energy recorded on channel 1 does not significantly change until 125,000 cycles into the test where the specimen fails by the tearing of the notched region. This is due to a lack of symmetry of the specimen and could again be due to the difference in the quality of the weld attaching the wave-guide to the steel rebar. Since fatigue signals produced between 113,800 cycles and 120,000 cycles were not detected on channel 1 (due to the high attenuation), emissions detected on channel 2 between 113,800 cycles and 120,000 cycles will not be located. Similar to the specimen failed in flexure (section 6.5), the amount of attenuation through the specimen affects the ability of AE techniques to detect and locate damage within the specimen.

Similarly it is important to be able to identify the initial emissions from the fatigue crack on the concrete sensors. The following plots display the amplitude and absolute energy of emissions recorded by one of the concrete sensors attached to the concrete covering during fatigue.

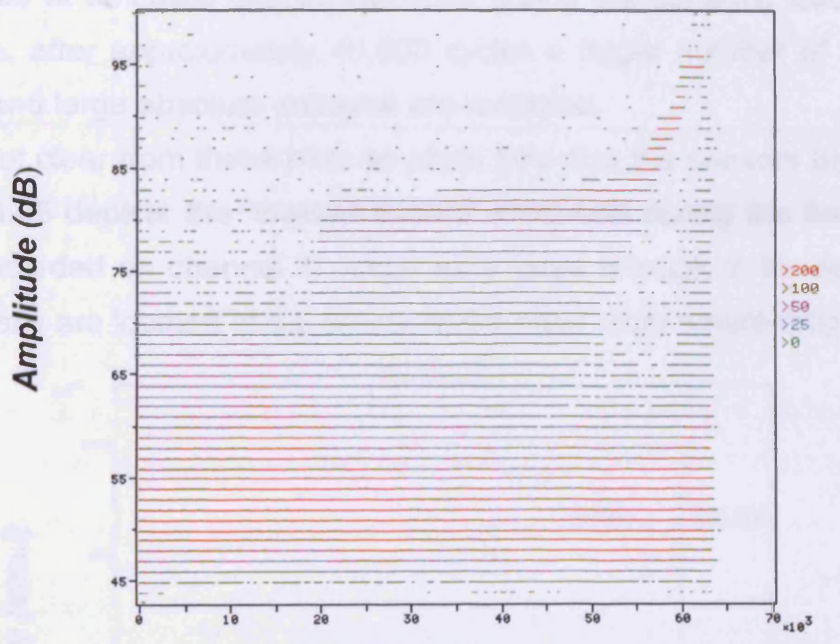

Figure 6.53. Amplitude recorded on channel 3 with respect to time for the complete test

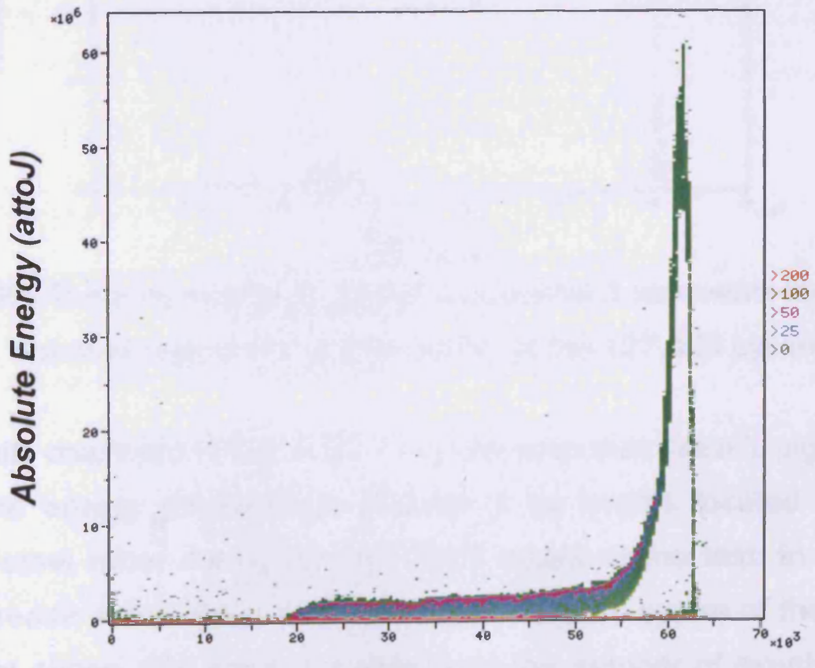

Figure 6.54. Absolute energy recorded on channel 3 with respect to time for the complete test

Figs. 6.53 and Fig. 6.54 display, respectively, the amplitude and absolute energy recorded on channel 3 for the complete test with respect to time. The amplitudes and absolute energy plots with respect to time for channels 4-6 produce similar results to channel 3 so are not presented here. From both of these plots it can be seen that different types of emission can be identified during the dynamic loading of the test. For example, after approximately 40,000 cycles a larger number of events of large amplitudes and large absolute energies are recorded.

It is not clear from these plots at which time that the sensors detect the fatigue crack. Fig. 6.55 depicts the "located events" produced during the final failure of the specimen recorded on channel 3, which were large enough to be detected at three sensors. These are located at the centre of the steel rebar where fatigue occurred.

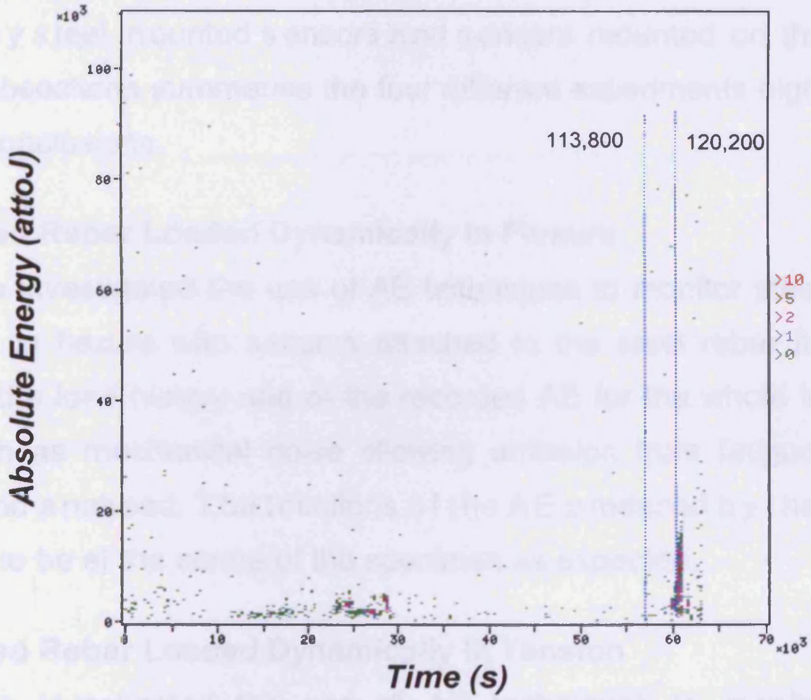

Figure 6.55. Absolute energy recorded on channel 3 for events located at the notched region of the steel rebar for the 127,000 cycles

From the results displayed in Fig. 6.55, it can be seen that there is significant change in the absolute energy recorded on channel 3 for events located at the notched region of the steel rebar during the last 7000 cycles of the test. In fact, there is a significant increase in the absolute energy after 120,200 cycles of the test. A closer look at the plot shows that there is a change in the number of events after 113,800 cycles of the test. The energies of these events are considerably smaller than the events recorded after 120,200 cycles. This corresponds with Figs 6.51 and 6.52 where no emissions were recorded on channel 1 between 113,800 and 120,200 but were recorded on channel 2. This suggests that during the early stages of fatigue smaller emissions were produced which can be detected but not always located on both steel and concrete mounted sensors.

6.7 CONCLUSIONS

This chapter has assessed the ability of AE to detect, locate and monitor steel fatigue using AE sensors on laboratory-based specimens. AE techniques were used to monitor the fatigue of deformed steel rebar and deformed steel rebar encased in concrete. Both types of specimen were fatigued in flexure and in tension. The aim of the research was to show if fatigue cracks produced in flexure and tension could be monitored by steel mounted sensors and sensors mounted on the concrete. The following subsections summarise the four different experiments highlighting the most significant conclusions.

1. Deformed Rebar Loaded Dynamically In Flexure

This section investigated the use of AE techniques to monitor steel rebar loaded dynamically in flexure with sensors attached to the steel rebar itself. From the analysis of the load history and of the recorded AE for the whole test, secondary signals such as mechanical noise allowing emission from fatigue cracks to be identified and analysed. The locations of the AE produced by the fatigue crack were found to be at the centre of the specimen as expected.

2. Deformed Rebar Loaded Dynamically In Tension

This section investigated the use of AE techniques to monitor steel rebar dynamically loaded in tension with sensors attached to the specimen via waveguides welded onto the steel rebar itself. Using similar analysis techniques to those used for the rebar failed in flexure, unwanted signals were distinguished allowing the fatigue crack to be detected and located at the notch as expected.

3. Deformed Rebar Encased In Concrete Loaded Dynamically In Flexure

This section investigated the use of AE techniques to monitor steel rebar fatigued in flexure partially encased within a concrete covering with sensors attached to the steel rebar and with sensors attached to the concrete encasement. Analysis of the recorded on the concrete sensors and the steel sensors were compared and analysed with respect to time.

It was discovered that for both sensor types, large amounts of events were recorded at the centre of the specimen during the last 7000 cycles of the test. The actual time at which the tearing crack started was confirmed by examination of the external parametrics recorded during loading. It was discovered that the fatigue crack was located on the concrete sensors and the steel sensors for a total of 5000 cycles where the tearing crack was only located for the final 2000 cycles of the test.

Even though it was possible to show that fatigue crack growth occurred during the final 5000 cycles of fatigue it was important to show that AE techniques can be used to detect the propagation of the complete fatigue crack. By studying the absolute energies recorded on selected channels it was possible to show that the fatigue crack could be detected for a total of 11,200 cycles by both the steel and concrete sensors, suggesting that AE techniques can be used to detect and locate steel fatigue using sensors mounted on both the steel and the concrete.

To apply similar techniques to in-service reinforced concrete structures some very important questions need to be asked. These include:

a. What types of loading will the reinforcement of the structure experience?
b. Is the reinforcement of the structure accessible?
c. If the reinforcement of the structure is accessible, can instrumentation such as strain gauges and AE sensors be safely attached?
d. Is it possible to perform pencil lead fractures on the surface of the structure safely?
e. What is the lowest threshold possible to record AE data without recording unwanted background noise?
f. Given the lowest possible threshold, what is the largest possible sensor spacing able to detect emissions produced from fatigue on both steel and concrete sensors?
g. Is the depth of cover consistent across the specimen?

These questions will need to be answered prior to the in-situ use of the technique if valid conclusions about the integrity of reinforced concrete structures are to be made. Previous testing has shown that the amount of concrete encasement not only affect the attenuation of the signal on the concrete mounted sensors but also affect the detection and location of signals recorded by the steel sensors. Thus to be able to monitor steel fatigue of reinforcement encased in concrete by sensors attached to the steel, the distance between sensor pairs must be carefully chosen. Similarly the ability of the technique will depend on the lowest possible threshold that can be set on the sensors. If a high threshold has to be set due to background noise produced in the structure, then the sensor spacing will have to be small. The sensor spacing will depend on the accessibility of the steel reinforcement.

As well as attenuation due to the nature of the structure, the ability to monitor any defects will depend on the type of loading that the reinforcement experiences. For the series of tests discussed in this chapter it was found that rebar failed dynamically in both tension and flexure could be monitored using AE techniques. In fact, for this series of tests it was found that, even though the test set-up changed, for each loading arrangement, fatigue of the steel rebar was detected by both steel and concrete mounted sensors. Additional research needs to be conducted to study the effects of different loading arrangements on the ability to detect fatigue.

CHAPTER 7. ACOUSTIC EMISSION ASSESSMENT OF CONCRETE HINGE "THRUST" JOINTS

7.1. INTRODUCTION

Concrete hinge joints are present in over 100 bridges in England and a further 12 over-bridges, each containing two hinge joints, in Wales. They were introduced into bridge decks as a means of simplifying the design and standardising details on bridges having a range of span and functional requirements. A schematic diagram of the reinforcement of a hinge joint can be seen in Fig. 7.1.

Hinge joints are not easily accessible for inspection or maintenance due to their form and location over or under live traffic lanes. They are vulnerable to deterioration in the event of bridge deck waterproofing failure, which can cause corrosion of the steel reinforcement. The reinforcement is crucial to the integrity of the joint, and the loss of reinforcement section can induce higher stresses leading to eventual failure by yielding. From previous experience of monitoring motorway bridges for cracks, Watson et al, (2000) established that one day's traffic provided sufficient fatigue cycles to conclusively identify active defects.

It is thought that the hinge joints transfer shear and accommodate small angular movements but restrict longitudinal movement (Wilson 1995). It is also assumed that the hinges were provided to enable the bridges to cope with possible differential settlement. Previous attempts to investigate the deterioration of hinge joints by visual inspection, which involves the removal of structural concrete around the joint to expose the reinforcement bars, have noted particular defects; the majority have cracks running through the throat and a loss of waterproofing. Waterproofing failure can lead to chloride rich seepage through the joint that can exacerbate corrosion of the reinforcement bar.

Researchers have used AE techniques to identify the deterioration of the reinforcement within a concrete structure. Yoon et al. (2000) studied the applicability of AE techniques as a potential method for detecting the extent of corrosion within reinforced concrete structures. Unreinforced, notched-unreinforced, reinforced and various levels of corroded-reinforced concrete specimens were failed in four-point bending with the aim of isolating AE response from concrete mircrocracking, localised crack propagation, corrosion and debonding of the reinforcing steel. The emissions produced by each of the failure modes were discovered by analysis of key parameters such as amplitude and duration. In fact, Yuyama and Ohtsu (2000) proposed a set of test criteria and procedures for the monitoring of reinforced concrete structures using AE techniques based on a series of tests that they carried out.

Many researchers have also suggested the appropriateness of the Kaiser effect or more importantly the Felicity ratio for the assessing the deterioration of concrete structures. Researchers discovered that the break down in the Kaiser effect correlated with the deterioration of the concrete specimen (Yuyama et al. 1999a). Yuyama et al. (1995b) compared the moment tensor analysis from events recorded during the failure of a reinforced concrete beam, loaded and unloaded with increasing loads in flexure, with the breakdown of the Kaiser effect and showed that during the deterioration of the Kaiser effect the contribution of shear cracks increased with the progress of the fracture. Similarly Yuyama et al. (2000) used the break down of the Kaiser effect to evaluate the integrity of an aging reinforced concrete dock that experienced three different loads.

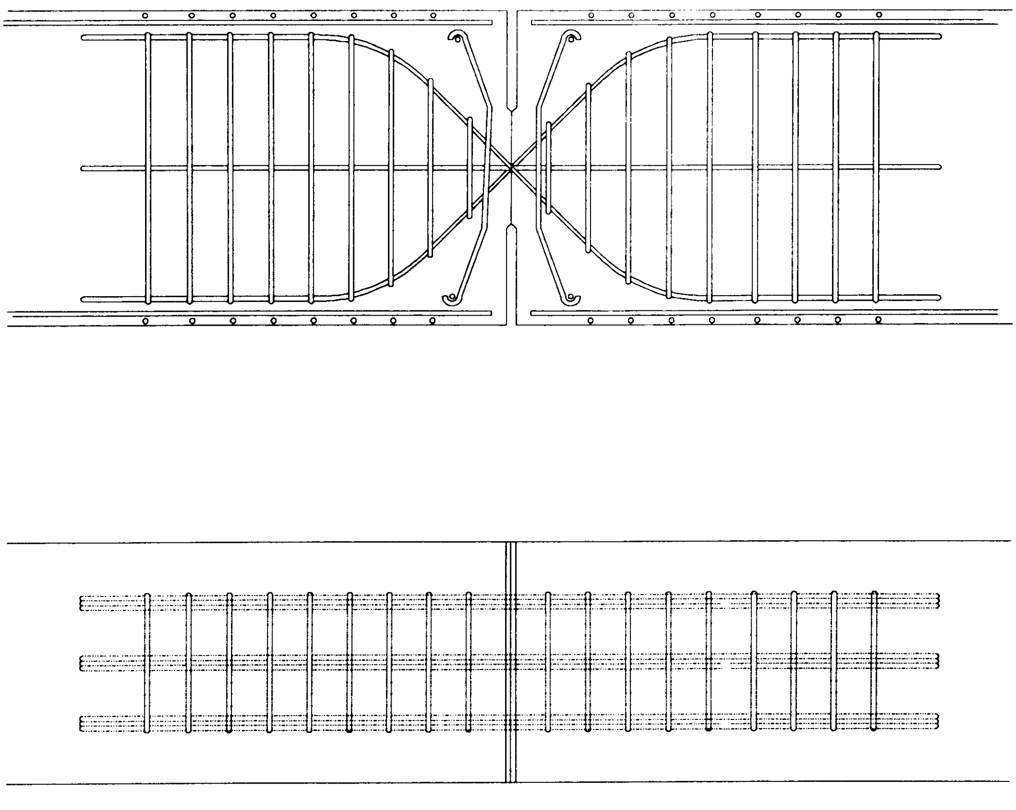

Figure 7.1. Example of the reinforcement within a hinge joint (Pullin et. al. 2003)

7.2. AE MONITORING OF M4 RIVER USK CROSSING

7.2.1. Aims ad Objectives

The aim of this investigation was to determine the feasibility of AE techniques for detecting defects in reinforced concrete bridges. This aim was addressed via a field trial completed on one hinge joint on the M4 River Usk Crossing where sensors were attached to the reinforcement steel via wave-guides and to the concrete on the face of the joint. Monitoring was undertaken during a one-day period of normal traffic. Depending on the attenuation of signals within the joint, it is expected that fatigue might be detected since the joint experiences repeated loading in tension and compression (Lark and Mawson 2003).

The experimental objectives were:

- To develop a procedure for identifying damage at the hinge joint, and any other identifiable defect.
- To demonstrate the use of AE techniques using steel sensors attached on the bar and concrete sensors attached to the concrete for the monitoring of a hinge joint.
- To obtain information on attenuation and background noise levels.
- To identify damage of the reinforcement bar using AE source location techniques, source characterisation and waveform analysis by comparing results from the field and laboratory investigations.
- To propose recommendations for more widespread and cost-effective implementation of the AE method.

7.2.2. Bridge Information, Structural Details and Experimental Procedure

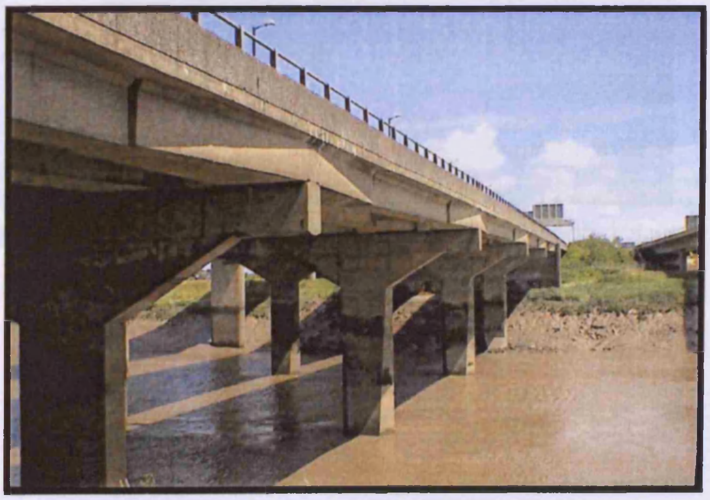

Figure 7.2. Photograph of the River Usk Crossing

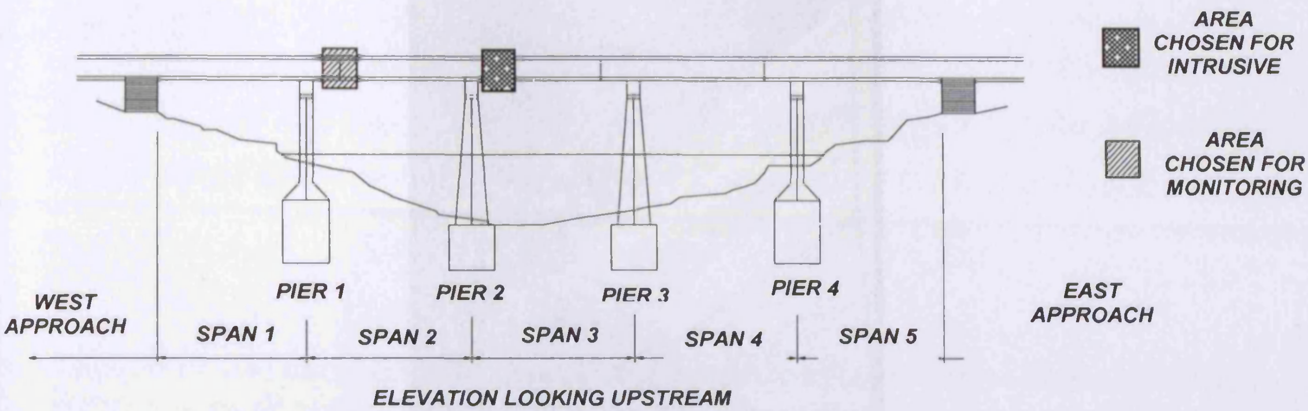

Figure 7.3. Position of the hinge joint on the structure (Pullin *et. al.* 2003)

Fig. 7.2 displays a photograph of the actual crossing. The hinge joint chosen for monitoring was immediately to the east of pier one as shown in Fig. 7.3 and the main area of concern was fatigue cracking of the steel reinforcement bar due to possible corrosion. Prior to the investigation, the condition of the hinge joint was evaluated visually. From Fig. 7.4 it can be seen that there was concern about the condition of the hinge joint due to the external appearance. Fig. 7.5 also shows signs that there may be waterproofing failure of the joint.

Figure 7.4. External appearance of hinge joint

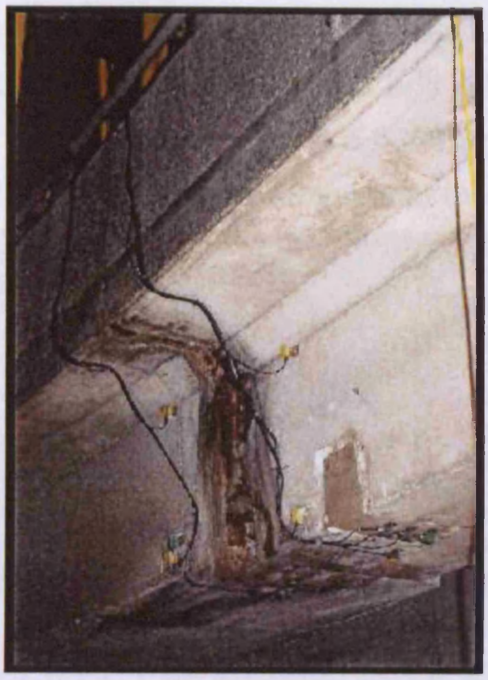

Figure 7.5. Sensor attachment and external signs of waterproof failure

To monitor the condition of the reinforcement within the hinge joint, sensors were attached to both the reinforcement and the concrete cover. Six sensors were attached to three sets of steel reinforcement bars using wave-guides. M5 nuts were welded to the reinforcement bar; threaded studding was screwed into the nut and cropped to finish flush with the re-instated surface. A conical wave-guide was screwed on to the studding. A sensor was clamped to the top of the wave-guide. The sensors attached to the wave-guides had a resonant frequency of 150kHz. The wave-guides attached to the top of the joint can be seen in Fig. 7.6. Sensors were also attached to the concrete surface of the joint using clamps as described in chapter 4. These sensors had a resonant frequency of 30kHz, the same as the concrete sensors attached to the laboratory-based specimens in chapter 6. The location of these sensors can be seen in Fig. 7.5 and Fig. 7.7. Following installation, the mounted sensitivity of each sensor was checked using an Hsu-Nielsen source (pencil lead fracture), and recorded. The sensitivity of the sensors was checked periodically using the automatic sensor test (AST) function in the AE system. During the monitoring of the structure, actual AE waveforms were recorded at specific times for short periods.

Hsu-Nielsen source tests were conducted to investigate wave propagation characteristics; signal attenuation and location analysis through the hinge joint. The sensor configuration shown in Fig. 7.7 was used for one full day of monitoring (05.00 –20.00hrs) of the detail for active cracking and any other identifiable defects. A controlled load test was also undertaken using a 63080kg vehicle. The load vehicle started on the span west of the joint and reversed over the span east of the joint.

Figure 7.6. Photograph displaying the wave-guides attached to the reinforcement

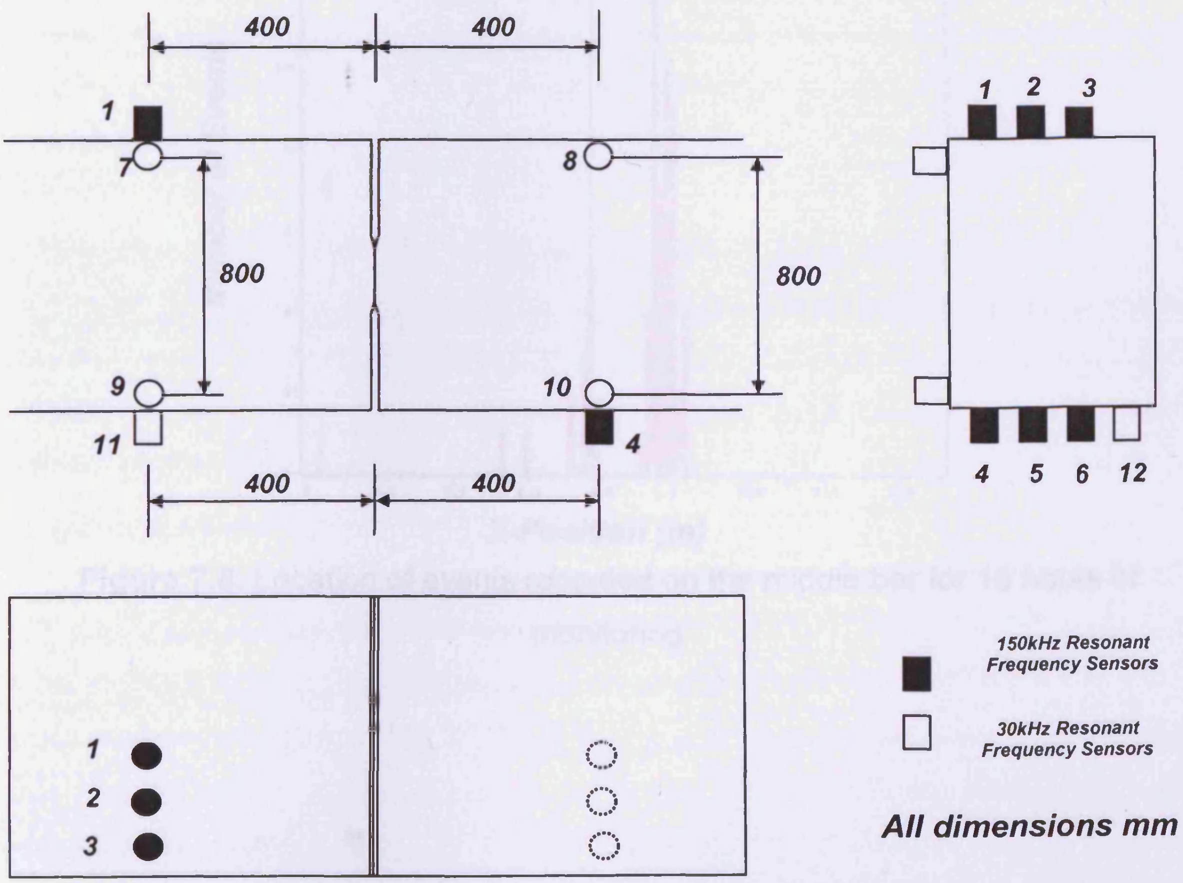

Figure 7.7. Schematic diagram of the hinge joint showing sensor positions

7.2.3. Results and Discussion

Chapter 6 assessed the ability of AE to detect and locate steel fatigue using AE sensors on laboratory-based specimens. It was shown that AE techniques could be used to detect and locate steel fatigue on sensors attached to both the steel and the concrete. Fig. 7.8 displays the location of events recorded on the steel sensors (channels 2 and 5) for the 15 hours of monitoring. During this time 63 events were recorded between the two channels where the amplitudes range between 45dB-60dB. Fig. 7.9 shows the absolute energies of the events located between channels 2 and 5. This pair located the most events over the 15-hour period.

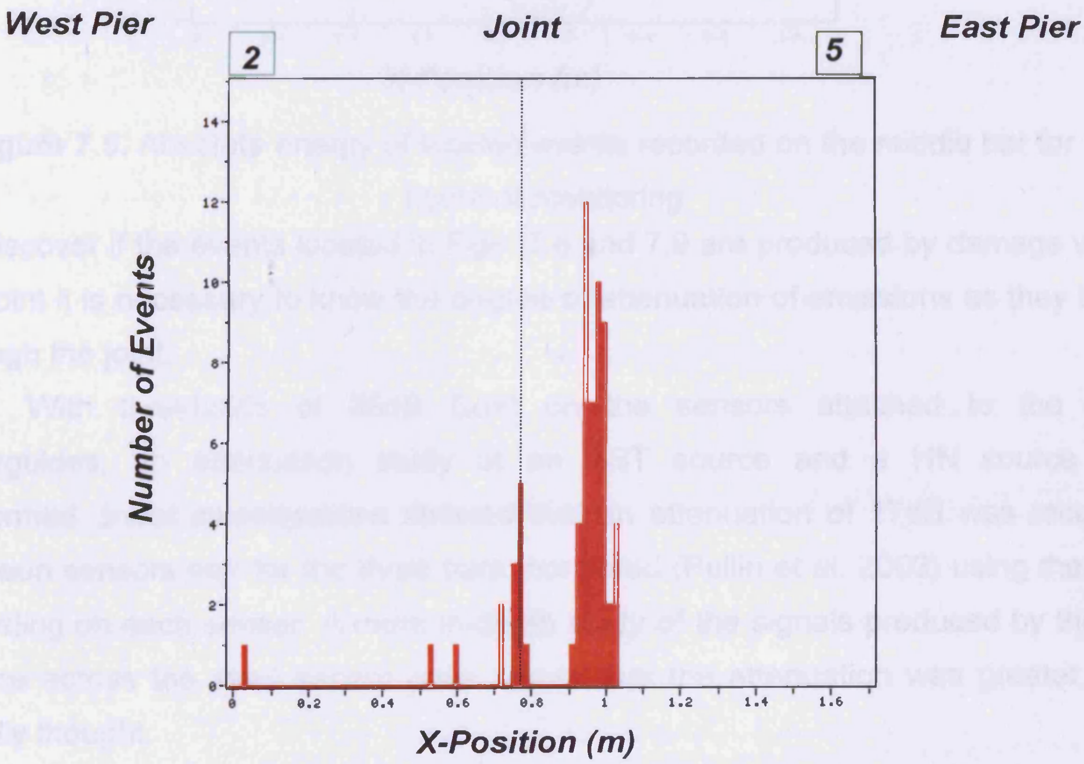

Figure 7.8. Location of events recorded on the middle bar for 15 hours of monitoring

that signals travel up the cone into the sensor and were not designed to transmit a signal the opposite way. This will affect the accuracy of the AST attenuation study. Also, the response recorded on the pulsed sensor does not reflect the condition between the sensor and the surface. This suggests that the signals produced by the AST are not suitable for an attenuation study of the structure.

A further attenuation study was performed applying an HN source at designated places on the structure. If the attenuation of the HN source between the pair of sensors attached to the reinforcement is too high then it cannot be assumed that any damage of the reinforcement during monitoring can be detected. In fact, the signal produced by the HN source at one sensor did not reach its opposite pair at the other side of the joint suggesting that the signal was highly attenuated across the joint. Since the threshold of each sensor was 35dB it can be assumed that the minimum a HN source attenuates between the sensors pairs is 65dB. Assuming that signals produced from defects within the joint attenuate in a similar manner to the HN source, the smallest signal that could be detected on the sensor pairs from the centre would be 67.5dB at source. Events located in Fig. 7.8 and 7.9 have amplitudes between 45dB – 60dB. Assuming that the minimum attenuation of an event is 65dB over the length of the steel rebar, these events could have had amplitudes over 90dB at the centre. These events are very large and could represent damage occurring within the joint assuming that signals from damage attenuate similarly to that of an HN source.

Many factors will affect the propagation of the signal produced by the HN source at the waveguide. As stated previously waveguides are designed such that signals travel from the tip of the cone to the sensor. This means a PLF on the waveguide may attenuate due to the nature of the waveguide. As well as this the attenuation of the HN source could be high due to the path over which it propagates. Since HN sources are primarily surface waves, the signal would be highly attenuated by the concrete encasement. Signals produced within the structure will travel mainly as bulk waves. This could affect the attenuation of the signal and thus the applicability of AE techniques to monitor the structure. This suggests that the attenuation of defects within the joint may attenuate differently to that of the HN source and thus may be detectable. Since an attenuation study of signals produced within the structure cannot be conducted, it is difficult to assess the integrity of the reinforcement within the joint from Figs. 7.8 and 7.9 alone.

Table 7.1 represents the amplitudes of emissions recorded for the attenuation study described in section 6.5 and includes amplitudes from signals recorded during fatigue. From this table the attenuation of a fatigue signal is found and related to the attenuation of a HN source.

Table 7.1. HN and fatigue signals recorded on "steel" sensors at the notch for the specimen failed in section 6.5

Channel	HN @ notch (dB)	Fatigue signal located between channels 1 and 2 (dB)	Fatigue signal located between channels 3 and 4 (dB)
1	60	43	-
2	90	73	-
3	53	-	38
4	95	-	77

It can be seen that an event detected at 73dB on channel 2 is detected at 43dB on channel 1. This is similar to the HN source where channel 2 recorded a 90dB reading compared with a 60dB reading on channel 1. This result from the laboratory-based test suggests that the attenuation of a fatigue crack is similar to that of a HN source.

Applying this result to events located during the 15hrs of monitoring of the hinge joint suggests that damage may be occurring within the joint. For the results in table 7.1 the HN source was applied at the notch where failure was expected. In the case of the hinge joint, the attenuation study was conducted by applying an HN source at each sensor and not at the centre of the joint. The path of the HN source at the sensor will be different to that of an HN source at the centre of the joint so it cannot be assumed that a signal produced from damage within the joint attenuates in a similar manner to that of an HN source applied at the waveguide.

Six 30kHz resonant frequency sensors were attached to the concrete with the aim of detecting and locating damage within the joint. An attenuation study of signals produced from a HN source was performed. Fig. 7.10 presents the loss in amplitude between channels 7, 8, 9, and 10, for PLF's at channels 7 and 9 and the loss in amplitude between channels 9, 10, 11 and 12 for PLF s at channels 9 and 11. The direction of the amplitude loss can be seen by the colour of the arrows where red arrows represent the attenuation loss of a PLF at channel 7, a turquoise arrow represents the attenuation loss from a PLF at channel 9 and a black arrow describes the attenuation from a PLF at channel 11. These values describe the attenuation of surface waves between the sensors.

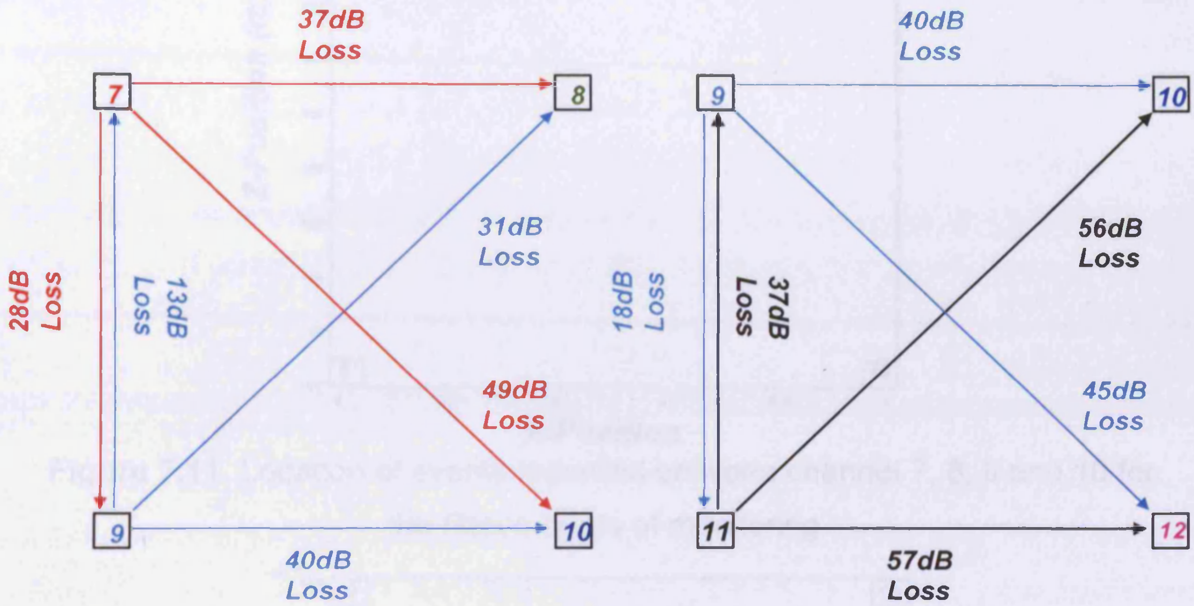

Figure 7.10. Attenuation study of the 30kHz resonant frequency sensors attached to the concrete surface of the hinge joint

From an analysis of these plots it is concluded that the concrete attenuates the signal produced by a HN source by approximately 40dB per metre, the same as found in section 6.5, depending on the orientation of the sensor. Sensors attached to the waveguides have spacing of approximately 1.7m. If the HN source is purely a surface wave propagating along the rebar-concrete interface then it would not be a surprise that the source attenuates over the sensor spacing.

Sections 6.5 and 6.6 have shown that steel fatigue can be detected and even located on sensors attached to the concrete encasement. In fact, it was shown that steel fatigue of rebar loaded in flexure with a notch set outside the concrete encasement (6.5) could be detected over 800mm from the notch on both 30kHz resonant frequency sensors and 60kHz resonant frequency sensors attached to the concrete encasement. Given the attenuation study displayed in Fig. 7.10, sensors attached to the concrete as described previously could be expected to detect damage.

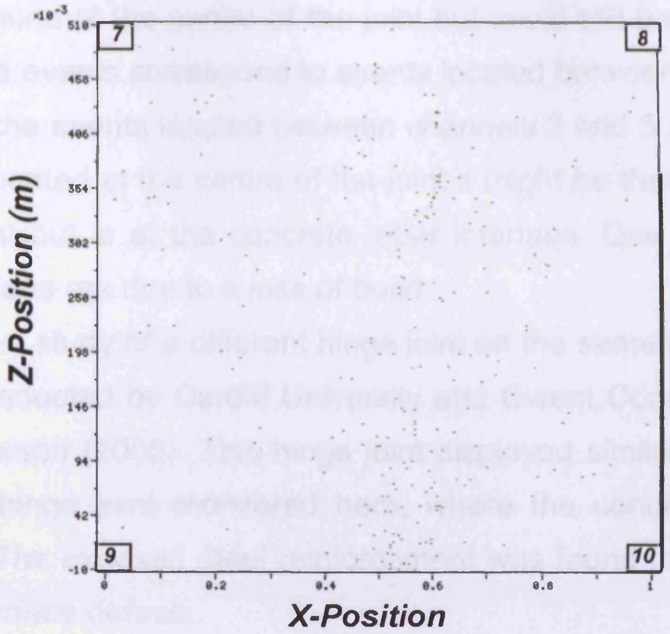

Figure 7.11. Location of events recorded between channel 7, 8, 9 and 10 for the fifteen hours of monitoring

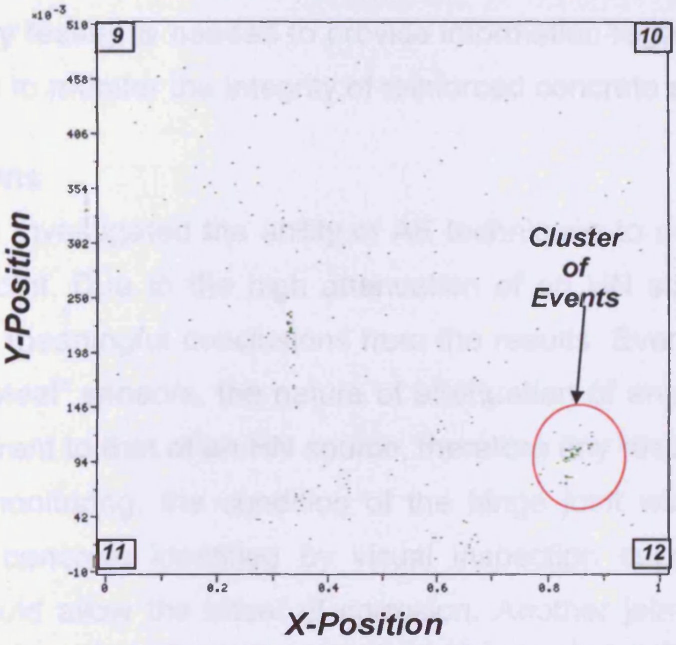

Figure 7.12. Location of events recorded between channel 9,10, 11 and 12 for the fifteen hours of monitoring

The location of events recorded for the fifteen hours of monitoring (0500-2000hrs) on the concrete sensors can be seen in Fig. 7.11 and Fig. 7.12. In Fig. 7.11, which describes the location of events between channels 7-10, a small number of events were observed with no clustering occurring. This is not the case for Fig. 7.12 (events located between channels 9-12) where a cluster of events can be seen. These events are not found at the centre of the joint but could still be due to damage. The locations of these events correspond to events located between channels 2 and 5 on the steel. Since the events located between channels 2 and 5 and channels 9,10,11 and 12 are not located at the centre of the joint it might be that the damage is not in the reinforcement but is at the concrete-rebar interface. One explanation could be that these emissions are due to a loss of bond.

An intrusive study of a different hinge joint on the same structure (as shown in Fig. 7.3) was conducted by Cardiff University and Gwent Consultancy and reported by Lark and Mawson (2003). This hinge joint displayed similar amounts of external damage to the hinge joint monitored here, where the concrete was stained and heavily spalled. The exposed steel reinforcement was found to be in good condition with negligible surface defects.

Since intrusive methods do not allow the condition of the bond to be examined it is difficult to validate the emissions recorded on the "concrete" and "steel" sensors. Further laboratory testing is needed to provide information regarding the applicability of AE techniques to monitor the integrity of reinforced concrete structures.

7.2.4. Conclusions

This chapter has investigated the ability of AE techniques to detect defects within a concrete hinge joint. Due to the high attenuation of an HN source it has not been possible to draw meaningful conclusions from the results. Even though events were located on the "steel" sensors, the nature of attenuation of any damage is unknown and may be different to that of an HN source, therefore any results are inconclusive.

Prior to monitoring, the condition of the hinge joint was unknown. External damage to the concrete identified by visual inspection suggested waterproofing failure, which could allow the onset of corrosion. Another joint also located on the River Usk Crossing was inspected using intrusive methods. The external appearance of the joint, which was badly stained and heavily spalled, again suggested that internal corrosion might be expected. However, when exposed, all the hinge bars appeared to be in good condition with negligible surface defects.

An intrusive investigation of the hinge joint monitored using AE techniques was not performed, so even though data recorded on the concrete sensors indicates that the joint may contain damage due to loss of bond, the integrity of the steel reinforcement has not been confirmed since the attenuation of signals within the steel rebar is unknown.

To validate the use of AE for the detection of defects within a hinge joint it is recommended that the AE technique be tested against known levels of damage. Similar tests could be performed on other hinge joints where the amount of deterioration is known. Collecting a database of signals from hinge joints with different degrees of damage could provide a clearer understanding, leading to a viable technique for assessing the integrity of such joints. It is also recommended that a series of laboratory-based model tests of hinge joints with an increasing amount of damage be conducted.

CHAPTER 8. SUMMARY OF CONCLUSIONS AND RECOMMENDATIONS FOR FURTHER WORK

8.1. SUMMARY OF CONCLUSIONS

This thesis has examined the role of the acoustic emission technique in the monitoring of laboratory-based and in-service concrete specimens and structures. The aim of this research was to develop AE techniques for use in global and local structural monitoring of concrete damage, in order to provide a commercial tool for the non-destructive evaluation of concrete structures. Four key themes have been investigated; optimum sensor type and method of attachment, post-test analysis techniques suitable for concrete monitoring, detection and location of steel rebar fatigue and the use of AE methods to monitor the integrity of an in-service concrete hinge joint.

Throughout this thesis, the attenuation of AE signals from different failure mechanisms within concrete has proven to be the important factor in deciding the applicability of the technique. Initial investigations studied the signals recorded on a variety of sensors of different frequencies during the failure of concrete specimens in flexure. Over a sensor-source distance of 0.5 metres it was found that high resonant frequency sensors did not detect emissions at final failure. Similarly throughout this thesis it has been seen that sensors of a low resonant frequency do allow the detection of spurious background noises impeding the detection of damage. This was seen in chapter 6 where fatigue of a steel rebar could not easily be detected on the 30kHz resonant frequency sensors since secondary emissions impeded the detection of the fatigue crack. This suggests that the applicability of AE for the monitoring of concrete structures will depend on whether a sensor can be chosen such that the frequency range of the sensor is within the range of the signal emitted by defects but above the range of background noise. If higher frequency sensors are needed to eliminate the detection of background noise, then the distance between sensor pairs will need to be smaller. This is not always possible for the testing of in-service concrete structures.

Chapter 5 investigated the different analysis techniques used when monitoring concrete specimens. The majority of the testing was concerned with the post-test analysis technique MTA.

From the series of tests conducted looking at the use of MTA it has been suggested that the technique is only suitable when used in tandem with conventional parameter-based monitoring. The following statements describe the problems that were found when applying the technique to recorded waveforms.

- The determination of the initial arrival-times and amplitudes of an event was a long and tedious task.
- Since the P-wave amplitude and arrival time of each channel is needed to complete the analysis any error in determining the correct P-wave components can lead to inaccuracies in location and the crack kinematics.
- Determining the initial P-waves of an event for moment tensor analysis by visual methods can be highly subjective, as well as time consuming suggesting that MTA is not suitable for large amounts of data.

Results from these tests were sometimes found to be confusing and did not always correspond to the failure expected. From the laboratory test described in section 5.5 it was suspected that not all types of emission produced waveforms with clear and defined P-waves. This suggests that MTA may not be suitable for all types of testing and thus needs to be performed in conjunction with the conventional parameter-based technique.

Chapter 6 evaluated the use of AE for the detection of steel fatigue even though the defect maybe within a concrete encasement. Fatigue cracks were produced in steel rebar loaded dynamically in flexure and in tension.

Prior to loading an HN source was applied at designated places on each of the specimens to evaluate how much attenuation would affect the ability to detect fatigue. It was found that sensors of 150kHz resonant frequency attached to plain rebar attenuated signals by approximately 10dB per metre compared with 40dB per metre when the rebar was encased in concrete. This means that to detect and locate AE from fatigue damage low thresholds are needed with sensor pairs in close proximity to each other. Due to background noise this level may not always be low enough to be able to locate and detect emissions throughout the entire duration of the defect.

Even though the signals were highly attenuated when the rebar was encased in concrete, it was shown that AE sensors attached to the steel rebar could detect and locate steel fatigue. It was also shown that sensors attached to the concrete could detect a change in AE during the expected duration of steel fatigue. In fact, for the specimen loaded in tension where the discontinuity was located within the concrete mounted sensor array, it was found that steel fatigue could be located. This is an important result suggesting that if the correct sensors are placed close to a source within a concrete structure then damage maybe detected and located. Thus to be able to monitor steel fatigue in reinforcement encased in concrete the distance between sensor pairs must be carefully chosen. The sensor spacing will depend on the accessibility of the steel reinforcement and the depth of the concrete covering.

Following these results the integrity of a reinforced concrete hinge joint (M4 River Usk Crossing, South Wales) was assessed using AE techniques. Prior to monitoring, the condition of the hinge joint was unknown. External damage to the concrete identified by visual inspection suggested waterproofing failure, which could allow the onset of corrosion.

The location of events located on sensors attached to the steel rebar and the concrete sensors during the fifteen hours of monitoring showed that some damage might have occurred within the structure. These events were not found at the centre of the joint but could be due to damage at the concrete-rebar interface, better known as loss of bond.

Prior to monitoring, an HN source was applied at several designated places on both the steel reinforcement and the concrete covering. Due to the distance between sensor pairs and the thresholds used, it was not possible to detect a HN source over the length of the joint. On the concrete covering it was found that the HN source attenuated by approximately 40dB per metre, similar to previous results. This suggested that the concrete covering would heavily attenuate any AE produced within the structure. Even though there has been a suggestion that damage may be occurring within the joint, since the nature of attenuation of any signal due to damage is unknown and may be different to that of a HN source, the results were inconclusive.

8.2. RECOMMENDATIONS FOR FURTHER WORK

In light of the conclusions of this work, the following topics are recommended for further study:

- A detailed investigation into the optimum set-up for the monitoring of reinforced concrete structures. This investigation will need to consider the lowest possible thresholds, optimum sensor spacing and resonant frequency to enhance the applicability of AE for the monitoring of concrete structures.
- A larger programme of laboratory fatigue studies to collect a database of signals to aid in the evaluation of fatigue cracks from real bridge structures. The programme should include a study of the effects of corrosion where corrosion is used in varying degrees to create a discontinuity within the specimen and the effect of different loading arrangements.
- Further investigation into the applicability of AE techniques for the monitoring of concrete hinge joints where the degree of damage within the joint is known. A database of signals from hinge joints with different degrees of damage could provide a clearer understanding, leading to a viable technique for assessing the integrity of such joint.
- A laboratory-based investigation of full size models of hinge joints with varying degrees of damage monitored using AE techniques.
- Studies into the characteristics of bond loss emission from the concrete/steel rebar interface to allow the difference between steel fatigue and bond loss within a reinforced concrete structure to be identified.
- A further investigation into the use of MTA and its applicability for the monitoring of in-service concrete structures.
- Development of an automated software package that could improve the accuracy and the time consuming determination of the initial P-wave amplitude and arrival time.

CHAPTER 9. REFERENCES

ASTM E1106-86, 1992, "Standard Method for Primary Calibration of AE Sensors"

ASTM E1823-96, 1996, "Standard Terminology Relating to Fatigue and Fracture Testing"

ASTM E976-84, 2001, "Standard Guide for Determining the Reproducibility of AE Sensor Response"

Beattie, A.G., 1983, "AE, principles and instrumentation", Journal of AE, Vol. 2, pp 95-128

Beck P., Bradshaw T. P., Lark R. J. and Holford K. M., 2003a, "A Quantitative Study of the Relationship Between Concrete Crack Parameters and Acoustic Emission Energy Released During Failure", Key Engineering Materials 4, volumes 245-246, pp 461-466

Beck P., Lark R. J. and Holford K. M., 2003b, "Moment Tensor Analysis of Acoustic Emission in Concrete Specimens Failed in Four-Point Bending", Key Engineering Materials 4, volumes 245-246, pp 443-450

Brindley, B.J., Holt, J., Palmer, I.G., 1973, "AE 3: The use of ring-down counting", Non-destructive Testing,

Broek, D., 1988, "The practical use of fracture mechanics", ISBN 0-7923-0223-0,

Carter, D.C., 2000, "AE techniques for the structural integrity monitoring of steel bridges", Ph.D.,

Castro-Montero, A., Shah, S.P. and Miller, R.A., 1990, Journal of Eng. Mech. 116, pp 2463-84

Clark, D., McCann, D. and Forde, M., 2001, "Infra-Red Thermographic Survey of a Railway Tunnel", Structural Faults and Repair, 9th International Conference and Exhibition, London, UK,

Cole, P.T., 1988, "AE, The Capabilities and Limitations of NDT", Part 7, A British Institute of Non-Destructive Testing Publication

Colombo, S., Forde, M.C., Das, P.C. and Halliday, J., 2001, "AE experiments on concrete beams: general overview and research in progress on bridges", 9^{th} International Structural Faults and Repairs Conference, 9th International Conference and Exhibition London, UK

Cullington, D.W., MacNeil, D., Paulson, P. and Elliot, J., 2001, "Continuous Acoustic Monitoring of Grouted Post-Tensioned Concrete Bridges", NDT&E International, Vol. 34, pp 95-105

Drouillard, T.F., 1986, "AE literature – Concrete", Journal of AE, Vol. 5, No.2, pp 103-109

Drouillard, T.F., 1996, "A history of AE", Journal of AE, Vol. 14, No. 1, pp 1-34

Dukes, R., and Culpan, E.A., 1984, "AE: its techniques and applications", IEE Proceedings, Vol. 131, Pt. A, No. 4, pp 241-251

Francois, D., 1984, " Fracture and damage mechanics of concrete", Application of Fracture Mechanics to cementious Composites

Frangopol, D.M., and Kong, J.S., 2001, "Bridge management based on reliability states and whole life costing: from theory to implementation", Structural Faults and Repairs Conference, 9th International Conference and Exhibition London, UK

Gordon, M.O., Hardy, M.S.A., and Giannopoulos, A., 2001, "Semi-intrusive determination of ground penetrating radar wave velocity", NDT&E International, Vol. 34, pp 163-171

Idrissi, H. and Limam, A., 2003, "Study and characterisation by Acoustic Emission and Electrochemical Measurements of Concrete Deterioration Caused by Reinforcement Steel Corrosion", NDT&E International 36, pp 563-569

Halmshaw, R., 1991, "Non-Destructive Testing", 2nd edition, Edward Arnold, pp.274

Hanstead, P.D., 1998, "Capabilities and Limitations of NDT", AE Part 7, The British Institute of Non-Destructive Testing, Chartwell Press Ltd, pp.7

Henkel, D.P., and Wood, J.D., 1991, "Monitoring concrete reinforced with bonded surface plates by the AE method" NDT&E International, Vol. 24

Higo, Y., and Inaba, H., 1991, "The general problems of AE sensors." AE: Current Practice and Future Directions, ASTM STP 1077, W. Sachse, J. Roget, and K. Yamaguch, American Society for Testing and materials, Philadelphia

Holford, K.M., 1987, "The Non-Destructive Testing of Wire Rope by Acoustic Emission", Ph.D. Thesis, University College, Cardiff

Hsu, N.N., and Breckenridge, F.R., 1981, "Characterisation and calibration of AE sensors", Materials Evaluation, 39

Huston, D., Fuhr, P., Kajenski, P., and Snyder, D., 1992, "Concrete beam testing with optical fibre sensors", Non-destructive Testing of Concrete

Jenq, Y.S. and Shah, S.P., 1988, "Mixed-Mode fracture of concrete", International Journal of Fracture 38, pp 123-142

Karihaloo, B.L., 1995, "Fracture mechanics and structural concrete", Harlow, Essex, England, Longman Scientific & Technical New York: Wiley

Knopoff, L., and Randall, M.J., 1970, "The compensated linear-vector dipole: a possible mechanism for deep earthquakes", Journal of Geophysical Research, Vol. 75, No. 26, pp 4957-4963

Kwon, O, Y. and Lee, K., 2000, "Acoustic Emission for the Detection of Fatigue Damage", Acoustic Emission - Beyond the Millennium, Tokyo, Elsevier, pp 93-108

Landis, E., Ouyang, C., and Shah, S., 1991, "Automated Determination of First P-wave Arrival and Acoustic Emission Source Location", Journal of Acoustic Emission, 10 1-2, pp 97-103

Landis, E.N., and Baillon, L., 2002, "Experiment to relate acoustic emission energy to fracture energy of concrete", Journal of Engineering Mechanics, pp 698-702

Lark R.L., and Mawson, B.R., 2003, "A Study of the Behaviour of Concrete "Thrust" Hinges", Proceedings of the 3rd International Conference on Current and Future Trends in Bridge Design, Construction and Maintenance, Shanghai, China,

Lenain, J.C., 1981, "General principles of AE", Materials Evaluation, 39

Leung, C.K.Y., 2001, "Fibre-optic sensors in concrete: the future?", NDT&E International 34, pp 85-94

Li, Z. and Shah, S., 1994, "Localization of Microcracking in Concrete under Uniaxial Tension", ACI Materials Journal, Vol. 91, No. 4, pp 372-381

Li, Z., Yuyama, S., Ohsawa, I., Kimpara, I., Kageyama, K., and Yamaguchi, K., 1998a, "Fracture Mechanics Study of Concrete Beams Reinforced with FRP Sheets by a Moment Tensor Analysis of Acoustic Emission", Fracture Mechanics of Concrete Structures, Proceedings FRAMCOS-3, AEDIFICATIO Publishers, D-79104, Germany, pp1863-1872

Li, Z., Li, F. Zdunek, A., Landis, E. and Shah, S.P., 1998b, "Application of Acoustic Emission Technique to Detection of Reinforcing Steel Corrosion in Concrete", ACI Materials Journal, Vol. 95, No. 1, pp 68-76

Li, Z. Li, F. Li, X, S. and Yang, W., 2000, "P-Wave Arrival Determination and AE Characterisation of Concrete", Journal of Engineering Mechanics, pp 194- 200

Lundgren, K. and Gylltoft, K., 1999, "Bond modelling in three-dimensional finite element analyses", Doktorsavhandlingar Chalmers Tekniska Hogskola, No. 1549, pp 1-22

Maierhofer, C. and Leipold, S., 2001, "Radar investigation of masonry structures", NDT&E International, Vol. 34, pp 139-147

Maji, A., and Shah, S.P., 1988, "Process zone and AE measurements in concrete", Experimental Mechanics, pp 27-33

Manthei, G., Eisenblatter, J., and Dahm, T., 2001, "Moment tensor evaluation of AE sources in salt rock", Construction and Building Materials 15, pp 297-309

Martin, J., Broughton, K.J., Giannopoulos, A., Hardy, M.S.A. and Forde, M.C., 2001, "Ultrasonic tomography of grouted post-tensioned RC bridge beams", NDT&E International 34, pp 107-113

McCann, D.M. and Forde, M.C., 2001, "Review of NDT methods in the assessment of concrete and masonry structures", NDT&E International 34, pp 71-84

Mehta, P.K. and Monteiro, P.J.M., 1993, "In Concrete, Structure, Properties, and Materials", Second ed., pp 36-41

Miller, R.K. and McIntire, P., 1987, "Non-destructive Testing Handbook", second edition, Vol. 5, American Society for Non-destructive Testing

Minemura, O., Sakata, N., Yuyama, S., Okamoto, T. and Maruyama, K., 1998, "Acoustic emission evaluation of an arch dam during construction cooling and grouting" Construction and Building Materials, 12, pp 385-392

Mouring, E., Barton, O. and Simmons, D., 2001, "External Retrofit of Reinforced Concrete Beams using Carbon Fiber Reinforced Polymer Laminates", Structural Faults and Repair, 2001, 9th International Conference and Exhibition, London, UK,

Murakami, I., Yuyama, S., Shimizu, S., Kouyama, H. and Matsushima, M., 1993, "Deformation behaviour and AE characteristics for anchorage pulling tests on the foundations of power transmission pylons (Part 2, Moment tensor analysis)" Proceedings of the 9th National AE Conference (JSNDI), pp 143-150

Munwam, M., and Ohstu, M., 1999, "Stress intensity factors in concrete by moment tensor analysis of AE", Materials and Evaluation, pp 1178-1182

Muravin, G.B., Lezvinskaya, L.M., and Ship, V.V., 1993, "AE and fracture criteria", Russian journal of Non-destructive Testing, Vol. 29, No. 8, pp 5-16

Neville, A.M., 1999, "Properties of Concrete", fourth Edition, Longman, pp 1-2

Nielsen, A., 1980, "AE based pencil lead breaking", Danish Welding Institute, report 80-15,

Ohtsu, M., and Ono, K., 1984, "A generalised theory of AE and Green's functions in a half space", Journal of AE, Vol. 3 No. 1, pp 27-40

Ohtsu, M., 1987, "AE characteristics in concrete and diagnostic applications", Journal of AE, Vol.6, No.2, pp. 99-108

Ohtsu, M., and Ono, K., 1988, " AE source location and orientation determination of tensile cracks from surface observation", NDT International, Vol. 21, No 3, pp 143-150

Ohtsu, M., 1989a, "A review of AE in civil engineering with emphasis on concrete", Journal of AE, Vol. 8, No. 4, pp 93-98

Ohtsu, M., 1989b, "Source Kinematics of AE Based on a Moment Tensor", NDT International, Vol. 22, No.1, pp 14-20

Ohtsu, M., 1991, "Simplified moment tensor analysis and unified decomposition of AE source: application to in-situ Hydrofracturing test", Journal of Geographical Research, Vol. 96, No. B4, pp 6211-6221,

Ohtsu, M., and Sakata, Y., 1992, "Non-destructive crack identification by AE analysis and Ultrasonic frequency response", Non-destructive Testing of Concrete Elements and Structures, pp 171-181

Ohtsu, M. Arao, K. and Yuyama, S., 1994, "Post-analysis of SiGMA Solutions for Error in RC Members", PROGRESS in ACOUSTIC EMISSION VII. The Japanese Society for NDI, pp

Ohtsu, M., 1996, "The history and development of AE in concrete engineering", Magazine of Concrete Research, Vol. 48, No. 177, pp 321-330

Ohtsu, M. Okamoto, T. and Yuyama, S., 1998a, "Moment Tensor Analysis of Acoustic Emission for Cracking Mechanisms in Concrete", ACI Structural Journal, pp 87-95

Ohtsu, M. Shigeishi, M. Munwam, M, C., 1998b, "Damage Mechanics and Fracture mechanic of Concrete By SiGMA", PROGRESS in ACOUSTIC EMISSION IX,

Ohtsu, M., 2000, "Moment Tensor Analysis and SiGMA Code", Acoustic Emission - Beyond the Millennium, Tokyo, Elsevier, pp 19-34

Ohtsu, M., and Watanabe, H., 2001, "Quantitative damage estimation of concrete by AE", Construction and Building Materials 15, pp 217-224

Ohtsu, M., Uchida, M., Okamoto, T. and Yuyama, S., 2002, "Damage Assessment of Reinforced Concrete Beams Qualified by Acoustic Emission", ACI Structural Journal, pp 411-417

Pao, Y.H., 1978, "Theory of AE", Elastic Waves and NDT of Materials, Vol. 29, pp 107-126

Physical Acoustics Corporation, 1995, "MISTRAS 2001 Users Manual", Princeton New Jersey, USA

Physical Acoustics Corporation, 2001, "DiSP 2001 Users Manual", Princeton New Jersey, USA

Pollock, A., 1986, "Classical wave theory in practical AE testing", Progress in AE iii, Proceedings of the 8th International AE Symposium, Japanese Society for Non-destructive Inspection, Tokyo, pp 215-239

Pullin, R., 2001, "Structural Integrity Monitoring of Steel Bridges Using Acoustic Emission Techniques", Ph.D. Thesis, University College, Cardiff,

Pullin, R., Holford, K. M., Lark, R. J. and Beck, P., 2003, "Acoustic Emission Assessment of Concrete Hinge Joints", Key Engineering Materials 4, volumes 245-246, pp 323-330

Raj, B., and Jha, B.B., 1994, "Fundamentals of AE", British Journal of NDT, Vol. 36, No 1, pp 16-23

Rindorf, H.J., 1981, "Acoustic Emission Source Location in Theory and in Practice", Brüel & Kjær Technical Review, No 2., ISSN 0007-2621, pp 3-44

Sadri, A., 2001, "Application of Impact-Echo Technique in Diagnoses and Repair of Stone Masonry Structures", Structural Faults and Repair, 2001, 9th International Conference and Exhibition London, UK,

Sansalone, M ., 1997, "Impact-echo: The complete story", ACI Structural Journal, V.94, No 6, pp 777-785

Scott, M., Rezaizadeh, A., Delahaza, A., Santos, C.G., Moore, M., Graybeal, B. and Washer, G., 2003, "A Comparison of Nondestructive Evaluation Methods for Bridges Deck Assessment", NDT&E International, 36, pp 245-255

Scruby, C.B., 1985a, "Quantitative AE techniques", Non-destructive Testing, Vol. 8, pp 141-210

Scruby, C.B., 1985b, "AE measurement using point-contact transducers", Journal of AE, Vol. 4, No. 1, pp 9-18

Scruby, C.B., Stacey, K.A. and Baldwin, G.R., 1986, "Defect characterisation in 3D by AE", Harwell, AERE R 12040

Shah, S.P. and Ouyang, C., 1993, "Toughening mechanisms in quasi-brittle materials", Journal of Engineering Materials and Technology

Shah, S.P. and Ouyang, C., 1994, "Fracture mechanics for failure of concrete", Annu. Rev. Mater. Sci. 24, pp 293-320

Shah, S.P. and Choi, S., 1999, "Non-destructive techniques for studying fracture processes in concrete", International Journal of Fracture 98, pp 351-359

Shigeishi, M., and Ohtsu, M., 1999, "Identification of AE Sources by Using SiGMA-2D Moment Tensor Analysis", AE: Standards and Technology Update, ASTM STP 1353, S.J. Vahaviolos, Ed., American Society for Testing and Materials, West Conshohken, PA

Shigeishi, M., and Ohtsu, M., 2001, "AE moment tensor analysis: development for crack identification in concrete materials", Construction and Building Materials 15, pp 311-319.

Shiotani, T., Shigeishi, M., and Ohtsu, M., 1999, "AE characteristics of concrete piles", Construction and Building Materials 13, pp 73-85

Smith, W.F., 1996, "Principles of Materials Science and Engineering", McGraw-Hill, pp 278-320

Spanner, J.C., 1974, "Acoustic Emission, Techniques and Applications", Intex Publishing Company, Illinois

Suaris, W. and Van Mier, J.G.M., 1995, "AE Source Characterisation in Concrete Under Biaxial Loading", Materials and Structure, Vol. 28, pp 444-449

Swindlehurst, W., 1973, "AE 1", A series on acoustic emission, Non-destructive Testing, pp 152-158

Titman, D.J., 2001, "Applications of thermography in Non-destructive testing of structures", NDT&E International, Vol. 34, pp 149-154

Ueda, T., Ohtsu, M., Shigeishi, M. and Yuyama, S., 1991, "AE waveform analysis for rock mass in grout injection of dam", Proceedings of the 4th World Meeting on AE (ASNT), pp 223-229

Wadley, H.N.G., Scruby, C.B., and Speake, J.H., 1980, "AE for physical examination of metals", International Metals Review, No. 2, pp 41-64

Watson, J.R., Holford, K.M., Davies, A.W. and Cole P.T., 2000, "BOXMAP- Non-Invasive detection of cracks in steel box girders", University of Surreys 4th International Bridge Management Conference, Guildford, Surrey, pp 80-87

Wilson, C. B., 1995, "Assessment of the Reinforced Concrete Hinges on Five M6 Over-Bridges in Staffordshire", Proceedings Institution Civil Engineers, Vol. 110, pp 4-10

Yoon, D.J., Weiss, W. Prine, D.W., and Shah, S., 1999, "Assessing Corrosion Damage in Reinforced Concrete Beams Using Acoustic Emission", SPIE Conference on Nondestructive Evaluation of Bridges and Highways III, California, pp 254-263

Yoon, D.J., Jung, J.C., Park, P. and Lee, S.S., 2000, "AE Characteristics for Monitoring Fatigue Crack in Steel Bridge Members", Nondestructive Evaluation of Highways, Utilities, and Pipelines IV, Proceedings of SPIE, Vol. 3995, pp 153-162

Yuyama, S., Okamoto, T., Shigeishi, M., Ohtsu, M., 1995a, "Cracking process evaluation in reinforced concrete by moment tensor analysis of AE", Journal of AE, Vol. 13, numbers 1-2, pp 14-20

Yuyama, S. Okamoto, T. Shigeishi, M. and Ohtsu, M., 1995b, "Quantitative Evaluation and Visualisation of Cracking process in Reinforced Concrete by a Moment Tensor Analysis of Acoustic Emission", Materials Evaluation, Vol. 53, No 6, pp 751- 756

Yuyama, S., Okamoto, T. Shigeishi, M., Ohtsu, M. and Kishi, T., 1999a, "A Proposed Standard for Evaluating Structural Integrity of Reinforced Concrete Beams by Acoustic Emission", Acoustic Emission: Standards and Technology Update, ASTM STP 1353, pp 25 – 40

Yuyama, S., Li, Z., Yoshihiro, I., Arazoe, M., 1999b, "Quantitative analysis of fracture process in RC column foundation by moment tensor analysis of AE", Construction and Building materials, Vol. 13, pp 87-97

Yuyama, S. and Ohtsu, M., 2000, "Acoustic Emission Evaluation in concrete", Acoustic Emission - Beyond the Millennium, Tokyo, Elsevier, pp 187-214

Yuyama, S., Li, Z., Yoshizawa, M., Tomokiyo, T., Uomoto, T., 2001, "Evaluation of fatigue damage in reinforced concrete slab by AE", NDT&E International, Vol 34, pp 381-387

Zhang, D., and Wu, K., 1999, "Fracture process zone of notched three-point bending concrete beams", Cement and Concrete Research, Vol. 29, pp 1887-1892

APPENDIX A

(SENSOR CALIBRATION CERTIFICATES)

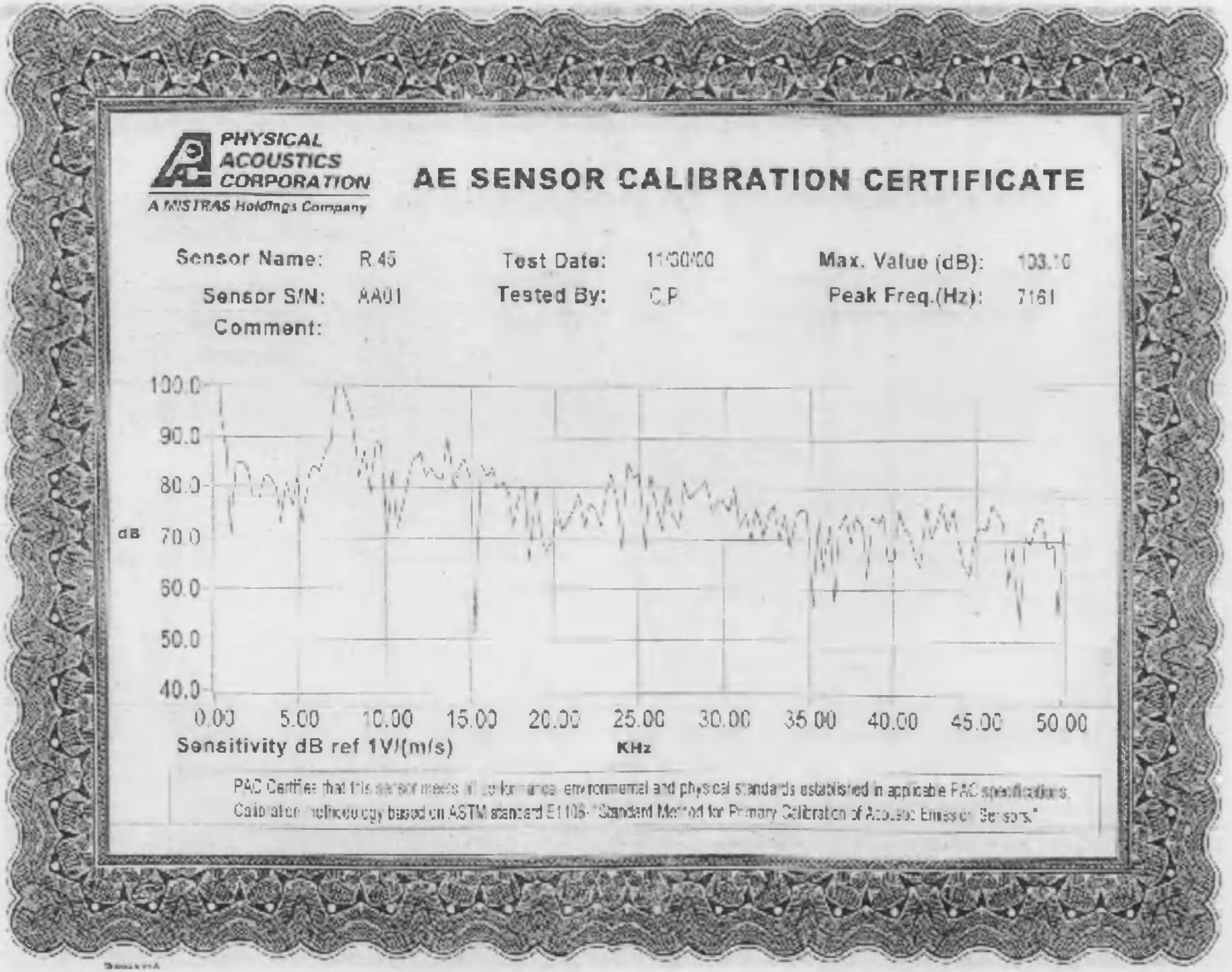

Figure A.1. AE sensor calibration certificate for R0.45

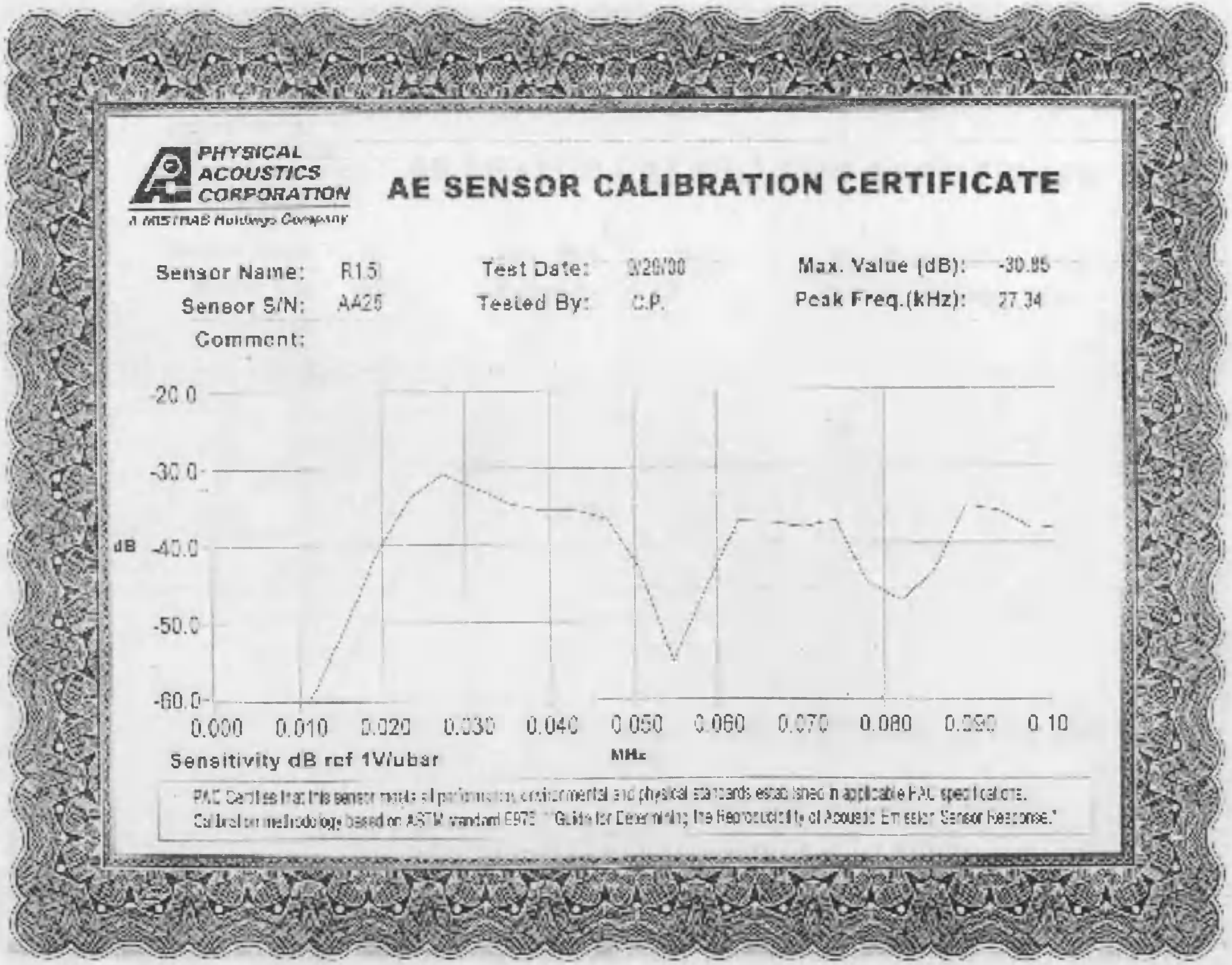

Figure A.2. AE sensor calibration certificate for R1.5I

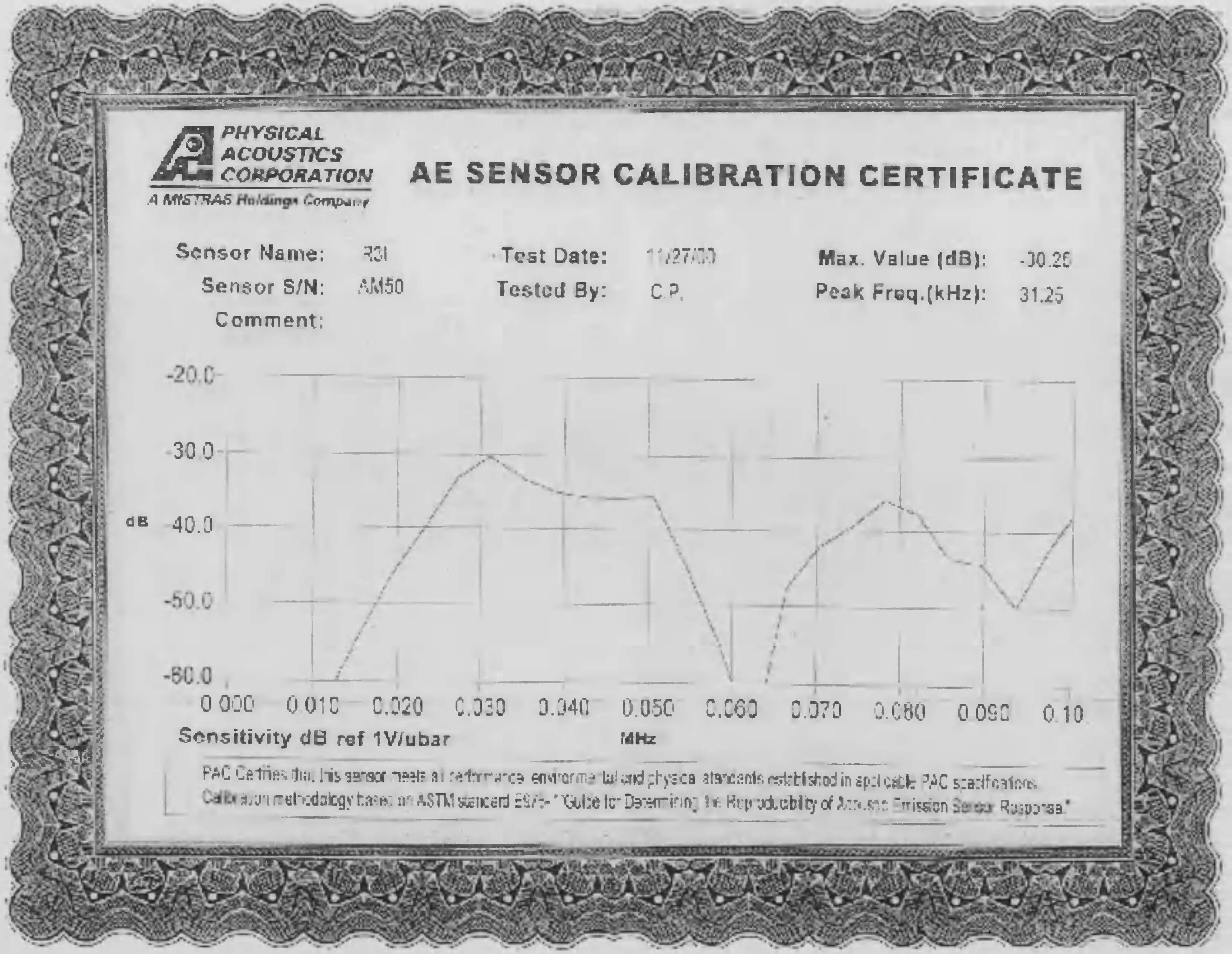

Figure A.3. AE sensor calibration certificate for R3I

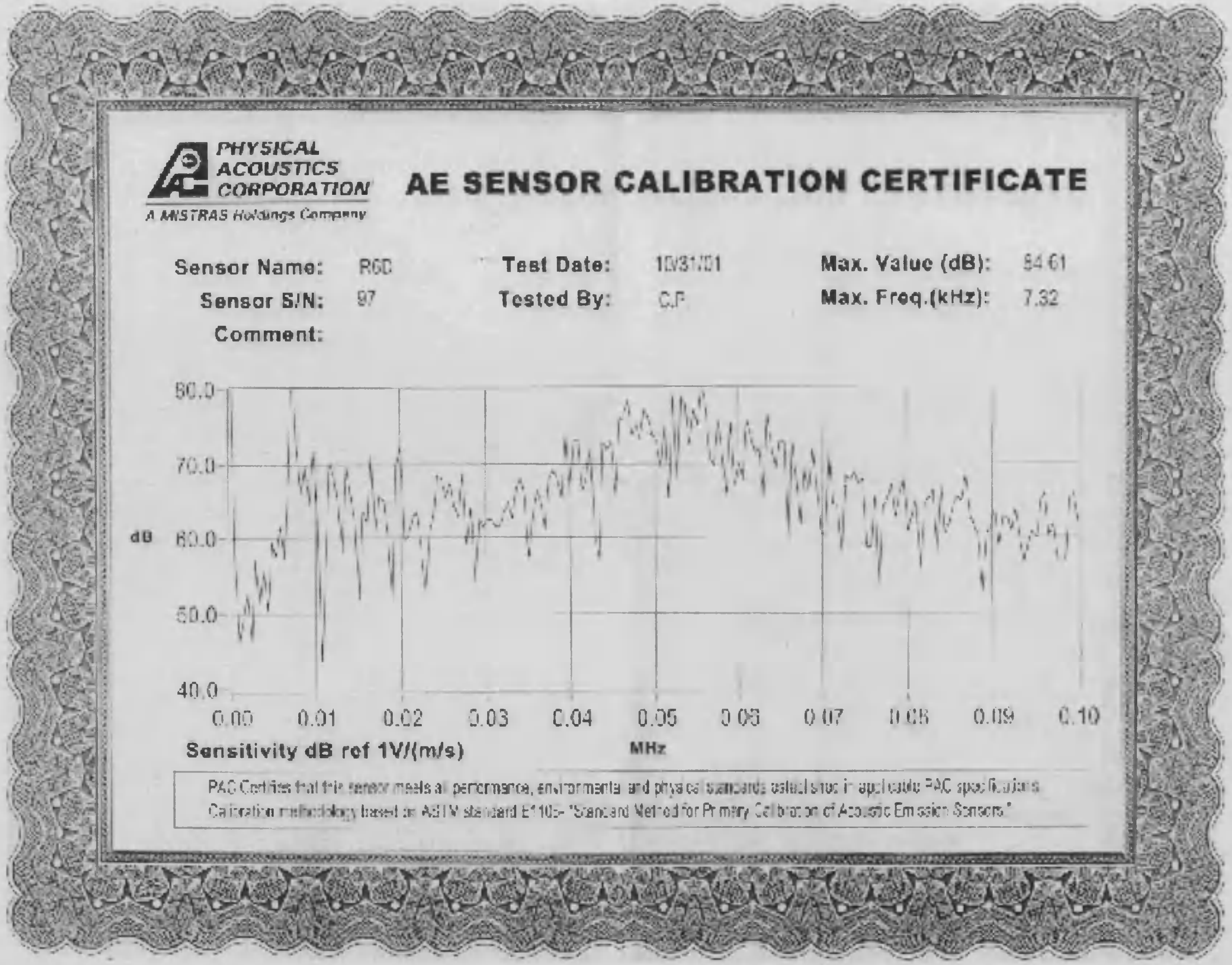

Figure A.4. AE sensor calibration certificate for R6D

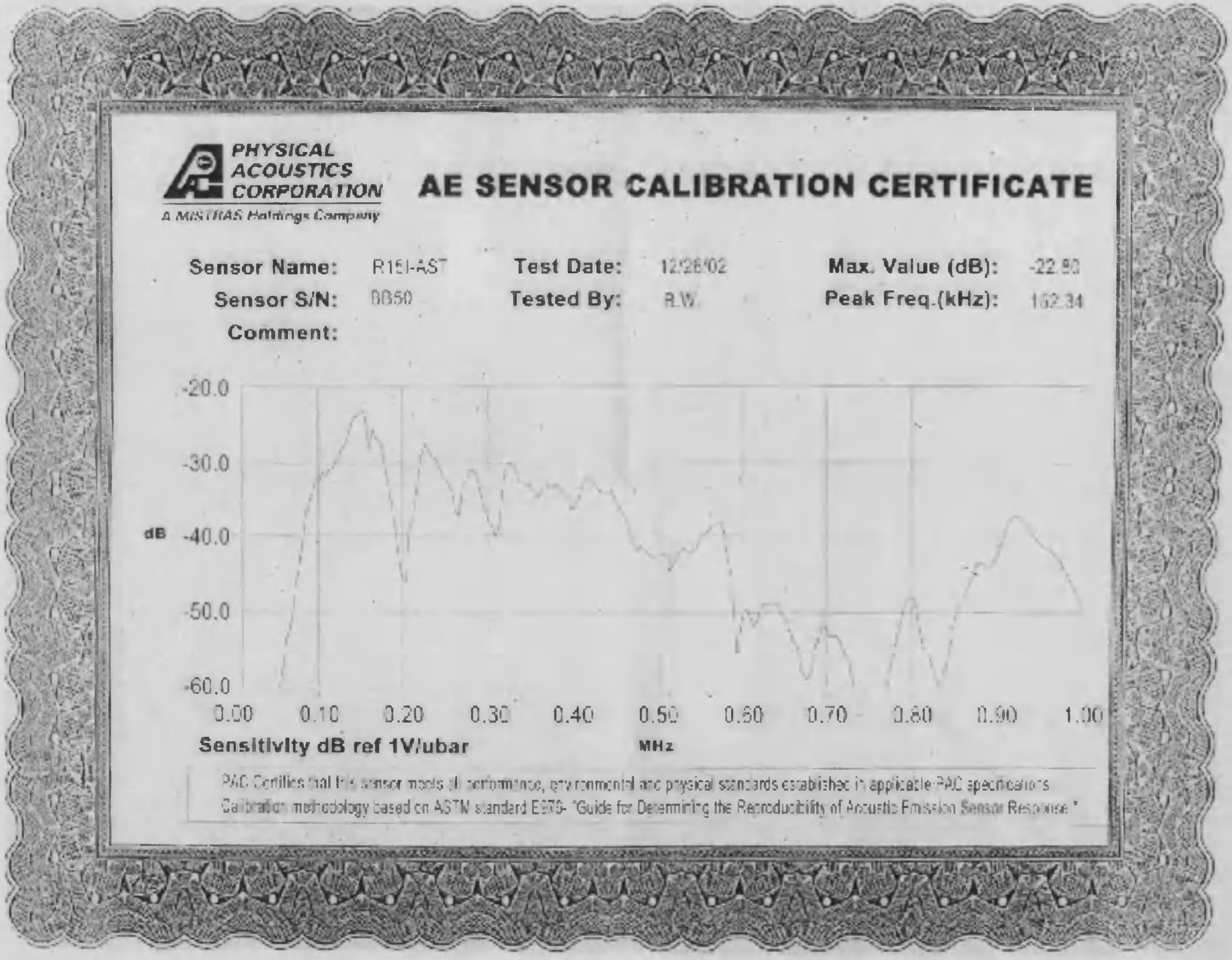
PHYSICAL ACOUSTICS CORPORATION
A MISTRAS Holdings Company

AE SENSOR CALIBRATION CERTIFICATE

Sensor Name: R15I-AST
Test Date: 12/26/02
Max. Value (dB): -22.80
Sensor S/N: 8850
Tested By: R.W.
Peak Freq.(kHz): 152.34
Comment:

PAC Certifies that this sensor meets all performance, environmental and physical standards established in applicable PAC specifications. Calibration methodology based on ASTM standard E976- "Guide for Determining the Reproducibility of Acoustic Emission Sensor Response."

Figure A.5. AE sensor calibration certificate for R15I-AST

PHYSICAL ACOUSTICS CORPORATION
A MISTRAS Holdings Company

AE SENSOR CALIBRATION CERTIFICATE

Sensor Name:	WDI-AST	**Test Date:**	1/27/03	**Max. Value (dB):**	-23.19
Sensor S/N:	AB03	**Tested By:**	N.M.	**Peak Freq.(kHz):**	550.78
Comment:					

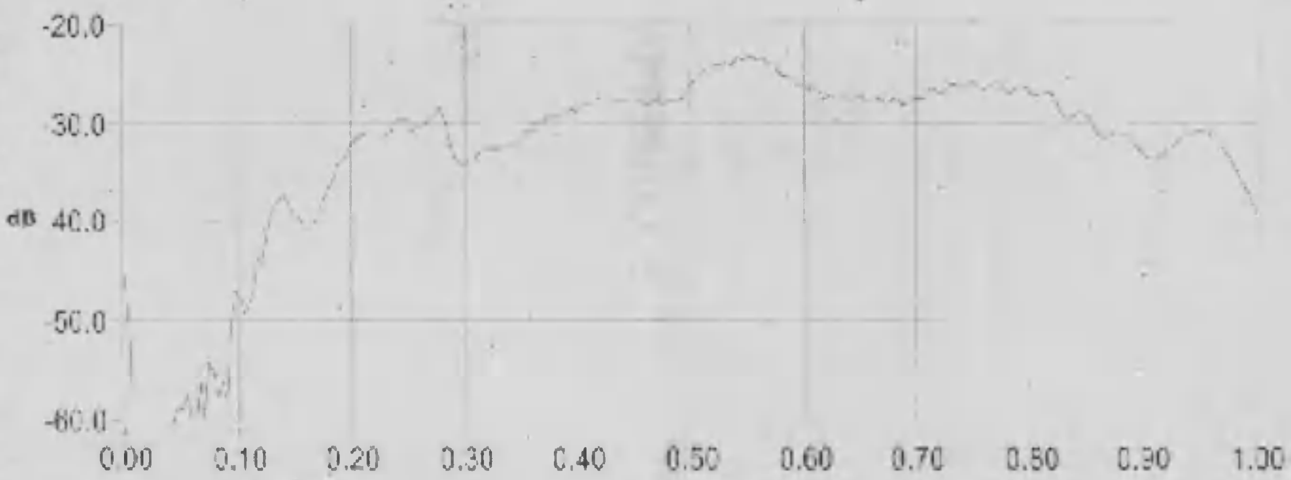

Sensitivity dB ref 1V/ubar

PAC Certifies that this sensor meets all performance, environmental and physical standards established in applicable PAC specifications. Calibration methodology based on ASTM standard E976- "Guide for Determining the Reproducibility of Acoustic Emission Sensor Response."

Figure A.6. AE sensor calibration certificate for WDI-AST

APPENDIX B

Table B.1. Hardware set-up for sensors in section 4.3.

Channel	Threshold	Pre-Amp Gain (dB)	Filter		Sample Rate	PDT (μs)	HDT (μs)	HLT (μs)
			Low (kHz)	High (kHz)				
1	40	40	10	200	10MSPS	1000	2000	400
2	40	40	10	200	10MSPS	1000	2000	400
3	40	40	10	200	10MSPS	1000	2000	400
4	40	40	10	200	10MSPS	1000	2000	400
5	40	40	10	400	5MSPS	400	800	400
6	40	40	100	400	5MSPS	400	800	400

Table B.2. Hardware set-up for sensors in section 4.4.

Channel	Threshold	Pre-Amp Gain (dB)	Filter		Sample Rate	PDT (μs)	HDT (μs)	HLT (μs)
			Low (kHz)	High (kHz)				
1	40	40	10	200	10MSPS	1000	2000	400
2	40	40	10	200	10MSPS	1000	2000	400
3	40	40	10	200	10MSPS	1000	2000	400

Table B.3. Hardware set-up for the specimen failed in section 5.4.

Channel	Sample Rate (kSPS)	Filter		Threshold (dB)	Pre-Trigger (μs)	Hit Length (k)	HLT (μs)
		Low (kHz)	High (kHz)				
1	500	10	200	60	-1000	4	100
2	500	10	200	60	-1000	4	100
3	500	10	200	60	-1000	4	100
4	500	10	200	60	-1000	4	100
5	500	10	200	60	-1000	4	100
6	500	10	200	60	-1000	4	100

Table B.4. Hardware set-up for the specimen failed in section 5.5.

Channel	Sample Rate (kSPS)	Filter		Threshold (dB)	Pre-Trigger (μs)	Hit Length (k)	HLT (μs)
		Low (kHz)	High (kHz)				
1	1000	10	200	65	-1000	30	100
2	1000	10	200	65	-1000	30	100
3	1000	10	200	65	-1000	30	100
4	1000	10	200	65	-1000	30	100
5	1000	10	200	65	-1000	30	100
6	1000	10	200	65	-1000	30	100

Table B.5. Hardware set-up for the 30kHZ resonant frequency sensors attached to the specimen failed in section 5.6.

Channel	Sample Rate (kSPS)	Filter		Threshold (dB)	Pre-Trigger (μs)	Hit Length (k)	HLT (μs)
		Low (kHz)	High (kHz)				
1	1000	10	200	65	-1000	30	100
2	1000	10	200	65	-1000	30	100
3	1000	10	200	65	-1000	30	100
4	1000	10	200	65	-1000	30	100
5	1000	10	200	65	-1000	30	100
6	1000	10	200	65	-1000	30	100

Table B.6. Hardware Set-up for the 60kHz resonant frequency sensors attached to the specimen failed in section 5.6

Channel	Threshold	Pre-Amp Gain (dB)	Filter		Sample Rate	PDT (μs)	HDT (μs)	HLT (μs)
			Low (kHz)	High (kHz)				
1	35	40	100	400	5MSPS	400	800	400
2	35	40	100	400	5MSPS	400	800	400
3	45	40	10	200	1000kSPS	1000	2000	400
4	45	40	10	200	1000kSPS	1000	2000	400
5	45	40	10	200	1000kSPS	1000	2000	400
6	45	40	10	200	1000kSPS	1000	2000	400

Table B.7. Hardware set-up for the specimen failed in section 6.3.

Channel	Threshold	Pre-Amp Gain (dB)	Filter Low (kHz)	Filter High (kHz)	Sample Rate	PDT (μs)	HDT (μs)	HLT (μs)
1	45	40	10	2000	10MSPS	400	800	400
2	45	40	10	2000	10MSPS	400	800	400
3	45	40	10	2000	10MSPS	400	800	400
4	45	40	10	2000	10MSPS	400	800	400

Table B.8. Hardware set-up for the specimen failed in section 6.4.

Channel	Threshold	Pre-Amp Gain (dB)	Filter Low (kHz)	Filter High (kHz)	Sample Rate	PDT (μs)	HDT (μs)	HLT (μs)
1	43	40	10	2000	10MSPS	400	800	400
2	43	40	10	2000	10MSPS	400	800	400

Table B.9. Hardware set-up for the specimen failed in section 6.5.

Channel	Threshold	Pre-Amp Gain (dB)	Filter Low (kHz)	Filter High (kHz)	Sample Rate	PDT (μs)	HDT (μs)	HLT (μs)
1	32	40	100	400	5MSPS	400	800	400
2	32	40	100	400	5MSPS	400	800	400
3	32	40	100	400	5MSPS	400	800	400
4	32	40	100	400	5MSPS	400	800	400
5	35	40	10	200	1000kSPS	1000	2000	400
6	35	40	10	200	1000kSPS	1000	2000	400
7	35	40	10	200	1000kSPS	1000	2000	400
8	35	40	10	200	1000kSPS	1000	2000	400
9	35	40	10	200	1000kSPS	1000	2000	400
10	35	40	10	200	1000kSPS	1000	2000	400
11	35	40	10	200	1000kSPS	1000	2000	400
12	35	40	10	200	1000kSPS	1000	2000	400
13	35	40	10	200	1000kSPS	1000	2000	400
14	35	40	10	200	1000kSPS	1000	2000	400
15	35	40	10	200	1000kSPS	1000	2000	400
16	35	40	10	200	1000kSPS	1000	2000	400

Table B.10. Hardware set-up for the specimen failed in section 6.6.

Channel	Threshold	Pre-Amp Gain (dB)	Filter Low (kHz)	Filter High (kHz)	Sample Rate	PDT (μs)	HDT (μs)	HLT (μs)
1	35	40	100	400	5MSPS	400	800	400
2	35	40	100	400	5MSPS	400	800	400
3	45	40	10	200	1000kSPS	1000	2000	400
4	45	40	10	200	1000kSPS	1000	2000	400
5	45	40	10	200	1000kSPS	1000	2000	400
6	45	40	10	200	1000kSPS	1000	2000	400

APPENDIX C
(Location and Crack Kinematics from the Push-out Test in Chapter 5)

Table C.1. The location, the shear percentage, the orientation of the motion and the normal of all events processed by the SiGMA procedure.

LOAD NUMBER	EVENT NUMBER	LOCATION			SHEAR	MOTION			NORMAL		
		X	Y	Z	%	X	Y	Z	X	Y	Z
1	21	**204**	**158**	**313**	43	-0.567	-0.775	-0.279	0.445	-0.386	-0.808
1	25	**208**	**91**	**363**	31	-0.443	-0.858	-0.259	0.494	-0.575	-0.652
2	1	**232**	**191**	**326**	90	-0.079	0.978	-0.195	-0.967	0.016	0.253
2	7	**180**	**146**	**262**	91	-0.030	0.961	-0.276	-0.902	0.073	0.425
2	15	**243**	**123**	**343**	33	-0.429	-0.892	-0.140	0.384	-0.527	-0.758
2	33	**201**	**188**	**267**	45	-0.377	0.919	-0.115	-0.980	0.148	0.130
2	35	**205**	**113**	**343**	37	-0.457	-0.886	-0.084	0.384	-0.542	-0.748
3	6	**167**	**201**	**280**	86	-0.690	-0.723	-0.026	0.501	-0.013	-0.865
3	7	**187**	**154**	**270**	85	-0.055	0.957	-0.283	-0.907	0.072	0.415
3	11	**179**	**153**	**249**	94	-0.012	0.968	-0.249	-0.918	0.047	0.394
3	38	**185**	**172**	**273**	72	-0.141	0.966	-0.216	-0.911	0.090	0.402
3	41	**190**	**172**	**266**	74	-0.113	0.968	-0.225	-0.925	0.095	0.368
3	42	**182**	**151**	**246**	80	-0.082	0.959	-0.272	-0.919	0.092	0.383
4	7	**179**	**175**	**263**	75	-0.135	0.959	-0.251	-0.914	0.090	0.395
4	11	**186**	**142**	**339**	51	-0.435	0.896	-0.090	0.448	-0.344	-0.825
4	12	**200**	**156**	**266**	85	-0.060	0.964	-0.260	-0.952	0.068	0.299
4	13	**179**	**176**	**285**	92	-0.009	0.968	-0.250	0.854	0.064	0.516
4	17	**182**	**149**	**263**	97	-0.550	-0.832	-0.072	0.724	-0.220	-0.654
4	29	**189**	**184**	**293**	81	-0.116	0.969	-0.218	0.918	0.051	0.393
4	45	**188**	**154**	**330**	66	-0.410	-0.911	-0.045	0.564	-0.257	-0.785
4	56	**183**	**158**	**275**	94	-0.007	0.960	-0.281	-0.888	0.054	0.456
4	58	**193**	**155**	**317**	71	-0.455	-0.890	-0.039	0.591	-0.241	-0.770
4	61	**180**	**146**	**253**	93	-0.011	0.960	-0.280	-0.910	0.064	0.409
4	66	**191**	**161**	**272**	95	-0.002	0.973	-0.231	-0.918	0.049	0.394
4	67	**177**	**194**	**335**	75	-0.257	0.911	-0.322	-0.816	0.073	0.573
4	71	**186**	**178**	**276**	31	-0.506	0.846	-0.170	0.953	0.203	0.224
4	72	**184**	**147**	**258**	89	-0.045	0.957	-0.287	-0.920	0.068	0.387
5	16	**211**	**137**	**361**	23	-0.437	-0.850	-0.292	0.311	-0.574	-0.758
5	29	**186**	**178**	**345**	42	-0.402	-0.897	-0.186	0.374	-0.323	-0.869
5	34	**160**	**142**	**258**	85	-0.059	0.956	-0.287	-0.866	0.103	0.490
6	38	**176**	**179**	**277**	53	-0.518	-0.848	-0.110	0.495	-0.325	-0.806
6	39	**173**	**155**	**335**	52	-0.558	-0.808	-0.186	0.451	-0.412	-0.792
6	52	**188**	**233**	**316**	53	-0.355	0.898	-0.261	-0.818	0.140	0.558
7	11	**230**	**270**	**761**	74	-0.071	0.912	-0.403	0.861	-0.035	-0.507
8	8	**199**	**159**	**333**	67	-0.379	-0.925	-0.019	0.567	-0.225	-0.792
8	12	**190**	**195**	**313**	78	-0.122	0.967	-0.222	-0.886	0.084	0.455
9	8	**184**	**139**	**207**	77	-0.105	0.961	-0.254	-0.956	0.084	0.280
10	11	**187**	**217**	**324**	59	-0.285	0.936	-0.206	-0.896	0.093	0.435
10	31	**206**	**185**	**163**	43	-0.359	0.933	-0.023	-0.991	0.092	0.096
11	8	**179**	**147**	**233**	81	-0.087	0.966	-0.245	-0.938	0.080	0.336
11	13	**186**	**133**	**235**	81	-0.089	0.954	-0.286	-0.943	0.088	0.320
12	1	**166**	**138**	**294**	50	-0.482	-0.863	-0.150	0.565	-0.369	-0.738
12	6	**181**	**174**	**290**	74	-0.486	-0.872	-0.059	0.663	-0.264	-0.701
13	5	**197**	**166**	**229**	87	-0.022	0.980	-0.199	-0.962	0.036	0.271
13	9	**163**	**137**	**235**	88	-0.098	0.955	-0.282	-0.923	0.054	0.380
13	20	**174**	**143**	**306**	55	-0.499	-0.864	-0.057	0.498	-0.407	-0.766
13	24	**187**	**159**	**284**	89	-0.037	0.965	-0.258	-0.897	0.067	0.436
14	36	**171**	**149**	**247**	84	-0.061	0.965	-0.256	-0.911	0.087	0.403
14	44	**200**	**146**	**349**	30	-0.430	-0.877	-0.214	0.355	-0.496	-0.793
14	66	**172**	**146**	**244**	95	-0.001	0.960	-0.281	-0.901	0.066	0.428
14	67	**162**	**163**	**233**	89	-0.060	0.976	-0.211	-0.918	0.048	0.393
14	70	**198**	**148**	**330**	75	-0.392	-0.920	-0.015	0.646	-0.221	-0.731
14	71	**170**	**135**	**268**	82	-0.106	0.946	-0.307	-0.894	0.111	0.435
2	12	**186**	**177**	**285**	99	0.001	0.978	-0.211	-0.894	0.031	0.446
2	27	**208**	**180**	**254**	13	0.954	-0.300	-0.002	0.623	-0.780	0.060
3	3	**204**	**149**	**347**	91	0.069	0.948	-0.310	0.743	0.110	0.660
3	8	**183**	**154**	**328**	75	0.098	0.951	-0.293	0.829	0.009	-0.559
3	12	**153**	**115**	**215**	100	0.179	0.952	-0.247	-0.848	0.119	0.517
3	43	**162**	**149**	**261**	58	0.373	0.926	-0.067	0.824	0.053	-0.565
4	5	**246**	**218**	**236**	99	1.000	0.002	-0.013	0.003	0.996	-0.085
4	14	**242**	**114**	**273**	100	0.997	-0.002	-0.073	0.008	-0.939	0.344
4	15	**199**	**162**	**223**	50	0.984	-0.112	-0.137	0.354	-0.919	0.171
4	19	**203**	**172**	**350**	99	0.035	0.948	-0.317	-0.750	0.057	0.659
4	55	**208**	**213**	**318**	69	0.177	0.929	-0.325	0.902	-0.049	-0.429
5	9	**341**	**117**	**91**	54	0.683	-0.645	-0.342	-0.421	-0.449	-0.789
5	18	**280**	**189**	**776**	74	0.294	-0.956	-0.019	-0.129	-0.025	0.991
7	1	**244**	**272**	**789**	99	1.000	-0.006	-0.020	-0.021	0.992	-0.126

7	8	**248**	**216**	**557**	91	0.999	-0.041	-0.005	0.041	-0.923	0.384
7	9	**189**	**151**	**354**	67	0.486	-0.873	-0.033	0.417	-0.188	-0.889
13	6	**163**	**169**	**225**	68	0.037	0.944	-0.328	-0.908	0.088	0.410
14	34	**204**	**145**	**192**	62	0.997	-0.054	-0.049	0.282	-0.943	0.175
14	64	**137**	**176**	**289**	95	0.009	0.977	-0.211	-0.764	0.073	0.641
1	22	**184**	**138**	**318**	92	-0.383	-0.919	0.095	0.650	-0.146	-0.746
2	25	**208**	**158**	**357**	12	-0.206	0.787	0.582	0.492	0.675	0.549
2	30	**181**	**140**	**313**	63	-0.346	-0.935	0.075	0.558	-0.316	-0.767
3	18	**272**	**213**	**854**	36	-0.345	0.907	0.241	-0.960	0.199	0.199
4	8	**191**	**172**	**265**	88	-0.041	0.973	0.227	-0.924	0.056	0.379
4	9	**186**	**136**	**312**	66	-0.365	-0.929	0.067	0.573	-0.299	-0.763
4	16	**203**	**137**	**280**	58	-0.185	-0.981	0.061	0.698	-0.230	-0.678
4	22	**180**	**140**	**289**	93	-0.343	-0.931	0.125	0.721	-0.129	-0.680
4	27	**178**	**152**	**292**	86	-0.375	-0.914	0.157	0.606	-0.153	-0.781
4	34	**176**	**143**	**345**	32	-0.375	0.560	0.739	0.572	0.775	0.267
4	49	**184**	**146**	**295**	94	-0.482	-0.876	0.015	0.675	-0.169	-0.718
4	50	**165**	**144**	**268**	78	-0.336	-0.939	0.069	0.679	-0.193	-0.708
4	64	**200**	**119**	**347**	43	-0.478	0.621	0.621	0.642	0.718	0.269
5	41	**257**	**200**	**832**	24	-0.125	0.190	0.974	0.476	-0.512	0.716
6	33	**150**	**140**	**234**	98	-0.387	-0.913	0.127	0.726	-0.193	-0.660
7	4	**169**	**180**	**224**	75	-0.573	-0.813	0.106	0.568	-0.178	-0.804
7	17	**152**	**172**	**162**	31	-0.276	0.681	0.678	0.425	0.859	-0.285
7	36	**260**	**203**	**203**	98	-0.007	0.965	0.261	1.000	-0.020	-0.011
8	18	**187**	**187**	**369**	26	-0.319	0.687	0.653	0.611	0.608	0.508
9	3	**256**	**204**	**805**	32	-0.314	0.894	0.319	-0.947	0.179	0.267
9	22	**171**	**125**	**295**	46	-0.488	0.546	0.680	0.656	0.732	0.183
9	28	**167**	**156**	**313**	73	-0.482	-0.873	0.066	0.512	-0.240	-0.825
10	15	**184**	**161**	**345**	27	-0.308	0.546	0.779	0.479	0.837	0.266
10	24	**258**	**173**	**786**	49	-0.191	0.841	0.506	0.977	0.135	0.163
11	4	**180**	**162**	**275**	94	-0.367	-0.928	0.065	0.734	-0.137	-0.665
12	18	**253**	**258**	**786**	80	-0.091	0.991	0.098	-0.994	0.052	0.095
13	1	**246**	**207**	**763**	98	-0.004	0.945	0.328	1.000	-0.012	0.015
13	17	**173**	**192**	**326**	33	-0.247	0.773	0.585	0.789	0.555	0.263
13	18	**193**	**166**	**314**	24	-0.223	0.790	0.571	0.672	0.688	0.275
14	39	**170**	**154**	**281**	91	-0.313	-0.942	0.125	0.707	-0.111	-0.699
14	58	**212**	**121**	**336**	97	-0.457	-0.880	0.127	0.680	-0.148	-0.718
1	11	**333**	**183**	**46**	71	0.978	0.084	0.189	0.131	0.972	-0.193
1	19	**181**	**196**	**311**	67	0.971	0.032	0.238	-0.218	0.947	0.236
2	26	**295**	**130**	**38**	89	0.993	0.034	0.112	0.039	0.978	-0.204
3	4	**194**	**169**	**234**	21	0.988	-0.152	0.024	0.644	-0.762	0.063
3	33	**198**	**133**	**357**	11	0.155	0.786	0.599	0.448	0.815	0.368
4	2	**258**	**193**	**760**	66	0.866	0.020	0.499	0.288	0.957	0.029
4	48	**167**	**86**	**319**	58	0.856	0.510	0.079	-0.488	0.873	-0.009
4	65	**85**	**181**	**172**	60	0.543	-0.565	0.621	0.194	-0.191	-0.962
4	69	**178**	**306**	**81**	5	0.572	0.820	0.003	0.874	0.486	-0.014
5	12	**203**	**144**	**350**	23	0.678	0.549	0.490	-0.186	0.909	0.373
5	14	**194**	**182**	**245**	18	0.958	-0.261	0.119	0.616	0.782	-0.093
5	15	**205**	**144**	**349**	21	0.623	0.590	0.513	-0.237	0.847	0.476
5	30	**207**	**170**	**364**	71	0.786	0.173	0.594	-0.424	0.854	0.302
5	56	**259**	**232**	**796**	11	0.245	0.233	0.941	0.135	-0.501	0.855
6	14	**249**	**212**	**623**	39	0.113	-0.353	0.929	0.884	0.095	0.457
6	53	**176**	**221**	**343**	10	0.066	0.582	0.810	0.545	0.762	0.350
6	57	**174**	**192**	**237**	8	0.154	0.926	0.345	0.719	0.666	0.197
7	41	**182**	**218**	**294**	9	0.130	0.836	0.533	0.736	0.635	0.234
7	43	**259**	**210**	**753**	38	0.912	0.203	0.358	0.357	0.905	0.231
9	25	**209**	**93**	**357**	56	0.867	0.406	0.290	-0.331	0.944	-0.018
10	1	**231**	**296**	**715**	26	0.875	0.484	0.020	0.328	0.913	-0.242
10	28	**252**	**199**	**794**	76	0.981	0.005	0.196	0.117	0.987	0.111
10	32	**259**	**226**	**838**	97	0.019	0.990	0.139	-1.000	0.007	0.017
12	4	**201**	**146**	**352**	55	0.801	0.373	0.469	-0.455	0.812	0.365
12	26	**286**	**232**	**887**	76	0.550	-0.258	0.794	-0.418	-0.895	-0.154
12	37	**185**	**152**	**356**	39	0.739	0.520	0.428	-0.359	0.866	0.348
14	25	**121**	**60**	**790**	25	0.391	-0.081	0.917	0.135	0.681	0.720
14	73	**172**	**155**	**344**	93	0.040	-0.922	0.386	0.598	-0.149	-0.787

Where:

Orange rows represent events with a negative x and z motion. ↙

Green rows represent events with a positive x motion but negative z motion. ↘

Pink rows represent events with a negative x motion but positive z motion. ↖

Blue rows represent events with a positive x and z motion. ↗

APPENDIX D

Key Engineering Materials Vols. 245-246 (2003) pp. 461-466
online at http://www.scientific.net

A Quantitative Study of the Relationship between Concrete Crack Parameters and Acoustic Emission Energy Released during Failure

P. Beck[a], T.P. Bradshaw, R.J. Lark and K.M. Holford

Cardiff School of Engineering, Division of Mechanical Engineering, Cardiff University
Queen's Building, The Parade, P.O. Box 925, Cardiff CF24 0YF, UK

[a]Beckp1@cf.ac.uk

Keywords: Acoustic Emission Energy, Concrete, Cracks

Abstract

Although acoustic emission (AE) techniques have been extensively studied in concrete engineering and been applied to monitoring structures in service, there has been very little research in relating AE parameters, such as energy, to physical properties such as crack area and crack depth. In this paper a study is performed using mortar specimens to investigate the relationship between AE energy and fracture area and depth.

A series of notched mortar specimens of known fracture area and depth, grouted into concrete beams, were loaded to produce instantaneous failure by a shear force. The waveforms created by the failure were monitored by AE sensors attached to the concrete beam.

Examination of the waveforms produced by a range of sensors with different frequency responses reveals that the fracture depth affects the AE energy detected during failure. No meaningful relationship between fracture area and AE energy was detected. These results can be used to aid the quantification of crack size based on energy release from concrete structures in the field.

Introduction

Recently it has been found that due to problems such as damage or deterioration by earthquakes, fatigue, long term environmental attack during service and ageing, there is a need to monitor concrete for structural purposes. A variety of inspection methods have been studied to provide early detection and warning of initial defects. As well as structural integrity there is a need for an inspection method that can provide useful information on concrete, such as the development of cementious materials and the study of fracture mechanics of concrete. A suitable technique, which has been used to provide information on these topics, is acoustic emission (AE). In fact AE techniques have been investigated in concrete for more than forty years [1]. Up until 1986 Drouillard [2] listed 76 papers referencing the work performed on concrete with AE.

In concrete engineering, AE has been used as both a technique to investigate the structural integrity of concrete structures and as an aid to study the material properties. AE monitoring has been applied in developing cement based materials. These materials include high alumina cement and asbestos cement [3]. AE monitoring has been used to study the freeze and thaw process. Ohtsu and Watanabe [4] studied the effect on cylindrical concrete specimens over 300 cycles using AE technology. AE measurements have been used to study micro and macrocrack propagation in concrete including fracture parameters and the fracture process zone. AE methods have been used to study reinforced concrete including the detection of cracking from the reinforcement and the concrete, delamination of the reinforcement and concrete, and to detect the corrosion of the reinforcement. Yuyama et al. [5] showed that AE can be used to study and compare the fatigue damage of an in-service and laboratory tested reinforced concrete (RC) slab. Henkel and Wood [6] monitored concrete reinforced with bonded surface plates using AE methods.

Although AE techniques have been extensively studied in concrete engineering and been applied to monitoring structures in service, there has been very little research in quantifying AE parameters, such as energy, to physical properties such as crack area and crack depth. Landis and Baillon [7] tried to relate AE energy to fracture energy by performing three-point bend tests on a mortar and concrete samples. It was found that for the mortar samples similar amounts of fracture energy and cumulative AE energy were produced each test. The concrete specimens made with larger aggregate did not produce regular results. The authors believe this is due to ultrasonic scattering causing signal attenuation.

In this paper a study is performed using mortar specimens to investigate the relationship between AE energy and fracture area and depth. A series of notched mortar specimens of known fracture area and depth, grouted into concrete beams, were loaded to produce instantaneous failure by a shear force. Previously at Cardiff University testing was performed on mortar specimens looking at the frequency recorded. It was revealed that crack areas of small depth produced high frequency signals and that crack areas with larger depths produced lower frequency signals. This suggests that the energy produced during failure be related to crack depth and not crack area.

Experimental Procedure

Specimen Details and Loading Method. The investigation studying the relationships between AE energy and fracture area and depth was applied to the practical AE waveforms recorded during the instantaneous failure of a notched mortar specimen of known fracture area and depth, grouted into concrete beams. The mix proportions of the concrete beams was arranged so that the mass ratios of the cement, fine aggregate, coarse aggregate and water were 1:1.8:2.8:0.5. The concrete specimens were of dimensions 100mm width, 150mm depth and 1000mm length. A large notch was cut into the concrete beam allowing the mortar specimens to be grouted in.

A total of 29 notched mortar specimens were created with mixture proportions of 1 part cement, 3 parts sand and 0.55 parts water. The specimens had dimensions of 20mm width, 50mm depth and a length of 150mm with the notch cut 50mm along the 150mm length as illustrated in Fig. 1. Each notch had different dimensions allowing for a change in fracture area and crack depth. Fifteen specimens were created with a constant crack depth but a varying crack area and fourteen specimens were created with a constant crack area but a varying crack depth. Table 1 shows the dimensions of all the notched areas.

The mortar specimens were grouted into the concrete beam and failed by an instantaneous force supplied by a kilogram weight dropped at a height of 1m from the specimen. Rubber was attached to both the specimen and the drop weight to prevent any crushing during testing. A diagram of the test set-up including the loading method can be seen in Fig. 1.

Table 1: Dimensions of the notched area of the mortar specimens a) initial testing using smaller depths and areas; b) secondary testing using larger fracture areas and depths

(a)

Notch Area (depth mm * width mm)	Area (mm^2)
25*8	200
25*12	300
25*16	400
25*20	500

Notch Area (depth mm * width mm)	Depth (mm)
10*20	10
20*10	20
25*8	25
40*5	40
50*4	50

(b)

Notch Area (depth mm * width mm)	Area (mm^2)
50*4	200
50*10	500
50*15	750
50*20	1000

Notch Area (depth mm * width mm)	Depth (mm)
10*50	10
25*20	25
50*10	50

Instrumentation. Three AE sensors were attached to the concrete beams to detect AE waveforms produced during the failure of the mortar specimens. The sensors had a resonant frequency of 7kHz, 30kHz and 60kHz and were pre-amplified by 40dB. A threshold of 50dB was used so that only large concrete cracks were monitored. AE waveforms detected at the sensors were recorded by a digital memory, which converted analogue records into digital records at a sampling rate of 1MHz. The frequency detection range employed was 10kHz-200kHz. The sensor positioning and location can also be seen in Fig. 1.

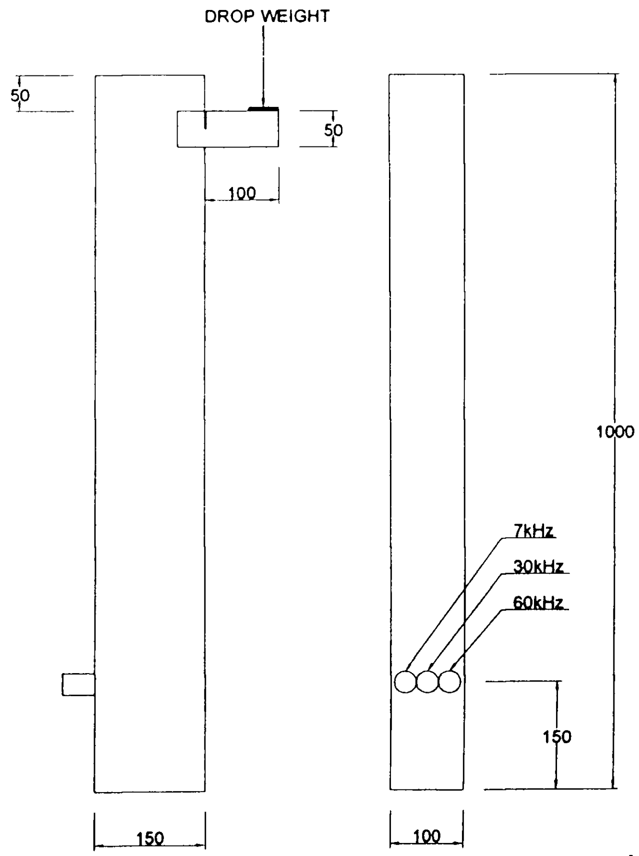

Figure 1: Illustration of mortar specimen grouted into concrete test with AE sensor location

Results and Discussion

When analysing the data it is important that the correct events are chosen. A waveform from a typical fracture is shown in Fig. 2 together with event based display. From this information the absolute energy recorded on each sensor during the fracture of the mortar specimen can be found. By highlighting a certain AE event all the parameters can be extracted. In this case the fracture is represented by the event with the largest amplitude as shown by the plot in the top left corner of Fig. 2. As well as amplitude versus time, the amount of energy recorded during the failure can be seen. Fig. 2 also shows the fast Fourier transform (FFT) of the waveform produced during failure.

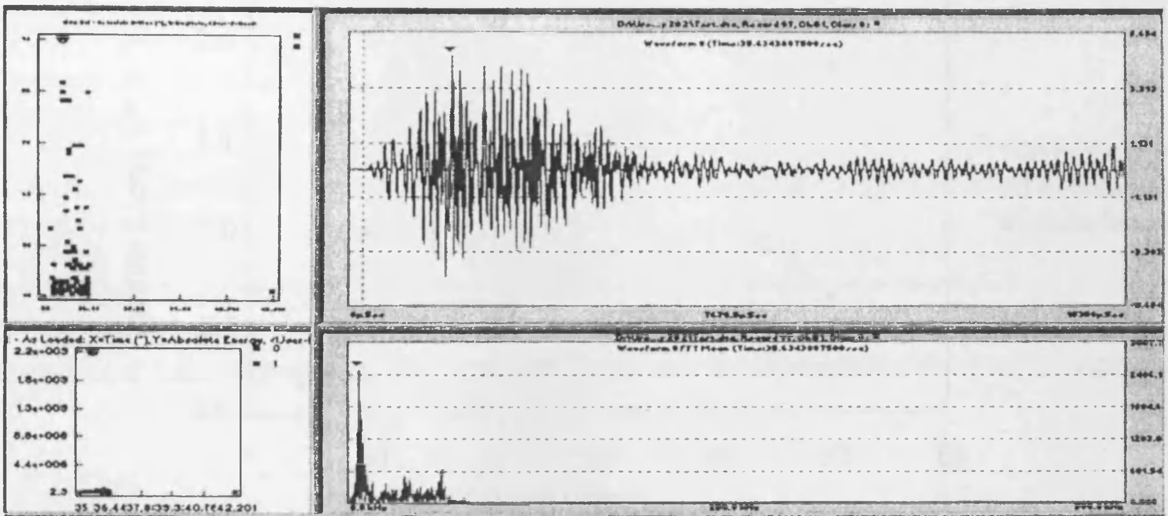

Number	Class ID	Channel	Parametric 1	Parametric 2	Risetime	Counts	Energy	Duration	Amplitude	Threshold
97	0	1	-0.00152593	0.0021363	1747	3556	65535	581418	98	40
98	0	3	-0.00274667	0.00457778	12	1	0	23	41	40
99	1	5	-0.00305185	-0.00366222	205	1195	747	25458	74	40

Figure 2: Waveforms and parameters from a typical small specimen fracture (200mm^2 Area).

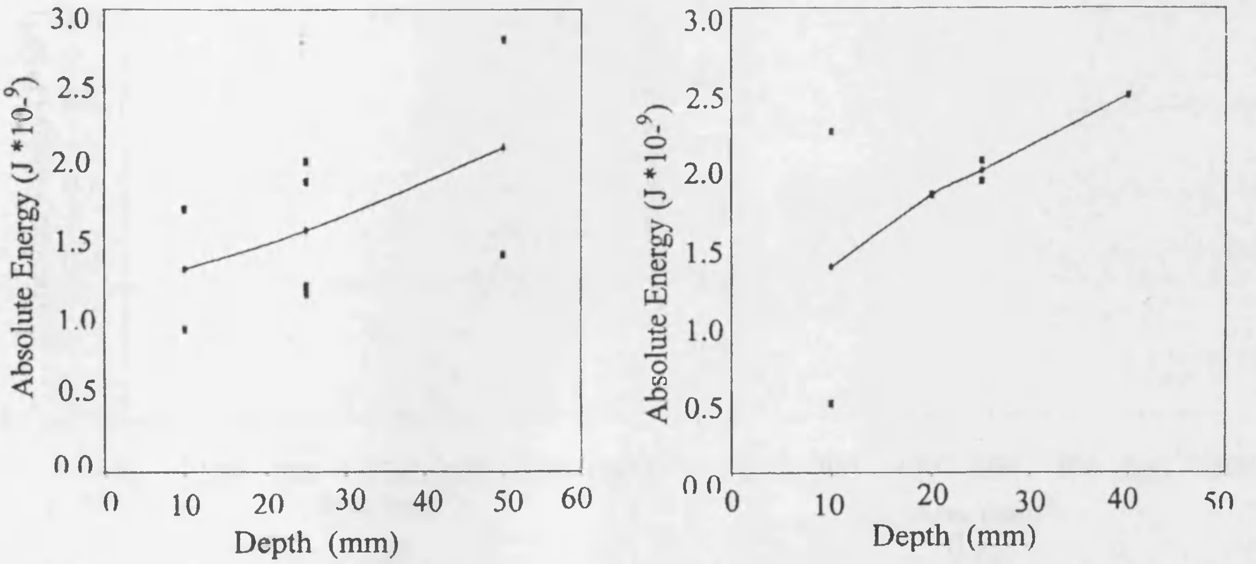

(a) (b)

Figure 3: (a) Variation of absolute AE energy produced during the failure of 200mm^2 area specimens with depth. (b) Variation of absolute energy produced during the failure of 500mm^2 area specimens with depth. (Low frequency sensors)

As mentioned previously the amount of AE energy recorded during the failure is expected to be related to the size of the crack in some way. Figs. 3a and 3b show the amount of energy recorded on the low frequency sensor for specimens with varying crack depths but with constant crack areas. These graphs show that even though the crack area is constant the amount of energy increases with crack depth. Fig. 4 represents similar data to that of Fig. 3a and 3b but shows how the energy varies with crack depth for all three of the sensors. Again even though the crack area is a constant 500mm^2 the energy increases with crack depth on all channels. Since high frequencies attenuate quickly in concrete, the sensors with lower resonant frequency record higher amounts of energy.

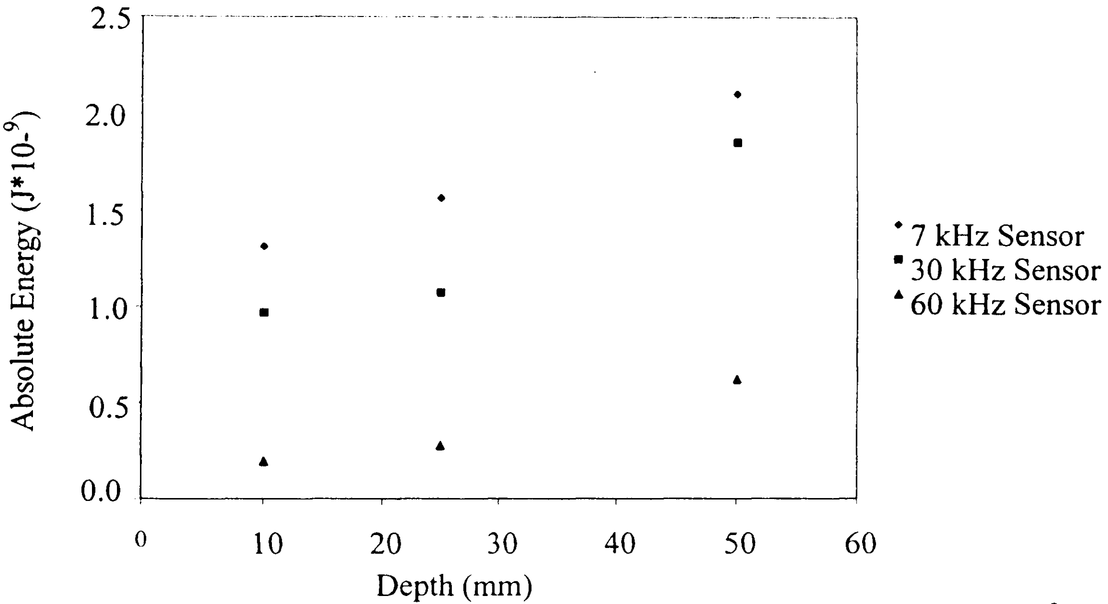

Figure 4: Variation of absolute AE energy with crack depth for a constant area of 500mm^2 on all channels.

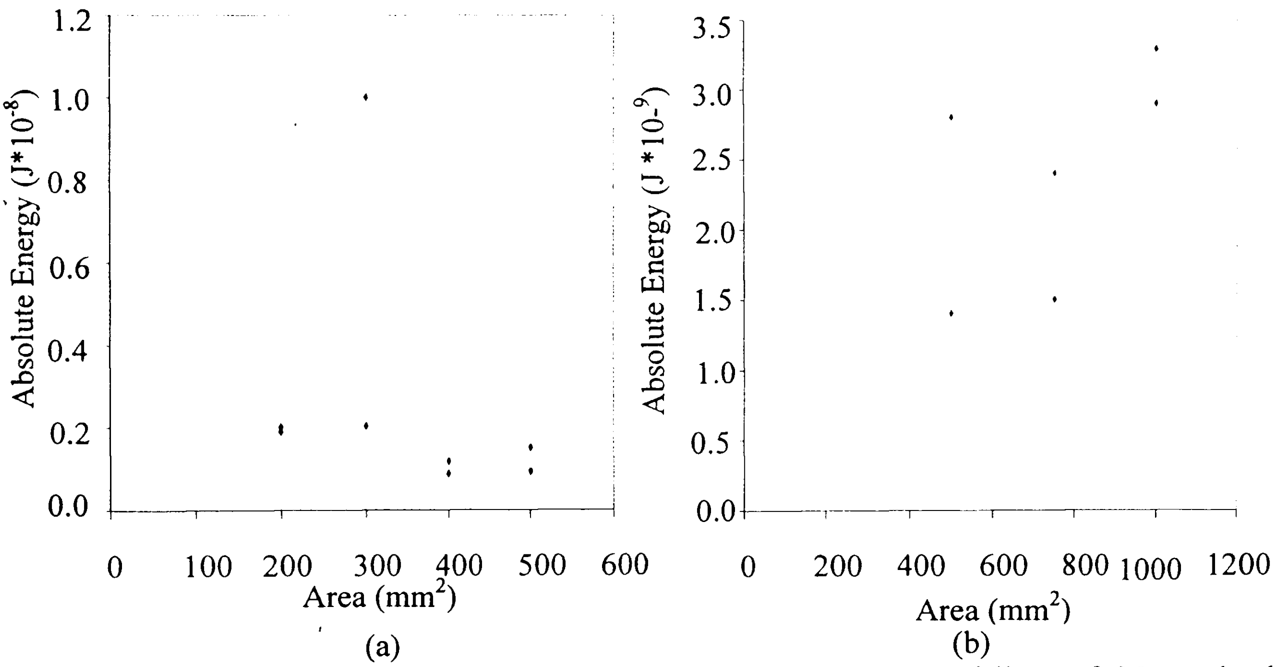

Fig. 5: (a) (a) Variation of absolute AE energy produced during the failure of 25mm depth specimens of varies with area. (b) Variation of absolute AE energy produced during the failure of 50mm depth specimens with area.

If AE energy is related to crack depth only then no increase between AE energy and crack area is expected. Figs. 5a and 5b show the amount of energy recorded on the low frequency sensor for specimens with varying crack areas but with constant crack depths. From these graphs it can be seen that even though there is an increase in crack area there is no increase in AE energy. In fact the amount of energy is very similar for all crack areas. This suggests that if the crack depth remains constant then there will be no increase in energy produced by the crack. Thus from this series of experiments it can be determined that the amount of crack energy could be related to the depth of the crack and not the size of its area. One reason for this could be the fracture velocity. A crack of increasing depth will produce a longer event. This will be investigated further.

Conclusions

In this paper a study was performed to correlate AE energy produced during the failure of mortar specimens to either crack area or crack depth. No significant relationship between AE energy and fracture energy was found. It was found that the amount of AE energy produced by the failure of the mortar specimens could be related to crack depth. This is probably related to fracture velocity and will be subject to further investigation. It is hoped that these results and results from further testing can be used to aid the quantification of crack size based on energy release from concrete structures in the field.

Acknowledgements

The authors would like to express their gratitude to all those who were involved in this research. They would like to especially thank Dr. Rhys Pullin at the Cardiff School of Engineering, Cardiff University, Mr Phil Cole and Mr Jon Watson of Physical Acoustics Limited for their valuable advice during of these experiments.

References

[1] Ohtsu, M. "A review of acoustic emission in civil engineering with emphasis on concrete" Journal of Acoustic Emission, Vol. 8, No. 4, (1989), pp 93-98

[2] Drouillard, T.F. "AE literature – Concrete" Journal of Acoustic Emission, Vol. 5, No.2, (1986), pp 103-109

[3] Ohtsu, M. "The history and development of acoustic emission in concrete engineering" Magazine of Concrete Research, 48, No. 177, (1996), pp 321-330

[4] Ohtsu, M., Watanabe, H. "Quantitative damage estimation of concrete by AE" Construction and Building Materials 15, (2001), pp 217-224.

[5] Yuyama, S., Li, Z., Yoshizawa, M., Tomokiyo, T., Uomoto, T. "Evaluation of fatigue damage in reinforced concrete slab by acoustic emission" NDT&E International 34, (2001), pp 381-387

[6] *Henkel, D.P., Wood, J.D.* " Monitoring concrete reinforced with bonded surface plates by the acoustic emission method" NDT&E International Volume 24 Number 5 (1991).

[7] Landis E.N., Baillon L. " Experiment to relate acoustic emission energy to fracture energy of concrete" Journal of Engineering Mechanics. (2002), pp 698-702

Key Engineering Materials Vols. 245-246 (2003) pp. 443-450
online at http://www.scientific.net

Moment Tensor Analysis of Acoustic Emission in Concrete Specimens Failed in Four-Point Bending

P. Beck[a], R.J. Lark and K.M. Holford

Cardiff School of Engineering, Division of Mechanical Engineering,
Cardiff University, Queen's Buildings, The Parade, P.O.Box 925, Cardiff CF24 0YF, UK

[a]Beckp1@cf.ac.uk

Keywords: Acoustic Emission, Concrete, Moment Tensor Analysis

Abstract

Acoustic emission (AE) has been applied extensively to the non-destructive evaluation of materials and structures. In traditional AE measurement, various AE parameters are detected, recorded and analysed to produce information on the characteristics of the material's fracturing behaviour. A quantitative analysis of AE waveforms, known as SiGMA (Simplified Green's Function for Moment Tensor Analysis), can also be used. From this analysis the location of the AE sources can be found and classified into shear or tensile cracks, and their orientations can also be determined.

Selection of the initial amplitudes of the P-waves of recorded waveforms enables six independent tensor components to be resolved. To determine source kinematics (crack type and orientation) of a crack, eigenvalues of the moment tensor need to be calculated. This leads to the unified decomposition of the eigenvalues into a shear component, a CLVD (Compensated Linear Vector Dipole) component and a mean component. The aim of the decomposition is to determine the magnitude of shear and tensile contribution of an AE source, thus classifying sources into a crack type. Since the orientations of a shear crack and tensile crack can be determined using eigenvectors, source kinematics can be completely identified from AE waveforms.

Notched concrete specimens were failed under a static four-point load. The AE waveforms produced during failure were analysed by the SiGMA procedure. The results demonstrate the ability of moment tensor analysis to determine the location, type and orientation of the crack.

Introduction

Acoustic Emission (AE) is commonly used as a non-destructive testing (NDT) technique, and has been used to monitor many types of concrete structures including bridges, dams, tunnels, and slopes and embankments [1]. In these structures, detailed observation is needed for the prediction of their service life. AE is a useful technique since it is a dynamic inspection method that provides information on the growth of a discontinuity or defect of both plain and reinforced concrete and it can detect and evaluate emissions generated throughout an entire structure in a single test. Also AE methods will not interfere with the users of the structure, such as traffic and pedestrians.

The majority of in-service concrete structures are reinforced with steel rebar. The use of AE methods to detect cracking on the reinforcement and concrete, delamination of the reinforcement and concrete, and detect the corrosion of the reinforcement, has been well documented. In concrete engineering, AE has been used as both a technique to investigate the structural integrity of concrete structures and as an aid to study the material properties. For concrete specimens there are two ways to analyse data acquired by the AE instrumentation. The first one is parameter analysis, which has been widely and frequently employed. The other method of analysis is quantitative waveform analysis. This method of analysis is known as moment tensor analysis (MTA).

MTA is an AE post-test analysis technique used to identify the crack kinematics (crack type and crack orientation) from the recorded AE waveforms. The procedure developed for MTA was discovered by Ohtsu [2] and is called *SiGMA* (*Si*mplified *G*reens function for *M*oment tensor *A*nalysis). This procedure determines the crack kinematics by investigating the eigenvalue analysis of a moment tensor. From the results of the eigenvalue analysis, the eigenvalues can be separated into three individual components: the shear component, the CLVD component (compensated linear vector dipole) and the hydrostatic/mean component. After considering the ratios of these components, the AE sources can be classified as either tensile, mixed-mode or shear cracks. Secondly, the eigenvectors of the moment tensor will allow the determination of the orientation of the crack. Thus from the moment tensor the crack kinematics can be found, [3].

The moment tensor representation has been used mainly to model the mechanisms of earthquakes. The mechanisms of earthquakes and of AE sources are in principal the same, in spite of the fact that the strengths and frequencies differ by orders of magnitude. Therefore, similar modelling can be used for AE sources. MTA has been used successfully on concrete in many applications. An early use of MTA was performed by Ohtsu [4] who embedded an anchor plate into a concrete specimen. This anchor plate was then pulled out of the concrete specimens creating AE. The AE was collected using six AE sensors and was analysed using MTA software. The results showed both shear and tensile cracks situated around the pullout area. Yuyama et al. [5] showed that AE can be used to study and compare the fatigue damage of an in-service and laboratory tested reinforced concrete (RC) slab. Henkel and Wood [6] monitored concrete reinforced with bonded surface plates using AE methods. Concrete beams with internal mild steel reinforcement were failed under four-point loading and a parameter analysis was performed on the recorded AE. Similar research has been carried out on reinforced concrete beams and cylinders including: Yuyama et al. [7], Yuyama et al. [8] and Shiotani et al. [9]. Other applications of MTA include: the study of plain concrete and other cementious materials [10], the study of fracture mechanic parameters [11], and the study of other rock-like materials such as salt rock [12].

Theory

Integral Representation. The displacement U_i (x, t) at a location x, at time t, due to a crack displacement $b_k(y,t)$ is given by integral [13]:

$$U_i(x,t) = \int G_{ip,q}(x,y,t) M_{pq} s(t) ds \,. \tag{1}$$

where:

$G_{ip,q}$ = Spatial derivative of Greens function

s(t) = Source kinematics

M_{pq} is the moment tensor, which is a 3x3 symmetrical matrix as shown below [13].

$$M_{pq} = b\begin{bmatrix} \lambda l_k n_k + 2\mu l_1 n_1 & \mu(l_1 n_2 + l_2 n_1) & \mu(l_1 n_3 + l_3 n_1) \\ Symm & \lambda l_k n_k + 2\mu l_2 n_2 & \mu(l_2 n_3 + l_3 n_2) \\ Symm & Symm & \lambda l_k n_k + 2\mu l_3 n_3 \end{bmatrix}. \tag{2}$$

where:

l_k = (l_1,l_2,l_3) = Displacement vector of the crack

n_k = (n_1,n_2,n_3) =Normal vector to the crack surface

λ,μ = Lame's constants

b = Magnitude of crack

Waveform Parameters. To calculate the components of the moment tensor, the original integral must be simplified so that only the initial motion of the P–wave is considered. The simplified integral can be represented as [14]:

$$U(x,t) = \frac{\gamma_i \gamma_p \gamma_q M_{pq}}{4\pi\rho R (V_p)^3}. \tag{3}$$

where:

R = Distance from an AE source y to the sensor point x.
γ = Direction cosine
V_p = Velocity of the p-wave
ρ = Density of material

So when an AE waveform due to a crack formation is recorded at the sensor, the amplitude of the wave's first motion is represented by the above formula. This means that when the AE waveforms are detected at six or more sensors, the AE source location procedure will attain information on the distance R, its direction cosine $\gamma=(\gamma_i,\gamma_p,\gamma_q)$, and the amplitude of the initial P-wave. To summarise, from the AE source location and the material being used, the velocity of the P-wave, the density of the material, the distance from source to sensor, its direction cosine and the amplitude of the P-wave are known. Thus the moment tensor M_{pq} can be calculated.

Eigenvalue Analysis. The kinematics of a crack are closely related to the principal components of the moment tensor. Since the moment tensor, represented by the matrix in Eq. 2, is a second rank tensor, determination of the principal components is readily performed by eigenvalue analysis. For an isotropic material, the three eigenvalues are obtained from Eq. 2 as follow [4]:

Maximum eigenvalue;

$$\omega = \mu b\left(\frac{l_k n_k}{1-2v}+1\right). \tag{5}$$

Intermediate eigenvalue:

$$\omega = \frac{2\mu b l_k n_k}{1-2v}. \tag{6}$$

Minimum eigenvalue;

$$\omega = \mu b\left(\frac{l_k n_k}{1-2v}-1\right). \tag{7}$$

where v is Poisson's ratio.

Three eigenvectors corresponding to these eigenvalues are also determined.

$$\text{Maximum Eigenvector} = l_k + n_k. \tag{8}$$

$$\text{Intermediate Eigenvector} = l_k n_k. \tag{9}$$

$$\text{Minimum Eigenvector} = l_k - n_k. \tag{10}$$

Components of a Shear Crack. When a crack is a pure shear crack, the angle between l and n is ninety degrees. Mathematically this means the dot product of l and n is zero, substituting this into the eigenvalues gives:

$$\text{Maximum eigenvalue;} \quad \omega = \mu b. \tag{11}$$

$$\text{Intermediate eigenvalue;} \quad \omega = 0. \tag{12}$$

$$\text{Minimum eigenvalue;} \quad \omega = -\mu b. \tag{13}$$

The eigenvalues can be represented by the vector *(X, 0, -X)*.

Components of a Tensile Crack. When there is a tensile crack the directions of l and n are parallel. Mathematically this means that the dot product of l, n is equal to 1. This can be substituted into the eigenvalues in a similar method as above to give:

Maximum eigenvalue $$\omega = \frac{2\mu b(1-v)}{1-2v} \tag{14}$$

Intermediate eigenvalue/minimum eigenvalue $$\omega = \frac{2\mu b v}{1-2v}. \tag{15}$$

Two components, the deviatoric component and the Mean/Hydrostatic component represent a tensile crack. In seismology, the deviatoric components are known as the compensated linear vector dipole (**CLVD**) ([4], [15]). The mean component can be calculated by adding the three eigenvalues and then dividing by three. The CLVD component is calculated by taking each eigenvalue, equations 16 and 17 and deducting the mean component.

The mean/hydrostatic component for all the eigenvalues is equal to:

$$\omega = \frac{2\mu b(1+v)}{3(1-2v)}. \tag{16}$$

The eigenvalues for the CLVD component are:

Maximum eigenvalue; $$\omega = \frac{4}{3}\mu b. \tag{17}$$

Intermediate/Minimum eigenvalue; $$\omega = \frac{-2}{3}\mu b. \tag{18}$$

From these values the vector *(Y, -0.5Y, -0.5Y)* represents the eigenvalues for the CLVD component and the vector *(Z, Z, Z)* represents the eigenvalues for the hydrostatic component. This is shown diagrammatically in Fig. 1.

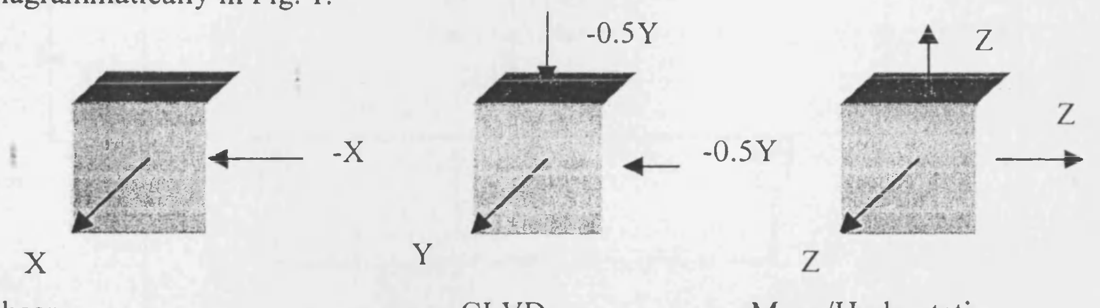

Figure 1. Illustration of eigenvalues for the three crack components [3]

By comparing each side of the cubes and normalising by the maximum eigenvalue equations 19 - 21 can be derived.

$$\frac{MaxEigenvector}{MaxEigenvector} = X + Y + Z = 1. \tag{19}$$

$$\frac{IntermediateEigenvalue}{MaxEigenvalue} = -0.5Y + Z. \tag{20}$$

$$\frac{MinEigenvalue}{MaxEigenvalue} = -X - 0.5Y + Z. \tag{21}$$

Since the eigenvalues are known, these equations can be solved simultaneously so that the values for X, Y and Z can be calculated. Since X was defined as the shear component, for a pure shear crack X=1 since there is no Y or Z component. Similarly if X=0, then there is no shear component so this means the crack is tensile. Therefore if X is less than 0.4 then the crack is tensile. If X is between 0.4 and 0.6 the crack is a medium crack or a mixed-mode crack and if X is greater than 0.6 then the crack is shear.

The eigenvectors of the moment tensor matrix in Eq. 2 can be represented in terms of l and n (the orientation and the normal of the crack). From eigenvalue analysis the eigenvectors can be calculated, as given in equations 10, 11 and 12. Using these equations the values for l and n can be calculated. Therefore the orientation is known. Thus from MTA the crack kinematics of an event can be found using the post-test analysis procedure known as SiGMA. This procedure was performed using software created by PAC (Physical Acoustics Corporation).

Experimental Procedure

Specimen Details and Loading Method. The SiGMA procedure was applied to the practical AE waveforms, which were recorded during the failure of a notched concrete beam in four-point bending. The mix proportions of the concrete specimen were arranged so that the mass ratios of the cement, fine aggregate, coarse aggregate and water were 1:1.8:2.8:0.5. The concrete specimens were of dimensions 150x150x600 mm and contained a notch at the centre with a depth of 60mm. The load applied during failure of the specimen was controlled by a crack mouth opening displacement (CMOD) gauge which was set to a constant rate of 0.0002mm/s. The configuration of the specimen and sensor locations are shown in Fig. 2.

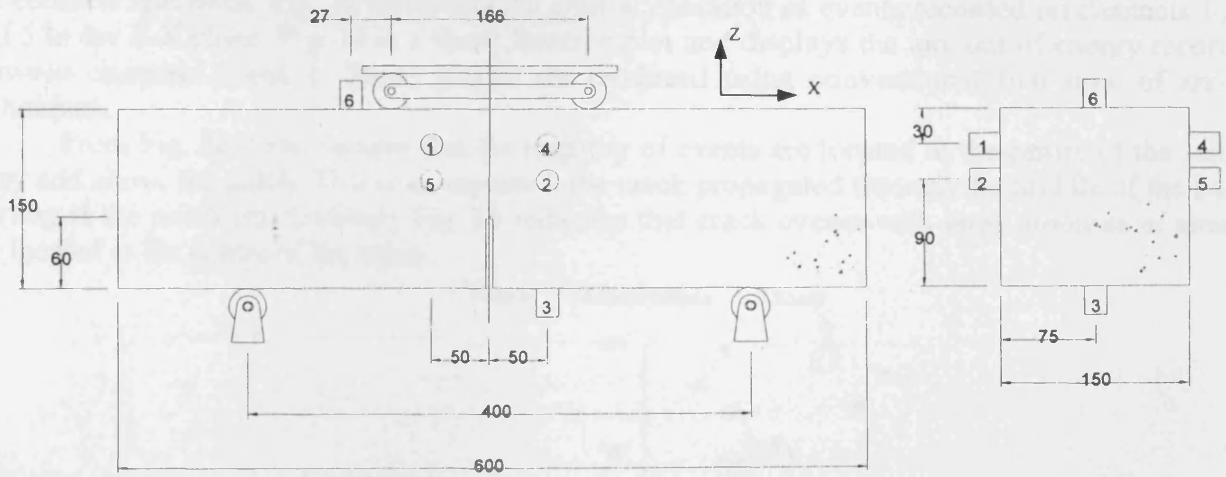

Figure 2: Illustrations of four-point bend test with AE sensor locations

Instrumentation. Six AE sensors were attached to the concrete specimen to detect AE waveforms during failure. These sensors had a resonance of 30kHz and were amplified by 40dB in the pre-amplifier. A threshold of 65dB was used so that only large concrete cracking was monitored. AE waveforms detected at the sensors were recorded by a digital memory, which converted analogue records into digital records at a sampling rate of 1MHz. The frequency detection range employed was 10kHz-200kHz. The number of AE events recorded was 65 from which 18 were selected for the SiGMA analysis. The P-wave velocity in concrete is 4000m/s.

Results and Discussion

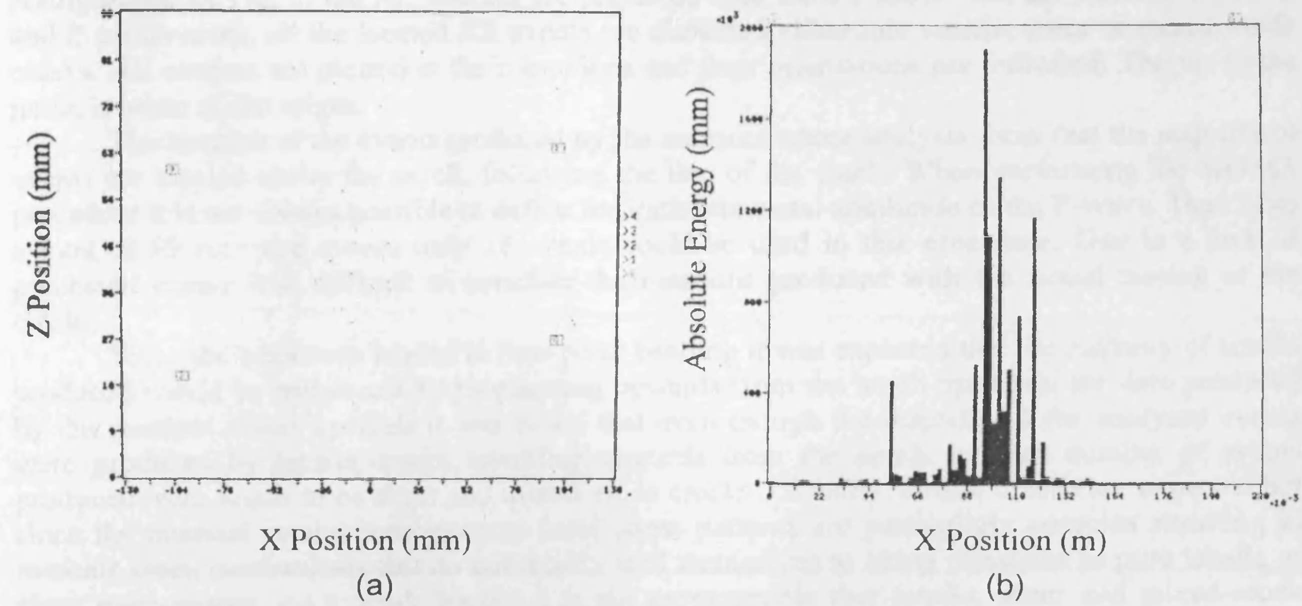

Figure 3: (a) Arbitrary location (produced by common time of arrival procedures) produced in the *x-z* plane where the tip of the notch is the origin. (b) Linear location plot showing the amount of absolute energy between channels one and two.

The above graphs, Fig. 3a and Fig. 3b, show two different location plots recorded during failure of the concrete specimen. Fig. 3a represents the arbitrary location of events recorded on channels 1,2,4 and 5 in the Z-X plane. Fig. 3b is a linear location plot and displays the amount of energy recorded between channels 1 and 2. These graphs are produced using conventional first time of arrival techniques.

From Fig. 3a it can be seen that the majority of events are located in the centre of the sensor array and above the notch. This is as expected: the crack propagated through the middle of the beam starting at the notch tip. Similarly Fig. 3b indicates that crack events with large amounts of energy are located at the centre of the beam.

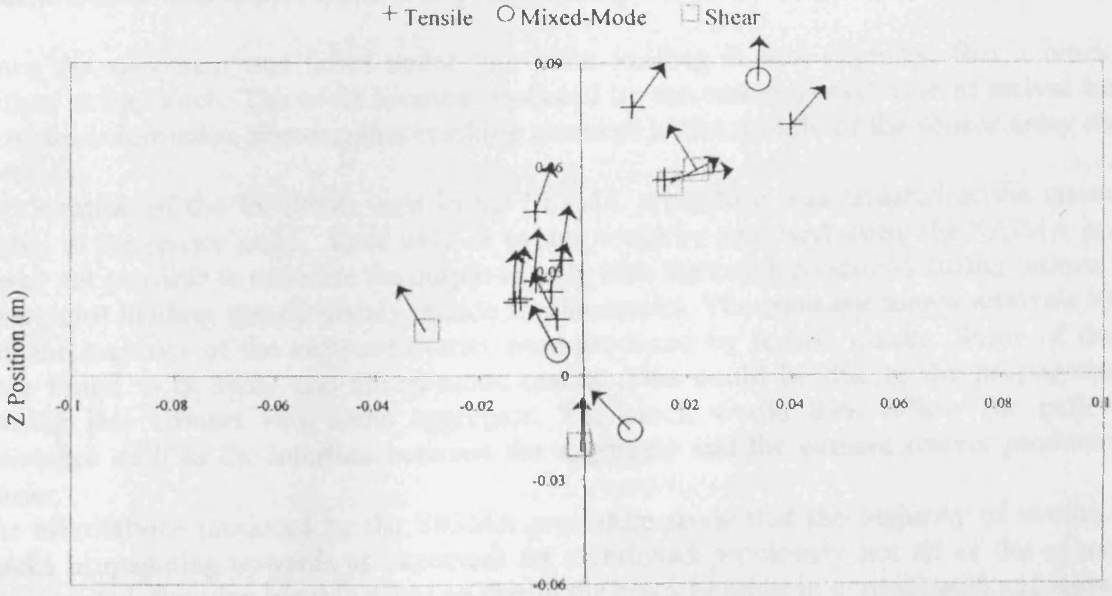

Figure 4: Location of AE sources and their crack kinematics produced by moment tensor analysis.

The results from the SiGMA analysis are plotted in Fig.4. With reference to the co-ordinate configuration of Fig. 3, the AE sources are projected onto the *x-z* plane. On the basis of the X, Y and Z components, all the located AE events are classified either into tensile, shear or mixed-mode cracks. AE sources are plotted at their locations and their orientations are indicated. The tip of the notch is taken as the origin.

The location of the events produced by the moment tensor analysis show that the majority of events are located above the notch, following the line of the crack. When performing the SiGMA procedure it is not always possible to define the initial time and amplitude of the P-wave. Thus from a total of 65 recorded events only 18 events could be used in this procedure. Due to a lack of processed events it is difficult to correlate the locations produced with the actual motion of the crack.

Since the beam was loaded in four-point bending it was expected that the majority of cracks produced would be tensile cracks propagating upwards from the notch tip. From the data produced by the moment tensor analysis it was found that even though the majority of the analysed events were produced by tensile cracks travelling upwards from the notch, a small number of events produced were found to be shear and mixed-mode cracks. Globally, tensile cracks are expected but since the material is non-homogeneous local stress patterns are particularly complex resulting in intricate crack mechanisms that do not readily lend themselves to being classified as pure tensile or sheer mechanisms. As a result, locally it is not unreasonable that tensile, sheer and mixed-mode cracks can be generated, propagating in any direction.

Arrows on Fig. 4 represent the orientation of the events. Again it was expected that the majority of the cracks produced during failure would moved upwards in the z-direction. This is not always the case since a crack could propagate into a piece of aggregate and then travel along the path of least resistance. Fig. 4 suggests that the cracks initiate at the notch, travelling to the left of the centre initially then passing to the right hand side before eventually failing.

Conclusions

Theoretical developments on the moment tensor analysis of AE waveforms have been summarised. The moment tensor analysis of AE based on the SiGMA procedure provides quantitative information of crack kinematics. The procedure was applied to AE data produced during the failure of a concrete specimen loaded under four-point bending. The following conclusions were derived:

1. Since the specimen was failed under four-point loading it was expected that a crack would initiate at the notch. The event location produced by the conventional time of arrival technique provides information showing that cracking occurred in the middle of the sensor array above the notch tip.
2. The location of the 18 events used in the SiGMA procedure was situated at the notch region within in the sensor array. Since only 18 events could be analysed using the SiGMA procedure it was not possible to correlate the output exactly with the crack produced during failure.
3. Four-point loading should mainly induce tensile cracks. The moment tensor analysis identified that the majority of the analysed events were produced by tensile cracks. Some of the events were found to be shear and mixed-mode cracks. This could be due to the propagating crack coming into contact with some aggregate. The crack would then follow the path of least resistance such as the interface between the aggregate and the cement matrix producing shear cracks.
4. The orientations produced by the SiGMA procedure show that the majority of events indicate cracks propagating upwards as expected. As mentioned previously not all of the events are in the expected direction but this could be due to the crack coming in contact with aggregate.

Acknowledgements

The authors would like to express their gratitude to all those who were involved in this research. They would like to especially thank Dr. Rhys Pullin at Cardiff School of Engineering, Cardiff University and Mr Timothy Bradshaw of Physical Acoustics LTD for their valuable efforts during these experiments.

References

[1] Ohtsu M. "A review of acoustic emission in civil engineering with emphasis on concrete" Journal of Acoustic Emission, Vol. 8, No. 4, (1989), pp 93-98.

[2] Ohtsu M. "Simplified moment tensor analysis and unified decomposition of acoustic emission source: application to in-situ Hydrofracturing test" Journal of Geographical Research, Vol. 96, No. B$, (1991), pp 6211-6221.

[3] Shigeishi M, Ohtsu, M " Identification of AE Sources by Using SiGMA-2D Moment Tensor Analysis" Acoustic Emission: Standards and Technology Update, ASTM STP 1353, S.J. Vahaviolos, Ed., American Society for Testing and Materials, West Conshohken, PA, (1999).

[4] Ohtsu, M "Source Kinematics of Acoustic Emission Based on a Moment Tensor" NDT International, Vol. 22, No.1, (1989), pp 14-20

[5] Yuyama S, Li Z-W, Yoshizawa M, Tomokiyo T, Uomoto T. "Evaluation of fatigue damage in reinforced concrete slab by acoustic emission" NDT&E International 34, (2001), pp 381-387.

[6] Henkel D.P, Wood J.D, " Monitoring concrete reinforced with bonded surface plates by the acoustic emission method" NDT&E International Volume 24 Number 5 (1991).

[7] Yuyama S, Li Z, Yoshihiro I, Arazoe M. " Quantitative analysis of fracture process in RC column foundation by moment tensor analysis of acoustic emission" Construction and Building materials 13 (1999), pp 87-97.

[8] Yuyama S, Okamoto T, Shigeishi M, Ohtsu M. "Cracking process evaluation in reinforced concrete by moment tensor analysis of acoustic emission" Journal of Acoustic Emission vol. 13, numbers ½ (1995), pp 14-20

[9] Shiotani T, Shigeishi M, Ohtsu M. "Acoustic emission characteristics of concrete piles" Construction and Building Materials 13 (1999), pp 73-85.

[10] Shigeishi M, Ohtsu M. " Acoustic emission moment tensor analysis: development for crack identification in concrete materials" Construction and Building Materials 15 (2001) 311-319.

[11] Munwam M, Ohstu M, "Stress intensity factors in concrete by moment tensor analysis of acoustic emission" Materials and Evaluation November (1999), pp 1178-1182

[12] Manthei G, Eisenblatter J, Dahm T, "Moment tensor evaluation of acoustic emission sources in salt rock" Construction and Building Materials 15 (2001), pp 297-309.

[13] Ohtsu M, Ono K. " A generalised theory of AE and Green's functions in a half space" Journal of Acoustic Emission, Vol. 3. No. 1. (1984), pp 27-40

[14] Suaris, W and Van Mier, J.G.M " Acoustic Emission Source Characterisation in Concrete Under Biaxial Loading" Materials and Structure, Vol. 28, (1995), pp 444-449

[15] Knopoff L., Randall M.J. "The compensated linear-vector dipole: a possible mechanism for deep earthquakes" Journal of Geophysical Research, 75, 26, (1970), pp 4957-4963